Fakultät für Mathematik, Informatik und Naturwissenschaften

RWTH AACHEN UNIVERSITY

Performance of the GE1/1 detectors for the upgrade of the CMS Muon Forward system

Von der Fakultät für Mathematik, Informatik und Naturwissenschaften der RWTH Aachen University zur Erlangung des akademischen Grades eines Doktors der Naturwissenschaften genehmigte Dissertation

vorgelegt von

M.Sc. Giovanni Mocellin

aus

Bassano del Grappa, Italy

CERN-THESIS-2021-327
19/07/2021

Berichter*:* *Univ.-Prof. Dr. rer. nat. Thomas Hebbeker*

apl. Prof. Dr. rer. nat. Oliver Pooth

Tag der mündlichen Prüfung*:* *19.07.2021*

Diese Dissertation ist auf den Internetseiten der Universitätsbibliothek verfügbar.

Abstract

The CERN Large Hadron Collider (LHC) will undergo major upgrades over the course of the decade that will lead to the High Luminosity LHC. The proton-proton collisions will reach a center-of-mass energy of 14 TeV, with an ultimate instantaneous luminosity of 7.5×10^{34} cm^{-2}s^{-1} delivered to each of the large experiments. The foreseen total integrated luminosity after ten years of operations is 4000 fb^{-1}. While this allows for high-precision studies and potential new discoveries, it also imposes upgrades to the experiments in order to sustain the higher particle fluxes and the larger radiation doses. This thesis focuses on the Gas Electron Multipliers (GEM) detectors that will contribute to the performance enhancement of the forward regions of the Compact Muon Solenoid (CMS) experiment. Triple-GEM chambers will be installed in three stations of the CMS endcaps with the aim of ensuring redundancy and increased coverage of the muon system. The pilot project of the CMS muon system upgrade is the first GEM station (GE1/1), which was installed between July 2019 and September 2020 and will begin operation in the LHC Run 3 in 2022. The GE1/1 is meant to complement the present Cathode Strip Chambers (ME1/1) in order to improve the muon track reconstruction and to reduce the trigger rate, thanks to the suppression of fake candidates. The main subject of the thesis is the GE1/1 detector validation, which ensured their conformity to the established requirements prior to the installation. An analysis of the chamber signal amplification has been conducted with a focus on the uniformity across their $\mathcal{O}(0.5\ \mathrm{m}^2)$ surface area. This revealed mild gas gain non-uniformities, mostly concentrated around the central part. The high voltage stability has been verified and improved thanks to a dedicated training. The frontend electronics has also undergone an in-depth study that established its optimal configuration. This led to a reduction of the applied frontend thresholds of about 30%. Subsequently, the detection performance has been thoroughly investigated with cosmic ray muons. The chambers were characterized in terms of detection efficiency, signal spatial extension and spatial resolution. The attained results confirmed an average efficiency plateau of $96 - 97\%$, an average signal width of $600 - 700$ µm and a spatial resolution of $150 - 200$ µrad at the efficiency plateau. Each of the qualification tests will be detailed in the thesis, as well as the encountered issues and the developed solutions. Finally, an outlook on the GE1/1 commissioning activities will give an insight on the steps for a full integration of the GEM subsystem within the CMS environment.

Zusammenfassung

Im Laufe des nächsten Jahrzehnts wird der CERN Large Hadron Collider (LHC) zum High Luminosity LHC (HL-LHC) aufgerüstet. Die Proton-Proton-Kollisionen werden eine Schwerpunktsenergie von 14 TeV erreichen, mit einer ultimativen instantanen Luminosität von 7.5×10^{34} cm^{-2}s^{-1}, die an jedes der vier großen LHC Experimente geliefert wird. Die voraussichtliche integrierte Gesamtluminosität nach zehn Jahren Betrieb beträgt 4000 fb^{-1}. Während dadurch einerseits hochpräzise Studien und potentielle neue Entdeckungen ermöglicht werden, sind andererseits Upgrades der Experimente zwingend notwendig, um die höheren Teilchenflüsse und die größeren Strahlungsdosen auszuhalten. In dieser Arbeit liegt der Fokus auf den Gas Electron Multiplier (GEM) Detektoren, die zur Leistungssteigerung des Compact Muon Solenoid (CMS) Experiment im Vorwärtsbereich beitragen werden. Triple-GEM Kammern werden in drei Stationen der CMS-Endkappen installiert, mit dem Ziel, volle Redundanz und einen größeren Detektionsbereich des Myonensystems zu gewährleisten. Das Pilotprojekt der Aufrüstung des CMS-Myonensystems ist die erste GEM-Station (GE1/1), die zwischen Juli 2019 und September 2020 installiert wurde und im LHC-Lauf 3 im Jahr 2022 in Betrieb gehen wird. Die GE1/1-Station soll die bisher installierten Kathodenstreifen-Kammern (ME1/1) ergänzen, um die Rekonstruktion der Myonenspur zu verbessern und die Triggerrate durch die Unterdrückung von Fake-Kandidaten zu reduzieren. Das Hauptthema der Arbeit ist die Validierung der GE1/1-Detektoren, die die Konformität der Detektoren mit den festgelegten Anforderungen vor der Installation sicherstellte. Eine Analyse der Signalverstärkung der Kammern wurde durchgeführt, wobei der Fokus auf der Gleichförmigkeit über ihre $\mathcal{O}(0,5\ \mathrm{m}^2)$-große Oberfläche lag. Dabei wurden leichte Ungleichmäßigkeiten in der Gasverstärkung festgestellt, die sich hauptsächlich auf den zentralen Bereich konzentrierten. Die Hochspannungsstabilität wurde verifiziert und dank eines speziellen Trainings verbessert. Die Frontend-Elektronik wurde ebenfalls einer eingehenden Untersuchung unterzogen, bei der ihre optimale Konfiguration ermittelt wurde. Dies führte zu einer Reduzierung der verwendeten Frontend-Schwellenwerte um etwa 30%. Anschließend wurde die Detektionsleistung mit kosmischen Myonen gründlich untersucht. Die Kammern wurden in Bezug auf die Detektionseffizienz, die räumliche Ausdehnung der Signale und die räumliche Auflösung charakterisiert. Die erhaltenen Resultate bestätigten ein durchschnittliches Effizienzplateau von $96-97\%$, eine durchschnittliche Signalbreite von $600-700$ µm und eine räumliche Auflösung von $150-200$ µrad auf dem Effizienzplateau. Jeder der Qualifikationstests wird in der Arbeit detailliert beschrieben, ebenso wie die aufgetretenen Probleme und die entwickelten Lösungen. Schließlich wird ein Ausblick auf die GE1/1-Inbetriebnahmeaktivitäten Einblicke in die Schritte zur vollständigen Integration des GEM-Subsystems in die CMS-Umgebung liefern.

Contents

Introduction **1**

1 LHC and CMS **3**

1.1 The Large Hadron Collider . . . 3

1.1.1 The LHC machine . . . 3

1.1.2 High Luminosity LHC . . . 7

1.2 The CMS experiment . . . 7

1.2.1 The CMS design and characteristics . . . 9

1.2.2 The Silicon Tracker . . . 11

1.2.3 The Electromagnetic Calorimeter . . . 11

1.2.4 The Hadron Calorimeter . . . 12

1.2.5 The solenoid magnet . . . 12

1.2.6 The Muon System . . . 13

1.2.6.1 Drift Tube Chambers . . . 15

1.2.6.2 Cathode Strip Chambers . . . 16

1.2.6.3 Resistive Plate Chambers . . . 16

1.2.7 The CMS trigger system . . . 17

1.2.7.1 The L1 Trigger . . . 18

1.3 The CMS upgrades . . . 20

1.3.1 The muon system upgrades . . . 20

2 Gas Electron Multipliers **25**

2.1 Interactions of ionizing radiation with matter . . . 25

2.1.1 Interactions of charged particles with matter . . . 26

2.1.2 Interactions of photons with matter . . . 30

2.1.3 Radiation detection . . . 32

2.2 Evolution of gaseous detectors . . . 32

2.3 Working principles of gaseous detectors . . . 35

2.3.1 Ionization of the gas . . . 35

2.3.2 Motion of charged particles in electric and magnetic fields . . . 36

2.3.3 Avalanche process . . . 39

2.3.4 Signal formation on the readout . . . 41

2.4 Fundamentals of the Gas Electron Multipliers . . . 41

2.4.1 The CMS GEM layout . . . 42
2.4.1.1 The structure . . . 42
2.4.1.2 The foils . . . 43
2.4.1.3 The applied voltages . . . 43
2.4.1.4 The gas mixture . . . 44
2.4.2 Signals in a GEM detector . . . 45
2.4.2.1 Study of GEM signals in Aachen . . . 46
2.5 The CMS GEM GE1/1 . . . 49
2.5.1 Location in CMS . . . 49
2.5.2 Structure of a GE1/1 detector . . . 50
2.5.3 Production of the GE1/1 detectors . . . 55
2.5.4 Services for the GE1/1 . . . 55
2.5.4.1 The gas system . . . 55
2.5.4.2 The low voltage system . . . 56
2.5.4.3 The high voltage system . . . 56
2.5.4.4 The Detector Control System . . . 56
2.5.4.5 The Detector Safety System . . . 57
2.5.4.6 The cooling system . . . 57
2.5.4.7 The backend electronics . . . 57
2.5.5 The GE1/1 on-chamber electronics . . . 58
2.5.5.1 The GEM Electronics Board . . . 58
2.5.5.2 The FEAST . . . 59
2.5.5.3 The OptoHybrid board . . . 59
2.5.5.4 The VFAT3 . . . 61

3 Requirements on GE1/1 65
3.1 Summary of the performance requirements . . . 65
3.2 How to verify compliance with the requirements? . . . 66

4 The GE1/1 chamber performance 69
4.1 Gas gain . . . 69
4.1.1 Effective gas gain . . . 69
4.1.2 Gas gain uniformity . . . 72
4.1.3 Gas gain results for GE1/1 chambers . . . 74
4.1.4 Overview of gas gain uniformity for the GE1/1 production . . . 77
4.2 High voltage stability . . . 79
4.2.1 Definition of HV instability . . . 79
4.2.2 Impact of discharges in early CMS tests . . . 80
4.2.3 Protection to the input of the VFAT channels . . . 82
4.2.4 Prevention of HV instabilities . . . 82
4.2.5 Other effects of the HV discharges . . . 84
4.2.5.1 Permanent short circuits . . . 84

4.2.5.2 Frontend electronics losing synchronization 86
4.3 Noise level and frontend thresholds 87
4.3.1 Determination of frontend thresholds 87
4.3.2 Threshold calibration and noise level quantification: s-curves 88
4.3.3 Instabilities in the VFAT noise levels 89
4.3.3.1 ENC instability 90
4.3.3.2 GEB s-bits issue 92
4.3.4 Quality control of electronics components 94
4.4 Channel response trimming 96
4.4.1 Definition of frontend channels trimming 96
4.4.2 Benefits of frontend channels trimming 98
4.4.3 Trimming procedure and main results 98
4.4.4 Further trimming results and considerations 100
4.5 Conclusions on the chamber performance 103

5 The GE1/1 detection performance 105
5.1 The experimental apparatus: the cosmic ray stand 105
5.1.1 The structure 105
5.1.2 The conventions 106
5.1.3 The services to the stand 107
5.1.4 Cosmic muon distributions 111
5.1.5 Technical choices for the operations and analyses 111
5.2 Data taking at the GEM cosmic ray stand 115
5.3 Detection efficiency 117
5.3.1 QC8: the efficiency test with cosmic rays 118
5.3.2 The data analyses 118
5.3.3 Typical results of the analyses 123
5.3.4 Significant efficiency results for the GE1/1 detectors 129
5.3.5 Summary plots of the GE1/1 production and validation 130
5.3.6 Issues concerning the GE1/1 efficiency 131
5.3.6.1 Disconnected high voltage partition 132
5.3.6.2 Basin effect 133
5.3.6.3 HV working point and environmental conditions 136
5.3.7 Conclusions on efficiency 142
5.4 Cluster size 143
5.4.1 Impact of cluster size on operations 144
5.4.2 Results of cluster size studies 145
5.4.3 Conclusions on cluster size 146
5.5 Spatial resolution 147
5.5.1 Software alignment of chambers for the cosmic ray stand 148
5.5.2 Spatial resolution results 150
5.5.3 Further results of the resolution studies 152

5.5.4 Basin effect impact on spatial resolution 154
5.5.5 Conclusion on spatial resolution 155

6 Conclusions on the GE1/1 performance 157
6.1 Principal results and compliance with the requirements 157
6.1.1 Gas gain 157
6.1.2 Detection efficiency 158
6.1.3 Spatial resolution 158
6.2 Final thoughts 158

7 An outlook on the GE1/1 integration in CMS 159
7.1 The GE1/1 installation in CMS 159
7.2 The GE1/1 commissioning in CMS 160
7.2.1 Local commissioning 161
7.2.2 Global commissioning 163
7.2.3 Preliminary results from the commissioning 164

Appendices 171

A List of acronyms 171

Introduction

Over the decade, the CERN Large Hadron Collider (LHC) will be upgraded to deliver proton-proton collisions at a center-of-mass energy of 14 TeV and an instantaneous luminosity up to 7.5×10^{34} cm^{-2}s^{-1}, exceeding 7.5 times the original design value. Consequently, the LHC experiments are currently undergoing an upgrade campaign that will let them sustain the increased particle rates without any performance degradation.
The Compact Muon Solenoid (CMS) experiment will introduce ameliorations to the DAQ and the trigger infrastructures, as well as extensive improvements of the existing detectors and the addition of new ones. In the muon endcaps, novel gas detectors based on the Gas Electron Multipliers (GEM) technology will be installed in the first and the second disks (GE1/1 and GE2/1) to complement the present Cathode Strip Chambers (CSC). They will also be employed in the ME0 station, in order to extend the muon system coverage up to a pseudorapidity $\eta = 2.8$.
The extensive number of planned interventions required the upgrade operations to start at the beginning of the LHC Long Shutdown 2 in 2019. More than three years of technical stop allowed for the installation of the first GEM station: the GE1/1.
The GE1/1 complements the CSC ME1/1 station, providing additional layers to sample the muon tracks. An increased lever arm in the track segment measurement will allow for an enhanced precision in the muon transverse momentum estimation. Consequently, it will be possible to select the interesting signals and discard the fake candidates more effectively, thus keeping the trigger rate under control. This task is accomplished by 72 GE1/1 detectors installed in the two CMS muon endcaps. Each detector is composed by two paired trapezoidal triple-GEM chambers, which form the so-called GE1/1 super chamber.
The 144 GE1/1 single chambers were produced and tested in $2017 - 2018$ by the CMS GEM collaboration in institutes of seven different countries around the world. After the shipment to the CERN GEM laboratory, the chambers were equipped with the final electronics components and paired into super chambers. The GE1/1 detection performance were then assessed utilizing cosmic ray muons. The verification of the compliance to the imposed performance requirements finally allowed the GE1/1 detector validation and their installation in the CMS endcaps in $2019 - 2020$.

The work reported in this thesis has been carried out in the context of the GE1/1 chamber and super chamber validation. Initially, I have taken part in the assembly and quality control process of some of the chambers, which provided the necessary knowledge to critically evaluate the single chamber behavior and performance. Subsequently, I've contributed to the super chamber

assembly, in particular in refining the high voltage training procedures with the final gas mixture and in defining the electronics tests acceptance criteria. I have also examined the issues of the on-chamber electronics, establishing solutions and workarounds for a reliable long term operation in the CMS environment. I concentrated then on the reduction of the frontend electronics noise and frontend thresholds, developing a new channel response alignment method. Afterwards, the focus was moved towards the definition and the optimization of the super chamber validation apparatus (cosmic rays stand) and of the validation procedures. In parallel, I played a leading role in the creation of the cosmic rays stand data analysis framework. The interpretation of the attained results allowed to identify the detector shortcomings and the possible corrections. For one, the definition of a new correction for the gas gain variations with the environmental conditions. Finally, the results of the cosmic ray tests allowed to validate the GE1/1 detectors for the installation in the CMS experiment. Once the chambers were inserted in the muon endcaps, I've also taken part in the local commissioning, contributing in the assessment of the frontend electronics status and in the HV training procedures.

Summary of the thesis content:

Chapter 1 presents the LHC and the CMS experiment, together with the HL-LHC upgrades.

Chapter 2 introduces the GEM technology, its main characteristics and its application in the first CMS muon endcap station.

Chapter 3 details the requirements imposed to the GE1/1 detectors, in order for them to adequately contribute to the muon track reconstruction and to the Level 1 muon trigger.

Chapter 4 focuses on the performance of the GE1/1 chamber constituents and components. First, the chamber gas gain parameter is evaluated. Then, the high voltage stability is assessed and the effects of the discharges are exposed. Finally, the studies on the noise level and the frontend thresholds are described.

Chapter 5 presents the results obtained in the cosmic rays tests, which characterized the GE1/1 efficiency, cluster size and spatial resolution.

Chapter 6 summarizes the GE1/1 detection performance, comparing it with the requirements.

Chapter 7 presents an overview of the GE1/1 installation and an outlook on the commissioning in CMS.

Chapter 1

LHC and CMS

1.1 The Large Hadron Collider

The Large Hadron Collider [1] (LHC) is the largest proton-proton and heavy ion accelerator ever built. It is based at CERN, Geneva, and it has been designed to allow for particle physics searches at the TeV scale. It can collide protons up to a center-of-mass energy of $\sqrt{s} = 14$ TeV at an instantaneous luminosity of $\mathcal{L} = 10^{34}$ cm^{-2}s^{-1}. It is also capable of colliding heavy ions (lead) with an energy up to 2.76 TeV and a peak luminosity of $\mathcal{L} = 10^{31}$ cm^{-2}s^{-1}.
The first LHC runs took place in 2008, while effective operations started in fall 2010. Since then, it has seen two intense periods of activity, Run 1 and Run 2, as well as two major Long Shutdowns (LS1, LS2) and an Extended Year End Technical Stop (EYETS). The accelerator shutdown periods allowed for upgrades of both the machine and the installed experiments.
The year of writing (2021) corresponds to the last year of LS2. Afterwards, LHC Run 3 is foreseen to last for three years, before the third Long Shutdown. From 2025, the High Luminosity LHC (HL-LHC) upgrades will be implemented, making possible to operate the collider at an instantaneous luminosity up to $5 - 7.5 \times 10^{34}$ cm^{-2}s^{-1}. The expected ultimate value of the integrated luminosity is 4000 fb^{-1}, which will be collected in more than ten years of HL-LHC runs. This will give the possibility to test the standard model predictions with high precision measurements, with the aim to find potential inconsistencies and to investigate the scenarios beyond the standard model.
The latest available update of the LHC project schedule is presented in Figure 1.1.

1.1.1 The LHC machine

The LHC machine is a circular superconducting accelerator and collider. It is installed in a 26.66 km long tunnel at a depth of $45-170$ m below the Swiss and French territories, between the Jura mountains and the Lake Geneva. The same tunnel was previously used for the Large Electron Positron accelerator (LEP), which was shut down in the year 2000.
The LHC consists of eight arcs interleaved by eight straight sections, kept at a temperature of 1.9 K using superfluid helium. This ensures the superconducting regime for the magnets located around the beam pipe. Two beams circulate around the ring in opposite directions within the same structure, crossing in four interaction points where the LHC experiments are installed.

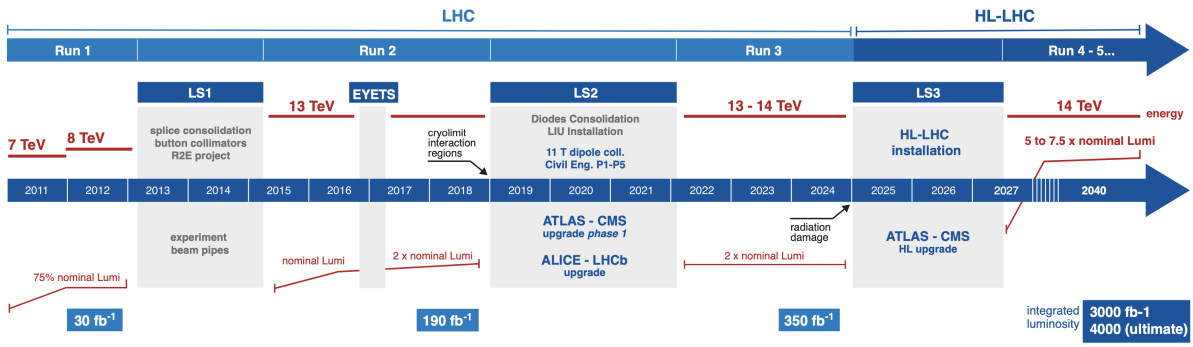

Figure 1.1: Latest available update of the Large Hadron Collider project schedule (April 2021), from [2].

ATLAS (A Toroidal LHC Apparatus) [3] and CMS (Compact Muon Solenoid) [4] are general-purpose experiments meant to study the standard model and the physics beyond the standard model. LHCb (LHC beauty experiment) [5] is focused on the beauty quark physics, in particular to investigate the CP violation mechanism. ALICE (A Large Ion Collider Experiment) [6] is devoted to study the quark-gluon plasma physics, using heavy ion collisions.

The protons for the beams are obtained by ionizing hydrogen gas atoms. They are then pre-accelerated in the chain of acceleration facilities built at CERN over the years for the past experiments (Figure 1.2a).

The beams start from the proton source with an energy of 750 keV. They are subsequently accelerated and organized in bunches in the LINAC2 and in the BOOSTER up to 1.1 GeV. Finally, through the Proton Synchrotron and the Super Proton Synchrotron they reach the injection energy for LHC, fixed at 450 GeV. The design foresees the two proton beams consisting in 2808 bunches, each having around 1.15×10^{11} particles. Initially, in the LHC Run 1 (until 2012), the bunches were separated by 50 ns. In Run 2, the spacing was reduced to 25 ns. This is equivalent to a frequency of 40 MHz, which is the repetition rate of the collisions in the interaction points, also known as 'bunch crossing' (BX). It is common practice to identify a 25 ns time interval as 1 BX, even when not describing a collision. Indeed, the LHC machine and experiments make use of clock sources for the electronics which are aligned to 40 MHz or multiples of it.

The acceleration that is needed to reach the collision energy in the LHC is provided by RF stations, composed of superconducting Radio-Frequency cavities running at 400.8 MHz. The beams are steered along the ring by superconducting Nb-Ti dipole magnets. For 7 TeV protons circulating in a 27 km circumference, equivalent to a radius $\rho \sim 4.3$ km, the required intensity of the magnetic field is 8.3 T. This can be calculated starting from the equation 1.1, applying some corrections due to the presence of bending magnets only in portions of the beam pipe length. In order to attain such fields the magnets are provided with a current of about 11.8 kA:

$$p\,[\mathrm{GeV}] = \frac{q}{e} \cdot 0.3 \cdot B\,[\mathrm{Tesla}] \cdot \rho\,[\mathrm{km}] \ . \tag{1.1}$$

In addition to the acceleration and steering elements, 23 superconducting Nb-Ti quadrupole

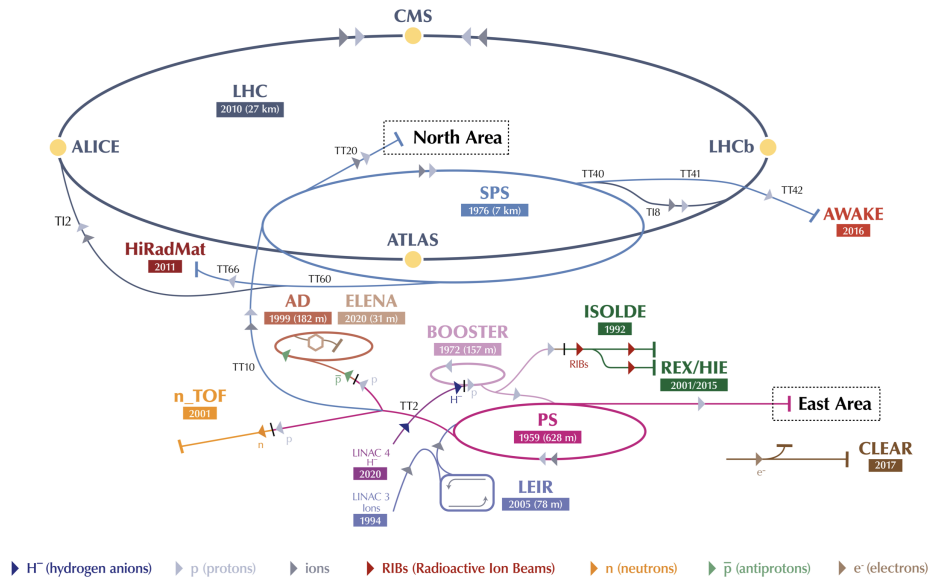

(a) CERN accelerator complex [7].

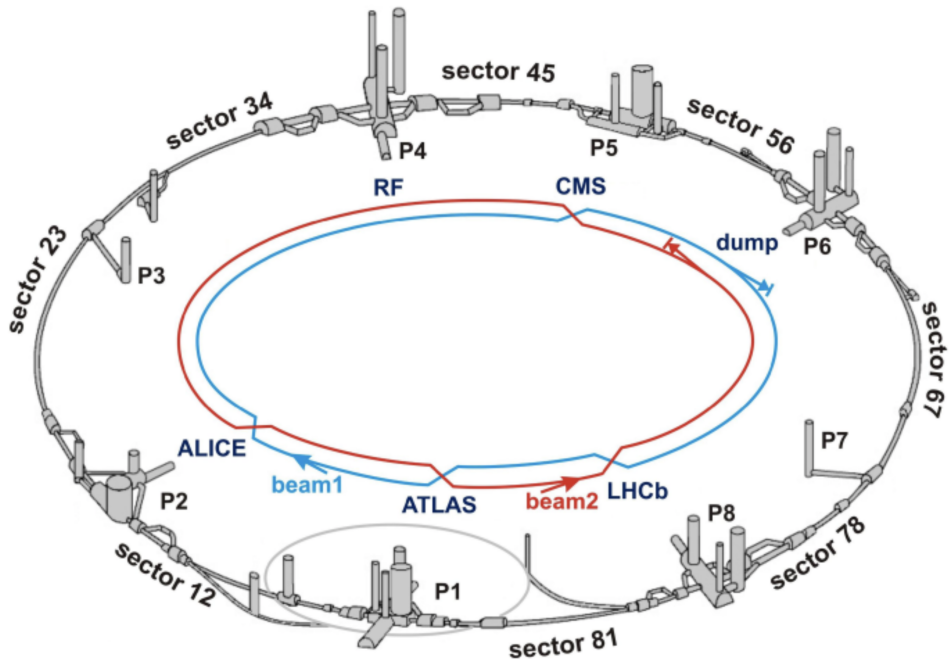

(b) LHC sectors [8].

Figure 1.2: The CERN acceleration chain is schematically presented on the top. The LHC sectors are shown on the bottom.

FODO (Focalizing-Defocalizing) cells [9] are installed, together with sextupoles and octupoles. These are necessary to reduce the cross section of the beams, especially in proximity of the experiments. The attained luminosity per collision region for two Gaussian beams is given by the equation 1.2

$$\mathcal{L} = \frac{N_1 N_2 k_b f}{4\pi\sigma_x\sigma_y} \cdot F \ , \tag{1.2}$$

where N_1 and N_2 are the number of particles in each bunch, k_b the number of bunches and f the revolution frequency. σ_x and σ_y represent the proton distribution widths in the transverse plane of the beam. F is a correction factor for the non-zero crossing angle between the two beams. The rate of events in the experiments can be calculated with the formula 1.3

$$R = \sigma \cdot \mathcal{L} \,, \tag{1.3}$$

where σ is the cross section for the process. Given that the total cross section for proton-proton interaction is $\sigma_{tot} \approx 80$ mbarn at $\sqrt{s} = 13$ TeV, the rate at the 2018 peak luminosity of 2.1×10^{34} cm^{-2}s^{-1} results in 1.7×10^9 events/s. This corresponds to around 37 events per bunch crossing (pile-up events). The total number of events in a period of time from 0 to T is calculated through the equation 1.4, where L indicates the integrated luminosity. The latter is measured in multiples and submultiples of barn^{-1}, normally in inverse femtobarns (fb^{-1}).

$$N = \sigma \cdot L = \sigma \cdot \int_0^T \mathcal{L} \, \mathrm{d}t \tag{1.4}$$

Table 1.1 presents a summary of the LHC characteristics, together with the design beam parameters. Some additional information is given about the 2018 operations, which was the last year of the LHC Run 2.

Machine parameters	
Parameter	Value
Circumference (km)	26.66
Radius (km)	~ 4.3
Dipole magnetic field (T)	8.3
Dipole magnets	1232
Quadrupole magnets	392
Sextupole magnets	2×1232
Octupole magnets	1232

Beam parameters	
Parameter	Value
Energy per beam (TeV)	7
Energy per beam in 2018 (TeV)	6.5
Design luminosity (cm^{-2}s^{-1})	1.0×10^{34}
Luminosity in 2018 (cm^{-2}s^{-1})	2.1×10^{34}
Luminosity lifetime τ (h)	15
Avg length of stable beams in 2018 (h)	8.3
Number of bunches	2808
Number of bunches in 2018	2556
Particles per bunch	1.15×10^{11}
Bunch separation (ns)	25
Beam radius $\sigma_{x,y}$ (µm)	16.6
Crossing angle (µrad)	285
Design Pile-up (collisions/BX)	~ 20
Pile-up in 2018	37
Energy stored per beam (MJ)	360
Energy stored per beam in 2018 (MJ)	320

Table 1.1: LHC proton operations parameters summary.

Figures 1.3a and 1.3b show the values of the peak instantaneous luminosity and the integrated luminosity in the first two runs of LHC. While in Run 1 the design luminosity of 1.0×10^{34} cm^{-2}s^{-1} was approached but still not reached, in Run 2 it was largely exceeded, becoming more than twice in 2018. For Run 3, the LHC is foreseen to keep the same peak instantaneous luminosity attained in the last year of Run 2. A small increase in the beam energy up to 14 TeV

is expected over the course of the three years.

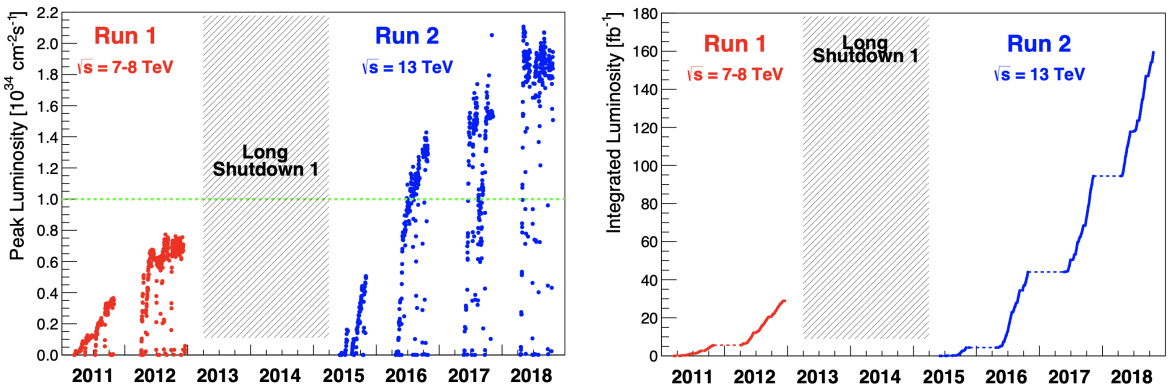

(a) Peak instantaneous luminosity.

(b) Integrated luminosity.

Figure 1.3: Peak instantaneous luminosity (left) and integrated luminosity (right) delivered to the ATLAS and CMS experiments in the first two runs of LHC, from [10].

1.1.2 High Luminosity LHC

From 2025, two and a half years of shutdown (LS3) are foreseen to allow for the installation of the new components for the High Luminosity LHC project [11]. New cavities and collimators will be used for the beam cleaning. To make space for these, the current dipoles will be replaced with shorter Nb_3Sn superconducting magnets, capable to reach magnetic fields up to $11 - 12$ T. The pre-acceleration chain will be also upgraded to obtain injected beams with twice the numbers of particles per bunch in the same volume.

The improvements will let to reach instantaneous luminosities up to 20×10^{34} cm^{-2}s^{-1}, which cannot be reliably and effectively handled by the experiments. Thus, a luminosity leveling will be put in place, which will allow for a long plateau at a constant luminosity value around $5 - 7.5 \times 10^{34}$ cm^{-2}s^{-1}, followed by a natural drop. The integrated luminosity delivered to both of the large experiments, ATLAS and CMS, after more than ten years of operations is expected to be around 4000 fb^{-1}.

These operating conditions will have an impact on the experiments imposing a high radiation tolerance, as well as improved performance to handle the much increased collision rate and pile-up.

1.2 The CMS experiment

The Compact Muon Solenoid (CMS) [4] is a multi-purpose detector installed at the Point 5 (P5) LHC experimental area. As for ATLAS, the CMS experiment is devoted to the search for new physics, mainly using proton-proton collisions.

The CERN CMS site is located in Cessy, France. On the surface, the present buildings include the control room and a surface experimental area (SX5). At approximately 90-100 m under the surface, the underground experimental cavern (UXC55) hosts the detector, while the services are situated in the adjacent Underground Service Cavern (USC55), as shown in Figure 1.4.

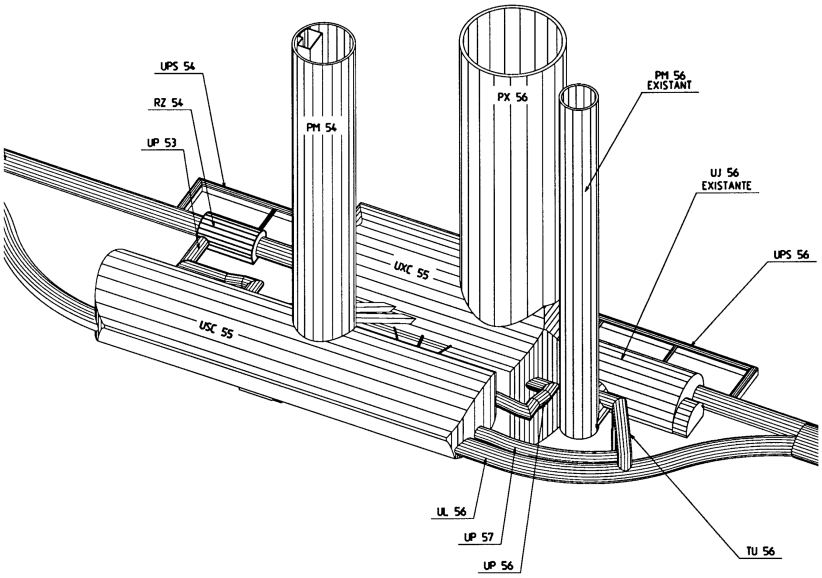

(a) Scheme of Point 5 caverns and shafts.

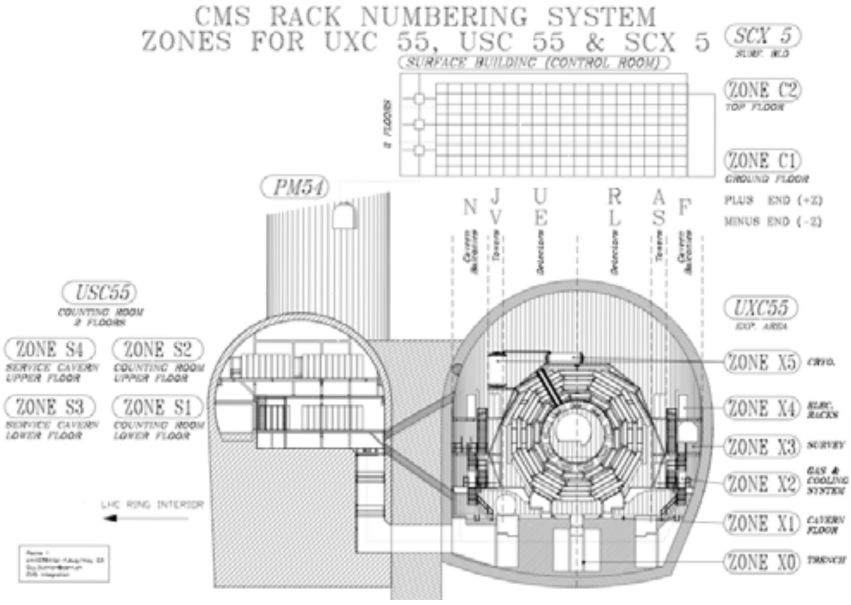

(b) Point 5 arrangement.

Figure 1.4: LHC Point 5 caverns, from [12].

The CMS detector is composed of several layers of high granularity synchronized detectors, each one specific for measuring the different properties of the particles generated in the collisions. A 4 T solenoidal magnet is employed to bend the particle trajectories.
The detector allows to identify the particles, to reconstruct their trajectories and decay vertices, as well as to calculate their energy and momentum. Moreover, since it offers an almost complete 4π coverage, it is possible to reconstruct the missing energy which derives from non interacting particles, like the neutrinos.

1.2.1 The CMS design and characteristics

The CMS detector is schematically depicted in Figure 1.5. It has a cylindrical shape with total dimensions of 21.6 m in length and 15 m in diameter. Its weight amounts to about 12500 tons. Due to the high symmetry of the collision topology, this particular shape grants to cover the largest variety of trajectory directions of the generated particles.
The entire structure is divided into three main blocks: the central barrel and the two endcaps.

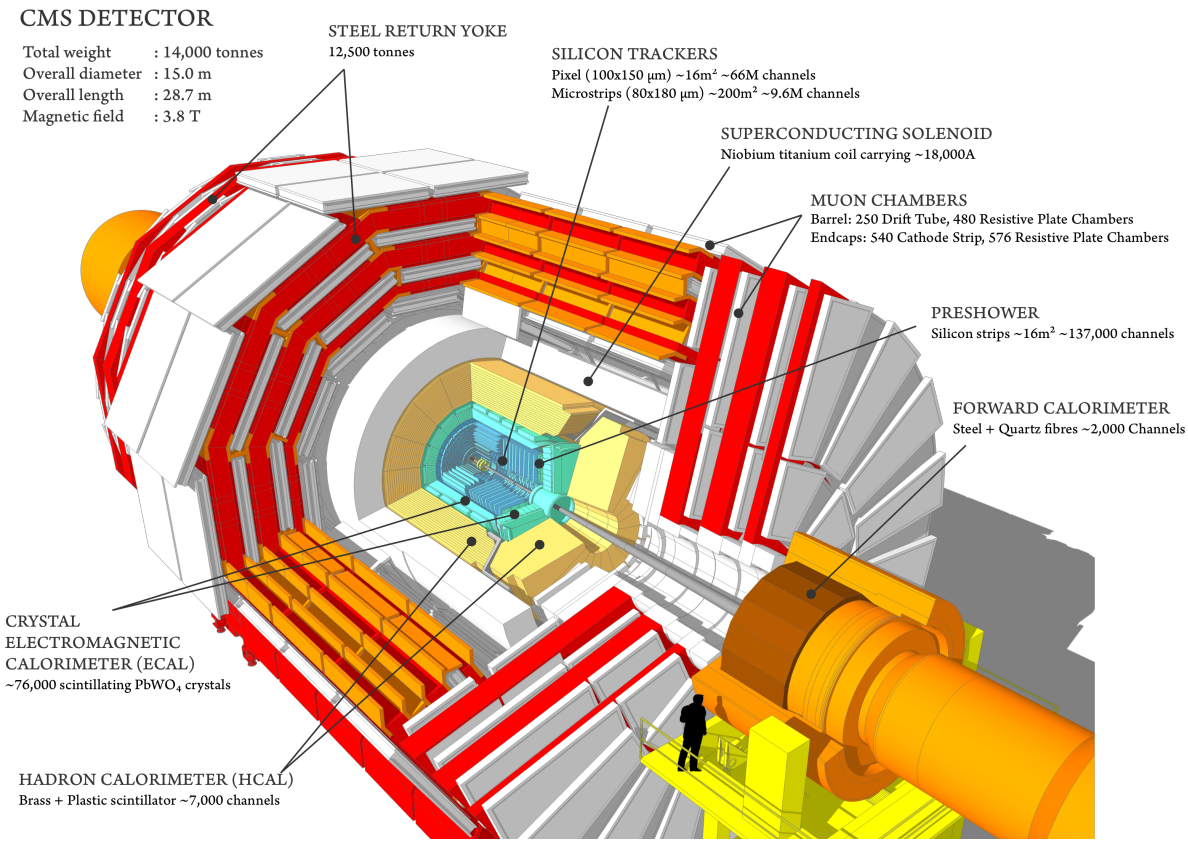

Figure 1.5: Schematic depiction of the CMS detector [13], with labels indicating the main characteristics of the whole detector and the various subdetectors. More details about the subdetectors will be given in the text.

The global cartesian coordinate system adopted in CMS is right-handed with its center in the nominal collision point. The x-axis points radially to the center of LHC, the y-axis is perpendicular to the ground plane and directed upwards, the z-axis runs tangential to the beam pipe. The x-y plane is referred to as the transverse plane. The projection of the particle energy and momentum on that plane are indicated as E_T and p_T, respectively.
A spherical coordinate system is also employed. It follows the ISO 80000-2:2019 convention [14], with the azimuthal angle ϕ defined in the x-y plane, starting from the x-axis, and the polar angle θ, referred to the z-axis. A more common way to represent the polar angle is through the pseudorapidity η, which can be calculated via the equation 1.5. The pseudorapidity becomes equal to the rapidity y in the ultra-relativistic limit, as proven in the equation 1.6

$$\eta = -\ln\left(\tan\left(\frac{\theta}{2}\right)\right) \tag{1.5}$$

$$y = \frac{1}{2}\ln\left(\frac{E+p_z}{E-p_z}\right) \approx \frac{1}{2}\ln\left(\frac{p+p_z}{p-p_z}\right) = -\ln\left(\tan\left(\frac{\theta}{2}\right)\right) = \eta\,, \tag{1.6}$$

where E is the particle energy, p is the particle momentum, and p_z is the component along the z-axis of the particle momentum.

Each part of CMS is composed by several layers of detectors with specific roles in measuring the particle properties. The inner part of the solenoid contains the silicon tracker system for measuring the trajectories of charged particles (starting point, direction and momentum) and for identifying the vertices. At a larger radius, still inside the solenoid, the electromagnetic calorimeter identifies and measures the energy of electrons and photons, while the hadronic particles and the jet properties are measured in the hadronic calorimeter. The muons are identified and their tracks are sampled with gaseous detectors placed outside the solenoid and sandwiched in the magnetic flux return yoke.

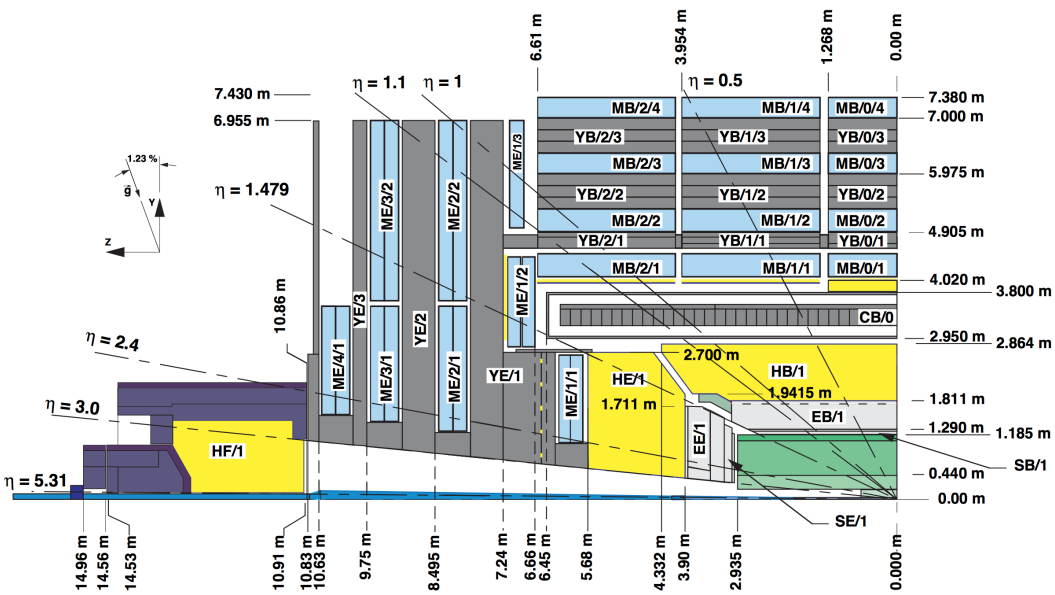

Figure 1.6: CMS detector longitudinal view [15]. Subdetectors highlighted in different colors with η ranges. The first letter in the labels refers to the subsystem: 'M' indicates the muon subsystem, 'Y' the iron yoke, 'C' the cryostat of the magnet, 'H' the hadron calorimeter, 'E' the electronic calorimeter and 'S' the electronic calorimeter preshower. The second letter in the labels refers to the detector position: 'B' stands for barrel, 'E' for endcap and 'F' for forward. Finally, the two numbers in the muon subsystem refer to the position of each chamber. In the barrel, the first number indicates the wheel, and the second one the station. In the endcaps, the first number refers to the disk, and the second one to the ring. The numbers grow moving away from the interaction point.

In the upcoming sections, the CMS subdetectors will be individually presented at the stage of

the Run 2 data taking. Subsequently, an overview of the upgrades will be given, starting with the LS2 installations, to finally move to the HL-LHC upgrades.

1.2.2 The Silicon Tracker

The innermost subdetector of the CMS experiment is the silicon tracker [16], [17]. It has a total length of 5.8 m and a diameter of 2.5 m, covering the pseudorapidity range $|\eta| < 2.5$. To cope with high particle fluxes during the collisions, a high granularity is required to reduce the occupancy and improve the spatial resolution. In the barrel, four layers of pixel detectors are employed close to the beam pipe, followed by silicon strips arranged in four inner and six outer layers. In the endcaps, two layers of pixels and three inner and nine outer layers of strips are used to track the paths of the particles generated in the interactions and the decay vertexes. Overall, the system is composed by 65 million channels for the pixels and 10 million channels for the strips.
The silicon tracker is operated at a temperature of $-20°$C in order to minimize the propagation of the radiation damages.
For low energy or low transverse momentum hadrons (1 GeV/c $<$ p$_T$ $<$ 10 GeV/c) the reconstruction efficiency is around 85%. For higher energies (p_T $>$ 10 GeV/c), it becomes 95%. For electrons the efficiency is estimated to be around 90%, and 98% for muons. In the region $|\eta| < 1.6$, the precision on the muon transverse momentum measurement is $\delta p_T/p_T < 2\%$ up to $p_T = 100$ GeV/c.

1.2.3 The Electromagnetic Calorimeter

The electromagnetic calorimeter (ECAL) [18] is designed to perform measurements of energy for electrons and photons with precision up to 1% and, working in team with the hadronic calorimeter, also for hadronic jets. A segmented, homogeneous and hermetic scintillation detector has been chosen to address these requirements. It utilizes inorganic crystals made of $PbWO_4$. This material has been selected because of the small Molière radius (22 mm), the short radiation length ($X_0 = 8.9$ mm), its radiation-hardness and the very short scintillation-decay time. The latter ensures to collect around 85% of the light emitted inside the crystal in the 25 ns between two consecutive bunch crossings.
The dimensions of the crystals are $2.2 \times 2.2 \times 23$ cm^3 for the barrel crystals and $2.9 \times 2.9 \times 22$ cm^3 for the endcap ones. The radiation lengths correspond to 25.8 X_0 in the barrel and 24.7 X_0 in the endcap. A total of 75848 crystals covers the pseudorapidity region $|\eta| < 3.0$. To collect and read the scintillation light produced, avalanche photodiodes are used for the barrel crystals, while vacuum photo-triodes are employed in the endcaps. The choice was dictated by the presence of an intense magnetic field in the solenoid (4 T) and the need of high intrinsic gain to match the low light output given by the $PbWO_4$ crystals. Indeed the scintillation photons are only 4.5 γ/MeV, at a temperature of 18°C. Moreover, the light yield strongly varies with the temperature. Therefore, a purpose built system has been adopted to maintain the temperature stable within 0.1°C.
The ECAL energy resolution is given by equation 1.7 [19]. $S = 0.028$ GeV$^{\frac{1}{2}}$ is the stochastic

term, $N = 0.128$ GeV is the contribution from noise and $C = 0.003$ contains all the other constant uncertainties, given for instance by the calibrations. To minimize the biases, accurate calibrations are continuously performed during the data taking.

$$\left(\frac{\sigma_E}{E}\right) = \frac{S}{\sqrt{E}} \oplus \frac{N}{E} \oplus C = \frac{2.8\%}{\sqrt{E[\text{GeV}]}} \oplus \frac{0.128}{E[\text{GeV}]} \oplus 0.3\% \tag{1.7}$$

1.2.4 The Hadron Calorimeter

The hadron calorimeter (HCAL) [20] is used to determine the energy of the hadronic jets and to estimate the missing transverse energy E_T^{miss} in the events. Thus, a hermetic detector with high granularity is needed, characterized by compact dimensions in order to fit the reduced space imposed by the solenoidal magnet. A sampling calorimeter has been chosen to fulfill these requirements. It is composed by alternating layers of brass absorber and active plastic scintillator. The scintillation light is carried out from wavelength shifting fibers and wave-guides towards hybrid photodiodes for the photon detection. The HPDs substitution with silicon photomultipliers has been completed during LS2, in order to improve the HCAL performance in Run 3.
To absorb the high energy hadrons generated in the 14 TeV collisions in 11.8 interaction lengths, it has been necessary to place the HCAL not only inside the magnet (HB and HE), but also to have additional layers outside of it (HO). The hadron calorimeter covers the pseudorapidity region $|\eta| < 3.2$; in addition, the forward hadron calorimeter (HF) extends the angular acceptance up to $|\eta| < 5.2$. Owing to the severe conditions of operation in the high pseudorapidity regions of HF, steel slabs have been used as absorber and quartz fibers as active layers, detecting the Cherenkov light produced by the traversing particles.
The HCAL energy resolution is given by equation 1.8 [20], where $S = 1$ GeV$^{\frac{1}{2}}$ and $C = 0.045$.

$$\left(\frac{\sigma_E}{E}\right) = \frac{S}{\sqrt{E}} \oplus C = \frac{100\%}{\sqrt{E[\text{GeV}]}} \oplus 4.5\% \tag{1.8}$$

1.2.5 The solenoid magnet

The CMS superconducting magnet has a length of 12.9 m, an inner diameter of 5.9 m, and a magnetic field of up to 4 T in the inner part and residual 2 T in the returning iron yoke. In normal operations, the magnetic field is about 3.8 T. This provides the bending of particle trajectories in the transverse plane, obtaining less than 5% of charge misidentification for muons with $p_T < 200$ GeV, $\delta p/p \approx 1\%$ for $p_T = 100$ GeV and less than 10% for $p_T < 1$ TeV for combined inner tracker and muon system measurements. Such performance is attained with 19.14 kA of current flowing in 2168 turns. This requires a temperature of 4.5 K, in order to keep the system in superconducting regime. Figure 1.7 presents a map of the magnetic field produced by the CMS solenoid.

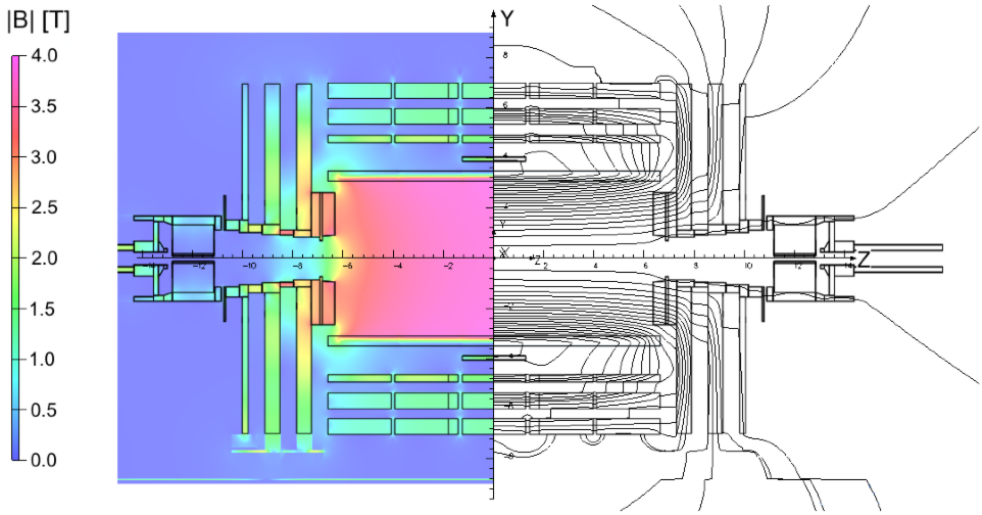

Figure 1.7: Map of the magnetic field generated by the superconducting solenoid in the CMS detector [21]. The value of $|B|$ is shown in the left, the field lines are shown on the right. Each field line represents a magnetic flux increment of 6 Wb.

1.2.6 The Muon System

The particles that can traverse the entire ECAL and HCAL without being stopped, such as muons with $p_T > 3$ GeV, are measured in the outermost group of subdetectors of the CMS experiment: the *muon system* [22]. It is constituted by four stations in the barrel and four disks in both endcaps, covering the range $|\eta| < 2.4$. In Figure 1.8, the muon system is shown in the state right before the LS2.

The CMS muon system is a robust and redundant muon spectrometer that can provide precise identification and high resolution p_T measurements thanks to three different types of gaseous detectors. A fourth type of gaseous detectors is being installed and commissioned during the LS2: the Gas Electron Multipliers (GEM). They will be presented in detail later in the chapter. Drift Tubes Chambers (DTs) are employed in the barrel region ($|\eta| < 1.2$) where the occupancy is low and there is a very low residual magnetic field in between the yoke iron. Faster and more radiation resistant Cathode Strip Chambers (CSCs) have been chosen for the two endcaps ($0.8 < |\eta| < 2.4$) to cope with higher particle fluxes and non uniformities in the magnetic field. Finally, Resistive Plate Chambers (RPCs) complement DTs and CSCs in both regions up to $|\eta| < 2.1$. Because of their fast response and excellent time resolution, they improve the precision in the determining of the bunch crossing (BX) of creation of the muons at the trigger level. Even though it was originally foreseen to have full coverage of RPCs up to a pseudorapidity of 2.4 to match the CSCs, the intrinsic limits of the technology did not allow their presence in regions with very high irradiation. Therefore, the muon system redundancy up to Run 2 was only granted in the region $|\eta| < 2.1$.

As shown in Figure 1.9, the tracker precision is the most relevant for muons with $p_T < 200$ GeV. This is due to the multiple scattering that the muons experience when traversing the calorimeters, the coil and the iron yoke. For muons with higher transverse momenta, the full system resolution

takes advantages of the inclusion of the muon system, improving the tracker resolution.

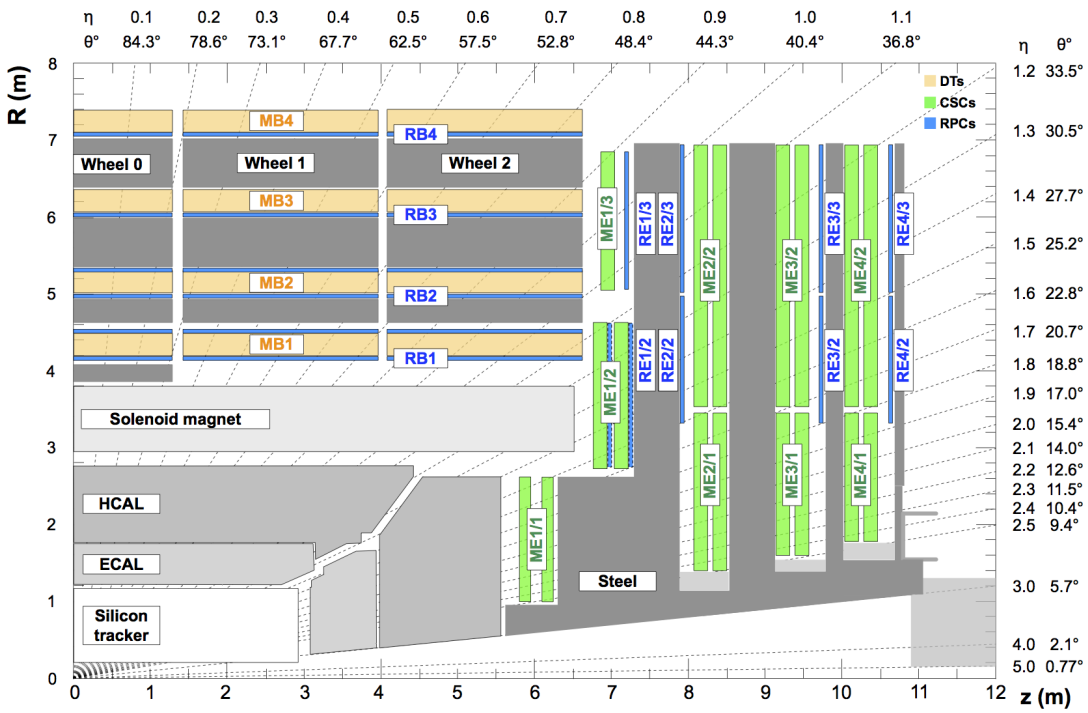

Figure 1.8: CMS muon system longitudinal view. The muon subdetectors are highlighted in different colors. From [22].

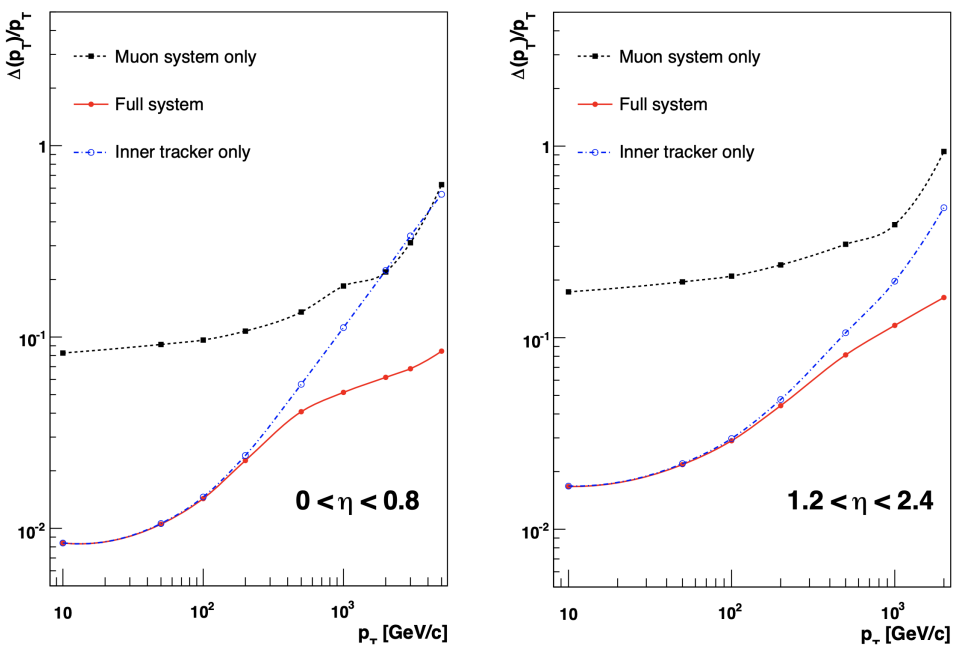

Figure 1.9: Muon transverse momentum resolution as a function of p_T for the inner tracker only, the muon system only and the two systems combined. The results for the barrel are shown on the left, the ones for the endcap are shown on the right. Both plots are from [4].

1.2.6.1 Drift Tube Chambers

The muon barrel region outside the solenoid is characterized by a low residual magnetic field, low occupancy and a large area to be covered. Because of those reasons, Drift Tube (DT) chambers have been employed [15]. The DTs are gaseous detectors fitting into the the iron yoke structure, which consists of 5 wheels and 12 azimuthal sectors (Figure 1.10). For each wheel, four concentric rings (stations) of DT chambers are installed. Each station in a sector is constituted by one DT chamber, except in sectors 4 and 10 where the MB4 are made by two chambers.

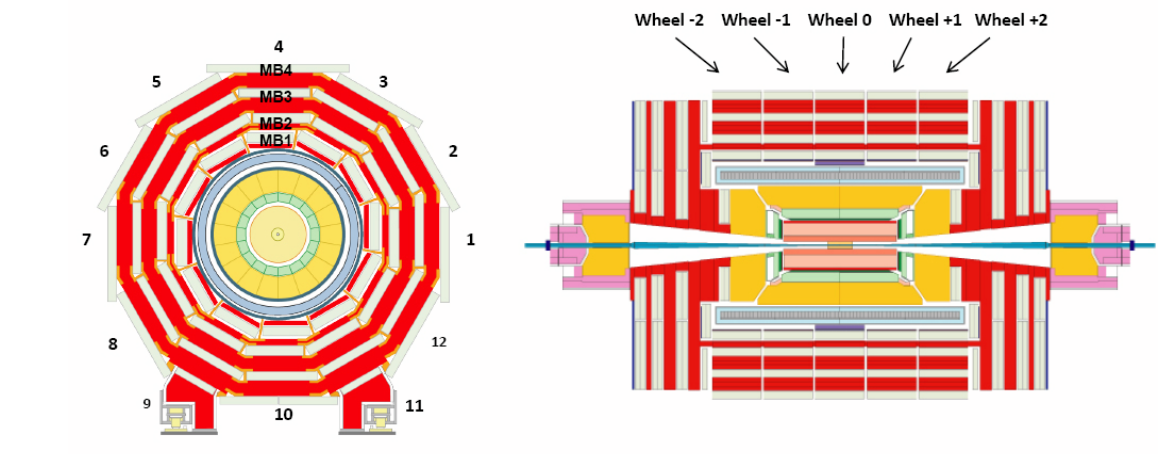

Figure 1.10: Drift Tubes Chambers in CMS: disposition of wheels, sectors and stations in the CMS detector [23].

The basic element of the DT chambers is the drift cell (Figure 1.11). The cell has a transverse size of 42×13 mm^2 with a 50 μm-diameter gold-plated stainless-steel wire at the center. The cell design employs five electrodes to shape the effective drift field: the anode wire, two cathode strips on the side walls of the tube and two strips above and below the wire. The design operating voltages are +3600 V, −1200 V and +1800 V for anode, cathode and strips respectively, generating a rather uniform electric field along the cell. The chosen gas mixture is Ar/CO_2 (85%/15%). It provides good quenching properties and, in the constant electric field of the cell, a drift velocity for the electrons of about 55 µm/ns, corresponding to a maximum drift time of around 385 ns.

Four staggered layers of parallel cells form a superlayer (SL). A DT chamber consists of two SLs with wires extending along the z-axis that measure the $r - \phi$ coordinate (in the bending plane), and an orthogonal SL that measures the $r - z$ coordinate. All the DT chambers have a length of 2.5 m, imposed by the dimensions of the wheels, while their width varies, ranging from 1.9 m to 4.1 m.

Up to Run 2, single DT cells had an efficiency greater than 98% and a spatial resolution of about 200 µm, once all the relevant systematics have been taken into account [22]. In the θ projection, the resolution of 200 µm in the central wheel becomes 600 µm in the external wheels. Given the $4 + 4$ layers of the two ϕ superlayers and their disposition, the offline reconstruction code manages to achieve an overall resolution along ϕ of 100 µm.

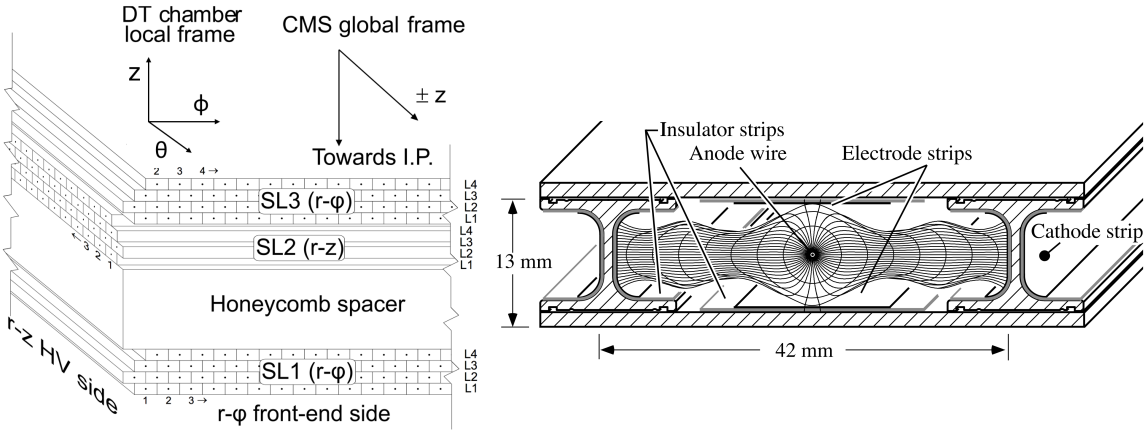

(a) Schematic view of a DT chamber.

(b) Schematic view of a DT cell.

Figure 1.11: On the left, schematic view of a DT chamber. On the right, section of a drift tube cell showing the drift and isochrone lines. Both figures are from [15].

1.2.6.2 Cathode Strip Chambers

The solution adopted for the muon endcaps to deal with a high magnetic field and large particle rates are the Cathode Strip Chambers (CSCs) [24]. The CSCs are gaseous trapezoidal Multi-wire Proportional Chambers (MWPC). They are characterized by a short drift length, which leads to a fast signal collection.

The CSCs are arranged in four disks (stations), as in Figure 1.12. The first disk is further subdivided into three rings, while the other three disks are made of two rings. All the rings, except ME1/3, have staggered, overlapping neighboring chambers that cover about 10° each.

A CSC detector is composed by six layers of anode wires enclosed between two planes of finely segmented cathode strips for the collection of the ionization signal produced in the $Ar/CO_2/CF_4$ (40%/50%/10%) gas mixture. In all the chambers, except the ME1/1, the wires are perpendicular to the central strip. In ME1/1, instead, due to the presence of a strong magnetic field (> 3 T), the wires are inclined by 29° in order to compensate for the the Lorentz angle of the drifting electrons. The wires are operated at a voltage of 3.6 kV, providing the information about the radial (polar) coordinate. The radial strips at ground voltage are used to determine the azimuthal coordinate. To increase the precision along ϕ, a weighted mean of the charge collected in neighboring strips is performed. The azimuthal track position resolution varies in the range $70 - 150$ µm depending on the station, while the radial position resolution is in the range $1.9 - 6$ mm [25].

1.2.6.3 Resistive Plate Chambers

Used as complementary detector for both the DTs and the CSCs, the Resistive Plate Chambers (RPCs) [28] ensure the redundancy of the muon spectrometer and improve the time resolution of the system. A total of six layers of RPCs are installed in the barrel; four on the inner side of all the DT stations, and two in the outer side of MB1 and MB2. In the endcap region, RPCs are present in all the four disks. They are usually placed on the outer side of the CSCs, except for the second disk.

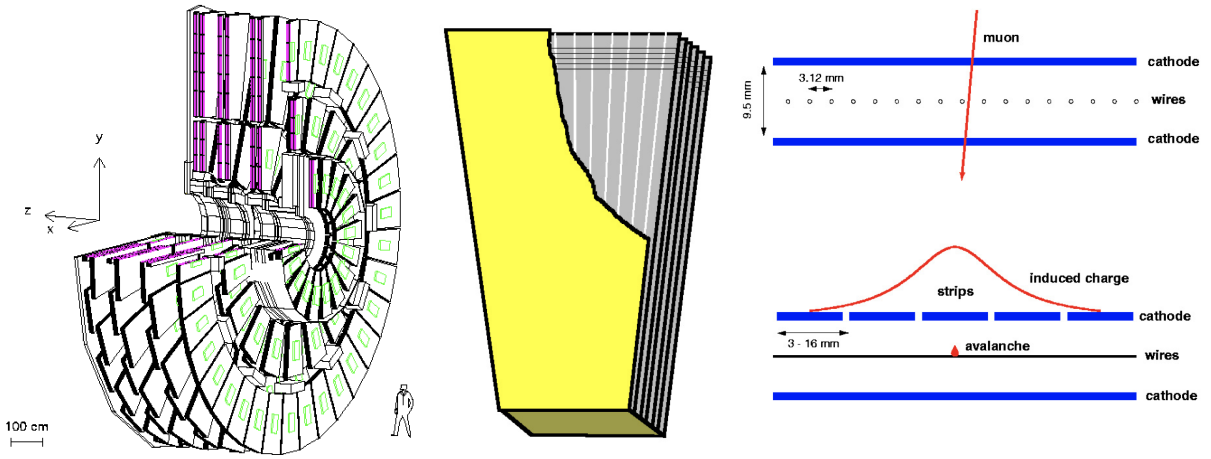

(a) CSC arrangement in the CMS muon endcap [26].

(b) Schematic view and principle of operation of a CSC chamber [27].

Figure 1.12: On the left, arrangement of the CSC subsystem in the CMS endcaps. On the right, schematic view of a CMS CSC chamber (non-ME1/1) with radial strips and perpendicular wires, and principle of operation of a CSC chamber.

RPCs are gaseous detectors characterized by a very precise time measurement. Indeed, their intrinsic time resolution is about 1.5 ns, once the geometrical position systematics are considered. CMS uses double-gap RPC chambers composed by four bakelite planes forming two 2 mm gaps filled with a freon-isobutane-sulfur hexafluoride (95.2%/4.5%/0.3%) gas mixture. The chambers are operated in avalanche mode, applying to the electrodes a voltage difference around 9.5 kV. The electrodes are constituted by graphite coating the bakelite planes. Insulated aluminum strips are used to collect and readout induced signals. Figure 1.13 presents a schematic view of a CMS RPC chamber.

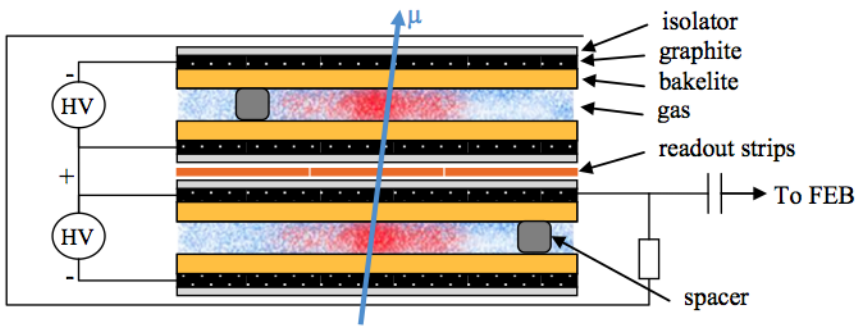

Figure 1.13: Schematic view of a CMS RPC chamber [29]. The acronym FEB stands for Front-End Board.

1.2.7 The CMS trigger system

The LHC collisions in Run 2 had a rate of 40 MHz. This implies that in the recent runs two bunches of protons intersected in the collision points every 25 ns = 1 BX. Owing to the fact that

in ATLAS and CMS each event has a size of about 1 MB, the actual data storage capability allow for a rate of recorded events up to 1 kHz.
The task of this dramatic rate reduction is demanded to the on-line trigger chain of the experiments: the selections are based on tuned identification of specific objects and properties and event topologies. In CMS, this is performed in two steps as shown in Figure 1.14. The two stages are named *Level 1 trigger* (L1) and *high level trigger* (HLT) [30].

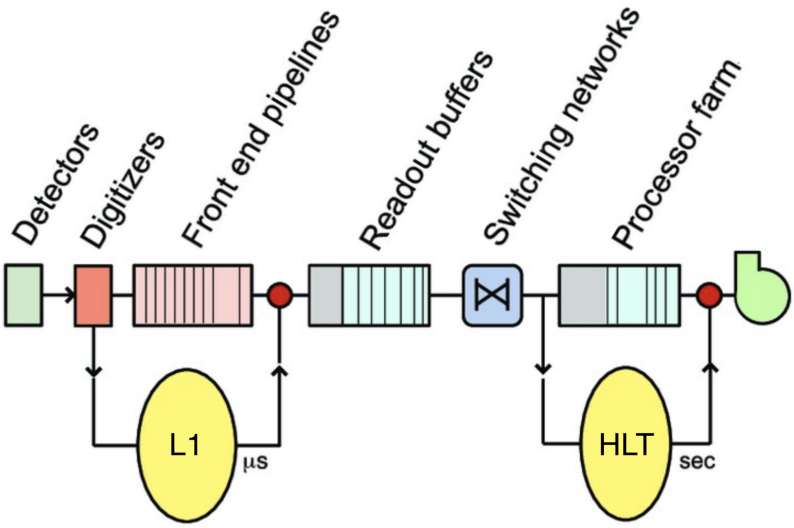

Figure 1.14: Scheme of the CMS trigger system [31].

The L1 trigger reduces the rate to a maximum of 100 kHz, elaborating the signals coming from the muon detectors and the calorimeters. The remaining selection is done by the HLT algorithms running on a large computer farm with commercial processors. The objects get reconstructed, and consequently selected. Some compromises are introduced in this reconstruction, in order to speed up the event processing.

1.2.7.1 The L1 Trigger

The CMS Level 1 trigger system is designed to accept or reject events at a 40 MHz rate (every BX). It is implemented in a pipeline mode using custom developed hardware. Field Programmable Gate Arrays (FPGA), Application Specific Integrated Circuits (ASICs) and Lookup Tables (LUTs) are programmed to complete every individual processing step in less than 25 ns (= 1 LHC clock cycle), and with a total latency of 4 µs.
Figure 1.15 presents a block diagram of the CMS L1 trigger system employed during LHC Run 2. It consists of two main branches: the calorimeter trigger which generates trigger candidates for electrons, photons and jets, and the muon trigger which deals with isolated and non-isolated muons.
The solution chosen for the L1 muon trigger is an integration between the different muon subdetectors belonging to the same regions of CMS. The result is the division in three pseudo-rapidity zones. The barrel with DTs and RPCs covers the pseudorapidity values of $|\eta| < 0.8$. The two

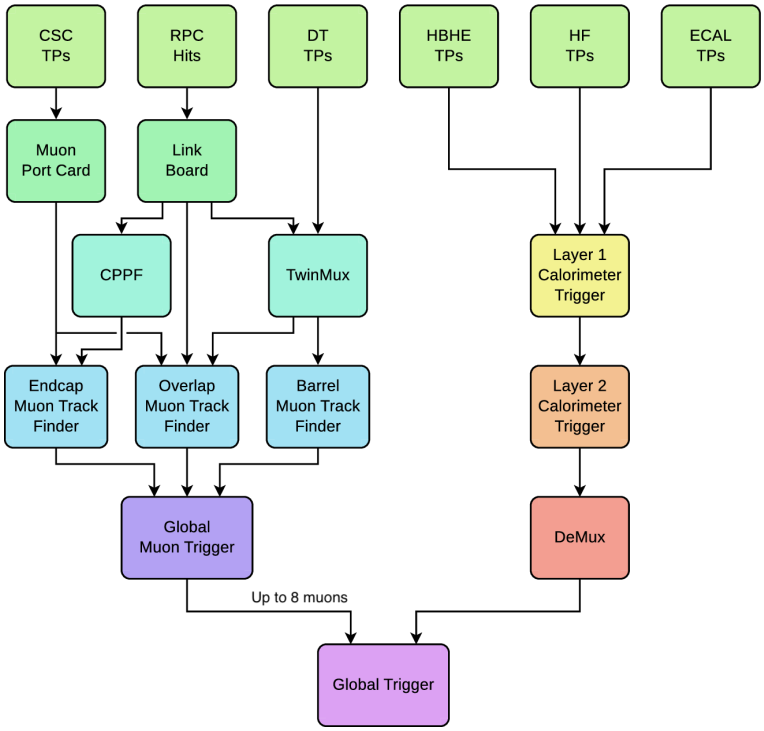

Figure 1.15: Block diagram of the CMS Level 1 trigger system [32]. The acronym TP stands for Trigger Primitive, while CPPF stands for Concentration Pre-Processing and Fan-out.

overlap regions at $0.8 < |\eta| < 1.2$ have contributions from DTs, CSCs and RPCs. Finally, CSCs and RPCs cover the endcap regions ($1.2 < |\eta| < 2.4$). With this configuration, the different performance in terms of time and spatial resolution of the subdetectors in each region can be combined to obtain improved and refined trigger candidates to be sent to the global muon trigger (µGMT).

In the barrel, the DT trigger primitives (TP) are combined with the information coming from the RPC hits in the TwinMux boards. These then are fed to the barrel and the overlap muon track finders (BMTF and OMTF). In the endcaps, instead, the CSC trigger primitives are sent to both the OMTF and the endcap muon track finder (EMTF), where they are integrated with the RPC hit information.

Each track finder roughly reconstructs the muon tracks at trigger level and transmits up to 36 candidates to the µGMT. There, the track candidates are sorted and the duplicates are removed. Finally, the eight best muons are forwarded to the global trigger (µGT).

In parallel to the muon trigger candidates, the trigger primitives coming from the ECAL and the HCAL are processed in the two-layer calorimeter trigger. The first stage receives the trigger hits from both the calorimeters in regions of $\Delta\eta \times \Delta\phi$ of 0.087×0.087 in the barrel and 0.17×0.17 in the endcaps. The energy deposits are calibrated, sorted, and finally sent to the second layer. There, the physics objects such as electrons, photons, tau leptons, jets, and energy sums are reconstructed and calibrated. Since the calorimeter trigger has a time-multiplexed design, its last stage is a demultiplexer (DeMux). The DeMux orders, serializes, and formats the events to be sent to the µGT.

As a last step, the global trigger analyses the received objects and, following the so-called *trigger menus*, it selects the events to be forwarded to the HLT.

1.3 The CMS upgrades

The systems described in the previous section are required to undergo a series of major upgrades before the LHC Run 4, in order to withstand the massive increase in the instantaneous luminosity foreseen for the HL-LHC. Indeed, more proton-proton interactions per bunch crossing not only give more data for the analyses, but also bring augmented irradiation and much larger rates to be handled both by the detectors and the trigger systems. Therefore, in addition to the amelioration of the DAQ and the trigger infrastructures, extensive improvements of the existing detectors and the addition of new ones are needed. All this will ensure to take full advantage of the enhanced capabilities of the collider, and to limit the downsides.
Since plenty of interventions are planned for the detectors, they have been scheduled to take place during all the shutdown periods of LHC. Hence, the activities have started already in LS2, in parallel to the preparation for Run 3. They will be then continued during the Year End Technical Stops (YETS) of Run 3, and finally they will be completed in the LS3.
The CMS detector upgrades include a new tracker with extended coverage and Level 1 trigger capabilities, new readout electronics and lower operation temperatures for the barrel ECAL, a totally redesigned endcap calorimeter named high granularity calorimeter (HGCAL) [33], and various innovations in the muon system.

1.3.1 The muon system upgrades

The upgraded CMS muon system is presented in Figure 1.16.
Some of the upgrades are not visible in the schematic view presented in the figure, since they correspond to improvements of the readout electronics of all the present muon subsystems. New on-chamber readout boards and faster optical links will allow to increase the capabilities both in handling the particle rates and to provide more precise hit information.

Three evident additions are present in the upgraded CMS muon endcaps, when comparing Figure 1.16 to Figure 1.8.
First, the RPC subsystem is expanded with the introduction of two new detector rings that will complement the ME3/1 and ME4/1. These employ an *improved* version of the double-gap RPC technology (iRPC), that utilizes thinner gaps of 1.4 mm instead of the original 2 mm ones. In addition, the high voltage applied will be lowered, with the consequence of decreasing the gas gain. The smaller avalanche produced by a traversing particle will deposit less charge, thus slowing down the aging process. On the other hand, a lower gain gives smaller signals. The front-end electronics will compensate for this by a large amplification and a better signal to noise ratio.

All the other installations in the rings GE1/1, GE2/1 and ME0 adopt the GEM technology, in the form of triple-GEM chambers. An in depth description of the design and the working

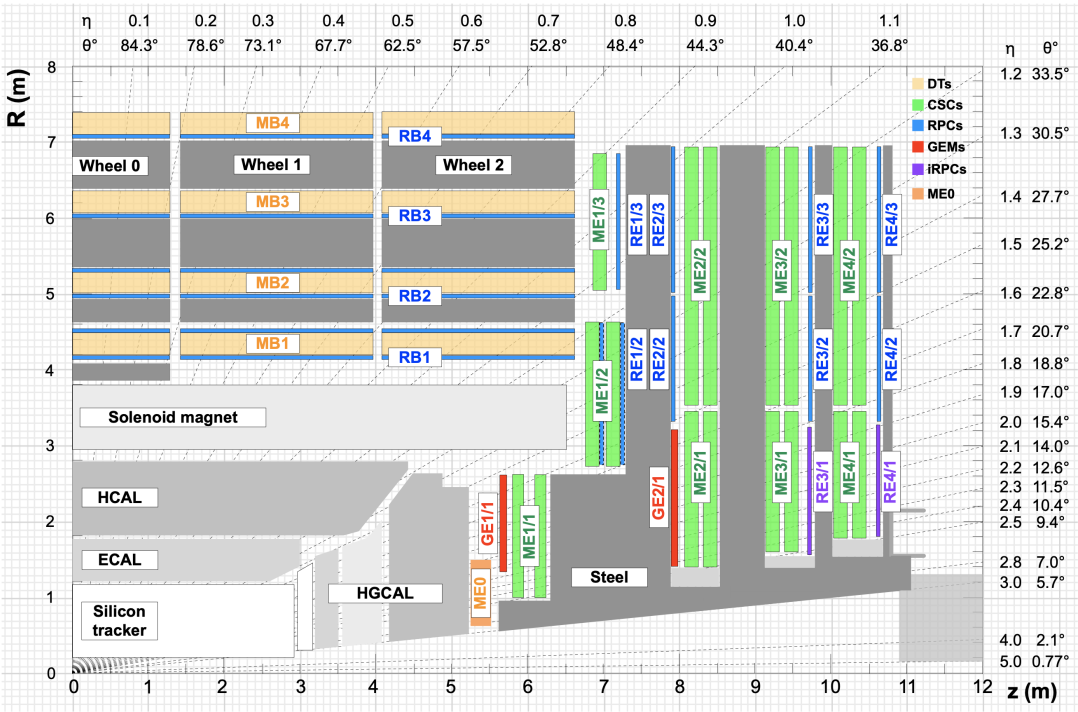

Figure 1.16: Longitudinal view of the CMS muon system with the HL-LHC upgrades. The muon subdetectors are highlighted in different colors. DT (MB) chambers are depicted in light yellow, CSCs (ME) in green RPCs, and (RB/RE) in blue. The new installations are: in red and orange the GEM chambers (GE and ME0), and in purple the improved RPCs (iRPC). Figure from [27].

principles of a GEM detector is given in section 2.4. The GE1/1 and GE2/1 detectors are meant to complement the CSC chambers and complete the redundancy of the muon system. The ME0 station, instead, is going to extend the coverage up to $\eta = 2.8$. The harsh radiation environment that prevented the use of RPCs can now be filled with these new-generation detectors. Indeed, the GEM technology has a high radiation tolerance, paired with an excellent rate capability. These allow it to withstand the radiation dose and the particle fluxes of the HL-LHC and reach detection efficiencies above 95%. Additionally, their fast signal response translates into a time resolution below 10 ns. This makes the GEM chambers perfectly suited as trigger devices for the CMS muon endcaps.

The GE1/1 detectors, 36 per endcap, are composed of two single chambers paired into a super chamber. Each super chamber covers 10.15° in the ring, allowing an overlap between neighboring detectors. A more detailed description is given in 2.5. The GE2/1 detectors consist of two layers as well. The difference with the first GEM station is that each GE2/1 chamber covers around 20° and it is made of four different modules. ME0 detectors also cover 20° each, but they are composed of six layers of chambers. Such design allows for effective muon tagging and background rejection.

The GE2/1 chambers are planned to be installed in the CMS endcaps over the Run 3 Year End Technical Stops. The ME0 station will be integrated during the course of the LS3.

The pilot project of the new detector installation is the GE1/1, which is the focus of this thesis.

Its full integration in CMS is being carried out during the LS2. Thus, they will start contributing to the data taking early on in the LHC Run 3. The improvements that the GE1/1 will bring at the trigger level are presented in Figure 1.17. The augmented lever arm between the muon hits in the first endcap station (Figure 1.18) allows to better distinguish particles with different transverse momenta and to reject the signals of no interest.

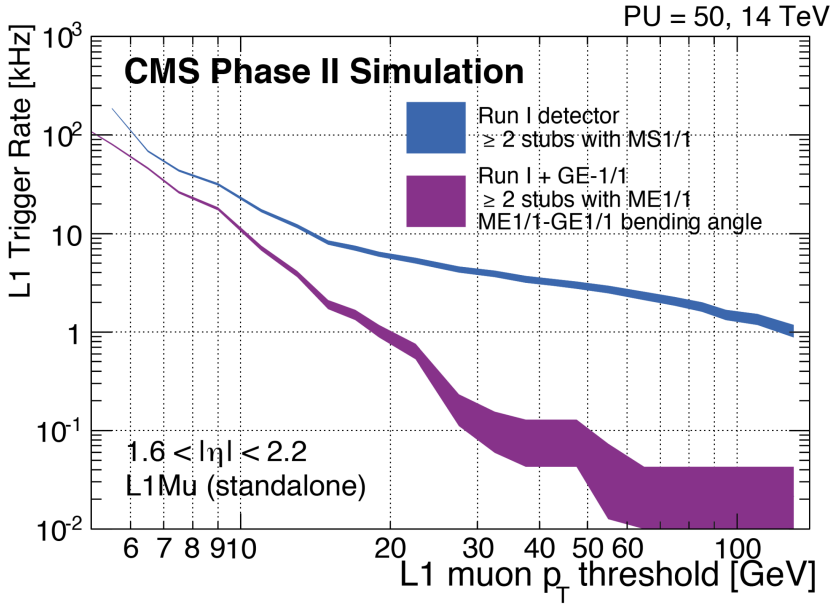

Figure 1.17: Level 1 muon trigger rates as a function of the applied p_T threshold before (blue) and after (purple) the GE1/1 upgrade, at a luminosity of 2×10^{34} cm^{-2}s^{-1} and a constant GE1/1 efficiency of 94%. The muon trigger primitives are required to have at least two stubs (primitives per muon station), with one stubs produced in the endcap muon station 1/1. The distances between the GEM and the CSC detectors act as lever arms in the muon momentum measurement, allowing to greatly reduce the trigger rate. From [34].

The aforementioned upgrades will allow the CMS muon system to have increased η coverage and full redundancy up to $\eta \approx 2.4$. Moreover, the added detection layers will allow for an improved measurement of the transverse momentum. A more precise estimation of the p_T at the trigger level will reflect on the reduction of the trigger rate. This will allow to reduce the threshold applied on the transverse momentum, while preserving the same L1 accept rate.

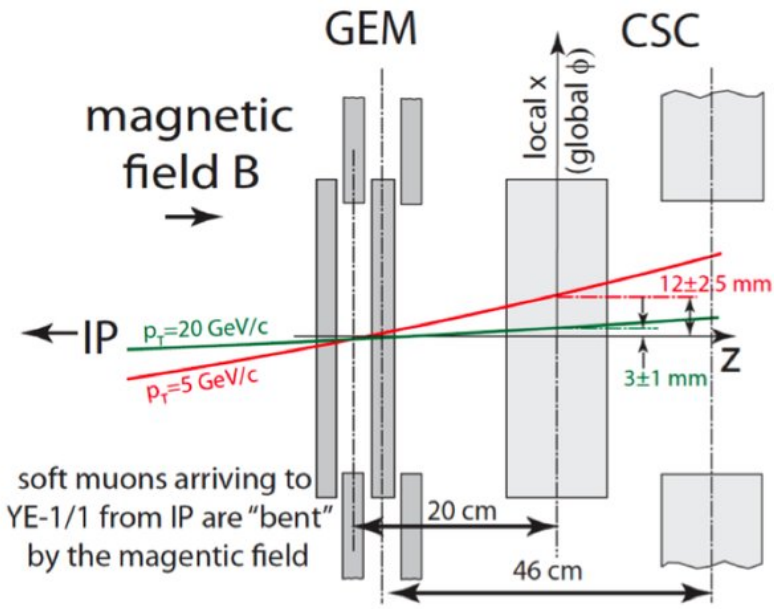

Figure 1.18: Visualization of the bending angle for a 5 GeV and a 20 GeV muon track traversing GE1/1 and ME1/1 chambers. From [34].

Chapter 2

Gas Electron Multipliers

The initial part of this chapter focuses on the presentation of the particle detection principles, the limitations of the past generations of gaseous detectors and the innovations brought by the GEM technology. Then, the realization of the concepts will be shown with an emphasis on the most relevant characteristics that make the GEM detectors suitable for the forward regions of the muon system in a LHC experiment. After that, the application of the GEM technology for the CMS detector will be presented. The GE1/1 chamber structure will be delineated as well as their needs and requirements in terms of readout electronics and services. The GE1/1 system as a whole will be described, detailing the principal characteristics of the frontend electronics. This will be instrumental for the chapters 4 and 5, where the configuration of the on-detector electronics will be examined, together with its implications on the GE1/1 detection performance.

2.1 Interactions of ionizing radiation with matter

Any particle detection starts with an interaction between the radiation and the detector sensitive material. Among all the interesting particles that are produced during the LHC collisions, the most relevant for the detection are those that live and travel long enough to intersect the sensitive layers of the experiments. Only a fraction of those particles are *stable*, all the others are referred to as *long lived*. Their mean path length, defined by

$$\lambda = \beta \gamma c \tau \ , \tag{2.1}$$

is at least on the order of the detector characteristic dimensions. To this category belong charged particles (e.g. electrons, muons), neutral particles (e.g. neutrinos, neutrons) and photons.
The ionization sources for the tests presented in this thesis are X-ray photons and cosmic ray muons. The next sections will briefly explain the interactions of photons and charged particles with matter, following [35], [36], [37], [38] and [39]. This will be a fundament for the understanding of the working principles of the GEM detectors.

2.1.1 Interactions of charged particles with matter

The charged particle interactions with matter depend on several factors: their mass, charge and energy, and the material properties. The principal mechanisms are here presented.

Excitation and ionization

Low to medium energetic particles mainly interact via electromagnetic forces with the electrons of the traversed material atoms or molecules. A small fraction of kinetic energy is transferred to the electrons in each scattering process, giving rise to excitation or ionization. If the material thickness is large enough, the particles may come to a stop inside the volume.

For particles with a velocity greater than the atomic electrons, the average energy loss ($-\mathrm{d}E$) over the traveled distance ($\mathrm{d}x$) can be described by the Bethe-Bloch formula [35]

$$-\langle\frac{\mathrm{d}E}{\mathrm{d}x}\rangle = \left(4\pi N_A r_e^2 m_e c^2\right) z^2 \rho \frac{Z}{A}\frac{1}{\beta^2}\left(\frac{1}{2}\ln\frac{2m_e c^2\beta^2\gamma^2 T_{max}}{I^2} - \beta^2 - \frac{\delta(\beta\gamma)}{2}\right) . \tag{2.2}$$

The first bracketed block on the right side of the equation consists in a series of constants as the Avogadro constant, the electron mass, the classical electron radius and the speed of light. It amounts to around 0.3071 MeV/(g/cm^2). z is the charge of the incoming particle in elementary charge units. Z and A are the atomic number and atomic weight of the material. T_{max} is the maximum energy transfer that can occur in a single collision, while I is the average excitation energy of the absorber, which can be approximated by the formula $I = 16 \cdot Z^{0.9}$ eV. $\beta = v/c$ and γ is the Lorenz factor. $\delta(\beta\gamma)$ is a parameter that accounts for the density effects of the absorber: the polarization of the material shields the electric field of the incoming particles.

After an initial steep decrease of the losses for increasing particle momenta, the so-called *relativistic rise* takes place. A naive interpretation for this behavior can be the following. Initially, with incrementing velocities, the particles have less and less time available for the interaction to occur and this reduces the losses. Then, the particles start to be increasingly relativistic, therefore their perception of the density of the material is different. The higher their momentum gets, the more the space in front of the particles becomes compact, leading to a larger density, and therefore a larger chance to lose energy. The minimum in the energy loss curve for many different particles is situated around $\beta\gamma = 3 - 4$. In this condition, they are called minimum ionizing particles (MIPs).

For thick materials, with $\mathrm{d}x > 1$ g/cm^2, the total energy loss has a Gaussian distribution due to the large number of individual interactions. For thin materials, instead, the distribution doesn't retain its symmetry, becoming a Landau curve. This is caused by rare events in which the kinetic energy transferred in a single ionization is very large. The electrons involved in those events are known as δ-rays.

The Bethe-Bloch formula is valid for a wide range of materials, from gases to solids, with mild discrepancies for very light materials ($Z < 7$). The Bethe-Bloch approximation is not valid for crystals, since they have a regular structure and therefore there are preferred directions and paths (channeling effect). On the other hand, for the interacting particles, exceptions are present for electrons and positrons, being them indistinguishable from the electrons of the material.

Bremsstrahlung

Charged particles with large momenta can lose energy through the bremsstrahlung process. When they are decelerated by the electromagnetic interactions with the nuclei of the material, they may emit photons with a cross section inversely proportional to the square of the particle mass.

The energy loss per unit length [35] can be expressed as

$$-\frac{\mathrm{d}E}{\mathrm{d}x} \approx \frac{E}{X_0} \,, \tag{2.3}$$

where X_0 is the radiation length. It can be approximated by [36]

$$\frac{1}{X_0} \approx 4\left(Z\,(Z+1)\,N_A\frac{\rho}{A}\right)\alpha\, r_0^2\left(\ln\frac{183}{Z^{1/3}} - f(Z)\right) \,, \tag{2.4}$$

where the symbols use the same conventions as for the Bethe-Bloch formula (2.2). α is the fine structure constant, while $f(Z)$ is a correction due to the Coulomb interactions. The factors $(Z\,(Z+1)) = Z^2 + Z$ account for the interactions with the nuclei (Z^2) and with the Z electrons. The energy spectrum of the emitted photons is constant, therefore, the number of photons becomes lower with increasing energies. The maximum energy corresponds to the emission of a single photon with all the initial kinetic energy of the decelerated particle ($E_{max} = h\nu_{max} = mc^2\,(\gamma - 1)$).

Critical energy

The predominant process through which the charged particles lose energy in matter depends on the atomic number of the absorber and on the energy of the interacting particle. For a given material, the point where the energy loss due to ionization equals the one lost via bremsstrahlung is called critical energy (E_C). Before that, ionization dominates; after that, bremsstrahlung prevails. The equation 2.5 provides an approximation of the critical energy of electrons in different materials.

$$E_C^e \approx \frac{A}{Z+B} \,, \tag{2.5}$$

Z is the atomic number of the absorber, while A and B are constants intrinsic to the material. In good approximation, for liquids and solids $A = 610$ MeV, $B = 1.24$; for gases $A = 710$ MeV, $B = 0.92$ [35].

To derive the critical energy for any particle (x), the approximation in equation 2.6 can be used [36].

$$E_C^x \approx E_C^e\left(\frac{m_x}{m_e}\right)^2 \tag{2.6}$$

The stopping power curve

The aforementioned mechanisms of energy loss for charged particles can be condensed in the stopping power curve. It shows the energy loss per unit length divided by the material density as a function of the particle momentum. An example is given in Figure 2.1 for positively charged

muons on copper.

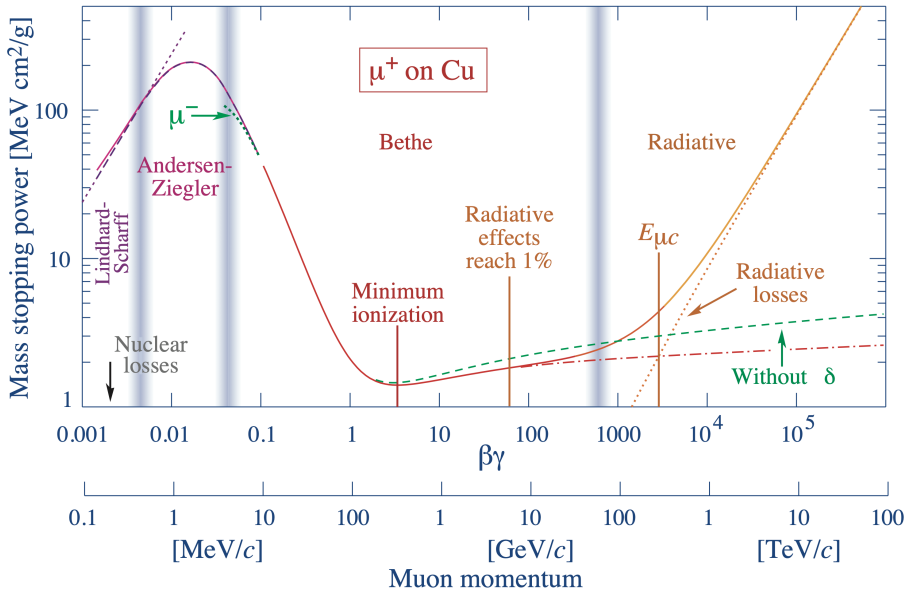

Figure 2.1: Stopping power as a function of the particle momentum for positively charged muons traversing copper. From [35].

Mixtures and compunds

Both for ionization and bremsstrahlung, in presence of compounds or mixtures the total energy loss and the total radiation length become a weighted sum of each of the components. In this case, the weights refer to the fraction in mass of the constituents. These are known as Bragg rules.

Multiple scattering

In the interactions, not only the energy is affected, but also the path is subjected to a variation. Indeed, each scattering deviates the trajectory of the incoming particle, resulting in the *multiple scattering* process. Considering a sequence of Rutherford scatterings, for which small angles are privileged and the energy transfer is small, the resulting total angular deviation has a Gaussian distribution. On a single plane, the RMS deviation is approximated by the equation [35],[40]

$$\theta_{RMS} \approx \frac{13.6\text{MeV}/c}{\beta p} z \sqrt{\frac{x}{X_0}} \left(1 + 0.038 \ln \frac{x z^2}{X_0 \beta^2}\right) , \tag{2.7}$$

where the symbols follow the same conventions as for the Bethe-Bloch formula (2.2) and x is the thickness of the material. In summary, the higher the particle momentum gets, the less the flight direction is changed, and the more thickness the particle has to travel through, the more it can be deflected.

Pair production

Particles that possess kinetic energies greater than 1.022 GeV might also undergo the pair production process by interacting with the nuclei of the materials. An electron-positron pair is emitted, hence the minimum energy required to generate the masses of the two particles. The

energy loss can be parametrized as

$$-\frac{\mathrm{d}E}{\mathrm{d}x} = B_{pair}(Z, A, E) \cdot E \ . \tag{2.8}$$

The coefficient B_{pair} slowly grows with the particle energy. At high energies, therefore, the pair production competes with the bremsstrahlung process for the total energy loss, and it might even dominate.

Cherenkov radiation

When the velocity of the charged particle is greater than the speed of light in the traversed material, the Cherenkov radiation process takes place. The condition for it to happen is $\beta \geq 1/n$, where n is the refraction index of the absorber. Traversing the material volume, a charged particle polarizes the atoms (molecules); if its speed is larger than c/n, the polarization becomes asymmetric and the generated dipoles emit radiation. The photons are emitted at a fixed angle, given by the equation $\cos(\theta_C) = 1/n(\omega)\beta$ [38]. The wavelength spectrum, instead, depends on the squared inverse of the wavelength itself.
The energy loss due to the Cherenkov radiation emission follows the formula [38]

$$-\frac{\mathrm{d}E}{\mathrm{d}x} = z^2 \frac{4\pi^2\hbar}{c} \int_{\beta>1/n(\nu)} \left(1 - \frac{1}{\beta^2 n(\nu)^2}\right) \nu \mathrm{d}\nu \ . \tag{2.9}$$

The Bethe-Bloch equation already accounts for this in the polarization term.

Transition radiation

Another mechanism through which charged particles lose energy is the transition radiation emission. When a charged particle moves towards a dielectric material with $n > 1$ while traveling in vacuum or an equivalent material with $n = 1$, it generates an equivalent image charge in the dielectric, in the form of dipoles. At the moment of the transition, the dipoles extinguish and return in a neutral configuration, radiating photons.
The energy loss due to the transition radiation emission depends on γ and it is normally small, generating photons with energies of $\mathcal{O}(\mathrm{keV})$ or lower.

Other interactions

Very energetic charged leptons and photons interacting with dense matter can give rise to electromagnetic showers, generating a cascade of electrons and photons through a sequence of radiative emissions and pair productions. A similar, yet more complex, mechanism also happens for hadronic particles: the hadronic showers. Through hadronic interactions between the particles and the nuclei of the absorber, a cascade of hadrons, leptons and photons is created.
For the muon systems of the LHC experiments, these processes are only relevant for the estimation of the background and the consequent aging effects, which are not discussed in this thesis. Thus, a more thorough description has been deemed not necessary.

2.1.2 Interactions of photons with matter

Contrarily to the particles with mass which release energy in multiple collisions, the photons can interact with matter matter and get absorbed. The reduction of the incoming photon flux (I_0) due to the presence of a material of thickness x can be described by [38]

$$I(x) = I_0 \mathrm{e}^{-\mu x} \ . \tag{2.10}$$

For photons with an energy greater than 1 keV (X-rays and γ-rays), the most relevant processes that occur when they interact with matter are the photoelectric effect, the Compton scattering and the pair production. The total coefficient of absorption μ is the sum of the three components. In formula [38],

$$\frac{\mu}{\rho}(E_\gamma) = \frac{N_A}{A}\sigma_{Photoelectric}(E_\gamma) + Z\frac{N_A}{A}\sigma_{Compton}(E_\gamma) + \frac{N_A}{A}\sigma_{Pair\,production}(E_\gamma) \ . \tag{2.11}$$

In the following, a brief description of the three processes will be given.

Photoelectric effect

Up to energies on the order of $0.1 - 1$ MeV, the dominant process is the photoelectric effect. In presence of a nucleus that grants the momentum conservation, the photon can release its whole energy to an electron and ionize the atom. The extracted electron kinetic energy is equivalent to the total photon energy subtracted by the ionization potential. The removal of an electron, especially if it is belonging to the internal shells, causes a rearrangement of the atomic energy levels that might induce the emission of another X-photon or even an electron (Auger effect). The photoelectric effect cross section can be approximated by [38]

$$\sigma^K_{p.e.} \approx \sqrt{\frac{32}{\epsilon^7}}\alpha^4 Z^5 \sigma_{classic} \ , \tag{2.12}$$

$$\epsilon = \frac{h\nu}{m_e c^2} \ , \tag{2.13}$$

$$\sigma_{classic} = \frac{8}{3}\pi r_e^2 \ . \tag{2.14}$$

In addition to the strong dependence on the atomic number and the photon energy, the cross section is also affected by the presence of quantized atomic energy levels. In correspondence to the shell energies, the absorption of the full photon energy is much favored, resulting in a sudden jump in the photoelectric cross section.

Compton scattering

Starting from photon energies of about 100 keV up to more than 1 GeV, another process becomes important: the Compton scattering. It consists in an electron-photon scattering, with an incoming photon and an electron bound to an atom in the initial state. The electron momentum is considered to be zero, which is a valid approximation since $E_\gamma \gg E_k^{e,bound}$. In the final state there are a free electron and a photon with diminished energy. The relation between the

wavelengths of the two photons is described by [38]

$$\lambda' - \lambda = \frac{h}{m_e c}(1 - \cos\theta) = \lambda_C^e (1 - \cos\theta) \ , \tag{2.15}$$

where λ' refers to the outcoming photon, and θ is the angle on a plane between the outcoming and the incident photons. Integrating the differential cross section, known as the Klein-Nishina formula [38], one gets

$$\sigma_C^e = 2\pi r_e^2 \left[\left(\frac{1+\epsilon}{\epsilon^2} \right) \left(\frac{2(1+\epsilon)}{1+2\epsilon} \right) + \frac{1}{2\epsilon} \ln(1+2\epsilon) - \frac{1+3\epsilon}{(1+2\epsilon)^2} \right] \ , \tag{2.16}$$

$$\epsilon = \frac{h}{\lambda m_e c} \ . \tag{2.17}$$

The maximum kinetic energy that the electron can have corresponds to the backwards scattering of the photon ($\theta = \pi$), thus with a forward emission of the electron. Its value is given by

$$E_{k,max}^e = \frac{hc}{\lambda} \frac{2\epsilon}{1+2\epsilon} \ . \tag{2.18}$$

Pair production

A photon with an energy greater than $2 \cdot m_e \approx 1022$ keV can give rise to the pair production process. Interacting with a nucleus of the material, which ensures the momentum conservation, the photon may produce an electron-positron pair. Hence, the need for the incoming photon to have at least the energy to generate the masses of the two particles. As for the bremsstrahlung, the process is also possible to happen in presence of an electron, but with less relevance in the total cross section. For high photon energies, the coefficient of absorption is approximated by

$$\mu_{Pair\,prod} \approx \rho \frac{N_A}{A} \sigma_{Pair\,prod} = \frac{1}{\lambda_{Pair\,prod}} \ , \tag{2.19}$$

where $\lambda_{Pair\,prod}$ is given by the formula [38]

$$\frac{1}{\lambda_{Pair\,prod}} \approx \frac{7}{9} 4Z(Z+1)\alpha r_e^2 \left[\ln(183 \cdot Z^{-1/3}) \right] \approx \frac{7}{9} \frac{1}{X_0} \ . \tag{2.20}$$

Cross section of photon interactions with matter

In Figure 2.2, two examples of the the cross sections for the processes of photons interacting with matter are presented. The photoelectric effect dominates in the initial part of the curve. The atomic energy levels can be noticed in the sudden jumps. The steeply falling curve flattens when the Compton cross section becomes comparable to the photoelectric one. Finally, the pair production kicks in at around 1 MeV and makes the photon cross section flat up to very high energies.

Electromagnetic showers

As for charged particles, also high energy photons can initiate electromagnetic showers. Their entire energy is released in the material through a cascade of photons and electrons generated by pair production and radiative processes. Since $\lambda_{Pair\,prod} \approx 1.3 \cdot X_0$, one can consider that after

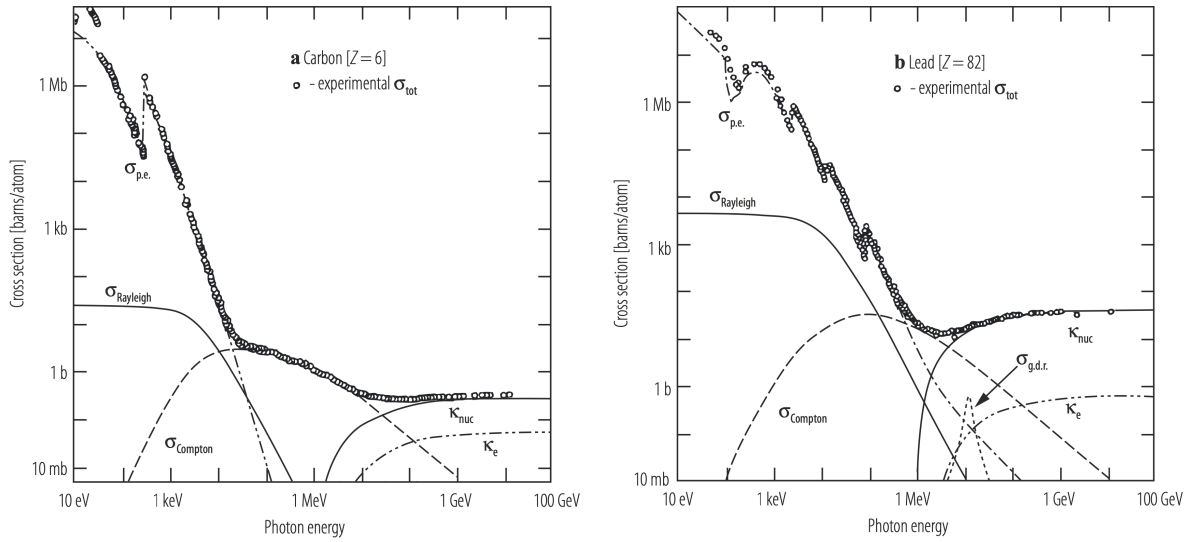

(a) Total photon cross section in carbon (light material).

(b) Total photon cross section in lead (heavy material).

Figure 2.2: Total experimental cross sections as a function of energy for photons in carbon and lead [36]. The different contributions are shown in solid and dashed lines. *p.e.* refers to the photoelectric effect; κ_{nuc} describes the pair production in the nuclear field, while κ_e in the electrons field. In the plot for lead, the peak present named *g.d.r.* refers to photo-nuclear interactions, and in particular to the Giant Dipole Resonance.

every radiation length a photon is emitted or an electron-positron pair is created. The shower stops when the energy of each particle in the cascade is below the required thresholds for the processes.

2.1.3 Radiation detection

Many techniques are available in the contemporary experimental physics to detect the presence of ionizing particles. Various detectors have been created to be sensitive to different radiation and the processes that it undergoes. They can have several targets, such as the measurement of the total amount of energy released, or only the energy loss in a thin layer. They can be position sensitive or very precise in measuring the time of the interaction. As detailed in the previous chapter, in complex experiments like the ones installed at the LHC, different detectors are employed in an organized structure. Each one is aimed to accomplish a specific task, exploiting the intrinsic characteristics.
The focus of this thesis are the GEM detectors. GEMs belong to the category of gaseous detectors, which will be the main topic of the upcoming sections.

2.2 Evolution of gaseous detectors

The history of gaseous particle detectors can be traced back to the beginning of the 20th century, when Ernest Rutherford and Hans Geiger built the first proportional counter. It consisted of a single wire concentric to an external cylinder filled with gas. Oppositely to what happens for

parallel plate ionization chambers, by applying a voltage difference between the two electrodes, they were able to obtain a magnification of the weak signal produced by the ionizing particles that were traversing the gas. Geiger and Walther Müller optimized the instrument, thus reaching high amplification factors to make possible to detect single electrons generated in the gas, even with the electronics available at that time. All this was supported by the studies of John Townsend, who developed the theoretical models on the collisional charge multiplication in gases at high electric fields.

Besides the actual particle detectors that these researches managed to produce, the major outcome was the deep understanding about the multiplication of the electrons in gases due to avalanches. Indeed, when electrons travel in a gas under the acceleration of intense electric fields, they may gain enough kinetic energy to ionize the gas atoms encountered in their path. A large cascade of further ionizations takes place and eventually the cloud of electrons reaches the anode. There, the produced current can be readout by means of dedicated circuitry. The latter can span a broad variety of more or less complicated pieces of equipment: from a simple beeper as for the traditional geiger counter, up to the ns-fast frontend electronics utilized in the contemporary HEP experiments.

These fundamental principles were used over the years to develop gaseous detectors with increasing performance. A major step forward was done with the invention of the Multi-Wire Proportional Chambers (MWPC) by Georges Charpak in 1968 [41]. A series of parallel anodic wires were surrounded by two planes of cathodic strips. The rate capability of these devices was orders of magnitude higher than the one of the proportional counters, due to the short drift path of the ions to reach the cathode. Variations and evolutions of the proportional chambers were proposed in the following years, with different geometries and topologies. One example of MWPC are the cathode strip chambers (CSC) of CMS, briefly described in section 1.2.6.2. If the time of the anodic/cathodic signals is measured, it is possible to evaluate the position of the ionizing radiation interaction via the electron/ion drift time and their drift velocity. These detectors are called drift chambers. A notable example are the CMS drift tubes (DT), described in section 1.2.6.1.

The proportional chambers present two main limitations. The first one is the *rate capability*. The cloud of ions that is generated in the avalanches modifies the local electric field, limiting the effective amplification factor in presence of high irradiation. The second one is *aging* [42]. When operated for long time under consistent irradiation, the wires present in the chambers tend to accumulate gas contaminants that stick to it. Around the wires, the amplification processes produce a localized plasma that may polymerize the organic gases or pollutants that might come from the pipes or the chamber components. When depositing on the wires, they increase the thickness and reduce the effective electric field ($\propto 1/r$). Therefore, the amplification factor drops.

To overcome these issues, new generations of gas chambers were recently invented. In 1988, Micro-Strip Gas Counters (MSGC) were introduced [43]. They eliminated the use of wires, utilizing instead a readout plane which integrated cathodic strips interleaved by thinner anodic strips. Unfortunately, after a sequence of naturally occurring discharges between neighboring anodes and cathodes, the electrodes tended to get compromised. After severe sparks, short cir-

cuits were generated and extended regions of the detectors were made unusable.
Even with impressive improvements over the past gas detectors, the MSGC did not represent the final answer to the needs in HEP. But, they opened the path for a novel (r)evolution in gaseous detectors: the Micro-Pattern Gaseous Detectors (MPGD).
The most notable members of the MPGD family are the Micro-Mesh Gaseous Structures (Micromegas) [44] and the Gas Electron Multipliers (GEM). Both of them are gaseous detectors that employ microscopic structures to amplify the electrons. However, the approaches are widely different.
The layout of the Micromegas (Figure 2.3) foresees a cathodic and an anodic plane, with a micro-mesh in between, which divides the gas volume in two regions. The first one that goes from the cathode to the micro-mesh is the conversion region. Usually, it is 3 mm thick to allow the traversing particles to ionize the gas multiple times. A moderate electric field makes the electrons travel towards the mesh and enter the second region. This is much thinner than the previous one ($\mathcal{O}(100\ \mu m)$) and subjected to a much larger electric field. There, the amplification takes place.

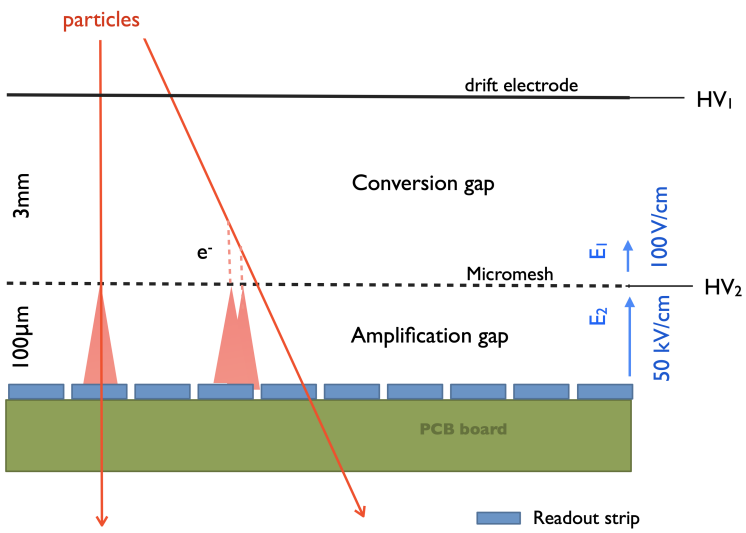

Figure 2.3: Schematic view of a Micromegas chamber. From [45].

These detectors provide enormous benefits in terms of spatial and time resolution, in addition to extraordinary results in terms of rate capability and aging robustness. Still, a single amplification stage with very large voltage differences applied might generate instabilities and destructive discharges directly facing the readout plane.
A totally different perspective in the history of gaseous detectors was brought in 1997, when Fabio Sauli invented the GEM [46]. As Micromegas, GEMs have an anodic and a cathodic planes that define the active volume. Two drastic changes in the concepts are applied, though. The first one is the decoupling of the amplification stage from the readout electrode. The second one is the possibility to introduce multiple stages of electron multiplication. Indeed, the avalanches only take place inside the key element of the GEM chambers: the GEM foils. Thin copper-cladded polyimide foils are chemically etched to obtain a regular pattern of holes. Applying a voltage

difference across the foils, the amplification of the electrons can occur inside the holes. Normally, the electric field in the holes is on the order of 100 kV/cm. If only one foil is interposed between the anode and the cathode, it gets the name of single-GEM. To avoid the need to apply large voltage differences across one foil to increase the electron multiplication factor, they can be arranged in sequence. The most frequent layout consists of a stack of three GEM foils, hence the name triple-GEM chambers. In this layout, each of the foils contributes to the amplification approximately by the cubic root of the total amplification factor. The ionization charge collection, the amplification and the final signal formation will be explained in detail in the the following sections, together with the peculiarities, the performance and the intrinsic limitations.

2.3 Working principles of gaseous detectors

As mentioned in the previous section, there are several peculiarities in the way the electrons are multiplied in the gas volume and collected. Many aspects, though, are in common to all of them. In this section, all the fundamental principles at the basis of the gaseous detectors will be described. They will be proposed with the same sequence as they occur in the chambers. First comes the ionization by the interacting particle, then the drift of electrons and ions in the electric fields, the avalanche processes and finally the signal formation.

2.3.1 Ionization of the gas

The initial step in the particles detection is the interaction of ionizing radiation with the gas. The energy released by the radiation may cause the ionization of the gas atoms/molecules, with the creation of electron-ion pairs. This process gives rise to the *primary ionizations*, whose number and spacing is determined by the gas, or gas mixture, the type of radiation and its energy. Primary electrons might have enough energy to further ionize other gas atoms/molecules, generating clusters of *secondary ionizations* at a scale of $\mathcal{O}(10\ \mu\text{m})$. The total number of electron-ion pairs present in the gas after an ionization event is the sum of primaries and secondaries; in formula $n_T = n_P + n_S$.
While traversing the gas volume, ionizing particles produce clusters along their path. The average number of total electron-ion pairs follows the statistics

$$\langle n_T \rangle = \frac{\langle \frac{\mathrm{d}E}{\mathrm{d}x} \rangle_{ion} \cdot L}{W} \ , \tag{2.21}$$

where L is the path length, $\langle \mathrm{d}E/\mathrm{d}x \rangle_{ion}$ is given by the Bethe-Bloch formula, and W is the average energy required to create an electron-ion pair in the gas. The main properties of common gases are listed in Table 2.1.
On the contrary, photons undergo only one interaction that release the energy to a gas electron. That electron, then, loses its kinetic energy through secondary ionization. Photoelectrons extracted by X-rays normally have ranges of a few millimeters in standard gases at normal temperature and pressure (NTP) conditions. The average number of total pairs can be derived

by

$$\langle n_T \rangle \approx \frac{E_\gamma}{W} \ , \tag{2.22}$$

where the energy required for the photoelectric extraction has been neglected, being much inferior than E_γ.

Gas	ρ (mg/cm^3)	$\langle dE/dx \rangle$ (keV/cm)	W (eV)	$\langle n_P \rangle$/cm	$\langle n_T \rangle$/cm
Argon	1.66	2.4	25	25	106
CO_2	1.84	3.35	34	35	100
CF_4	3.78	6.38	54	63	120
CH_4	0.667	1.61	30	37	54

Table 2.1: Physical constants for gases commonly utilized in gaseous detectors at $T = 20°$ and $p = 1$ atm, from [39]. The values of energy loss refer to MIPs with charge $q = e$. W denotes the average energy required to create an electron-ion pair.

As a first approximation, the number of primary ionizations generated by charged particles traversing a gas volume can be modelled as a Poisson distribution around the mean $\langle n_P \rangle$. The probability to have k clusters per unit length in one event becomes then

$$P(k, \langle n_P \rangle) = \frac{\langle n_P \rangle^k \exp(-\langle n_P \rangle)}{k!} \ . \tag{2.23}$$

The probability for a charged particle to pass through the gas volume without any ionizing interaction is $P(0, \langle n_P \rangle)$. Consequently, the theoretical maximum value of the efficiency of a gaseous detector is given by

$$\epsilon = 1 - P(0, \langle n_P \rangle) = 1 - \exp(-\langle n_P \rangle) \ . \tag{2.24}$$

A detector with an ionization region of 3 mm that utilizes an Ar/CO_2 (70/30%) gas mixture at NTP conditions has a theoretical efficiency $\epsilon \approx 1 - \exp(-28 \cdot 0.3) = 99.98\%$.
The probability density function of the distance (Δx) between two successive ionizations by a MIP is modelled as a decreasing exponential curve, as for a process without memory of the previous steps. In formula

$$\Delta x \left(\frac{\langle n_P \rangle}{\text{cm}} \right) = \frac{\langle n_P \rangle}{\text{cm}} \exp\left(-\frac{\langle n_P \rangle}{\text{cm}} \cdot x \right) \ . \tag{2.25}$$

For a unitary thickness of an Ar/CO_2 (70/30%) gas mixture at NTP conditions, $\langle \Delta x \rangle = (\langle n_P \rangle/\text{cm})^{-1} = 357$ µm.

2.3.2 Motion of charged particles in electric and magnetic fields

Once the electron-ion pairs are created, they tend to diffuse in the gas and recombine. To collect them, an external electric field (E) has to be applied. As a result, the ions drift towards the cathode, while the electrons in the direction of the anode. The trajectories followed are a

superposition of the drift caused by the electric field and a series of collisions with the gas atoms and molecules. The component of the averaged velocity aligned to the applied field is called *drift velocity*.

Let us first consider the ions, with mass M. Let us also assume that the drift velocity is equal to zero right after each collision. The final drift velocity reached before the following collision, happening after a time interval τ, is

$$v_{ion}^{max} = a \cdot \tau = \frac{eE}{M}\tau \ . \tag{2.26}$$

The average drift velocity ($v_{D,ion}$) is half of the maximum one. The final equation for the drift velocity is then

$$v_{D,ion} = \frac{e\tau}{2M}E = \mu_+ E \ , \tag{2.27}$$

where μ_+ is the ion mobility. For the commonly used gases, the values of μ_+ are around $1-2$ cm/ms $\cdot$ cm/kV. The drift velocity of argon ions in a field $E = 2.6$ kV/cm amounts to around 4 cm/ms [47]. Magnetic fields have negligible effects on ions.

To derive the gas electrons drift velocity, let us consider a time interval larger than the characteristic time between their collisions with the gas atoms ($\Delta t \gg \tau$). Their drift velocity can then be averaged, and the collisions can be thought as friction, hence proportional to the velocity. The equation of motion for the electrons in electric ($\vec{E}$) and magnetic ($\vec{B}$) fields becomes

$$\langle m\frac{\mathrm{d}\vec{v}}{\mathrm{d}t}\rangle = e\left(\vec{E} + \vec{v}_D \times \vec{B}\right) - \frac{m}{\tau}\vec{v}_D = 0 \ . \tag{2.28}$$

Defining, the electron mobility as $\mu_- = e\tau/m$, and the Larmor frequency as $\omega = eB/m$, the equation gets simplified into

$$\vec{v}_D = \mu_- \vec{E} + \omega\tau(\vec{v}_D \times \vec{B}) \ , \tag{2.29}$$

whose solution is

$$\vec{v}_D = \frac{\mu_- E}{1+\omega^2\tau^2}\left[\hat{E} + \omega\tau\hat{E} \times \hat{B} + \omega^2\tau^2\left(\hat{E}\cdot\hat{B}\right)\hat{B}\right] \ . \tag{2.30}$$

There are two main categories of gases in terms of electron mobility: hot and cold gases. Hot gases have atoms/molecules with few low-lying energy levels. This results in a small loss of energy when electrons collide with the gas atoms. Thus, μ_- is proportional to τ and not constant for increasing electric fields. The opposite happens in cold gases, which are characterized by atoms/molecules with plenty of low-lying degrees of freedom. As a consequence, electrons have a similar behavior to ions, and μ_- results to be almost constant. An example of a hot gas mixture is Ar/CH_4, while Ar/CO_2 is a cold gas.

Electrons and ions drift velocities are shown in Figure 2.4a and Figure 2.4b for a few gases and gas mixtures. In Ar/CO_2 (70/30%), with an external electric field $E = 2.6$ kV/cm, the electrons drift velocity is around 70 mm/µs. This results to be around one thousand times larger than ions drift velocity.

Electrons and ions not only undergo drift in gases, but also diffusion. If no external fields are applied, the thermal motion causes an isotropic spread of the charges. A point-like charge density

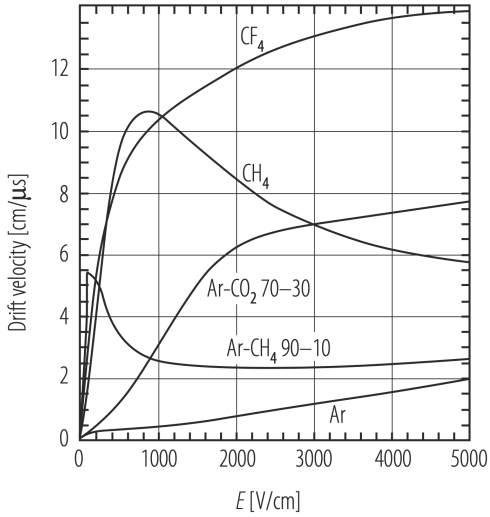

(a) Electrons drift velocity for typical gases.

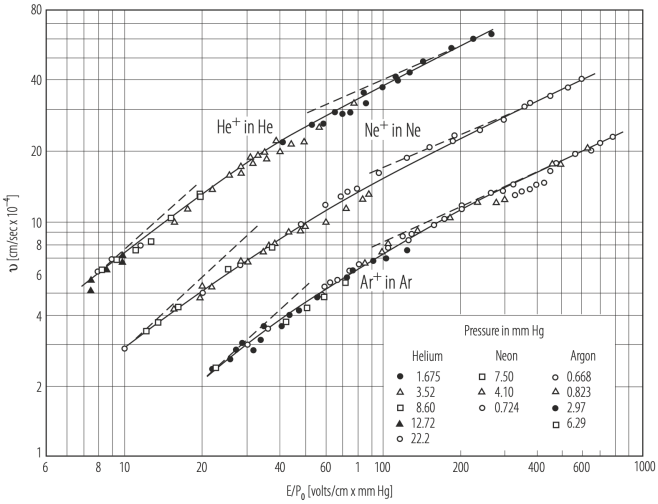

(b) Ions drift velocity for typical gases.

Figure 2.4: Electrons and ions drift velocities for typical gases and gas mixtures utilized in gaseous detectors. From [36].

evolves in time following the equation of charge conservation, which has as solution

$$\rho(r,t) = c \cdot \exp\left(-\frac{r^2}{4Dt}\right) \ . \tag{2.31}$$

D is defined as the diffusion coefficient, which depends on the mean free path λ and the typical collision time τ as $D = \lambda^2/\tau$. The width of the cloud of charge is $\sigma = \sqrt{2Dt}$.
Since the diffusion is isotropic, in one direction the diffusion coefficient becomes $D_x = 1/3\,D$. In terms of thermal energy $T_e = 1/2\,m\langle v_{thermal}\rangle$, $D_x = 2/3\,T_e/m\,\tau$. The relation between the diffusion coefficient and the mobility coefficient is therefore $D/\mu = 2/3\,T_e/e$.
When applying an external electric field in one direction, it is possible to define the longitudinal and the transversal components of the diffusion coefficient (D_L and D_T, respectively). In hot gases $D_L > D_T$, because of the kinetic energy spread in the electron cloud. In addition, the diffusion is pretty large. On the contrary, in cold gases the two components are similar and small, getting closer to the pure thermal diffusion.
Longitudinal and transverse widths of electron clouds after a drift length of 1 cm are shown in Figure 2.5 for typical gases.
By applying external magnetic fields, instead, the transverse component of the diffusion gets limited. Indeed, the Lorentz force acts to keep the electron cloud together by making the charges spiral around the longitudinal axis. The transverse diffusion coefficient becomes

$$D_T(B) = \frac{D_T(0)}{1+\omega^2\tau^2} \ . \tag{2.32}$$

No influence is introduced, instead, on the motion and the diffusion in the direction longitudinal to the magnetic field.
Both longitudinal and transverse diffusion in presence of electric and magnetic fields are essential

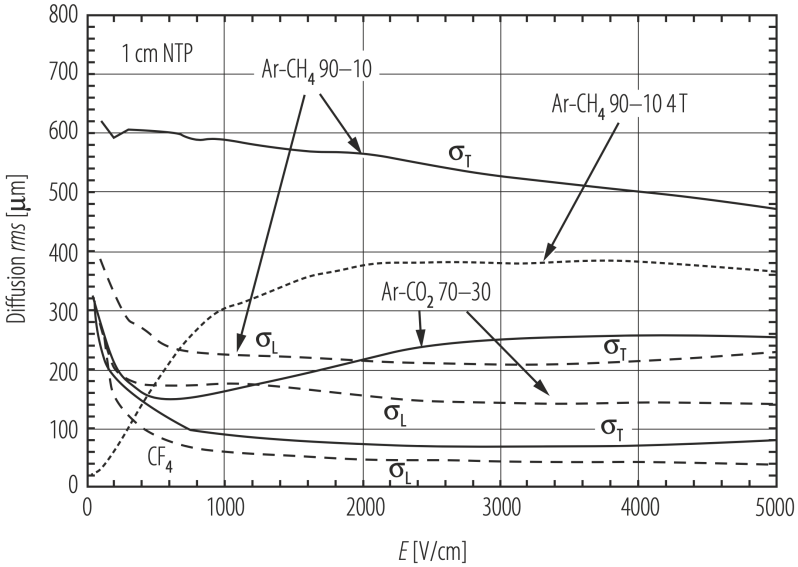

Figure 2.5: Longitudinal and transverse widths of electron clouds after 1 cm of drift as a function of the applied electric field. The curves are shown for typical detector gases at normal temperature and pressure, with no magnetic field applied and with 4 T applied for the Ar/CH_4 gas mixture ($\vec{B} \parallel \vec{E}$). From [36].

components that determine the positional accuracy of a gaseous detector.

Finally, in their travel inside the gas, electrons can be absorbed by atoms/molecules to create negative ions. This happens in presence of very electronegative elements, such as oxygen or fluorine. This is why in gaseous detectors it is needed to protect the gas from contaminants, such as the oxygen present in air.

2.3.3 Avalanche process

When the external electric fields applied to a gaseous detector become sufficiently large, the accelerated electrons might ionize the gas in their motion. This gives rise to an avalanche process.

From an ionization chamber regime, where the charge amplification is zero, a sequence of regimes start with larger and larger electron multiplication factors. As depicted in Figure 2.6, initially the charge grows proportionally with the applied fields (proportional region), then the proportionality saturates. Streamers start to appear, which consist in fully conductive channels in a limited region of the gas. At even larger electric fields, when an amplification process is triggered by the incoming radiation, the entire gas volume gets ionized. This is the so-called Geiger-Müller regime. If the electric field is further increased, the breakdown of the dielectric occurs igniting a discharge.

The processes that lead to the electron amplification were extensively studied by Townsend, who modeled the multiplication with the formula

$$\mathrm{d}n = n \cdot \alpha \cdot \mathrm{d}s \,, \tag{2.33}$$

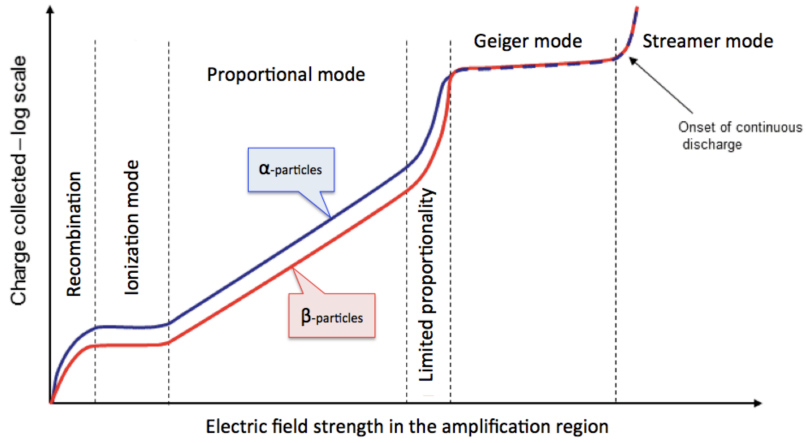

Figure 2.6: Regions of operation of a gas-filled detector. In the y-axis the charge collected at the electrodes is represented in logarithmic scale; the electric field strength in the amplification region is on the x-axis. Both the quantities are represented in arbitrary units. From [48].

where n is the number of created electron-ion pairs, α is the first Townsend coefficient, and ds the infinitesimal distance that the electron cloud travels. The solution of the equation is the exponential function $n = n_0 \exp(\alpha \cdot s)$.
The coefficient α depends on the applied electric field, as well as on the gas conditions, such as its pressure and temperature. Therefore, it can be represented as $\alpha(E, p, T)$. Examples of the dependence of α on the electric field and the gas conditions are displayed in Figure 2.7a and Figure 2.7b for noble gases and Ar/CH_4 mixtures.

Figure 2.7b shows that the simulations disagree with the experimental data for large electric fields. The main causes of the higher numbers of electron-ion pairs in that region are the photo-ionization effect and the Penning effect.
During the electron avalanches, not only ionizations but also a large number of excitations happen. Two mechanisms can take place during the de-excitation.
In the first process, a photon is emitted. Normally, the photon energy is in the ultraviolet range. The photon can then extract an electron via photo-electric effect either from the gas or from the cathode, hence increasing the electron cloud population. The probability of a photon to generate a new ion pair is called second Townsend coefficient, and denoted γ. If the amplification factor multiplied by the second Townsend coefficient becomes greater than one ($A\gamma > 1$), a breakdown occurs. If that product is much smaller than one, it represents the probability to produce an after-discharge.
The other process is the Penning effect [49], which can only happen in gas mixtures. If the excited atom transfers its energy to an atom/molecule of the other species, and that results to be larger than the binding energy of one of its electrons, it gets ionized.
The photo-ionization can be suboptimal in detectors, since the photon might travel far from the main avalanche and generate a secondary one. That one then could be misidentified as an additional interaction of an ionizing particle, spoiling the measurements. To avoid this undesired effect, it is possible to utilize gas mixtures with quenching gases. These have molecules

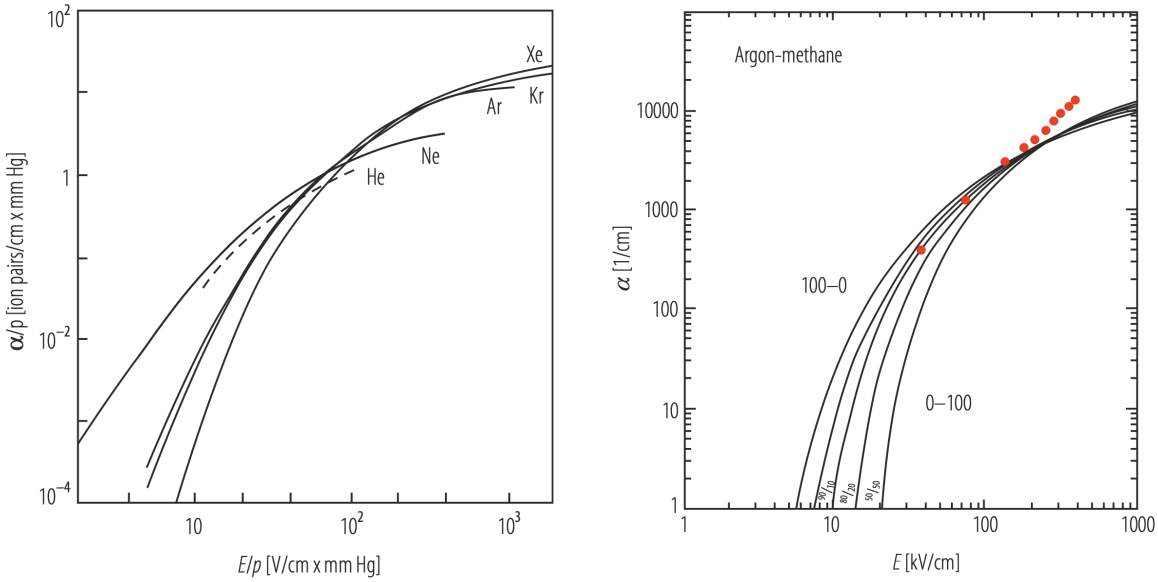

(a) Measured α of noble gases.

(b) Simulated (black lines) and measured (red circles) α of Ar/CH_4 mixtures.

Figure 2.7: First Townsend coefficient for different gases as a function of the applied electric field. On the left plot, the gas pressure is absorbed in both x and y axes. On the right plot, the pressure was fixed to 1 atm. Both plots are from [36].

with many low-lying energy levels that can absorb the emitted photons during the de-excitation processes of the other gas species. For example, excited Argon atoms can transfer their energy to a CO_2 molecule that possesses plenty of rotation and vibration states.
The amplification process undergoes natural fluctuations. In the proportional regime, the amplification factor A for single or few initial electrons follows a Pólya distribution [37], [50]. With increasing numbers of primaries and secondaries, the central limit theorem makes the overall distribution become a Gaussian.

2.3.4 Signal formation on the readout

The avalanche developed in the multiplication process induces a signal on the readout electrode. The signals have two main components. The first one is very fast ($\mathcal{O}$(10 ns)) and it is generated by electrons moving towards the anode. The second component, instead, is much slower (up to $\mathcal{O}$(µs)). It is caused by the ions drifting in the direction of the cathode.

2.4 Fundamentals of the Gas Electron Multipliers

As mentioned in the section 2.2, GEMs are one of the latest inventions in gaseous detectors. Belonging to the MPGD family, they rely on microscopic structures to generate the avalanches and multiply the electrons. Their key element is the GEM foil (Figure 2.8), which consists in a thin sheet of polyimide, coated with a layer of copper on the top and one on the bottom. Holes with a double-funnel (hourglass) geometry are chemically etched with the aid of photolithography.

A high voltage difference is applied across the top and the bottom electrodes, conventionally with the lower potential on the top. This produces strong electric fields inside the holes, where the avalanches can take place. The created ions travel towards the top, while electrons are directed to the bottom of the foil. The chamber is built around the GEM foil. A cathodic and an anodic plane, usually in the form of PCBs, are place above and below the foil at distances of $\mathcal{O}$(mm). Since a single amplification stage would put too much stress on the foil to have a recordable signal size, multiple foils can be utilized in series with a spacing of $\mathcal{O}$(mm) among them. Voltage differences in cascade are then utilized to make the electrons and ions drift through the gaps and be multiplied in the GEM foils.

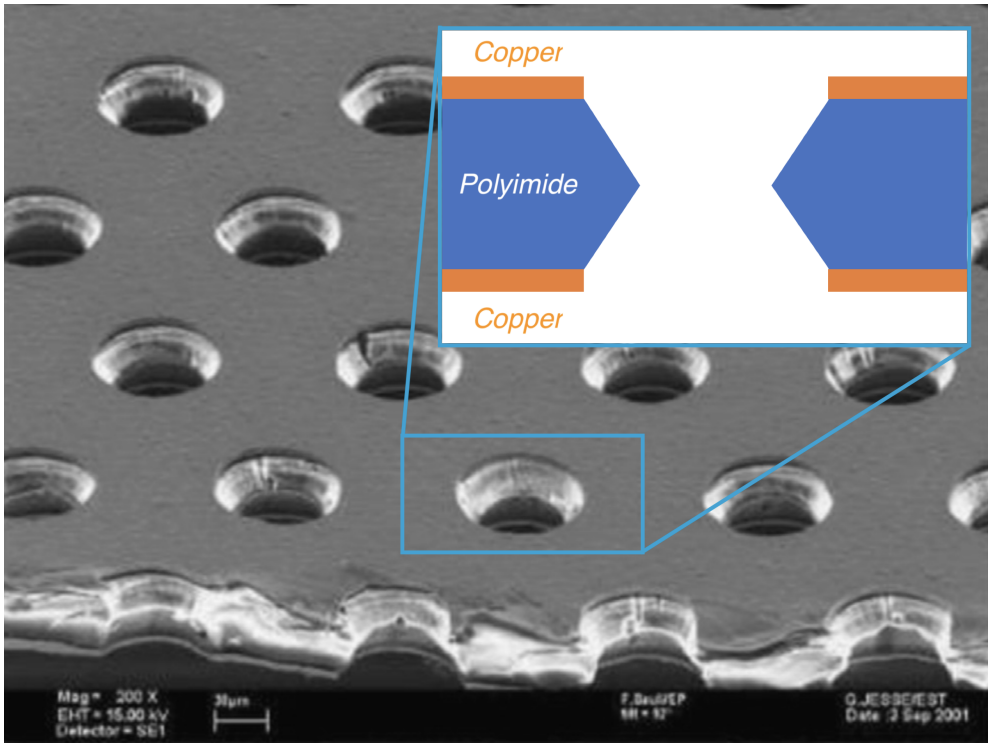

Figure 2.8: Electron microscope picture of a typical GEM foil [46], with the addition of a single GEM hole sketch.

2.4.1 The CMS GEM layout

Thanks to the extensive studies conducted over the years in the R&D phase ([46],[51], among many others), it was possible to select an optimized design for the CMS GEM chambers.

2.4.1.1 The structure

A triple-GEM layout was deemed to best suit the needs. Indeed, it provides a considerable signal amplification, while maintaining the discharge probability at its minimum. The spacing between cathode, GEM1 foil, GEM2 foil, GEM3 foil and anode has been chosen to follow the scheme 3/1/2/1 mm, as shown in Figure 2.10a. In the following a brief justification for this disposition is given.

The distance between the cathode and the first amplification stage, also known as *drift gap*, is 3 mm thick. This allows more than 99.9% of the MIPs to ionize any gas of the common gases at least once.
The *transfer 1*, that separates GEM1 and GEM2, is a 1 mm gap. This keeps the overall structure as thin as possible, while preserving the foils to get in touch. Additionally, if the holes in the two foils are not aligned, such a gap allows the electrons to be sufficiently redirected.
The gap between GEM2 and GEM3 is called *transfer 2* and it amounts to 2 mm. It is larger than *transfer 1* because it reduces the probability of the propagation of a discharge between GEM3 and GEM2.
The *induction* gap, which is situated between GEM3 and the anodic readout plane, is 1 mm thick. This minimizes the drift time during the signal induction, as well as the overall detector thickness.

2.4.1.2 The foils

For what concerns the GEM foils, the CMS GEMs adopt a thickness of 50 µm for the polyimide, and 5 µm for the copper. The holes are arranged in a hexagonal pattern, with 140 µm pitch between two neighboring ones. The hole diameters are 70 µm at the top electrode, 50 µm in the inner part and 85 µm at the bottom[1]. These ensure optimal results in directing the electrons inside the holes, as well as letting them exit without major losses on the bottom of the foil [48]. During the production processes, of course, variations are possible. Normally, the hole diameters tolerances are about ±3 µm.

2.4.1.3 The applied voltages

Not only the voltage difference applied to the foils determines the final signal size, but also the one applied to the gaps. Indeed, the charge produced in the avalanches inside the GEM holes needs to be extracted from the foils and directed either towards the next stage of amplification or to the readout. The ratio between the total charge of the avalanche and the extracted amount is named *extraction efficiency*.
In the case the electrons have to undergo another multiplication step, they have to be correctly steered into the holes of the next foil. Otherwise, they might end up on the copper at top of the foil and get lost. The parameter that characterizes this process is called *foil transparency*.
To maximize both the foil transparency and the extraction efficiency, the electric fields applied and their ratios have to be finely tuned. Examples of studies carried out in the R&D phase of the GEM detectors are summarized in Figures 2.9a and 2.9b.
The electric field scheme employed for the CMS GEM chambers is indicated in Figure 2.10a. In Figure 2.10b, the simulated electric field lines inside a CMS GEM hole are shown for $\Delta V_{GEM} = 384V$.
The asymmetry in the voltage differences among GEM1, GEM2 and GEM3 stems from the results in [51]. A decreasing amplification factor over the three stages provides the minimal

[1]The asymmetric hole shape is intentionally obtained through a specific etching technique. Such a shape provides optimal collection and extraction efficiencies, as proven in [48].

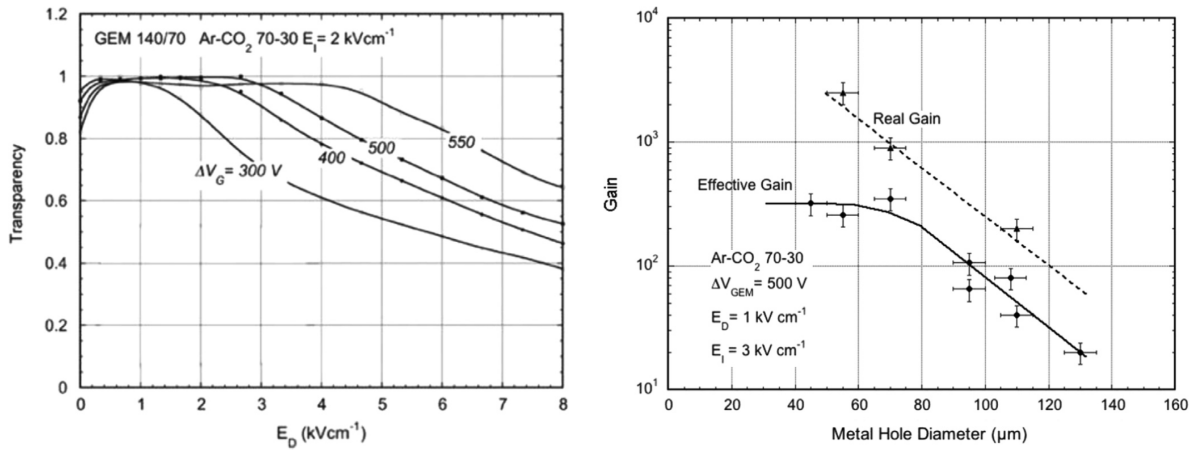

(a) Foil transparency example.

(b) Gain and extraction efficiency example.

Figure 2.9: On the left, electron transparency of a GEM foil with CMS GEM hole dimensions as a function of drift field for fixed induction field, for several values of GEM voltage. On the right, effective and real gain as a function of hole diameter. The ratio between real and effective gain gives the electron extraction efficiency from the GEM holes. The fraction of electrons that end up in the bottom electrode is around 50% for the CMS GEM hole dimensions. From [46].

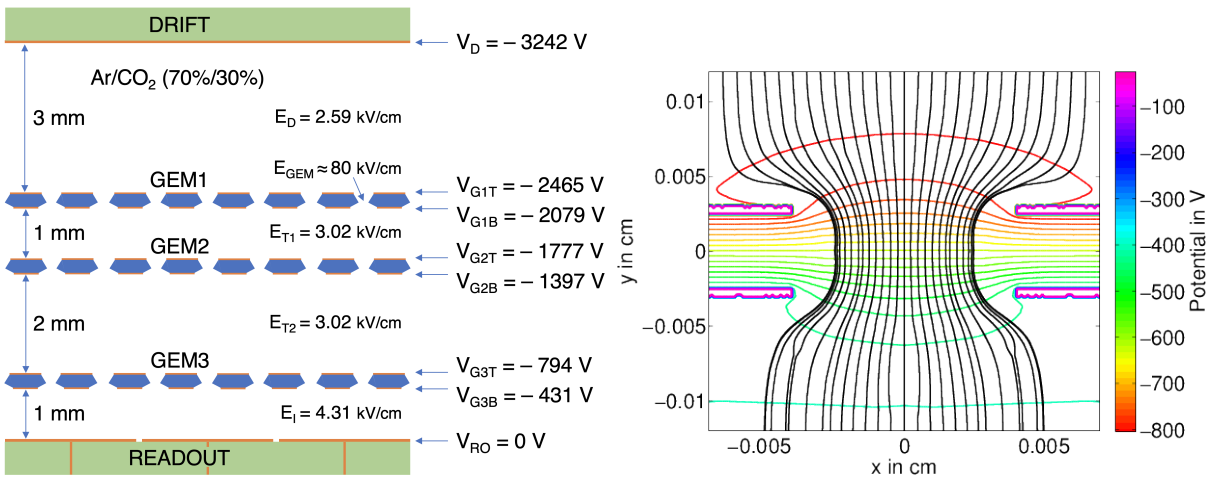

(a) Schematic sectional view of a CMS GEM chamber.

(b) Simulated electric field lines in CMS GEM hole.

Figure 2.10: On the left, schematic view of a section of a CMS GEM chamber. The PCBs are depicted in green, the copper in orange, the polyimide in blue. The naming conventions are the ones in use in the CMS GEM community. The voltages and the electric field values are typical for the CMS GEM operations. On the right, simulated electric field lines in a CMS GEM hole, from [52]. The voltage difference applied between the top and the bottom electrodes amounts to 384 V.

probability for the propagation of discharges.

2.4.1.4 The gas mixture

The gas mixture that was deemed the most suitable choice for the CMS GEM consists of 70% of Argon and 30% of CO_2. First of all, it does not contain any polymerizing gas, which is

optimal for operations in harsh radiation environments. In addition, it is not flammable and it does not contribute to the greenhouse effect. Even though it is not the most performing in terms of electrons drift velocity, electrons diffusion and discharge probability, it is the best overall compromise.

2.4.2 Signals in a GEM detector

The readout plane of most GEM detectors is segmented into strips. The length, the width and the pitch of the strips depend on the specific application.
As soon as the electrons approach the exit of the GEM3 holes, they start to induce signals on the readout strips. During their journey in the induction gap, they keep inducing a current until they reach the anode. When that happens, the signal goes back to the baseline. The long signal tail that is typical in wire detectors is not present in GEMs. Indeed, the ions produced in the GEM holes either end on the top electrode of the foil or keep travel towards another foil. Both of these drifts are not perceived by the readout plane.
As a consequence, the GEM signals produced by a single cluster of electrons have a steep rise, a narrow flat central part and a steep fall. When multiple clusters are generated by ionizing particles, a train of (partially) overlapping signals is induced on the readout. The time of arrival of each cluster depends on the position where it was initially created.
Two major characteristic of the GEM detectors depend on the position of creation of the clusters. Let us consider only the ones that had their origin in the drift gap, since all the others undergo an amplification at least twenty times smaller.
The time resolution depends on the distance of the last primary ionization form the first GEM foil (z_{last}). The *last* cluster is the one that first approaches the readout, defining the absolute time at which the particle interaction is recorded. The intrinsic time resolution of the chamber is then determined by the standard deviation of the distribution of z_{last} divided by the drift velocity in the drift gap. Being the standard deviation of the equation 2.25[2] equal to $(\langle n_P \rangle/\mathrm{cm})^{-1}$, the expected time resolution is given by $(\langle n_P \rangle/\mathrm{cm} \cdot v_D^e(E_{\mathrm{Drift}}))^{-1}$. In the case of a CMS GEM, the expected chamber time resolution results in about 5 ns.
The other consequence that the position of ionized clusters has is the total signal width. Indeed, the spatial difference between the z_{last} and z_{first} translates into a time difference in the arrival at the GEM stack. From there on, the time taken by each cluster is almost the same. The central part of the signal is therefore as large as the time taken by the *first* cluster to get to z_{last}. In the CMS GEM, dividing $\langle z_{first} - z_{last} \rangle \approx 3$ mm by $v_D^e(E_{Drift}) \approx 70$ mm/µs, the width of the central part of the signal results in about 43 ns.
The rise and the fall time of the signals correspond to the drift time of the electrons in the induction gap, which amounts to about 13 ns. Thus, the total width becomes then around 70 ns. Naturally, a smearing is also to be expected. This can be caused by the longitudinal diffusion and the local variations in the drift fields due to the shielding effect by the charge clouds.
The expected integral of the signal can be calculated as the total charge of the primary and secondary electrons due to the ionizations in the drift gap, multiplied by the total effective

[2] In this section, the z-axis defines the particle travel path that previously was called x.

amplification factor. In this case, the term *effective* denotes the convolution of the total amplification in the GEM holes, the foil transparency, the extraction efficiency and the recombination processes. At nominal high voltage values (Figure 2.10a), the order of magnitude of the total signal charge is tens or hundreds of femtocoulombs, depending on the incident radiation.

2.4.2.1 Study of GEM signals in Aachen

A dedicated study of the GEM signal shape in time has been conducted for this thesis. The obtained results provide a solid justification for the what has been recorded during the GE1/1 detector validation, presented in section 5.3.6.2.
The employed detector was a 10×10 cm^2 triple-GEM, produced by TECHTRA[3]. This small-sized chamber ensured an extraordinary flexibility in terms of configurations. Indeed, the GEM hole shape, the orientation of the foils and the spacings could all be easily modified by changing the components in the assembly [53].
The adopted layout for the hole diameters of the three foils was $70 - 50 - 70$ µm. The spacings were variations of the standard 3/1/2/1 mm. The readout board has two layers of perpendicular strips that provide the spatial hit information in two axes. Each layer has 256 strips with a pitch of 390 µm. Four groups of 128 strips are routed to four 130-pin panasonic connectors.
The detector was flushed with the standard CMS GEM gas mixture. The high voltage power supply was an adaptation of the CAEN SY127 with negative voltage power boards; single channels were used to independently power each electrode.
The ionizing radiation came from a ^{109}Cd source. It decays into a metastable level of ^{109}Ag via electron capture, which then can emit X-ray photons with energies of about 23 keV [54]. Those X-rays interact with the copper present on the cathode of the chamber, which subsequently emits fluorescence photons[4]. Finally, these extract a primary electron via photoelectric effect, that generates around 295 electron-ion pairs in the drift gap.
The readout electronics can be seen in Figure 2.11b. It was custom made by the Aachen IIIA electronics workshop, employing a very fast 2-channel current feedback amplifier with a slew rate of 9 V/ns (Texas Instruments THS3202 [55]). The chip is powered by batteries in order to minimize the electronics noise. The feedback circuit built around the amplifier utilizes a 1000 kΩ resistor, that gives a trans-amplification factor of 1000 V/A. This way, it was possible to directly sample the amplified GEM readout signals from two neighboring strips[5] by means of a highly performant oscilloscope. The panasonic connector on the same side of the chamber was left unplugged, while the perpendicular strips were terminated with a 50 kΩ resistor for each of the 128-strips group. Such a configuration ensured a low noise level and a negligible reflection of the signals on the other layer of strips.
The setup can be seen in Figure 2.11a.
The main targets of this study were to evaluate the shape and the width of the signals in different

[3]Technology Transfer Agency TECHTRA Sp. z o.o.
[4]The main copper fluorescence peaks correspond to the energies of $K_{\alpha 1} = 8.048$ keV, which is the most intense, and $K_{\beta 1} = 8.905$ keV, with a relative intensity to the $K_{\alpha 1}$ of 13%.
[5]Reading out two strips was enough for the studies presented in this thesis. A new expanded version of the board has also been made, which employs two chips and is capable of reading out four neighboring strips.

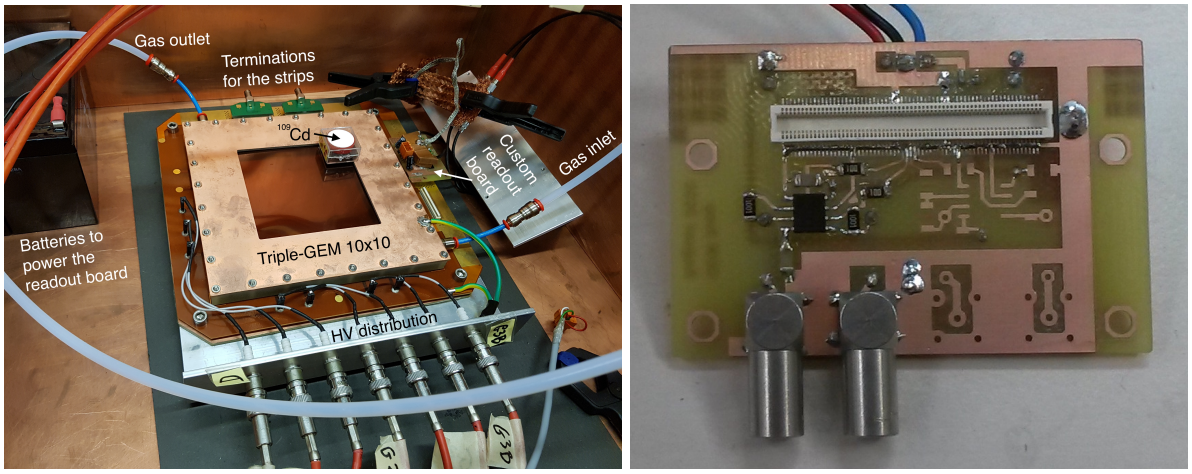

(a) GEM 10×10 cm^2 setup arrangement. (b) Custom readout electronics board.

Figure 2.11: On the left, a picture of the experimental setup with the 10×10 cm^2 triple-GEM TECHTRA chamber in the center and all the services around it. On the right, a picture of the custom made readout electronics board based on the THS3202 2-channels chip. It allows to amplify the GEM signals without introducing distortions.

configurations. The variations regarded the drift and the induction fields, as well as the width of those two gaps. The baseline measurements were conducted with the standard 3/1/2/1 mm spacing, with voltages proportional to the ones in Figure 2.10a, and scaled to a $V_D = -3453$ V[6]. In addition, a high voltage scan measurement has been conducted. All the configurations derived from that starting point are presented in Table 2.2.

For each of the chamber configurations, 2×7500 signals were digitized and stored. A post processing allowed to characterize the GEM signals in terms of induced charge and time width. In this study, the signal width is defined as the total signal length, from the beginning of the rising edge to the end of the falling edge. It is computed as the longest time interval between two consecutive points in which the signal crosses the 3% of its minimum value[7].

Examples of GEM signals with A1 configuration are given in Figures 2.12a and 2.12b, where one signal width has been depicted for convenience. In the first presented event, the amplified charge was shared between the two neighboring readout strips. In the second one, instead, one strip was at the side of the electron cloud. It recorded then a bipolar signal that integrates to zero.

The analysis of the signals revealed that:

- In the CMS configuration (A1), the average total charge seen by one strip is about 500 fC.
- In all A# and S# configurations, the GEM signals have an average width of 75 ± 2 ns, confirming the predictions.
- When the induction field is halved, the effective gain results also halved.

[6]The applied voltages are higher than the nominal one for the CMS GEM chambers ($V_D = -3242$ V). This because the employed readout electronics imposed higher gas gain values than the nominal one (20000) in order to obtain measurable signals.

[7]Consider that the signal is negative, so the minimum corresponds to the maximum of the absolute value.The 3% value for the signal time width estimation has been chosen minimizing the influence of the baseline oscillation on the signal length estimation.

Configuration	Spacings	Electric fields variations	Effective gas gain
A1	3/1/2/1 mm	Baseline HV	41919
A2	3/1/2/1 mm	0.5× induction field	/
A3	3/1/2/1 mm	0.5× induction field and 0.75× drift field	/
B1	3/1/2/2 mm	Baseline HV	41919
B2	3/1/2/2 mm	2× induction field	/
B3	3/1/2/2 mm	1× induction field and 0.75× drift field	/
C1	4/1/2/2 mm	Baseline HV	41919
C2	4/1/2/2 mm	2× induction field	/
C3	4/1/2/2 mm	1× induction field and 1.33× drift field	/
S1	3/1/2/1 mm	Baseline HV	41919
S2	3/1/2/1 mm	$V_D = -3430$ V	34285
S3	3/1/2/1 mm	$V_D = -3406$ V	28041
S4	3/1/2/1 mm	$V_D = -3383$ V	22934

Table 2.2: Configurations of the 10×10 cm^2 GEM utilized in the signals evaluation study. In the A# and B# configurations, the induction fields and the spacings of the drift and the induction gaps were varied. The S# configurations correspond to a high voltage scan. The effective gas gain values indicated in the rightmost column were obtained following the procedure detailed in section 4.1.1. All the gain values are larger than the nominal gain for a CMS GEM chamber (20000); this was imposed by the employed readout electronics, which required larger gas gain values to obtain measurable signals.

- When the induction gap is doubled and the applied voltage is the standard one, the effective gain is halved and the average signal width increases from 75 ± 2 ns to 102 ± 5 ns.
- If the induction gap is doubled and the electric field is kept as nominal, the average signal width becomes 93 ± 4 ns. No major gain difference is noticed, remaining about 92% of the nominal one.
- The drift gap variations have a negligible impact both on the gain and on the signal shape.

An additional analysis has been conducted, considering the CMS GEM GE1/1 on-chamber electronics shaping time. By design, it can be set to a maximum value of 45 ns, as described in section 2.5.5.4.
Instead of integrating the whole signal, a sliding window of 45 ns was implemented. The maximum value that was integrated in that time window was taken as the recorded charge. The ratio between the charge in the 45 ns window and the total one was then computed for each of the configurations. It resulted to be around 84% with the nominal electric field in the induction gap, while it was reduced to 72% in the configurations with half of the induction field.
Finally, the high voltage scan results (S# configurations) were elaborated to obtain the curve of the charge seen by one strip as a function of the HV working point. The plot in Figure 2.13a shows that the recorded charge in one strip does not grow exponentially with the applied voltage, as the avalanche processes would suggest. Indeed, the electron cloud not only grows in

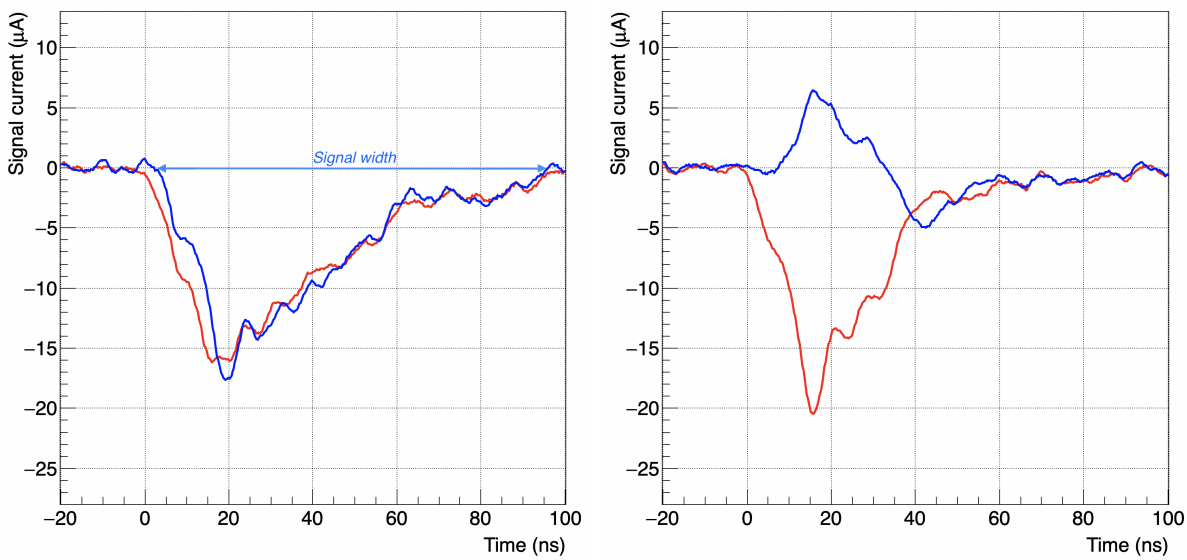

(a) GEM typical signals.

(b) GEM bipolar signal.

Figure 2.12: On the left, typical GEM signals induced on two neighboring strips that share the charge produced in the ionization event. The signal shape has a minimal influence given by the amplifier shaping, since the utilized THS3202 chip has a slew rate of 9 V/ns. On the right, one strip is involved by the avalanche charge, while the other is on its side. That strip records a bipolar signal that integrates to zero.

magnitude with the HV, but also in size. Therefore, the charge gets shared among an increasing number of strips. As a confirmation, Figure 2.13b shows that the fraction of the total avalanche charge recorded by a single strip diminishes with the HV.

2.5 The CMS GEM GE1/1

After the explanation of the CMS GEM chamber details in the previous section, this section will be focused on the technical aspects of the CMS GEM GE1/1 chambers. The location in CMS with the consequent limitations will be explained. The design will be then detailed showing the peculiarities and the novelties introduced. Finally, the services and the readout electronics will be described, with an accent on the aspects that will serve as a basis for the chapters 4 and 5.

2.5.1 Location in CMS

As briefly mentioned in the previous chapter, the GE1/1 detectors are located in the two endcaps of the CMS experiment. More specifically, they dwell in the so-called nose of the endcap, between the HCAL and the CSCs. There, they cover the pseudorapidity region $1.55 < |\eta| < 2.18$. In that position, the magnetic field is about 3 T, with an angle of about 8° with relation to the CMS z-axis.

The GE1/1 slot was initially foreseen to host RPC chambers, in order to complement the ME1/1 CSCs. Since the RPCs could not sustain the rate and the dose of the 1/1 ring of the endcaps, at the CMS construction time the place was left empty. The challenging harsh radiation envi-

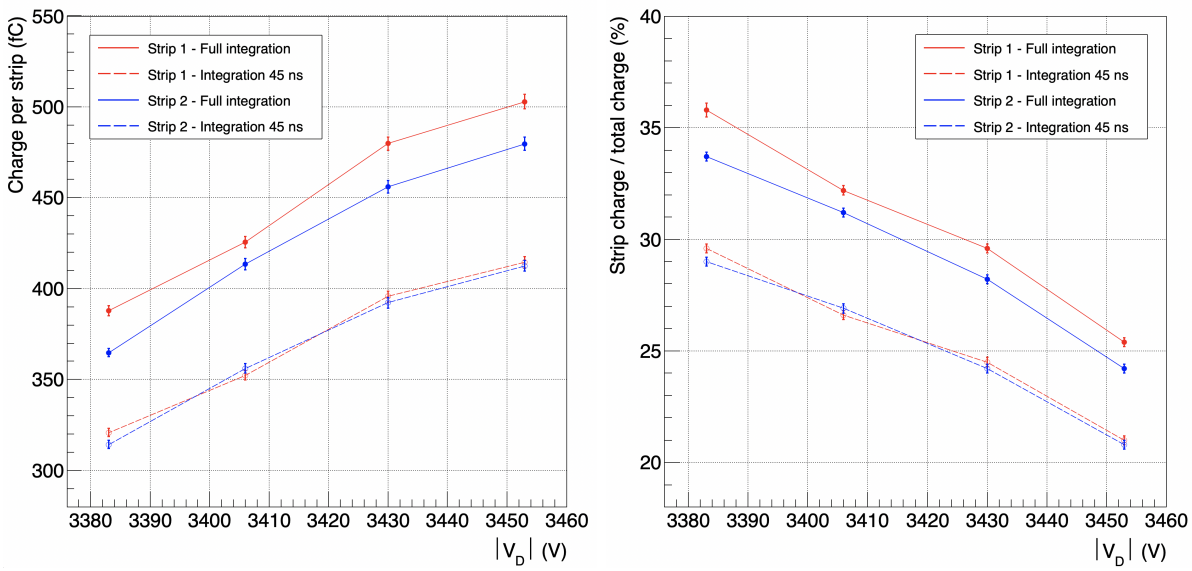

(a) Average signal charge per strip as a function of the applied HV.

(b) Ratio of strip charge over the total avalanche charge as a function of the applied HV.

Figure 2.13: On the left, average charge seen by a single strip in the S# configuration as a function of the applied high voltage. On the right, ratio between the average charge recorded by one strip and the average total charge produced in the avalanches, as a function of the applied HV. While the total avalanche charge grows exponentially with the high voltage, the single strip sees a diminishing fraction of it. As a result, the curves on the left plot are not exponential. In both plots, the high voltage working points are represented by the absolute value set to the drift cathode. All the other electrodes were powered proportionally, as in Figure 2.10a.

ronment required a new type of detector, with the constraint of fitting the thin gap left by the RPCs. The GEM technology fulfills the requirements. Indeed, it has an abundant rate capability and it is not prone to aging. Moreover, with a gas volume thickness of less than 1 cm, it fits very narrow locations while maintaining a theoretical efficiency for MIPs larger than 99%.

Not only the physical volume for the chambers is limited, but also the structure of the CMS endcap nose is relatively complex. Indeed, it has massive metallic supports along its perimeter every 20°.

In the following section will be shown how these constraints reflect on the design of the GE1/1 detectors.

2.5.2 Structure of a GE1/1 detector

The shape of the GE1/1 detectors is trapezoidal to allow for an optimal coverage of the surface of the ring. Each detector spans 10.15° in angle, allowing an overlap between neighboring ones. Therefore 72 GE1/1 are needed to fully instrument the two rings. Moreover, to cope with the structural blocks present, *long* and *short* types of detectors are present, covering the regions $1.55 < |\eta| < 2.18$ and $1.61 < |\eta| < 2.18$ respectively. They both share the same characteristic angles of the trapezoids, and the same size of the narrow basis. They are alternately installed and arranged as depicted in Figures 2.14a and 2.14b.

The thin space left by RPCs, allowed for two layers of individual GEM chambers. The structural

combination of two chambers into a single module produces the *super chambers*. The criterion adopted for the pairing of the two chambers is the similarity in their gas gain at a fixed applied voltage. This stems from the choice of having a common HV supply for the two layers of each super chamber, in order to reduce by half the number of required HV power supply boards, and consequently diminish the required budget.
The two chambers of a super chamber are held together by a screwed aluminum plate on the narrow side, and two L-brackets on the wide side. These are also used as mounting points. On the narrow side, a pin sliding in a rail acts as the fixing structure. For both super chamber types, the chamber facing the interaction point is referred to as *Layer* 1 (L1), while the one facing the experimental cavern walls is conventionally named *Layer* 2 (L2).
Two layers of muon detection have two main benefits. Firstly, the combined efficiency gets increased. Secondly, when both layers record a hit, it is possible to reconstruct a segment and assign positional and angular information.

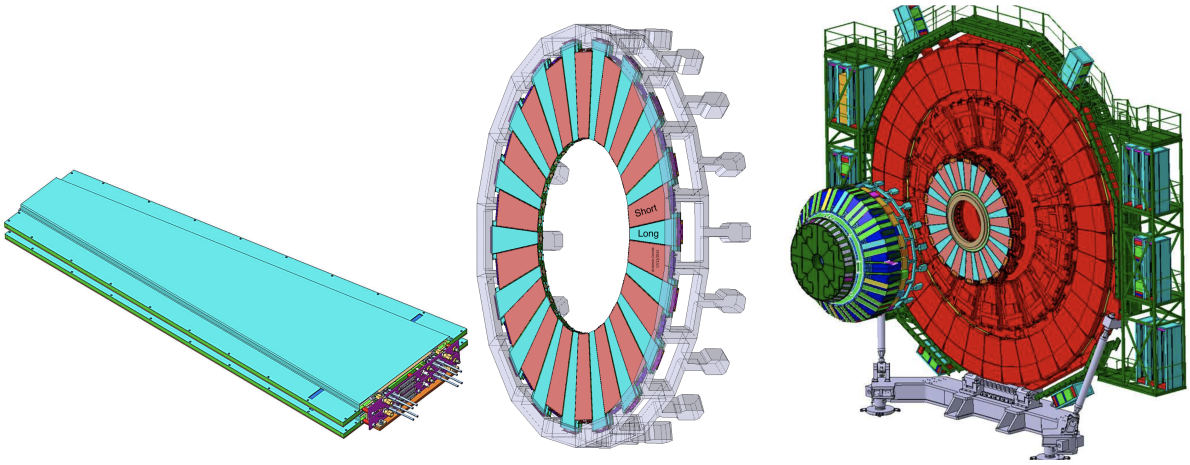

(a) GE1/1 super chamber and ring. (b) GE1/1 location in CMS.

Figure 2.14: Drawing of a GE1/1 super chamber, on the left. Super chambers arranged into the GE1/1 disk, in the center. The orange chambers are of the short type, and they have the readout board facing the outside of CMS. The azure chambers are of the long type, which have the readout board facing the interaction point. On the right, the GE1/1 detectors are shown integrated in the CMS endcap. The drawings are from [34].

The fundamental element of a GE1/1 detector is the *single chamber*. It is composed of a triple-GEM stack with 3/1/2/1 mm spacing, sandwiched between cathodic and the anodic PCBs made of FR4 material. Each foil has a single copper layer on the bottom, while the top is segmented into slices perpendicularly to the η direction (Figure 2.15). Each partition has an area of about 100 cm^2. The high voltage sectors on the top of the foils are powered through a 10 MΩ protection resistor, while the bottom has no protection resistor installed. This has been made for two reasons. The first is that, if a short circuit is generated across the foil, only 1/40 (1/47) of the total area of a short (long) chamber experiences a gas amplification drop. The second is that, when a discharge occurs only the limited amount of charge stored in the involved partition can contribute to the spark.
The cathodic and the anodic PCBs are called respectively *drift* and *readout* boards. While the

copper surface of the cathode is a single plane, the anode is finely segmented into radial strips. Along the ϕ direction, the strips have a pitch of 461 µrad. They are then further divided into eight regions along the chamber longitudinal axis (iη sectors), each one with 384 strips (Figure 2.15). Each iη partition is further subdivided into three groups of 128 strips, whose traces are routed to a 130-pin panasonic connector placed on the outer side of the PCB. The remaining two pins are connected to ground.
As previously mentioned, the gas in use is a mixture of Argon (70%) and CO_2 (30%). The high voltage values applied to the eight chamber electrodes are normally proportional to the one presented in Figure 2.10a.

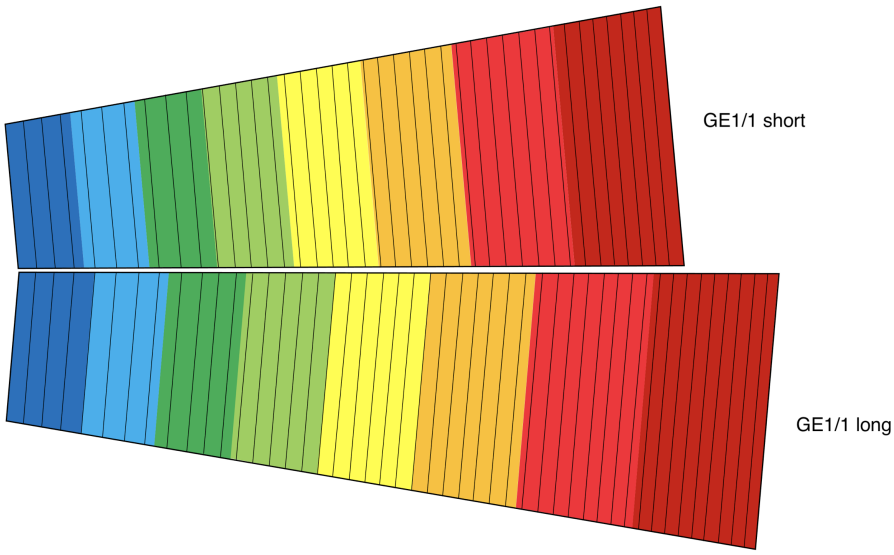

Figure 2.15: The HV segmentation on the top of the short (long) GE1/1 GEM foils into 40 (47) strips is schematically represented in black lines, with superimposed readout board segmentation depicted in colored blocks.

The entire structure is assembled with screws and without the use of any type of glue, in order to avoid any possible outgassing source. A plastic internal frame equipped with a rubber gasket seals the gas volume. Together with the choice of the gas mixture, which contains no polymerizing gases, the absence of glues ensures a minimal aging. This also allows for a chamber re-opening without any damage. The large-area GEM foils are kept together and stretched by a plastic frame that screws onto metallic pull-out structures present in the drift board. The applied tension amounts to 5 N/cm.
All the mentioned specifications and other characteristics are summarized in Table 2.3. The bare chambers are then completed by several other components, which can be seen in Figure 2.16.
The external aluminum frame, the aluminum cover (chimney) and the back of the drift board, which is covered with 140 µm of copper, create the detector Faraday cage. This protects the readout strips and electronics from any undesired interferences by external RF noise.
The cooling plate is entirely made of copper and serves as a heat dissipation element for all the installed on-chamber electronics, which will be described more in depth in the upcoming sections. A copper pipe is routed on top of the plate, meant to carry the liquid coolant: water at about

Specification / Parameter	**GE1/1**
Detector technology	Triple-GEM; Micro-Pattern gaseous detector
Total number of single chambers	144
Total number of super chambers	72
Chamber shape	Trapezoidal; opening angle 10.15°
Active area overlap in adjacent chambers	2.6 mrad = 5.7 readout strip pitches
Short chamber dimensions	L: 106.1 cm (center line), W: (23.1 - 42.0) cm, T: 0.7 cm
Long chamber dimensions	L: 120.9 cm (center line), W: (23.1 - 44.6) cm, T: 0.7 cm
Total chamber thickness	T: 3.5 cm
Active readout area	0.345 m^2 (short ch.); 0.409 m^2 (long ch.)
Active chamber volume	2.6 liters (short ch.); 3 liters (long ch.)
Radial distance from beam line	130.2 cm (at inner edge of active readout area)
Geometric acceptance in η	$1.61 < \|\eta\| < 2.18$ (short ch.); $1.55 < \|\eta\| < 2.18$ (long ch.)
Signal readout structure	Truly radial readout strips
Readout strip dimensions	463 µrad angular pitch
Number of η-partitions in readout	8
η-partition length at the center (short ch.)	$101.81, 102.06, 119.57, 119.57, 140.57, 140.57, 166.55, 166.14$ mm
η-partition length at the center (long ch.)	$113.22, 113.07, 134.56, 134.56, 161.07, 161.07, 195.05, 194.2$ mm
Number of readout strips per η-partition	384
Number of readout strips per chamber	3072
Counting gas mixtures	Ar/CO_2 (70/30%)
Nominal operational gas flow	5 liters/hour
Number of gas inlets per chamber	1
Number of gas outlets per chamber	1
Nominal HV applied to drift electrode	−3242V
Nominal operational effective gas gain	2×10^4
Number of HV sectors per foil (top)	40 (short ch.); 47 (long ch.)

Table 2.3: Main specifications and parameters for the design and operation of the GE1/1 chambers [34].

16°C.

Another essential element of the chamber is the aluminum patch panel (Figure 2.17), which acts as an interface between the detector and the external world. It holds the feedthroughs for the gas inlet and outlet, as well as the ones for the optical fibers. It also carries a 3-pin low voltage connector, and a high voltage 9-pin Amphenol connector. From the inside of the HV feedthrough, eight individual HV wires come to the so-called HV filter box, which is directly screwed onto the patch panel. Inside the box, a PCB hosts seven low-pass circuits to filter the possible noise brought by the HV cables. Each filter circuit is composed by a 320 kΩ input resistor, followed by a 2.2 nF capacitor that goes to ground and a 10 kΩ resistor that connects to the GEM chamber electrode. The patch panel also serves as the ground star point for the chamber. It is connected to the main ground of the CMS endcap through a thick braided cable, and thin wires bring the ground to all the electronics components and to the Faraday cage conductors. To the star point are also connected the minus terminal of the low voltage, the ground of the HV filter board

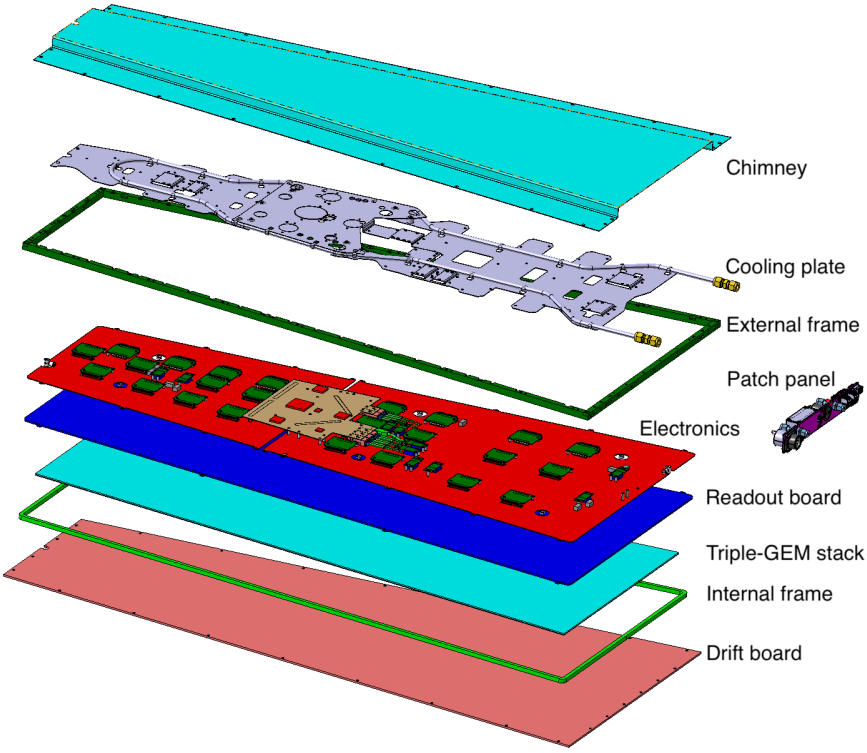

Figure 2.16: Exploded view of a schematic drawing of a GE1/1 single chamber. The major design blocks are labeled following the CMS GEM conventions. Credits to the CMS GEM group.

and the return of the HV cable. Indeed, the GE1/1 power supplies are floating and receive the ground reference point from the detector.

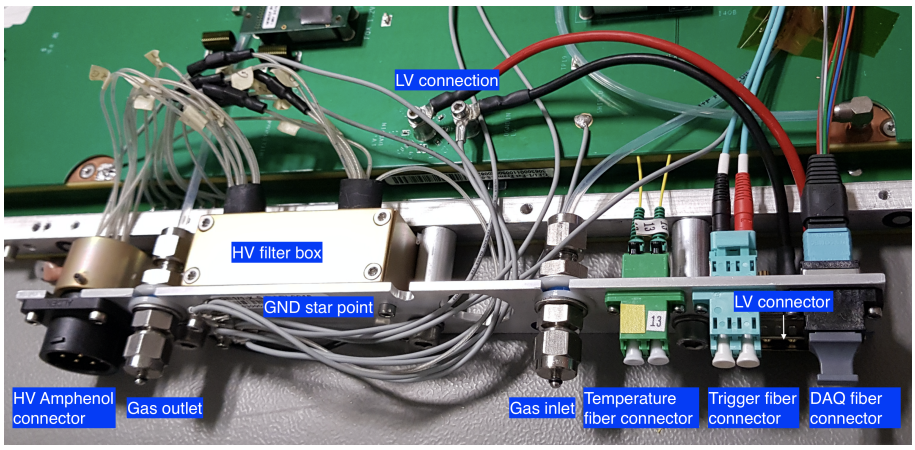

Figure 2.17: GE1/1 patch panel with labels on the main visible components.

In addition to the mentioned elements, which are present in every chamber, two components are specific to some of them. Namely, the temperature and the radiation sensors.
Fiber Bragg Grating (FBG) temperature sensors [56] are routed between the readout board and the electronics of each short chamber. In CMS a chain of eighteen sensors, each sensitive to a different wavelength, is readout simultaneously. Two chains are present in each of the GE1/1

rings, for a total of four.
The layer 1 of six long super chambers installed in each endcap is equipped with a radiation monitor (RADMON). It is mounted on the cooling plate and it is used to record the integrated absorbed dose.

2.5.3 Production of the GE1/1 detectors

The effort of the production of 144 GE1/1 chambers was shared among institutes of seven different countries around the world. USA, Italy and India were devoted to the production of short chambers. Belgium and Germany collaborated in the assembly and test of long chambers. CERN and Pakistan contributed to the production of both long and short chambers. The Physics Institute IIIA of the RWTH Aachen University served as a test site, validating in total 16 long chambers.
Each single chamber was given a unique serial number at the assembly stage. The defined format is 'GE1/1-X-PROD_SITE-ZZZZ'. 'X' represents the last iteration in the chamber design. 'PROD_SITE' is the name of the university or the location where the assembly has taken place. 'ZZZZ' is a four digit incremental number. For instance, the first long chamber assembled in Ghent is identified by the serial numbers GE1/1-X-L-GHENT-0001.
The production of the super chambers has taken place in the CERN GEM laboratory. In that stage, the bare chambers have been equipped with all the components depicted in Figure 2.16 and paired into super chambers. The super chambers have been assigned a unique ID in the formats 'GE1/1-X-SCS-ZZZZ' and 'GE1/1-X-SCL-ZZZZ' for short and long super chambers, respectively.

2.5.4 Services for the GE1/1

In order for a GE1/1 detector to be operated, it needs to be provided with all the necessary services. Low voltage, cooling, and an adequate readout chain are needed for the electronics. High voltage and gas are required by the chambers. Dedicated systems control and monitor the set points and any possible malfunctioning. All the cables, pipes and optical fibers are routed from the service cavern to the experimental cavern of CMS, where they reach the first GEM station on the endcaps disks. In the following, the services and the systems will be briefly presented.

2.5.4.1 The gas system

The GE1/1 gas system in CMS is designed to have a main and a spare line for the two endcaps. The two then come to a conjunction valve and from there it gets subdivided into 12 individual lines per endcap, 24 in total. Each gas line supplies one chain of six neighboring single chambers belonging either to layer 1 or to layer 2. Every individual line is continuously monitored by a flowmeter at the input and one at the output.
A gas mixer is installed at the beginning of the main gas line. It is used to combine Argon and CO_2 with the desired percentages. It can also be set to deliver pure CO_2. Normally, the Ar/CO_2 mixture is utilized in operations, while pure CO_2 is used during the initial phases after

a long system shutdown (for instance, after the Christmas break). Indeed, when the high voltage power is not provided for extended periods, it is mandatory to train the electrodes to stably reach the desired operating working points. This is called *HV training*. The procedure foresees a first step to be performed in pure CO_2, in which avalanches cannot take place at the standard GEM operating voltages. Subsequently, the chambers can be flushed with the standard GE1/1 gas mixture (Ar/CO_2) to complete the training.

2.5.4.2 The low voltage system

The GE1/1 low voltage system in CMS is composed of three main stages. First come four branch controller boards (CAEN A1676A [57]) installed in a CAEN mainframe located in the Underground Service Cavern (USC). These propagate the commands to the entire low voltage system. Each branch controller is then connected to a pair of MAO power supplies (CAEN A3486 [58]), situated in the Underground Experimental Cavern (UXC). They are responsible to deliver 48V for power and service to the following stage. Finally, two EASY3000 crates are connected to each couple of MAOs. Each crate hosts a total of six low voltage floating power supply boards (CAEN A3016HP, special version of CAEN A3016 [59]). Every A3016HP board supplies the LV to three super chambers.
The low voltage cables routed from the GEM LV racks to the GE1/1 detectors host four conductors. One pair is devoted to supply the power, while the other pair serves as sense wires. These allow to measure the voltage at the detector end. This information is used by a dedicated circuit inside the A3016HP boards that adjusts the set point to compensate for the voltage drop in the LV cables. In CMS, the chamber input LV is set to 8V, with a compensation that normally amounts to a few tenths of a volt.

2.5.4.3 The high voltage system

The GE1/1 high voltage system in CMS is entirely located in the USC. There, each of the four CAEN SY4527 [60] HV mainframes hosts nine CAEN A1515TG [61] stacked-HV floating power supply boards. Every board powers all the electrodes of two neighboring super chambers. The two layers of each super chamber share the same high voltage supply. A Y-splitting of the cables is done within the HV racks in USC through patch panels. After that, each cable powers a single chamber.

2.5.4.4 The Detector Control System

The three systems that were just described are all controlled by a unified Detector Control System (DCS). It is responsible to send the commands to the LV and HV boards, and to receive the possible alarms that may arise in any part of the LV, HV or gas systems. In case of undesired or abnormal events, the DCS is programmed to react ensuring the safety and preserving the integrity of the detectors. Moreover, it is deputed to constantly monitor the status of the systems, recording the current values and storing them in a dedicated database. This includes LV, HV and gas, together with the sensors installed on the chambers, namely the temperature sensors and the radiation sensors (RADMONs).

The DCS has two main modes of operation. The first one is the *local* mode, which allows GEM DCS experts to modify the parameters to be applied, as well as to manage the alarms. The second one is the *central* mode. This is integrated within the CMS DCS, and allows to control all the subsystems from a single node, via a Finite State Machine (FSM) schema. That way, when the whole CMS experiment has to be operated in concert, the commands can be propagated simultaneously and the alarms can be gathered and managed from a single point.

2.5.4.5 The Detector Safety System

Together with the DCS, the Detector Safety System (DSS) is meant to preserve the integrity of the systems. Its main responsibility is to activate safety procedures in case of severe emergencies like fire, smoke, water leaks and others. For instance, it can send a *kill* signal to the racks containing the GEM power supplies if dangerous situations like a CMS magnet fast discharge occurs.

2.5.4.6 The cooling system

The GE1/1 cooling system is responsible to keep the temperature of the on-chamber electronics within the limits of operability. It pumps water at a temperature of about 16°C and a pressure of about 9 bar through the cooling pipes of the chambers.

2.5.4.7 The backend electronics

The GE1/1 DAQ system deployed in CMS [62] can be divided into two parts: the on-chamber (frontend) electronics and the backend electronics. The frontend electronics will be presented in detail in the following section, while a brief overview of the backend electronics will be given here.
The backend electronics is based on the µTCA standard [63], which employs advanced mezzanine cards (AMCs). This is one of the most commonly adopted nowadays by HEP experiments, including a large fraction of the CMS off-chamber electronics and the central CMS DAQ (CDAQ). Two µTCA shelves (crates) are located in the USC, one for the positive and one for the negative GE1/1 endcap. In each µTCA shelf are present a commercial MicroTCA Carrier Hub (MCH), an AMC13 and six specialized AMCs.
The commercial MCH allows to manage and to provide services to all of the cards in the shelf through an Ethernet connection.
The AMC13 has been specifically developed for the CMS application to fulfill several duties. First, it is used to receive and distribute the central clock (40.079 MHz) and the synchronization commands to the cards in the shelf. Second, it takes care to collect the frontend status information and to propagate it to the central CMS control system. These two functions together summarize into the acronym TCDS, which stand for Trigger Distribution and Control System. In addition to this, the AMC13 is also responsible to collect the DAQ stream coming from the AMC modules and to transmit it to the central CMS DAQ.
Finally, the six Calorimeter Trigger Processor cards (CTP7) [64] are present in each of the shelves. These were originally created for the CMS trigger calorimeter upgrade, but their high

flexibility makes possible to adapt them for other purposes. They are based on a combination of a Xilinx ZYNQ, a Xilinx Virtex-7 FPGA and an AXI infrastructure. Each of the CTP7s can handle multi-gigabit input/output optical communication through 36 TX and 36 RX links on three Avago CXP, as well as 12 TX and 31 RX links on the Avago MiniPODs. This allows slow control, DAQ and trigger data transfer with 12 single chambers for every CTP7 card.

2.5.5 The GE1/1 on-chamber electronics

The frontend on-chamber electronics is the first stage of the GEM signal processing. It comprises various components, each specialized to carry out a set of tasks.
Attached to the readout board, 24 VFAT3 [65] (HV3b_V3) hybrid boards[8] are responsible of converting the avalanche charge induced on the strips into binary information. Their 128 channels read out the strips present in each of the 24 sectors, which are numbered following the convention in Figure 2.18. Once the digital information about the hits has been elaborated, it takes two paths: the full-granularity data path and the half-granularity trigger path. Indeed, while the DAQ records the hits from each of the 128 channels, in the trigger path the information from two neighboring strips is merged into a single one - resulting in 64 bits. The digital signals are sent from the VFATs to the OptoHybrid (OH) board through the GEM Electronics Board (GEB). Finally, after a final signal processing in the OH, the information is sent to the GEM backend and to the CSC trigger mother board (TMB) [66] via optical links.

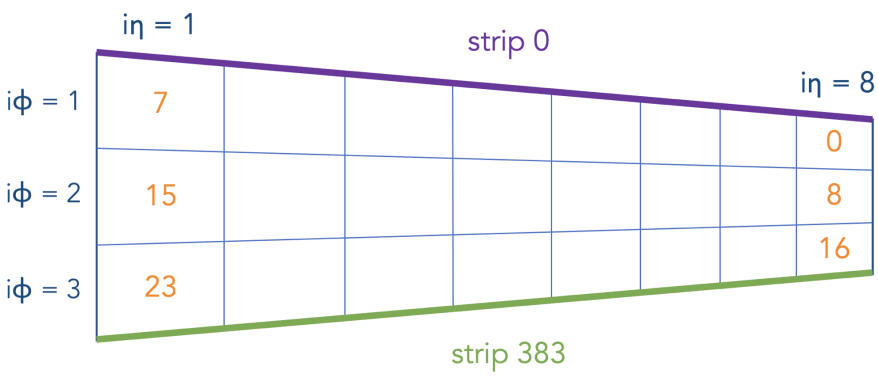

Figure 2.18: Conventions adopted for the numbering of the GE1/1 readout sectors and strips.

2.5.5.1 The GEM Electronics Board

The GEB consists of a fully passive multi-layer PCB that routes the low voltage lines and the signal transmission lines among the active components. Due to manufacturing limitations, it had to be produced in two pieces (wide and narrow parts), each covering four iη partitions. They are interconnected by LV cables for the main supply, and screwed to the chamber external aluminum frame. In addition, small copper tongues are soldered to the PCB and screwed onto the external

[8]The VFATs are often referred to as *hybrid* boards, or just *hybrids*, since they manipulate both analog and digital signals.

frame to bring the main ground.
On the GEB are present multiple connectors for the various electronics components. 100-pin connectors are used for the VFATs, 12-pin connectors for the on-chamber DC-DC converters, while SAMTEC connectors on both halves of the GEB are hosting the OH board. In addition, screw terminals are used for the plus and minus poles of the low voltage supply.

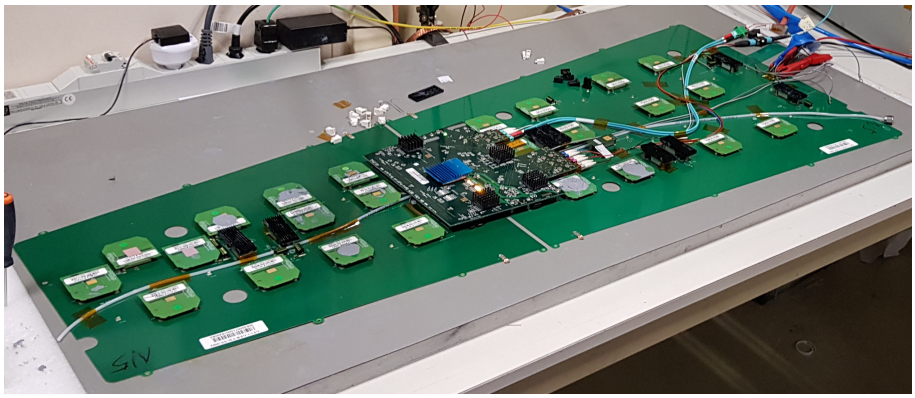

Figure 2.19: Fully equipped GE1/1 GEB under electronics test.

2.5.5.2 The FEAST

Although having a single low voltage supply per chamber is very convenient for the management of power supplies and cables, on the other hand a single voltage value introduces the need to adapt the voltage level for the individual components directly on the chamber. Indeed, the operating voltages of the different GE1/1 electronics components are not uniform; they vary between 1 V to 2.55 V with several other values in between. The adopted solution is represented by the FEASTMP_CLP DC-DC voltage converters [67], which are built around the highly radiation tolerant FEAST2 ASIC. Mounted locally on the GEB, they provide the required operating voltage to the pieces of electronics transforming the 8 V given at the input with efficiencies above 70%. The heat generated is dissipated by the cooling plate in order to avoid damages.
A total of nine FEASTs are installed on the chambers. As shown in Figure 2.20, FQA, FQB, FQC, FQD provide 1.3 V to a domain of six VFATs. The other five FEASTs provide the power to the OptoHybrid. The FPGA core requires 1.0 V, 2.58 V are needed by the VTTRx, and 1.55V by the GBTX and the SCA chips.
Each FEAST is thermally coupled with the cooling plate with non-conductive thermal paste, which carries away the heat produced in the voltage conversion.

2.5.5.3 The OptoHybrid board

The OptoHybrid board (OHv3c) depicted in Figure 2.21 is the custom PCB at the core of the GE1/1 on-chamber electronics. It is deputed to carry out two main duties. The first is to process and elaborate the trigger hits, thanks to a Xilinx Virtex-6 FPGA. The latter also directly drives two VTTRX optical transceivers, which let the GE1/1 chambers to communicate with the GEM backend trigger links and with the CSC Trigger Mother Board (TMB). The second task

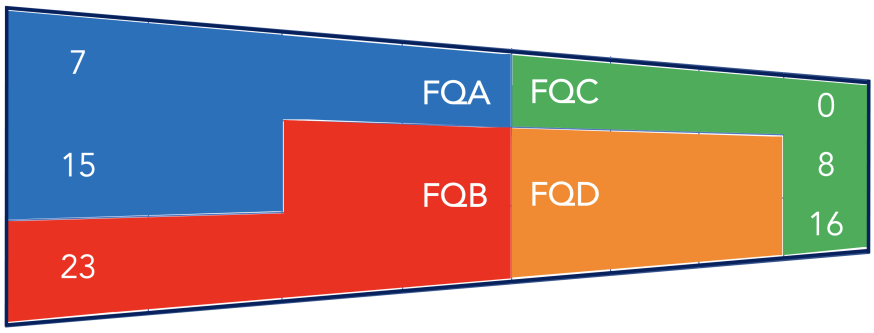

Figure 2.20: GE1/1 VFATs power domains.

is to mediate the data transfer between the chamber frontend boards (VFATs) and the GEM backend. This is carried out by three gigabit transceiver ASICs (GBTXv2) [68],[69], that drive three VTTRX optical links. These are dedicated to the DAQ communication with the CTP7s, as well as to the propagation of the the slow control commands, which is carried out by the GBT-SCA ASIC (Giga-Bit Transceiver - Slow Control Adapter) [70].
The optical link assignment to the VFATs is shown in Figure 2.22. The GBTx1 and the GBTx2 links are each connected to nine VFATs. The GBTx0 is only linked to six VFATs, since it is also responsible for the slow control communication and the FPGA programming. Indeed, the GE1/1 OH has no PROM installed where to store the firmware. This was is not possible, since the commercial PROMs have proven not to be radiation hard. This implies that each time the LV power is cycled, the FPGA needs to be re-programmed from the backend.
Every chip installed on the OH is thermally coupled with the cooling plate via a drop of non-conductive thermal paste, granting an optimal heat dissipation.

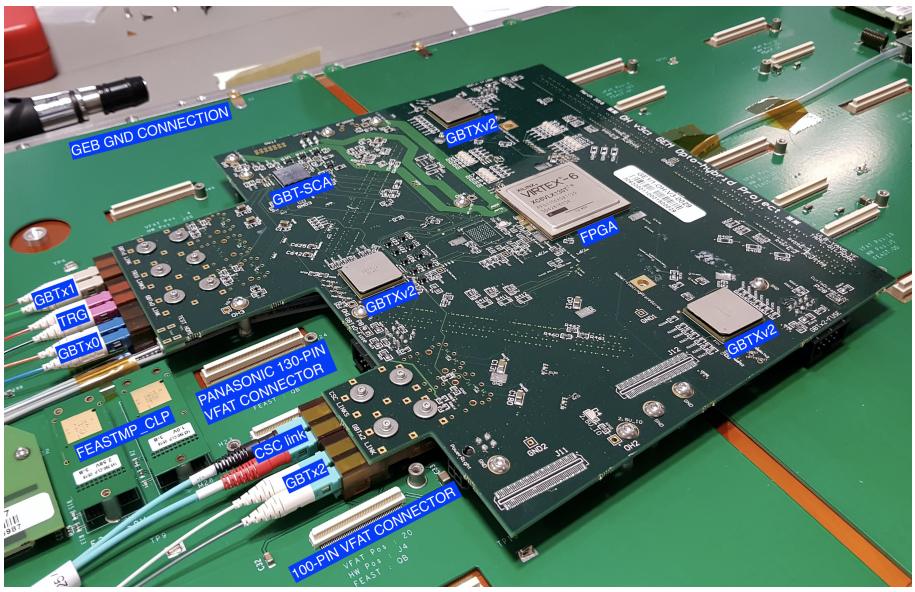

Figure 2.21: GE1/1 OptoHybrid board (OHv3c) installed on a chamber.

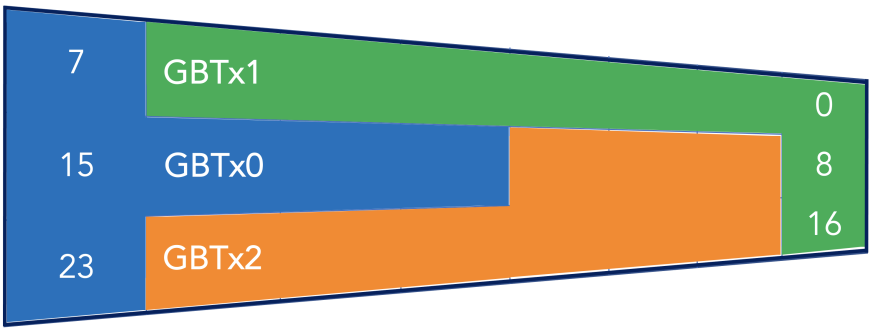

Figure 2.22: GE1/1 GBTx links domains. GBTx1 and GBTx2 links are each connected to nine VFATs. GBTx0 is only linked to six VFATs, since it is also responsible for the slow control and the FPGA programming.

2.5.5.4 The VFAT3

The Very Forward Atlas and Totem ASIC, in short VFAT, is the chip around which the GE1/1 frontend electronics is built. The VFAT2 version was originally designed to readout silicon and gaseous detectors of the LHC TOTEM experiment. A new version of the chip has been created in order to satisfy the needs of the CMS GEM detectors - the VFAT3 [65]. As the VFAT2 [71], it is a radiation tolerant trigger and tracking frontend ASIC designed in 250 nm CMOS technology. The block diagram of the VFAT3 is presented in Figure 2.23.

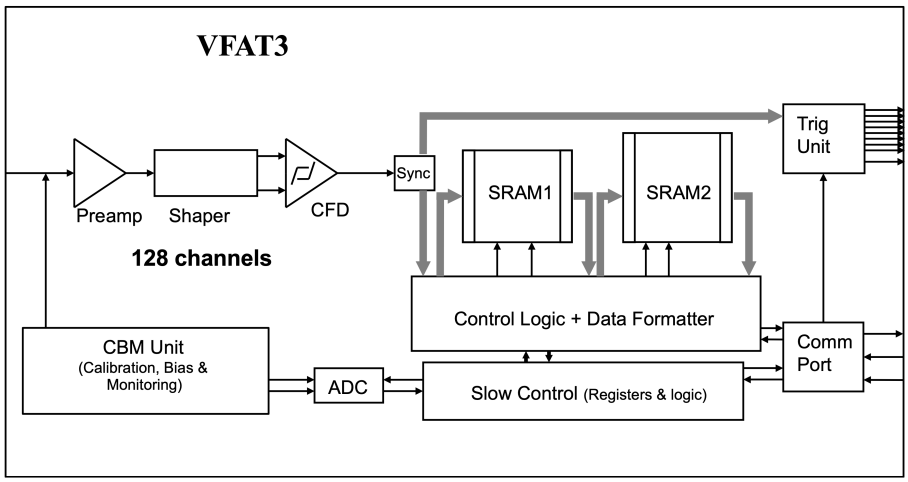

Figure 2.23: VFAT3 block diagram [34]. CFD stands for Constant Fraction Discriminator, SRAM stands for Static Random Access Memory, ADC stands for Analog to Digital Converter.

The VFAT3 has 128 charge-sensitive analog channels, which can be programmed to respond to either positive or negative signals. Initially, the analog signals undergo three stages of manipulation by a preamplifier, a shaper and a single to differential amplifier. The charge sensitive amplifier can be set at *low*, *medium* or *high* gain, with amplification factors of 1, 2, 6 mV/fC respectively. The peaking time can be chosen among the effective[9] values 15, 25, 36, 45 ns [65].

[9]The frontend peaking time by design can assume four values: 12.5, 25, 37.5, 50 ns. The measurements

The processed signals then come to a constant fraction discriminator (CFD), shown schematically in Figure 2.24.

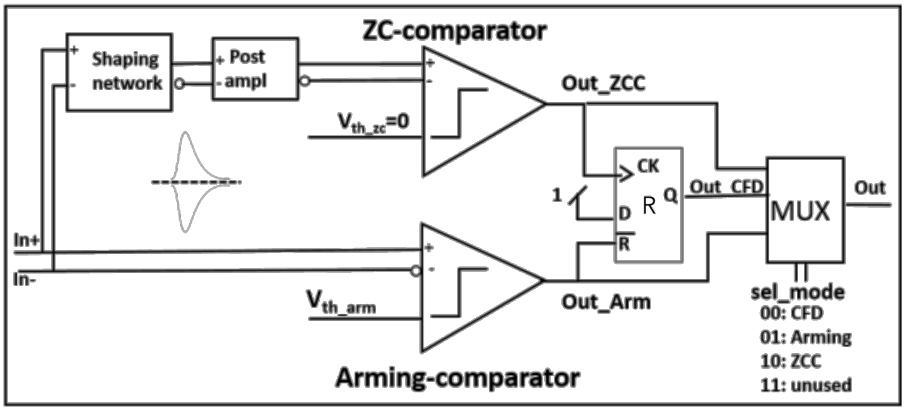

Figure 2.24: VFAT3 constant fraction discriminator (CFD) block diagram. From [65].

At the input of the discriminator, the signals take two paths. One goes to the CFD block, which through a zero crossing comparator (ZCC) precisely identifies the time of the signal. The other path leads to the so-called arming comparator (ARM), which checks the amplitude of the signal against a fixed threshold. The threshold value applied to each channel is the sum of two components: a global threshold value, that is applied to all the 128 channels of the VFAT, and a local per-channel value that can slightly adjust the global one. The *arming* name comes from its function. Indeed, in case the signal amplitude is larger than the set threshold, the outcoming logic 1 signal arms the CFD, allowing the record of the event. At the output of the CFD, the digitized signals get synchronized with the 40 MHz clock distributed through the GBTX links. Together with the sync, it is also possible to program the circuit to hold the level "high" of the digital signal for a fixed number of clock cycles (BXs). This is called *pulse stretch*.
At that point, the digital signals take two distinct paths: the trigger and the data paths.
The trigger path uses a fixed latency and it is synchronous with the external (CMS) clock. It provides fast hit information transmission through eight SLVS pairs running at 320 MHz. In GE1/1, the trigger hit information of $8 \times 8 = 64$ pairs of strips (s-bits) are transferred every BX. The trigger path has half of the detector granularity: the digital signals from two neighboring channels are merged through a "fast-OR".
The data path transmits the hit information with full granularity and variable latency via the Comm-port. The digital signals from the 128 channels are continuously stored and kept in a 128×1024 bits circular buffer called SRAM1, that shifts every BX. Upon arrival of an external trigger (L1A, in case of CMS), the data found in the buffer position defined by a configurable latency parameter are transferred and queued to SRAM2, adding a time stamp. The maximum value that can be set for the latency is the depth of the SRAM1 buffer, i.e. 1024 BXs (25.6 µs). The SRAM2 buffer has a size of 176×512 bits. It is used as a FIFO, storing the data before the transfer to the data formatter for data packet construction, which is followed by the

performed on the production ASICs revealed a contraption of the interval with a larger minimum and a smaller maximum peaking time. In the text are reported the measured *effective* values.

transmission off chip. The presence of the SRAM2 FIFO implies a variable latency path for the data transmission, here is why a proper tagging of the data packets is essential.
Although the VFAT3 is capable of triggering on multiple successive BXs, the GE1/1 detectors employ a single BX readout.

Other two essential blocks are present on the VFAT chip: the Calibration, Bias and Monitoring (CBM) unit and the Slow Control unit. These are intimately linked and utilized to properly configure the entire VFAT3 chip. Indeed, the Slow Control provides the communication necessary to read and write the desired register values, while the CBM sets or fetches the required quantities.
The VFAT configuration parameters are stored in digital format in dedicated registers. They are transformed into analog bias voltages and currents by a total of nine 6-bit DACs and eight 8-bit global DACs. In addition, 129 local DACs are present to perform local threshold adjustment in each channel. To monitor the applied values, it is possible to readout the voltages and the currents through two dedicated ADCs.
The CBM is also employed to test the frontend status. Indeed, it contains a dedicated calibration module that can send either voltage or current pulses of variable magnitude to the input of the analog circuitry. These, mimicking the real GEM signals, provide a tool to check the signal elaboration and the response of the VFAT channels.

For the GE1/1 project, the VFAT3 ASIC has been installed on a 46.5×47 mm^2 PCB (Figure 2.25). The board hosts two connectors; a female 130-pin panasonic connector for the chamber side and a female 100-pin connector for the GEB side. In addition, a battery of 128 470 Ω resistors is installed between the panasonic connector and the ASIC channel inputs. These are used as protection resistors in case of discharges propagating to the readout.
On the other side of the PCB, a rectangular gold heat exchanger is placed in correspondence of the ASIC. That part is thermally coupled with the cooling plate by non-conductive thermal paste.

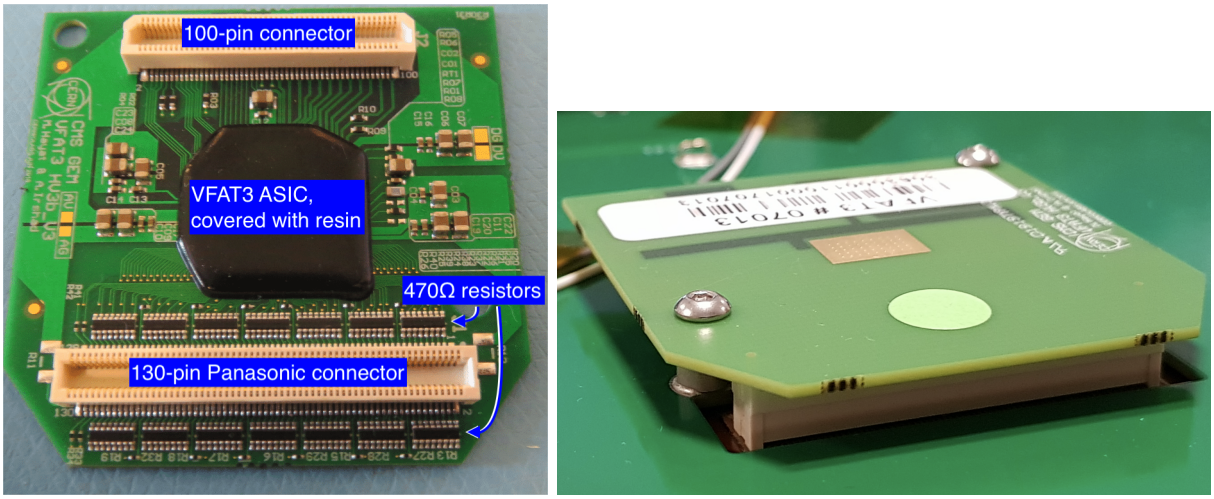

(a) GE1/1 VFAT3 board - bottom view.

(b) GE1/1 VFAT3 board - top view.

Figure 2.25: GE1/1 VFAT3 board from bottom (left) and from top (right).

Chapter 3

Requirements on GE1/1

This chapter defines the requirements imposed on the GE1/1 detectors in order to adequately contribute to the trigger and the tracking in the CMS muon endcaps.
First, the requisites are listed and the reason for each of them is detailed. Then, a brief overview of the studies to prove the compliance of the performance to the demanded standards is presented.

3.1 Summary of the performance requirements

The GE1/1 requirements have been defined in the Technical Design Report written in 2015 [34]. Subsequently, some of the criteria have been re-evaluated and the acceptance values have been redefined. Here is presented the list of the final imposed requirements; details will follow.

- Provide the maximum geometric acceptance within the given CMS envelope.
- A rate capability of 10 kHz/cm^2 or better.
- No gain loss due to aging effects after 200 mC/cm^2 of integrated charge.
- A single chamber efficiency of 95% or better in the detection of minimum ionizing particles.
- A spatial resolution of 300 µrad or better on $\Delta\phi = \phi_{\mathrm{GE1/1}} - \phi_{\mathrm{ME1/1}}$.
- A single chamber time resolution of 10 ns or better.
- A gain uniformity of 37% or better across a chamber.

The geometric acceptance requirement results from the restricted available space that is left in the first station, first ring of the CMS endcaps for a subsystem to complement the CSCs. Given the structure of the so-called endcap nose, it demands a specific design to deal with the bulky metallic supports spaced by 20°. In response, two types of chambers are employed: long and short, that were described in 2.5. The alternating lengths of the installed super chambers ensures the maximum coverage of the available surface area, maintaining a relative ease in their insertion and extraction. Additionally, the alternating orientation of their placement is a key factor in granting the overlap between the active areas of neighboring detectors.
The rate capability has been extensively studied in the GE1/1 prototyping phase and exceptional performances have been proven. Indeed, all MPGDs and thus GEMs have a structure that produces very localized avalanches that only last for less than 100 ns. Considering only the

chamber per se, these characteristics would allow for rates up to $\mathcal{O}(\mathrm{MHz/cm^2})$. The limiting factors for the sustainable rate are the abilities of the HV power supply, the HV filters and the distribution to maintain the adequate voltage levels of the electrodes. Additionally, the readout electronics would need to sustain the high particle fluxes. From the results in [34] and the expected rates in HL-LHC operations, the GE1/1 performance will ensure to handle the rate of incident ionizing particles in the harsh environment of the CMS muon endcaps.
As for the rate capability, dedicated aging studies were conducted in the GE1/1 R&D period. No signs of gain losses were seen even after 1.56 $\mathrm{C/cm^2}$ of accumulated charge. This outstanding performance, for a gaseous detector, confirms the long term reliability of the chambers in the CMS environment even when subjected to the dose received by the detectors in the full HL-LHC campaign.
Being sure that the GEM technology and the GE1/1 design can sustain the doses and the rates in the experiment, it is needed to test the abilities of the detectors to contribute to the muon detection in the CMS endcaps. An intrinsic time resolution better than 10 ns has been verified in the test beam studies [72]. This makes possible to identify the correct bunch crossing of the hits in more than 97% of the cases, as confirmed later in the slice test results [73].
The gain uniformity requirement allows the chamber to have a similar gas gain over the active area of the chamber. This makes the avalanches have a consistent magnitude in all the chamber regions, which then reflects on the uniformity of all the other performance parameters. Originally in the GE1/1 TDR the limit on the gain uniformity was set to 15%. Afterwards, it was considered too stringent given the tolerances in the production of the components. Thus, a more relaxed limit of 37% was imposed [74].
The detection efficiency is another essential performance figure. In principle, GEM chambers with 3/1/2/1 mm spacing can attain more than 97% efficiency at the plateau. Therefore, 97% was adopted as the target value in the GE1/1 TDR. After having considered the gain non uniformities and the performance of the latest frontend electronics, the requirement was reduced to an efficiency $> 95\%$ for MIPs. This value is still larger than the 94% efficiency utilized in trigger rate studies presented in figure 1.17. Therefore, no major impact in the CMS operations is foreseen due to the redefinition of this requirement.
Finally, the spatial resolution of at most 300 µrad is needed to reliably determine the difference in position of a muon track between the GE1/1 and the ME1/1 subsystems ($\Delta\phi = \phi_{\mathrm{GE1/1}} - \phi_{\mathrm{ME1/1}}$). This reflects on the precision in the muon transverse momentum measurement, that determines the lowering of the L1 trigger rates (Figure 1.17).

3.2 How to verify compliance with the requirements?

Even though most of the performance parameters were tested and met the requirements during the R&D phase of the GE1/1 project, many others need to be evaluated with the final version of the detectors.
The rate capability and the aging, which are intrinsic to the GEM technology and the utilized materials, could be checked with one-off dedicated studies and allowed to validate the design. The gain uniformity and the efficiency, instead, have to be assessed for each of the GE1/1 cham-

bers.
The gain uniformity has been evaluated immediately after the chamber assembly in the production/test sites by means of specific analog electronics. The utilized procedures and the setup were standardized in order to obtain consistent results. Once the chambers successfully passed the tests, they were shipped to the GEM laboratory at CERN. There, they have been equipped with the final digital electronics and all the components described in 2.5 and paired into super chambers. Subsequently, each GE1/1 detector has been characterized in terms of efficiency in the cosmic rays stand test. The spatial resolution has been studied for a representative sample of chambers utilizing the same setup of the efficiency test. Such a check was done in order to confirm the results obtained with the GE1/1 prototypes, utilizing detectors equipped with all the final components.
In the following two chapters, the experimental setups to validate the chambers will be presented, as well as the analyses and the obtained results. Chapter 4 considers the individual chambers; chapter 5 evaluates the system performance. The issues discovered during the tests are described, with an accent on the proposed and applied solutions or workarounds.
Finally, the overall performance is discussed, giving an outlook on the future of the GE1/1 detectors.

Chapter 4

The GE1/1 chamber performance

This chapter focuses on the performance of a single GE1/1 chamber in terms of its constituents and components. In particular, the examined aspects are the gas gain, the high voltage stability, the noise level and the frontend thresholds. An emphasis is put on the interplay among these parameters.
The ultimate target of the conducted studies is to determine the optimal configuration for a detector to deliver the required performance and meet the demanded standards in operations.

4.1 Gas gain

The first parameter presented is the so-called *gas gain*.
The signal given by the exiguous number of electron-ion pairs produced by an ionizing particle traversing the gas volume would be too small to stand out from the noise pedestal of the readout electronics. Thus, the signal amplification is of the utmost importance for all gas detectors. The three stages of electron multiplication of the GE1/1 chambers are tailored to provide a final detectable signal collected by the readout strips.
The conditions to achieve sufficient amplification in triple-GEM detectors have been worked out during the R&D phase. What is left to be determined are the aspects related to mass-produced large-size chambers. In particular, it is required to characterize each GE1/1 chamber in terms of:

- Average electron amplification factor, in order to properly match the two layers of a super chamber;
- Gain uniformity over the almost 0.5 m^2 active area.

These two aspects of the gas gain will be discussed in depth in the following sections.

4.1.1 Effective gas gain

The effective gas gain is defined as the ratio between the total charge induced on the readout strips and the charge of the electrons released by the ionizations in the drift gap. The latter includes primary and secondary electrons, and possible δ-rays.

The evaluation of the gain is performed during the fifth stage of the quality controls (QC) for one of the readout sectors in the chamber, namely $(i\phi, i\eta) = (2, 4)$[1].
The measurement is carried out inside a shielding copper box, utilizing an Amptek Mini-X X-ray Tube [75] equipped with a silver target and operated at a voltage of 40 kV (Figure 4.1). Such a source was chosen for its capability to illuminate the entire chamber area, supplying a high rate of particles with well-defined energy. The outcoming X-ray energy spectrum is shown in Figure 4.2. A large fraction of the photons, interacting with the copper layers of the drift PCB of the chamber, excite the copper electrons which then emit 8.05 keV fluorescence photons (K_α lines) [76].

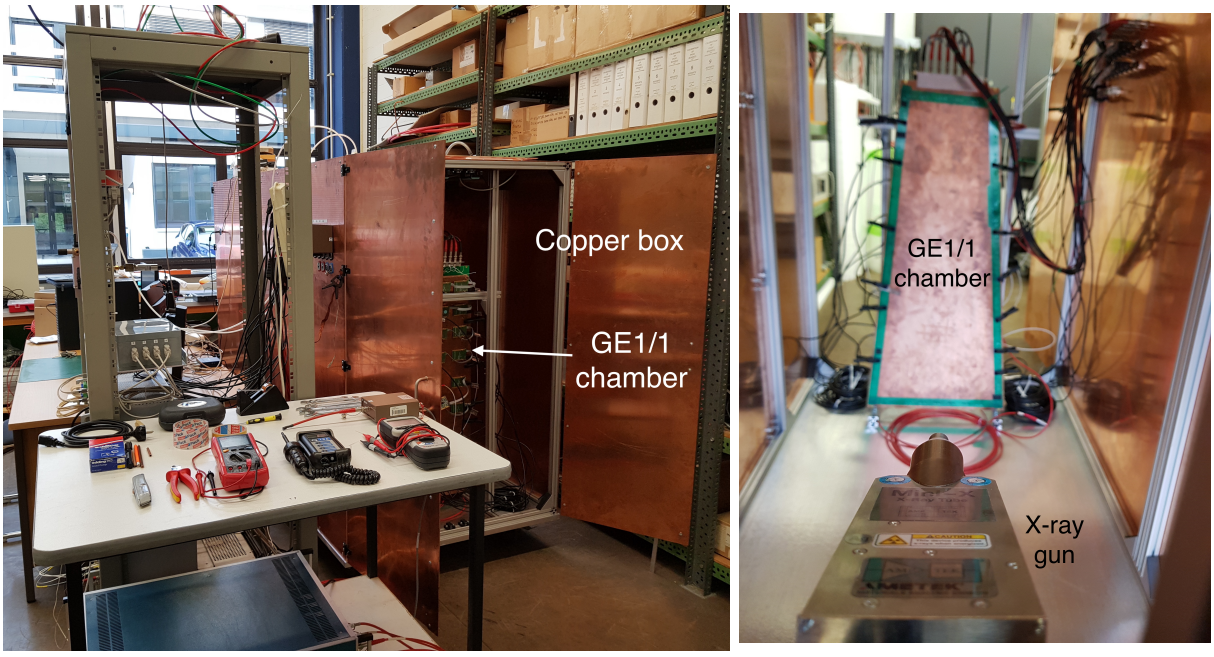

Figure 4.1: Pictures of the shielding copper box and of the Amptek Mini-X X-ray Tube, employed for the GE1/1 gas gain tests.

The copper fluorescence photons, together with the ones that got through the copper layers, finally interact with the standard Ar/CO_2 (70/30%) gas mixture in the chamber mostly via photoelectric effect. The photoelectrons travel for around 2 mm in the drift gap [77] and create an average of $n_T = 346 \pm 2.9$[2] electron-ion pairs.
To measure the total gain, all the 128 strips are merged and readout by a single channel which consequently sees the entire charge produced in the avalanche. This is a key point, since in the following validation tests and chamber operation the total charge will be spread over many strips and each of them will receive only a fraction of the signal. The two observables in the gain test are the readout current (I_{RO}) and the rate of the incoming photons (R_γ). Given the electron charge (q_e) and the number of electron-ion pairs generated in the drift gap ($n_T = 346 \pm 2.9$), one gets [78]:

[1]The choice of a central readout partition has been done to ease the test execution. This selection has no influence in the gain characterization, since the relative gain variation in each chamber region will be determined in the subsequent test.

[2]The n_T measurement was performed during the CMS GEM R&D phase by comparing the gain calculated from different photon spectra [53].

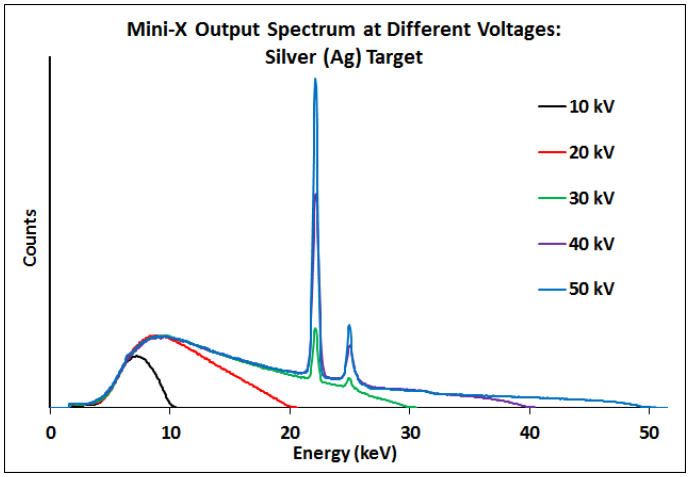

Figure 4.2: X-ray energy spectrum of the Amptek Mini-X X-ray Tube with silver target, as given in the instructions manual and data sheet [75]. The chosen working point for the effective gas gain measurement is 40 kV.

$$G_{eff} = \frac{I_{RO}}{q_e \cdot n_T \cdot R_\gamma} \,. \tag{4.1}$$

The readout current (I_{RO}) is measured by means of a pico-ammeter (Keithley 6487 [79]), while the rate (R_γ) is determined utilizing a NIM module chain composed by a pre-amplifier, a shaping amplifier, a discriminator and a counter. During the test, the high voltage is supplied to the chamber by means of a resistive voltage divider with a total resistance of about 4.7 MΩ. The HV divider is supplied with a fixed current, and it distributes voltages to the eight electrodes of the chamber with values proportional to the ones in Figure 2.10a. The divider current is scanned in the range $[550, 700]$ µA in steps of 10 µA. In standard test conditions, at the highest working point, the readout current is in the order of 1 nA and the rate in the order of 1 kHz.
The typical curves of readout current and rate as a function of HV for a GE1/1 detector can be seen in Figure 4.3a. The rate curve shape is determined by the thresholds applied in the discriminator, and the final plateau region provides the total rate of incoming photons in the region of the measurement. Thereby, the gain is calculated dividing each point of measured current by the rate at the plateau. An example of the resulting effective gas gain plot can be found in Figure 4.3b. The gas gain curve confirms the expected exponential trend described in section 2.3.3.
It is worth reporting that the environmental parameters have a significant impact on the gas gain. A correction for pressure and temperature is needed to be able to compare the performance of detectors produced and tested in different countries around the world (section 2.5.3) with different climatic conditions. The formula utilized during the GE1/1 chamber production foresees a linear correction of the electric fields by the factor T/p:

$$G_{eff} \propto \exp\left(g \cdot E_{field} \cdot \left(\frac{p_0}{p}\right) \cdot \left(\frac{T}{T_0}\right)\right) \propto \exp\left(g' \cdot I_{divider} \cdot \left(\frac{p_0}{p}\right) \cdot \left(\frac{T}{T_0}\right)\right) \,, \tag{4.2}$$

$$\implies I_{divider,0} = I_{divider} \cdot \left(\frac{p_0}{p}\right) \cdot \left(\frac{T}{T_0}\right) . \tag{4.3}$$

Ultimately then, the correction can be applied to the divider current by normalizing pressure and temperature to the average environmental conditions present in the CMS cavern, namely $p_0 = 964.4$ mbar and $T_0 = 297.1$ K.

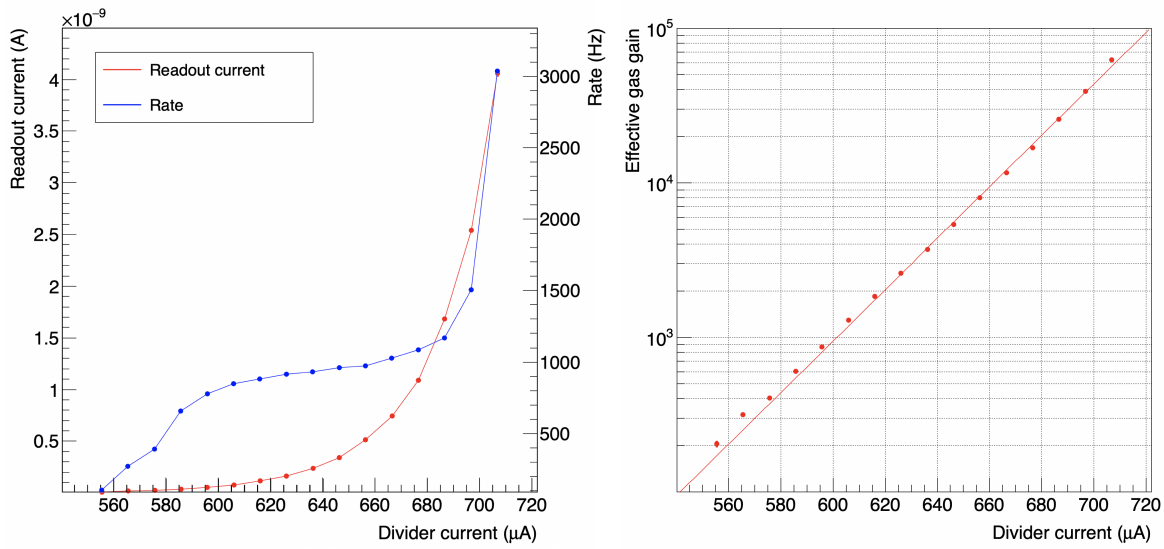

(a) Readout current and rate vs divider current

(b) Effective gas gain vs divider current

Figure 4.3: Typical results of effective gas gain measurements, here for the GE1/1-X-L-CERN-0001 chamber. In the x-axis, the divider current is corrected for environmental parameters. The turn-on shape of the rate is given by the thresholds of the discriminator. The plateau provides the total rate of incoming photons in the region of the measurement. The readout current has an exponential increase with the HV, determined by the growth of the electron multiplication factor. The gas gain curve directly follows the readout current exponential shape. Data taken during the GE1/1 QC phase by the CERN GEM team.

Even though the signals become larger and easier to manipulate at higher gain values, the probability of having discharges increases as well. Thus, a compromise between signal charge and HV stability has to be made. Thorough studies on this topic will be reported in section 4.2.

4.1.2 Gas gain uniformity

The gas gain uniformity is defined as the variation of the effective gas gain over the large active area of the GE1/1 chambers. It is quantified as the standard deviation divided by the average gain of the different readout regions.
The main aspects that contribute to the variations are:

- The tolerances in the GEM hole geometry deriving from the etching procedure;
- The tolerances in the thickness of the foils and the spacers in the stack;
- The bending of the readout and drift PCB due to the gas overpressure or mechanical stress.

The estimated total amount of gain variation caused by the convolution of these factors was $\sim \pm 37\%$ [74]. Considering the efficiency and the time resolution curves for a GEM detector prototype operated in the same configuration as the final GE1/1, such gain variation would ensure to safely meet the performance requirements (Figure 4.4). A 37% acceptance limit has therefore been set for the quality control test that assesses the chamber gain uniformity.

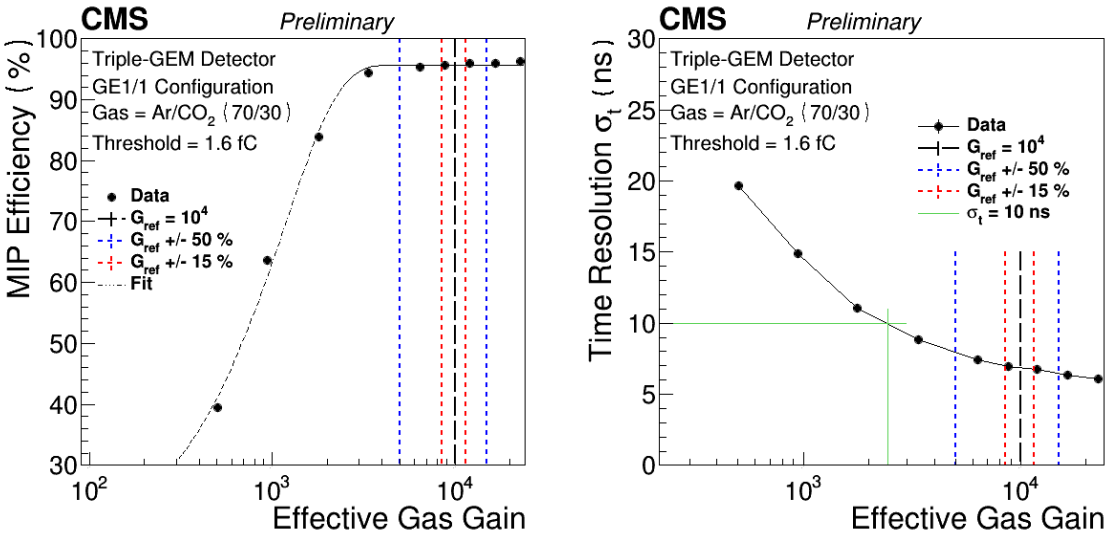

(a) Efficiency vs effective gas gain (b) Time resolution vs effective gas gain

Figure 4.4: Efficiency and time resolution curves as a function of the effective gas gain for a GEM chamber operated in the GE1/1 configuration. The vertical black line represents the nominal effective gas gain value of 10^4, the blue line corresponds to a gain variation of 15%, while the red line refers to variation of 50%. The imposed limit of 37% would ensure to safely meet the performance requirements throughout the entire readout area of the chambers. Data from [80], available at [81].

The measurements use the same setup as for the effective gas gain, illuminating the entire detector area with the X-ray gun. This test requires a specific analog readout electronics, different from the final digital one installed at a later stage. It is composed by 24 APV25 [82] frontend boards and a Scalable Readout System (SRS) [83] as the backend. This provides full granularity readout and it is capable of digitizing the signals with a sample rate of 40 MHz. Thus, it is possible to record a rough signal shape in each of the 3072 readout strips. The integrated signal in ADC counts is then proportional to the charge induced on the strip. The total charge of the avalanche is obtained by summing the integrated signals in neighboring strips, forming the so-called *clusters*. The chambers are flushed with the standard gas mixture, and the high voltage working point is set to provide an average effective gas gain of about 600. Such low gain is chosen not to saturate the dynamic range of the APV25 chip.

At the time of establishment of the quality control procedures and analyses, it has been decided to present the response of the detector in '*slices*' of 4 neighboring strips. The integrated charge of a cluster gets assigned to the slice where the central strip lies. An example of a spectrum of the integrated charge of the clusters in one slice is presented in Figure 4.5a. The centroid of the main peak in the distribution represents the signal charge in ADC counts corresponding to

the copper fluorescence emission line ($E_\gamma = 8.05$ keV). Its position in the spectrum is directly proportional to the local gas gain in the area of the slice. The peak positions for the slices of an entire GE1/1 detector can be seen in Figure 4.5b.

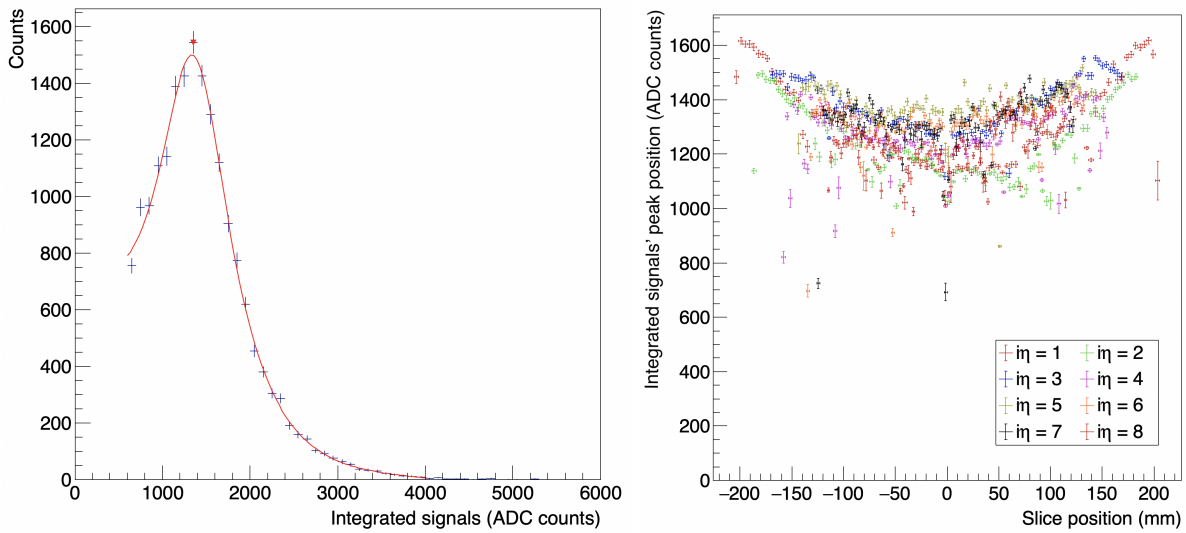

(a) Spectrum of integrated charge of the clusters in one slice.

(b) Gain response of each slice.

Figure 4.5: On the left, histogram of integrated signals in ADC counts recorded in slice 21 of $i\eta = 1$ of the GE1/1-X-L-CERN-0001 chamber during the gain uniformity test. The main peak of the distribution is fitted with a Cauchy function over a 5th-order polynomial for the background. The position of its centroid represents the signal charge in ADC counts corresponding to the copper fluorescence emission line. On the right, peak positions of the spectra for the 768 slices of a GE1/1 detector (GE1/1-X-L-CERN-0001). The x-axis represents the slice position with respect to the central axis of the chamber. Data taken during the GE1/1 QC phase by the CERN GEM team.

Finally, the histogram of the integrated signal peak positions in the 768 slices is produced (Figure 4.6). The CMS GEM gas gain test procedures define the gain non-uniformity as the ratio between the sigma and the mean $\left(\frac{\sigma}{\mu}\right)$ of the function that fits the distribution (Gaussian or Landau[3]). The uniformity parameter is defined from the fit parameters and not from the distribution parameters in order to mitigate the possible presence of malfunctioning channels in the APV25 channels giving a bias to the histogram mean and/or standard deviation.

4.1.3 Gas gain results for GE1/1 chambers

The results of the effective gas gain and the gain uniformity measurements can be combined to get an overall picture of the GE1/1 chamber electron amplification factor. The two main characterizations needed to properly operate a chamber are:

- The average effective gain as a function of the HV working point;
- The gas gain map for the 24 readout sectors at the operating HV working point.

[3]Throughout the GE1/1 production, both gaussian and landau curves have been used to fit the gain uniformity histograms. The choice was made on a case-by-case basis, opting for the curve that better fitted the distribution.

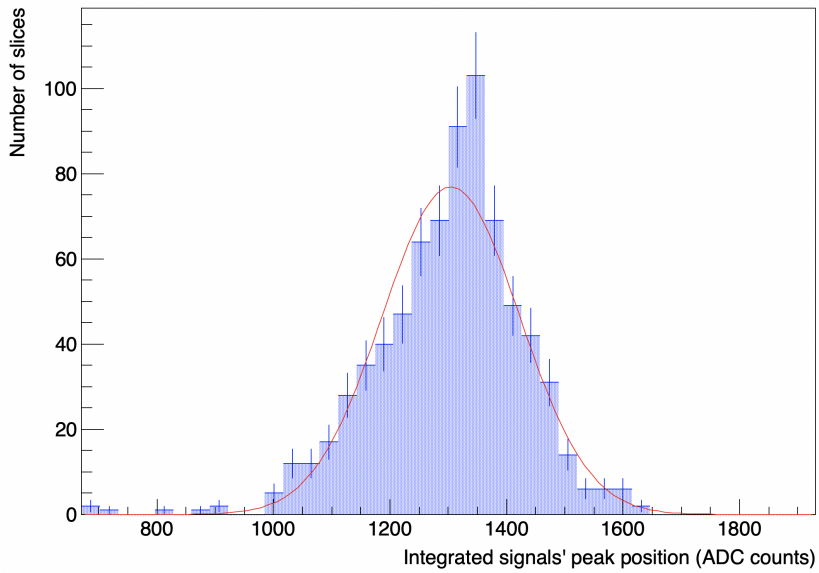

Figure 4.6: Histogram of the integrated signal peak positions in the 768 slices of the GE1/1-X-L-CERN-0001 chamber. The mean value is (1300 ± 5), the RMS is (126 ± 3). The $\left(\frac{\sigma}{\mu}\right)$ of the fit function defines the gain non-uniformity, which amounts to $\left(\frac{118 \pm 4}{1304 \pm 5}\right) = (9.0 \pm 0.3)\%$ for this chamber. Data taken during the GE1/1 QC phase by the CERN GEM team.

Once the desired average amplification factor is fixed, the corresponding HV setting can be extracted from the gain curve. The gain map then allows to check that the local values do not exceed the safe-operation limit that ensures the long term detector stability (< 50000 at the nominal average gain of 20000). The gain map is also very significative in the interpretation of the chamber detection performance, detailed in the next chapter. Indeed, the performance results are usually presented with a readout-partition granularity, matching the frontend electronics one, since the electronics settings are the other component that determines the detector response.
The average effective gas gain is obtained calculating the weighted average of the integrated signal peak positions of all the chamber slices, using the area of the slices as weights. Then, the same is done for the slices of the readout sector $(i\phi, i\eta) = (2, 4)$, where the effective gas gain was measured. An example of the resulting average gain versus the high voltage working point is presented in Figure 4.7a. It follows an exponential curve reaching the gain of ~ 30000 at a divider current of 690 µA. These curves are utilized to match the gain characteristics of the two single chambers composing the GE1/1 super chambers.
The gas gain map is computed utilizing the data from the gain uniformity test, presented in Figure 4.5b, averaging the results of the integrated signal peak positions in the slices belonging to the same readout sector. The ADC counts are then rescaled imposing the desired average amplification factor for the chamber. Figure 4.7b shows an example of a gas gain map per readout partition.

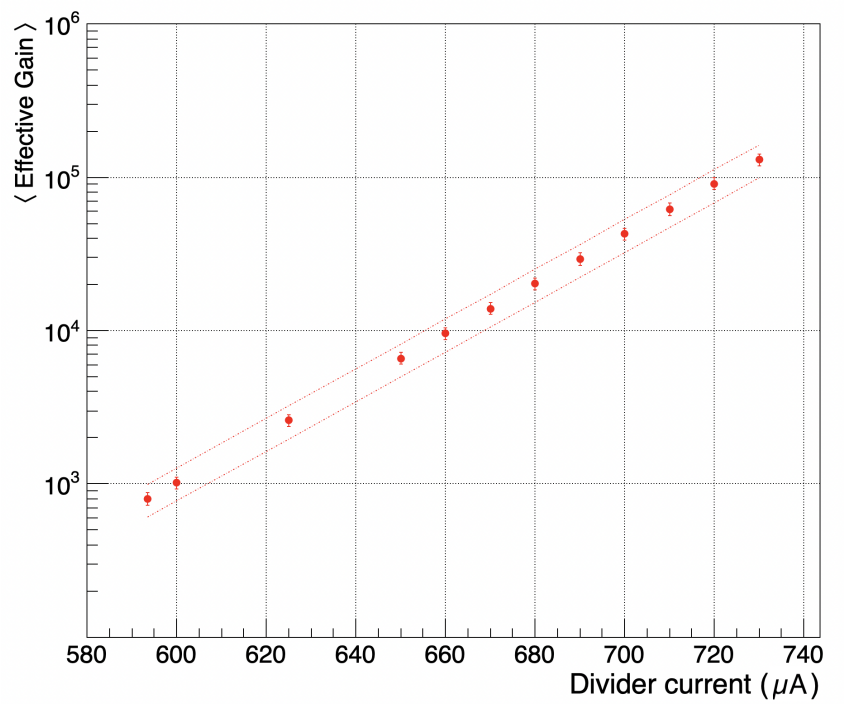

(a) Average gas gain vs HV working point.

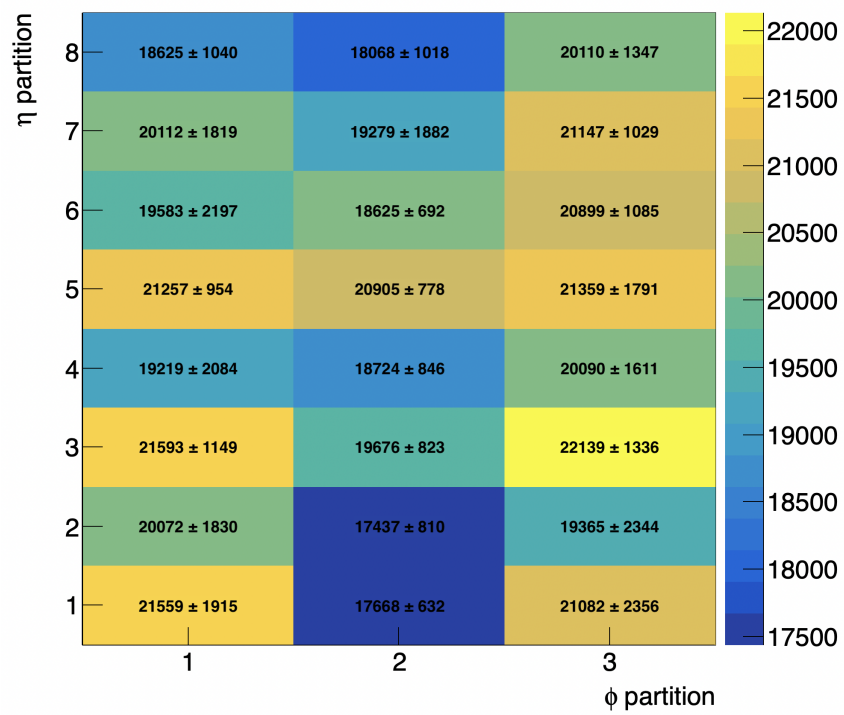

(b) Gas gain variation per readout partition.

Figure 4.7: On the top, typical curve of average gas gain as a function of the applied high voltage, represented by the current supplied to the resistive high voltage divider. On the bottom, average gas gain per readout sector ($mean \pm std.dev.$). Both of the plots present the gain performance of the GE1/1-X-L-CERN-0001 chamber. Data taken during the GE1/1 QC phase by the CERN GEM team.

4.1.4 Overview of gas gain uniformity for the GE1/1 production

The final part of this section is dedicated to give an overview on the gas gain uniformity across the entire GE1/1 production. All the chambers that underwent the quality control steps testing the gas gain have been considered: 157 out of the 161 chambers produced. The 4 chambers discarded by the initial tests for gas tightness or high voltage stability have been repurposed in the GE1/1 project for aging, high voltage instabilities and GEM upgrade studies.

The plot in Figure 4.8 presents the results of the gain uniformity tests, showing the σ/μ for long and short chambers, in red and blue respectively. The two distributions clearly show that the long chambers got higher values than their short counterpart, even though still being within the acceptance limit. The same behavior is confirmed in Figure 4.9, where the σ and minimum-maximum values of the gain uniformity distribution (e.g. Figure 4.6) have been normalized by the mean value. From this plot it is also possible to see that the long chambers had more variations in the results of the gain uniformity test. These dissimilarities seem to have happened in batches, possibly depending on the production of the components (e.g. readout and drift boards, GEM foils and GEM foil spacers).

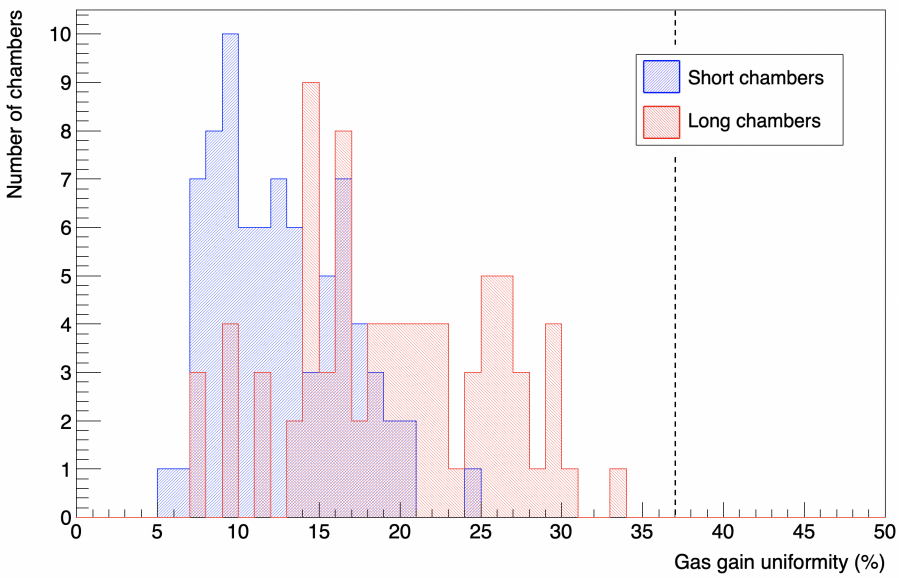

Figure 4.8: Gas gain uniformity σ/μ for the 157 GE1/1 production-grade chambers. Long (short) chambers are presented in red (blue). The vertical dashed black line at 37% represents the QC requirement, that is met by all the chambers. The long chambers, though, exhibit a less uniform gain than short ones. This might be expected, considering their 20% larger surface area, even though the difference in gain uniformity can't be only explained by their size.

From the presented results it is possible to infer the non-uniformities in the performance results that will be presented in chapter 5. The gain uniformity will reflect on the efficiency uniformity, which is expected to be greater in short chambers than in long ones, and better in some long chambers than in others.

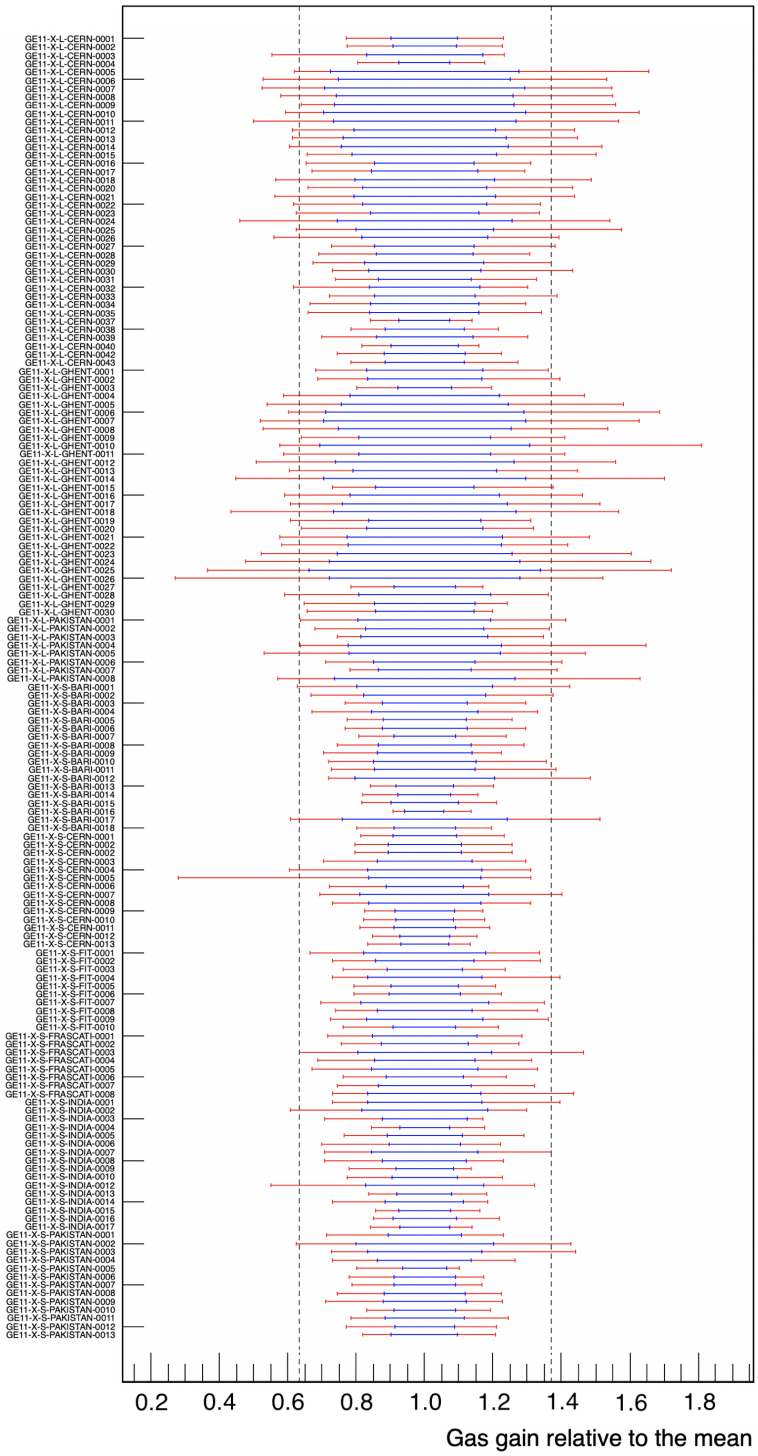

Figure 4.9: Gas gain uniformity results for the 157 GE1/1 production-grade chambers (chamber IDs in the x-axis). The standard deviation (σ) and the minimum-maximum values were normalized by mean value (μ) of the gain uniformity distribution. The σ/μ is presented in blue, while the $(min \leftrightarrow max)/\mu$ is in red. The horizontal dashed black line at 37% refers to the QC requirement. While all the σ/μ values are well within the specs, many chambers exhibited regions with pronounced non-uniformities that exceed the limit. These were mostly present in long chambers.

4.2 High voltage stability

An essential parameter to ensure proper chamber performance in long term operations is a continuous electron multiplication over time, hence the chamber HV stability is of the utmost importance.

4.2.1 Definition of HV instability

The high voltage instabilities are the conditions when the voltages applied to the electrodes dramatically and permanently change their values, causing a disruption of the detector operations. They are a common issue of all gaseous detectors, originating from the high voltage discharges. One of the factors that contributes to the discharge probability are the operating conditions. The incoming particle flux and the presence of highly ionizing particles, combined with high gas gain, can create high spatial charge density, reaching locally the gas breakdown potential. This gives rise to streamers and eventually self sustaining discharges.
In addition to these operational aspects, the imperfections present on the copper edges of the GEM foil holes from the production can generate edge effects that facilitate the breakdown. In addition, the dust coming from the chamber components that end up in a hole can trigger an instability.
The discharges manifest themselves as sudden and violent events that create a local short circuit between two electrodes at different voltages. A large amount of current is then drawn from the electrodes through a spark in the gas, causing two effects. The first one is located around the area of the discharge. It corresponds to a rapid increase of the gas temperature, turning it into a conductive plasma. The heat generated is such that it can locally melt the polyimide, and even vaporize the copper layers of the GEM foil. The metal can then be sputtered towards the other GEM foils and give rise to other discharges or permanent short circuits.
The second effect is located on the HV distribution and power supply. A considerable amount of current has to be provided to sustain a discharge. To prevent damages, it is necessary to catch the spikes in the monitored HV current, and safely turn off the chamber HV channels. Such intervention is called *trip*, and it is triggered by exceeding a defined threshold I_0 for a time interval longer than the set trip time (t_{trip}). When using the multichannel supply, the two trip parameters can be manually set by the operator for each of the electrodes. The most common values in use for the GE1/1 detectors are $I_0 = 2$ µA during regular operations and $I_0 = 20$ µA while in ramping up the voltages. t_{trip} is normally set to 1 second, since it is the smallest, thus safest, selectable time interval greater than zero. If any of the 7 HV channels detects an overcurrent, the entire GEM stack and the drift cathode get switched off.
One example of overcurrent event that triggered a trip is displayed in Figure 4.10. The sampling time for the data recorded by the DCS is much larger than the time resolution of the trip circuit installed in the HV power supply boards, thus it is rarely possible to spot the positive overcurrent spike present in the plot on the right.
While a HV trip is essential for a GEM chamber to prevent irrecoverable damages to the foils, on the other hand it generates a non-negligible amount of dead time in which particles can't be detected. A trip event followed by a recovery might take up to 4 minutes, depending on the

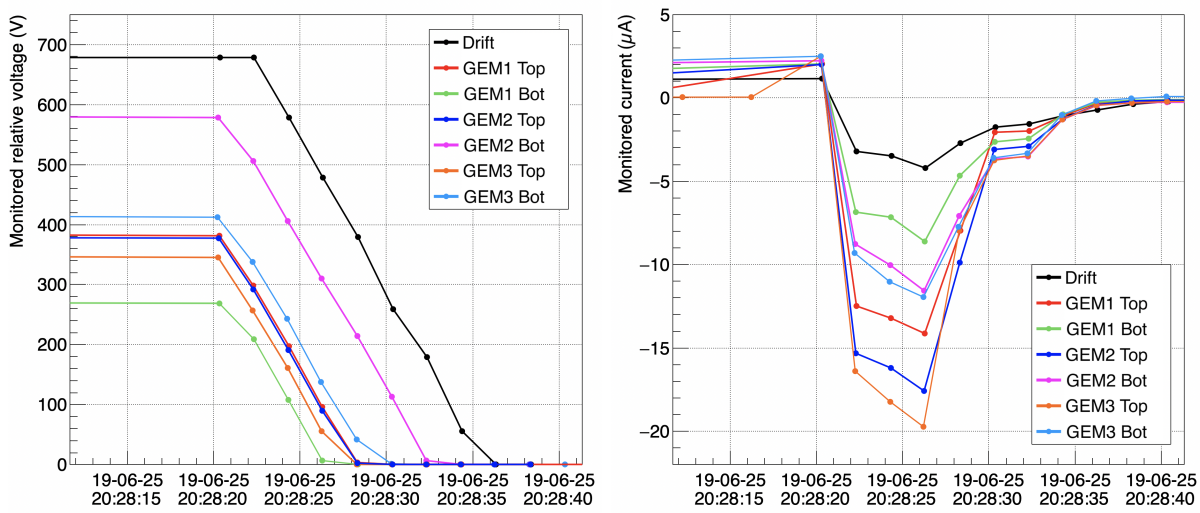

(a) Monitored electrode voltages.

(b) Monitored electrode currents.

Figure 4.10: DCS monitoring plots for a high voltage instability that led to a power supply trip. On the left, status of the relative voltages applied to the seven chamber electrodes. On the right, current drawn by the electrodes. The instability caused a sudden (positive) spike in the absorbed current, and the power supply responded by cutting off the applied high voltage. The negative currents are relative to the HV ramp down.

ramp-up and ramp-down speeds.

In the following subsections, the other consequences of discharges in GE1/1 detectors will be presented, as well as the implemented mitigation strategies.

4.2.2 Impact of discharges in early CMS tests

During the Year End Technical Stop of LHC of 2016 – 2017, five GE1/1 super chambers were installed in the CMS negative endcap as a demonstrator (slice test) (Figure 4.11). Initially, all the detectors were instrumented with VFAT2 hybrids as on-chamber frontend electronics.

The services and the detector installation were successfully tested in every aspect. The GEM Detector Control System [84] and the Data Acquisition System were fully integrated within the CMS online systems [85]. The status of the detectors and their frontend channels was daily monitored and data were taken in proton-proton collision runs until the end of LHC Run 2 in October 2018.

While for some chambers the efficiency was proven to be greater than 95% [73], in others the discharges were a problem yielding a growing number of lost readout channels [86], as shown in Figure 4.12. After one and a half years of operations in CMS, the fraction of dead channels was ranging from a minimum of around 1‰ in chamber 28 layer 2 to almost 30% in the chamber 29 layer 2.

The loss of a large amount of readout channels in a relatively short operation period has determined the necessity to study the process, give an interpretation and provide feasible measures to mitigate it.

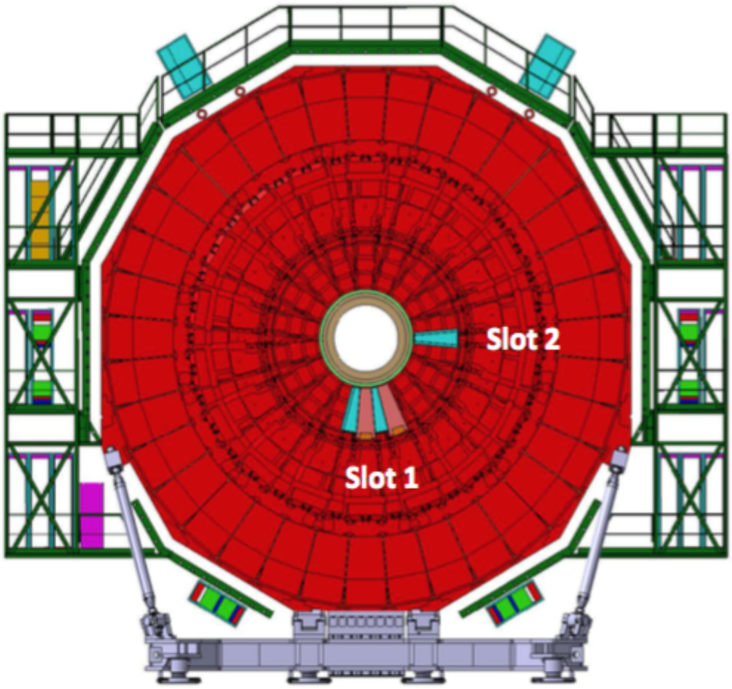

Figure 4.11: Schematic drawing of the CMS negative endcap. Slot 1 and slot 2 represent the two positions were the five slice test super chambers were installed. From [85].

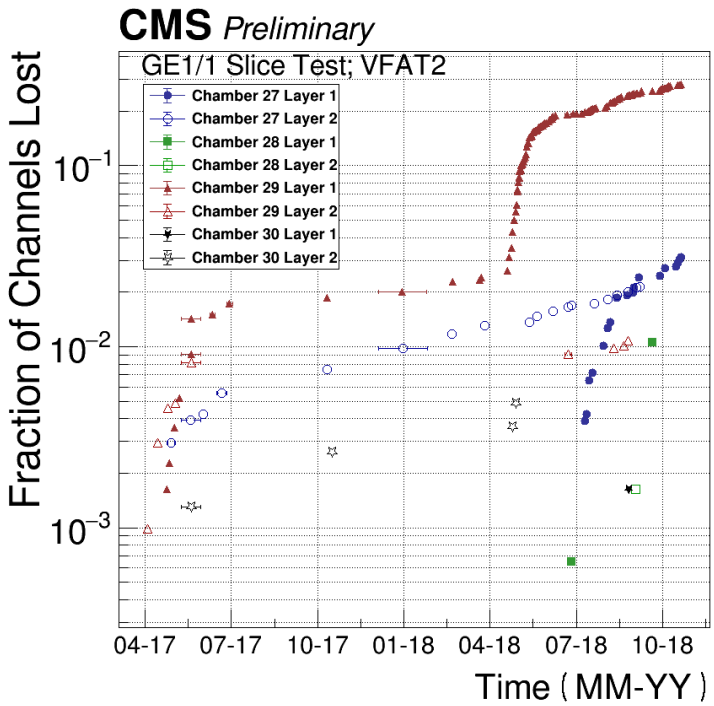

Figure 4.12: Fraction of frontend channels lost during the slice test operations for the eight single chambers installed in slot 2. From [87].

4.2.3 Protection to the input of the VFAT channels

In the course of 2018, the GEM community performed many investigations about the loss of frontend channels in the VFAT2 hybrids during operations. The process at its origin was discovered to be the propagation towards the readout strips of the primary discharges occurring in the GEM foils. The large area of the GE1/1 detectors results in a large capacitance of the foils and of the gaps. For that reason, a considerable amount of energy is stored when the chambers are powered. If that energy gets released to the input of the VFAT channels in a very short time, it could melt the channel-inputs bonds on the chip. The usual scales for energy released is $\mathcal{O}$(mJ) and the time scale is $\mathcal{O}$(µs).
After an intensive test campaign, the protection offered by the VFAT2 and the initial VFAT3 design was deemed not sufficient to prevent damages. Many studies were therefore performed adding resistors and diodes at the channel inputs. The configuration adopted for the final VFAT3 hybrids (HV3b_v3) used for the chamber assembly foresees a 470Ω input protection resistor. This solution ensures to have damages in the VFAT3 channels only in 3% of the discharges that reach the readout plane [88].

4.2.4 Prevention of HV instabilities

Even if the VFAT3 package has been equipped with input protection resistors, the chance of losing channels after propagating discharges is still non-negligible (Figure 4.13). Consequently, reducing the rate of the primary discharges is of the utmost importance.

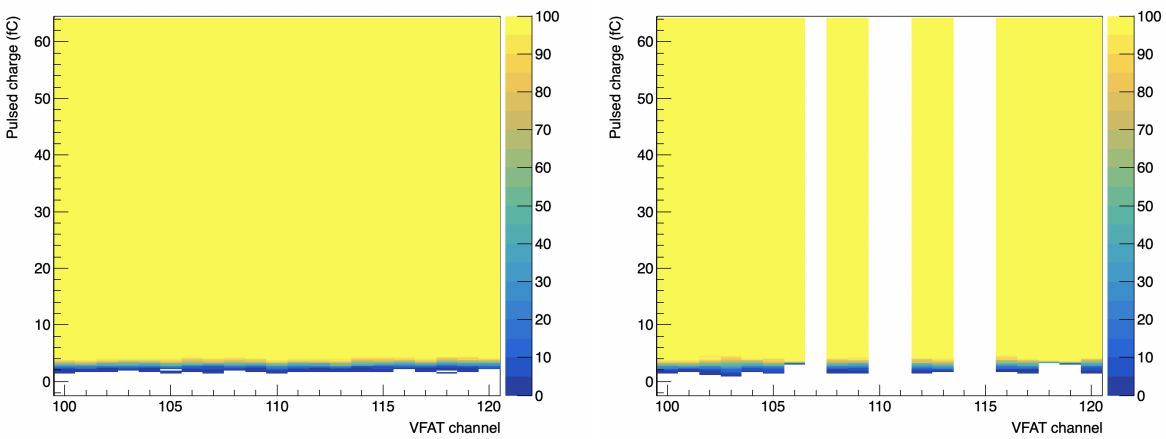

(a) All channels correctly respond to test pulses. (b) Some channels were lost.

Figure 4.13: Example of frontend channels loss during the chamber validation tests with the final on-chamber electronics. On the left, all the VFAT3 channels between 100 and 120 were normally responding to test pulses. On the right, some of those channels were lost after a HV instability. The chamber GE1/1-X-S-BARI-0014 experienced a HV discharge which damaged 8 channels in the VFAT in the readout partition 6. Some channels got their input disconnected (very thin blue edge in channels 106, 118 and 119), others had permanent damages to their frontend circuits (totally not responsive).

Over the total of eight quality control tests, three are devoted to check and improve the high voltage stability of the GEM foils. Here the standard procedures are briefly presented.

Before the assembly of a single chamber in the clean room, each of the three foils is tested and cleaned by means of physical dust removal tools and high voltage (Quality Control step 2, in short QC2). Every discharge triggered by impurities, either external or in the foils themselves, is locally melting or burning whatever caused the instabilities. In case of dust, it gets carbonized and it becomes non conductive; oppositely, if the copper edges of the holes present coarse shapes, the hot plasma generated during the discharge is capable of melting all the excesses and regularize the structure. This cleaning technique is used not only when GEM foils are tested in the production phase, but also in case of frequent trips or short circuits during the QC operations in the lab. By means of an insulation tester (MEGGER MIT485 [89]), 550 V or even 1000 V are momentarily applied across the two conductive sides of the foil to clear the issue.
After the chamber assembly, two additional tests are performed at the production/test sites. A quick immediate one to ensure that no contaminants reached the foils before closing the chamber, and a full quality control devoted to ensure the high voltage stability (QC4). In this stage, pure CO_2 is flushed through the chamber and the high voltage is ramped up in steps to $|V_D| = 4900$ V. All along the ramp, the presence of one or more short circuits in the foils is monitored through the absorbed current. Indeed, the 10MΩ protection resistors installed on the GEM foil HV partitions cause a well defined ohmic current drawn in case of short circuits.
Once the single chamber is assembled and tested, it gets shipped to CERN; in the transportation, mechanical stress could affect the components generating and depositing dust on the foils. Thus, another full HV training in pure CO_2 (QC6 [90]) is performed before mounting the final electronics on the chamber, in order not to damage the frontend channels. This stage does not only test the bare chambers, but also the final high voltage filter and the distribution circuits. Similarly to the QC4, it starts with a test to quickly spot the presence of any short circuit with the MEGGER set at 550V. After that, three steps are foreseen to improve the high voltage stability. First, the foils are gradually brought to $\Delta V = 650$ V and the maximum voltage before a trip occurs is recorded. Second, the voltages applied to the chamber electrodes are proportionally ramped up to $|V_D| = 4600$ V and the current drawn by each electrode is recorded, expecting values below 1 µA. Finally, the foils are kept at $\Delta V = 580$ V for around 24 hours to check the long term stability. Here, the key variable to be monitored is the trip rate. A successful completion is declared when the instabilities are less or equal to one per hour.

After QC6, the chambers are equipped with the readout electronics. Subsequently, they undergo additional validation tests that require the Ar/CO_2 gas mixture and the full HV on. Before these operations, a new procedure has been introduced to reduce discharges by cleaning and training the foils.
At this stage, the final components are mounted and the gas mixture allows the propagation of the discharges. On the other hand, triggering instabilities is essential for the procedure to be functional. The compromise is reached through the following procedure:

- Turn on the single foils and gradually reach $\Delta V = 420$ V. Let them on for around 4 hours.
- Ramp up the electrodes between Drift and GEM2B to an equivalent divider current of 720 µA and keep the rest off. Let the chamber stabilize for 4 hours.

- With the induction gap off and the transfer 2 gap at 50% of its nominal value, increase the other electrodes HV up to an equivalent divider current of 710 µA. Let the chamber stabilize for 4 hours.
- Perform the same actions as in the previous step, but with transfer 2 gap at 75% of its nominal value, and then again at 100% of its nominal value.
- Ramp up the entire chamber at nominal value at the desired working point.

The described procedure is focused on preserving the frontend, while allowing increasing intensities of discharges to ensure a final optimized high voltage stability. For instance, the lower transfer 2 field utilized in the intermediate steps mitigates the propagation of the discharges through the entire foil stack. Additionally, it is worth mentioning that no events with frontend damages have ever been recorded while the induction gap was kept off.
The application of this additional HV training reduces the frequency of trips down to one every few days when operating the detectors at the nominal HV working point (average gas gain of ≈ 20000). This reduces the chances to have events originating VFAT channel losses and damages to the GEM foils. Moreover, it diminishes the detector dead time introduced by the power supply trips and recoveries, ensuring smoother operations both in the GEM QC lab and in CMS.
The experience gained in the quality control tests is being consolidated and transferred to the operations of the detectors in the CMS experiment. There, after the chamber transportation and installation, a high voltage training in two steps is performed in order to ensure the detectors long term operability at the most convenient high voltage working point. First, a QC6-like procedure in pure CO_2 cleans the electrodes and tests the HV filters and connections. Second, a HV training in Ar/CO_2 is performed to stably reach the chamber working point.

4.2.5 Other effects of the HV discharges

The last part of this section will present other consequences of the high voltage discharges. Contrarily to the previous presented issues, the following ones are very rarely recorded and easier to recover from; therefore, they result to be less concerning.

4.2.5.1 Permanent short circuits

Dramatic high voltage discharges can not only cause the loss of frontend readout channels, but also damage the GEM foils. Indeed, while the spark traverses a hole, it transfers a large quantity of heat to the polyimide and to the copper, melting and even vaporizing them. The plastic material could then be deformed and distort the structure of the hole; this is not catastrophic, given the density of holes available to amplify the electron avalanches. Contrarily, if the molten metal drops inside the hole, it can create a permanent short circuit or an irregular structure that ignites other sparks. The normal procedure to attempt to cure this consists in applying across the foil a voltage of 550 V or 1000 V with the MEGGER for a period of time shorter than one second. Would this not be successful, the gas mixture might be changed. It has been noticed that flushing the affected chambers with compressed clean air and then burning the short circuits with the MEGGER was more effective than in Ar/CO_2. The reason could be identified in the

fact that air contains a fraction of O_2, which creates non conductive metal oxides in the damaged regions.
During the GE1/1 chamber production, it has never been necessary to operate or validate a chamber with a short circuit in one of the foils. They were all removed applying the aforementioned methods. Anyway, a permanent short circuit appearing in one chamber has the following effects:

- The voltage difference between top and bottom electrodes in the interested HV partition is 0V, resulting in absence of amplification.
- The voltage difference in the other HV partitions of the same foil experience a reduction, since the current drawn by the foil give a voltage drop across the filter resistors. One short circuit causes a 3% drop in the voltage supplied to the foil.
- The current flowing through the short circuit might generate a source of noise in the detector.

In order to study the noise level with permanent short circuits, a chamber rejected in the initial quality controls because of two short circuits in GEM3 foil has been selected and fully equipped with final electronics. The intrinsic noise was recorded for each of the readout channels in conditions of HV off and HV on at nominal values. No significant change in the noise level was noticed (Figure 4.14).

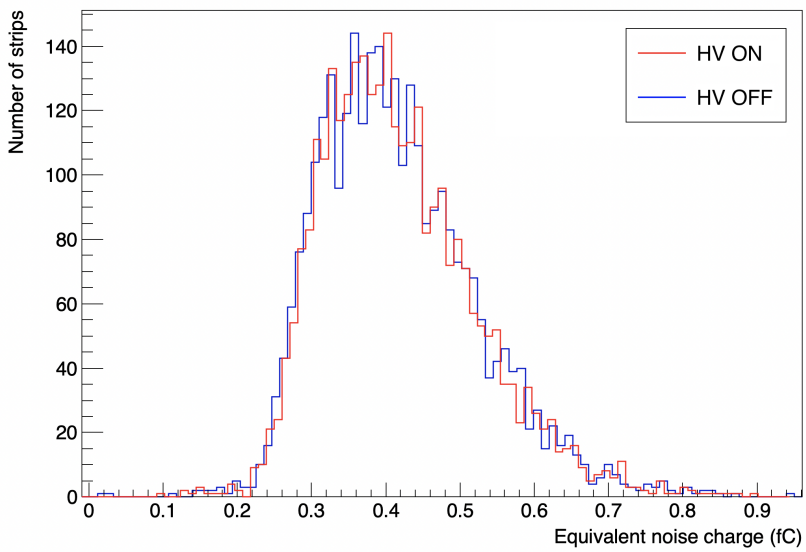

Figure 4.14: Equivalent noise charge[4] for the 3072 channels of a chamber with two short circuits in GEM3 foil (GE11-X-L-CERN-0026). In blue, noise measurement with HV off. In red, full stack was turned on at nominal voltage.

[4]More details about how the ENC is measured can be found in the section 4.3.2.

4.2.5.2 Frontend electronics losing synchronization

The last effect that a high voltage discharge could have is a sudden variation of the ground level of the entire detector. Even though the main safe ground cable provides a good path for the electrons to ground, a very short transient can induce an instantaneous ground voltage level shift. Since the high voltage and the low voltage have the ground in common, a HV event might have repercussions on the voltage provided to the on-chamber electronics. Thus, in some rare occasions either VFATs or GBTs can lose the synchronization with the backend.
This issue has been spotted during the data taking in the cosmic ray stand QC test, and an example can be seen in Figure 4.15. A trip occurred around event 600k of a cosmic run. Consequently, nine VFATs stopped communicating and one lost the synchronization. No data was then recorded from the nine non communicating VFATs and the other kept sending incoherent hits for the rest of the run. In the quality control operations there isn't a strong interest in an immediate recovery of the communication, thus no actions are taken and new runs are started after issuing a reset. On the contrary, in the CMS operations periodic hard resets will come from the central CMS Timing and Trigger Control (TTC) during the runs, allowing all the detectors to re-synchronize and re-establish a proper communication.

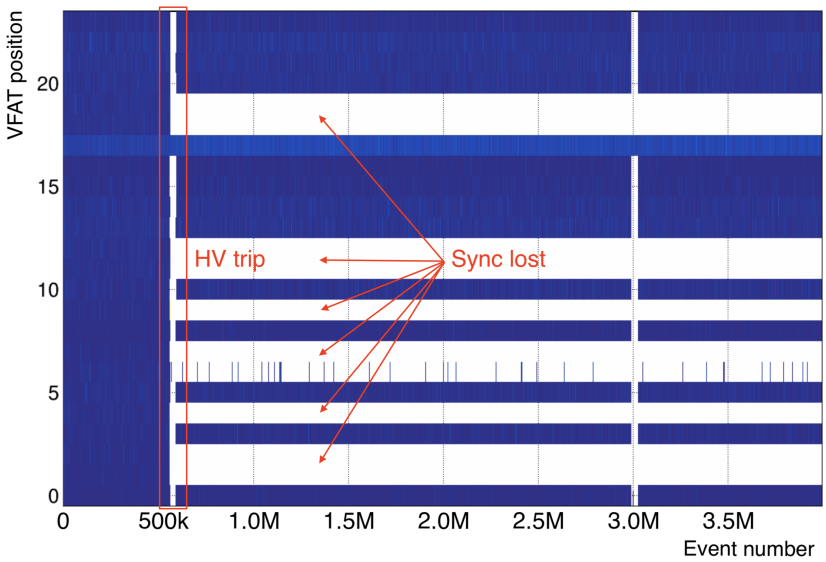

Figure 4.15: Example of high voltage instability event after which many VFATs lost the synchronization during a run at the cosmic ray stand. The events with hits (in blue) represent the normal behavior. The events for with zero hits (in white) for almost all the VFATs represent the time when the high voltage was off or being ramped up after the trip. Subsequently, the registered number of hits is zero only for some sectors, suggesting a desynchronization of those VFATs. The communication is not restored for chambers in QC8 after such events, contrarily to what will happen in the CMS experiment.

4.3 Noise level and frontend thresholds

As presented in section 2.5.5.4, the GE1/1 frontend thresholds consist on voltage levels set to the VFAT3 arming comparators, that determine if a detector signal is recorded (logic '1') or discarded (logic '0'). The threshold value of each VFAT channel is given by two components: a global common value for all the 128 channels and a local per-channel value that can slightly adjust the global one. The global threshold is set through an 8−bit DAC reading the *CFG_ THR_ ARM* register; the local thresholds are set via 128 6−bit DACs reading the *trimDAC* registers.
The first part of this section explains how the global threshold value is determined. The second one focuses on translating the threshold value into charge units, allowing for a comparison with the expected detector signal charge. The third one presents two frontend noise level instabilities and the developed mitigation procedures.

4.3.1 Determination of frontend thresholds

The global VFAT thresholds are determined by the noise hit rate that each of the 24 readout sectors is allowed to send to the Level 1 trigger. The acceptable noise rate is fixed based on the foreseen total background rate during the operation of GE1/1 in the CMS endcaps (Figure 4.16). In HL-LHC proton-proton collisions, the GE1/1 chambers will receive at most 1.5 kHz/cm^2 of background hits in the regions closer to the beam pipe. Since the $i\eta$ readout partitions have been subdivided for a uniform illumination of the active area, it is possible to assume that every VFAT partition will experience a total background rate on the order of 10^5 Hz. Therefore, noise trigger rates up to 10^4 Hz represent only a fraction of the background.
In the GE1/1 validation tests 100 Hz of noise per readout partition are commonly allowed. The same criterion is adopted for the GE1/1 frontend configuration in CMS.

GEM Station	Max. neutron flux [MHz/cm^2]	Max. neutron induced hit rate [Hz/cm^2]	Max. photon hit rate [Hz/cm^2]	Max. e$^+$/e$^-$ hit rate [Hz/cm^2]	Max. total hit rate [Hz/cm^2]	Total acc. charge after 10 HL-LHC years [mC/cm^2 - no safety factor]
GE1/1	0.277	499	847	123	1469	6
GE2/1	0.191	343	273	56	672	3
ME0	3.28	5910	33900	7700	47510	283

Figure 4.16: Expected background components and their corresponding hit rates in the GE1/1, GE2/1 and ME0 regions during operations in HL-LHC proton-proton collisions. From [27].

The noise rate is calculated for each VFAT by a specific routine implemented in the OptoHybrid FPGA. Once the global VFAT thresholds for the arming comparators are set, the noise trigger hits are counted for a fixed period of time, normally 1 second. A hit is defined as a logic state 1 after the OR of the incoming 64 trigger s-bits, in order to easily account for noise hit clusters. The present routine will be upgraded for the CMS operations for a more precise identification of the clusters.
The noise rate is checked against the global thresholds, scanning the *CFG_ THR_ ARM* register values in the entire range $0-255$. This procedure is named *s-bits rate against threshold scan*, and it produces curves like in Figure 4.17a for each of the 24 VFATs in a chamber. The initial plateau

is an artifact of the saturation of the processing capabilities of the VFAT channel analog part. The steeply falling part of the curve represents the noise rate reduction for increasing thresholds. The *CFG_ THR_ ARM* register value corresponding to 100 Hz is selected independently for each VFAT.

A deviation from a smoothly falling curve indicates faulty channels or poorly connected VFATs (Figure 4.17b). Poorly connected VFATs result in interrupted ("broken") s-bit lines between the VFAT and the OptoHybrid which are corrected by unplugging and replugging the electronics components.

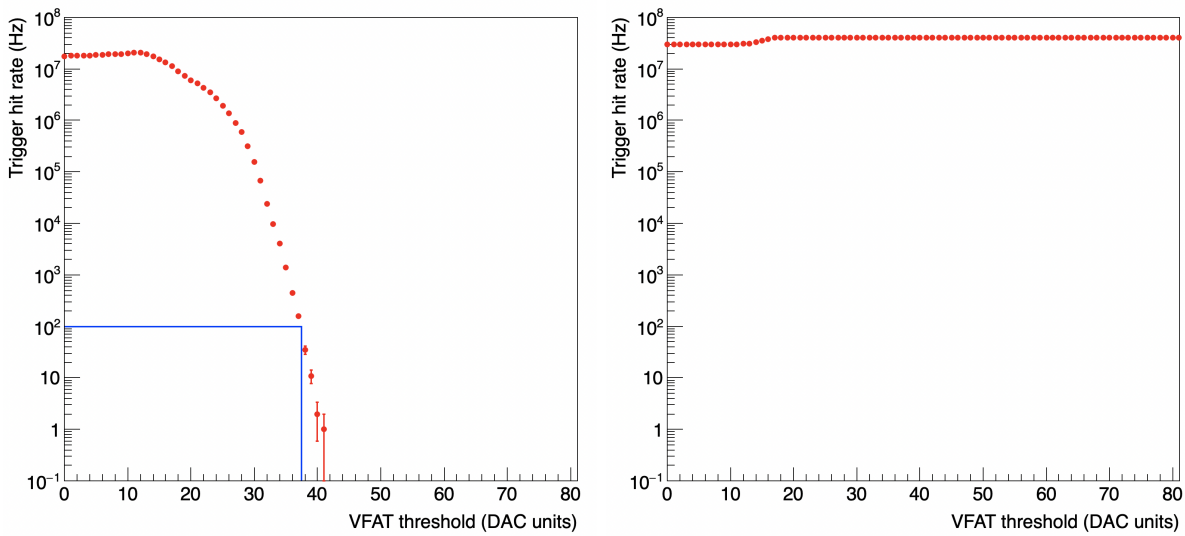

(a) Noise rate as a function of the threshold for a normally behaving VFAT

(b) Noise rate as a function of the threshold for a misplaced VFAT, resulting in one "broken" s-bit line

Figure 4.17: On the left, example of s-bits noise rate curve for a perfectly functional VFAT. The blue lines represent the threshold that corresponds to 100 Hz of noise. On the right, s-bits noise rate curve for a VFAT presenting issues (right). Any misplacement can be simply solved during the super chamber assembly by re-plugging the VFAT or the OptoHybrid board and making sure that all the connectors are properly clean.

4.3.2 Threshold calibration and noise level quantification: s-curves

Once VFAT threshold values are assigned, it is possible to convert them from DAC to charge units through an *s-curve* scan. Test signals of increasing charge are injected to the readout channels utilizing an internal VFAT pulse generator, and the response is recorded. The calibration of the pulser is provided for every chip by the VFAT manufacturer. Usually, 100 consecutive pulses are supplied to the channel inputs for every given charge. The resulting distributions are fitted with sigmoid functions; an example for the 128 channels of a VFAT can be seen in Figure 4.18.

The response has a sigmoidal shape resulting from a step function smeared by white noise. The latter is the sum of the intrinsic noise of the readout electronics, the noise picked up by the strips and the one picked up by the traces between the strips and the VFAT ASIC. Its amplitude spectrum can be modeled as a Gaussian centered at 0. The standard deviation of such distribution is referred to as *equivalent noise charge* (ENC), which represents the channel

noise level. The channel threshold in charge units is defined at the 50% response. A visual representation is shown in Figure 4.19.

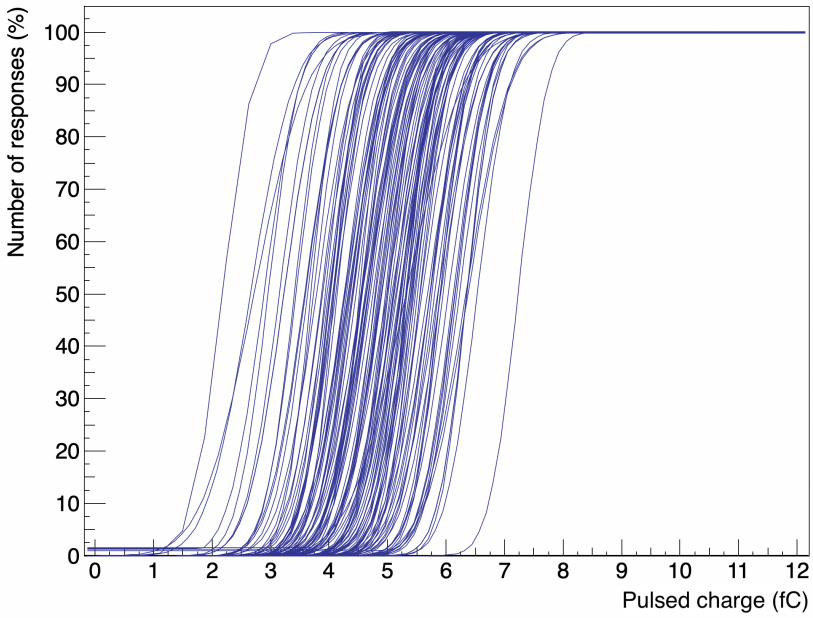

Figure 4.18: Sigmoid curve fit to the response of the 128 VFAT channels to 100 test pulses of increasing charge, also know as s-curve scan.

An ideal VFAT would have identical values for the ENC and the individual thresholds of all the 128 channels. In reality though, the transistors, the resistors and the other components of the VFAT ASIC are produced with a certain tolerance. This generates slightly different amplification factors for the incoming signals, that reflect on the response of the channels when the thresholds of the arming comparators are set to a common voltage. The alignment of the channel response through the adjustment of the local thresholds will be detailed in section 4.4.
In terms of ENC, the VFAT channels have similar characteristics from the production. Typically, the channels on the edges exhibit a $\approx 10\%$ increased intrinsic noise with respect to the bulk. The largest noise variation over the chamber area is due to the component picked up by the readout strips. Indeed, the intrinsic noise depends on the strip capacitance, which is proportional to their area. Thus, the ENC becomes larger going from $i\eta = 8$ to $i\eta = 1$, as in Figure 4.20a. This behavior is reflected on the frontend thresholds corresponding to 100 Hz of noise hits, which are presented for the same chamber in Figure 4.20b. For larger readout partitions, the noise level is higher, and therefore the frontend thresholds have to be larger to provide the same noise rate.

4.3.3 Instabilities in the VFAT noise levels

Two kinds of electronics noise instabilities were spotted during the super chamber validation tests: the *ENC instability* and the *GEB s-bit issue*. In the following sections the issues will be presented, together with the applied workarounds that permit a reliable operation of the GE1/1 detectors.

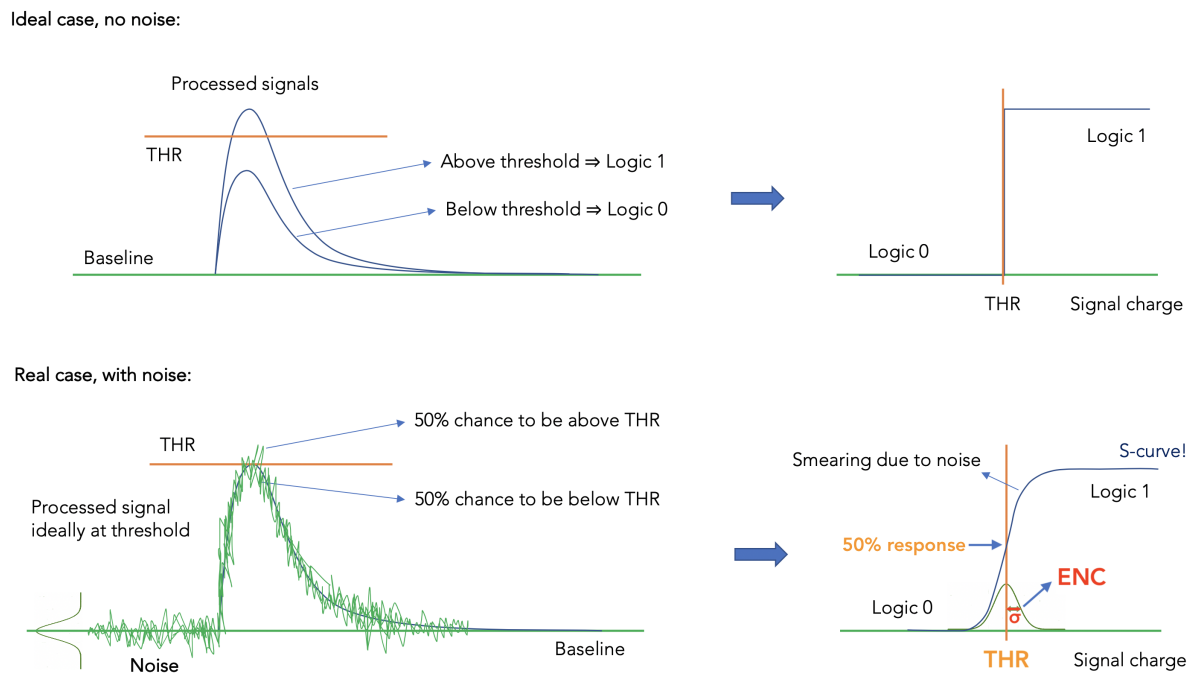

Figure 4.19: Depiction of ideal vs real response of a readout channel to an incoming signal. The noise affects the response in smearing the step function, making it become an sigmoidal curve (s-curve). The noise affecting the baseline represents the convolution of the one present in the threshold level and the one intrinsic to the baseline itself. The s-curve mean corresponds to the channel threshold, while its standard deviation represents the channel noise level (ENC).

4.3.3.1 ENC instability

The VFAT *ENC instability* affects all the chips, and it consists in the variation of the channel noise level when the ASIC transitions between the SLEEP and the RUN modes. The transition is controlled by the single-bit register *RUN_MODE*, normally toggled between scans and runs. The SLEEP mode minimizes the power consumption and maximizes the lifetime of the chip by applying default values to all the registers and not powering the channel analog part. When the RUN mode is turned on, the frontend gets configured with the proper values for the registers set through the slow control.

An example of the ENC variation between different s-curve scans is presented in Figure 4.21a. Without toggling the *RUN_MODE* between the scans, no influence on the noise level is recorded, as in Figure 4.21b.

Tests conducted at the CERN electronics test lab [91] on a bare VFAT board proved that the amplitude of the intrinsic noise variation depends on the capacitance at the VFAT channel inputs. A custom made board with a capacitance of $C_{PCB} \sim 40$ pF was attached to the VFAT Panasonic readout connector to simulate a detector capacitive load and a series of s-curve scans was taken. The same procedure was performed with $2 \times C_{PCB}$ and without a capacitive load ($0 \times C_{PCB}$[5]). The ENC values were extracted and the results are presented in Figure 4.22.

[5] $0 \times C_{PCB}$ does not imply that the capacitance seen by the channels input is 0 pF, because of the intrinsic capacitance of the paths on the VFATs themselves

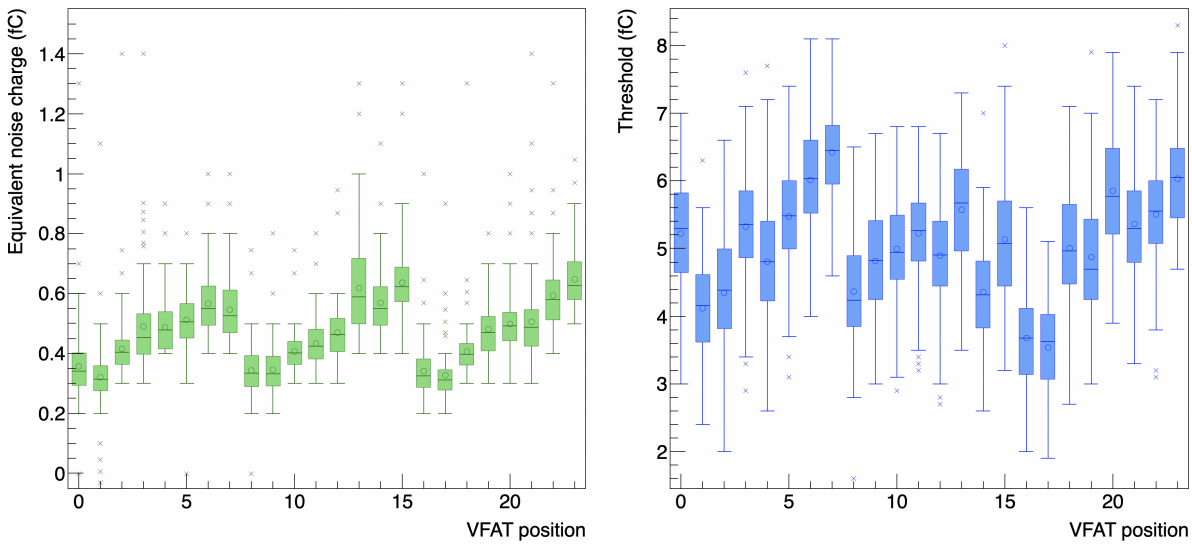

(a) ENC per VFAT slot (b) Threshold per VFAT slot

Figure 4.20: Box plot [92] representing the distributions of the ENC (left) and the thresholds corresponding to 100 Hz of noise hits (right) of the 128 channels of the 24 VFATs of the chamber GE1/1-X-S-INDIA-0017. The recorded noise level increases going from the readout partitions in $i\eta = 8$ to the ones in $i\eta = 1$, which is reflected on the threshold assignment. This is caused by the larger area of the strips in the wide side of the chamber, which consequently have larger capacitance. For each of the 24 VFATs, the crosses represent the outliers, the bars and the box are the interquartile ranges of the distribution, the line (circle) in the box is the median (mean) value.

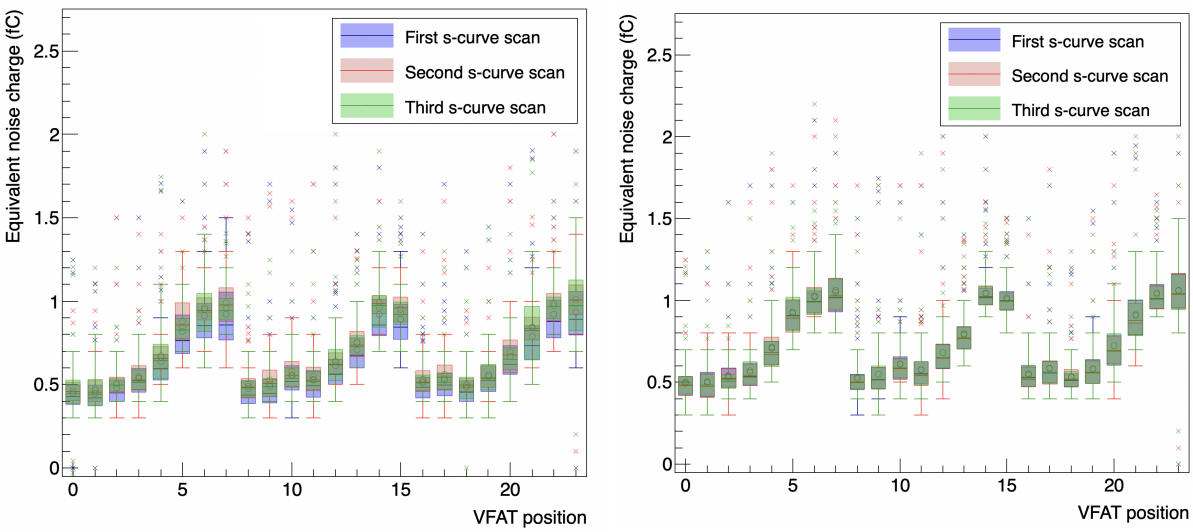

(a) ENC variations toggling *RUN_MODE* (b) ENC variations not toggling *RUN_MODE*

Figure 4.21: Equivalent noise charge measured in three consecutive s-curve scans for the GE1/1-X-S-PAK-0008 chamber, with and without toggling *RUN_MODE* between scans. If the *RUN_MODE* is toggled, the intrinsic noise level varies over the scans; oppositely, it remains stable if the *RUN_MODE* is kept turned on.

The behavior recorded in the s-curve scans is also confirmed by the s-bits rate against threshold

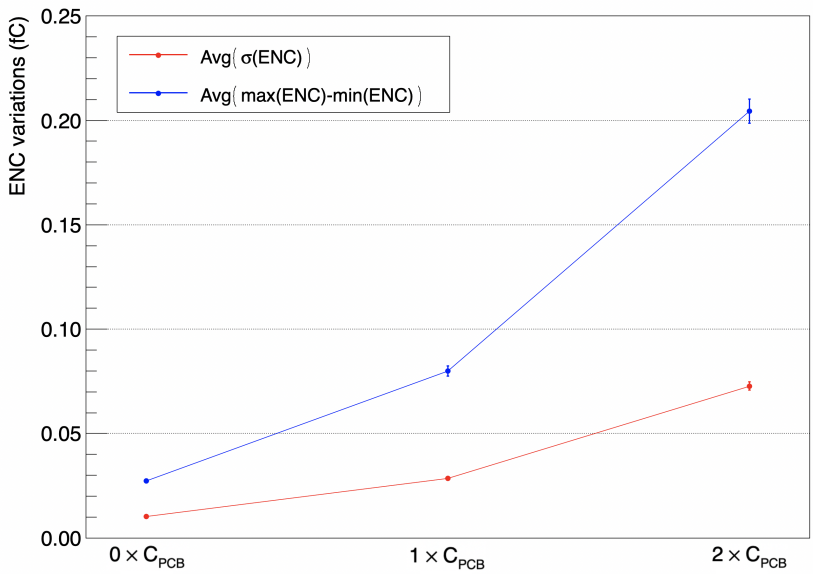

Figure 4.22: Production-grade VFAT tested in electronics lab taking series of 6 s-curves and varying the additional input capacitance C_{PCB}. The average standard deviation of the ENC values for the 128 channels against the value of C_{PCB} is represented in red, while the $avg\,(max_{ENC} - min_{ENC})$ is plotted in blue.

scans. The shape of the curves changes over the scans, with variations that depend on the VFAT sector. Such change in the shape directly implies that the global threshold value corresponding to a fixed noise rate is not stable and it can shift by many units, as presented in Figure 4.23. Therefore, when operating at fixed frontend thresholds, the noise level instability can give rise to a variable noise rate sent to the Level 1 trigger.

Workaround:
A new procedure for the VFAT threshold determination has been developed and followed both in the GE1/1 validation and in the operations in CMS. It foresees a sequence of six s-bit threshold scans[6] from which the global threshold values corresponding to a noise rate of 100 Hz are extracted for each VFAT.
Applying the lowest attained thresholds would provide the best signal detection efficiency, while the highest would ensure low noise rates. The safest compromise for the operations is to apply the average of the six values.

4.3.3.2 GEB s-bits issue

An additional source of unpredictable noise reflecting on the threshold assignment is the *GEB s-bits issue*. It consists in an anomalously shaped curve of the s-bits rate against threshold: instead of a smoothly falling curve (Figure 4.24a), the affected VFAT positions exhibit a much broader initial plateau followed by a steeply falling curve with a visually discontinuous set of

[6]This number of scans is determined by the time required for the detector configuration. Each scan takes approximately 5 minutes, thus a serie of six can be performed in half an hour.

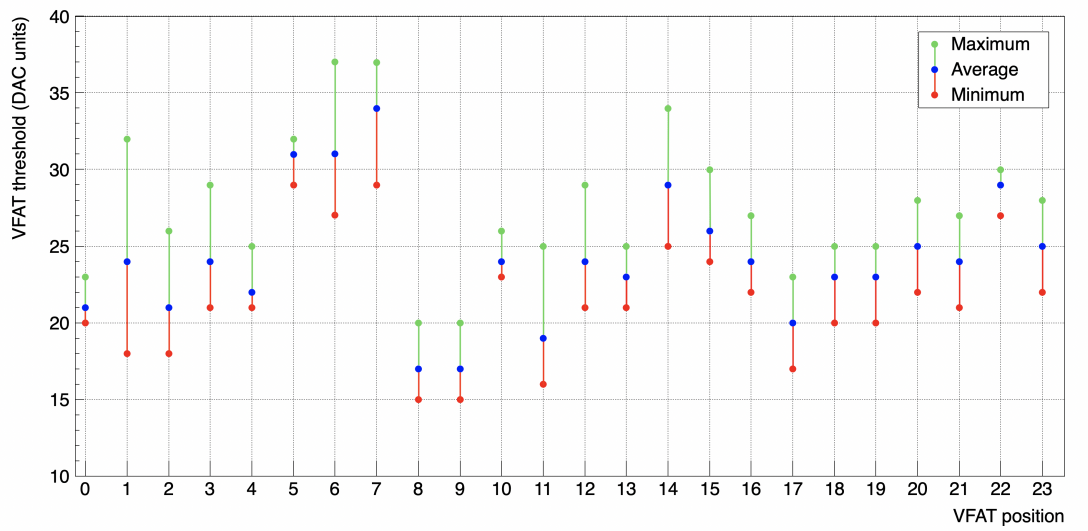

Figure 4.23: Results of 14 subsequent scans of the noise rate vs threshold value for the GE1/1-X-L-CERN-0009 chamber. The three points for each of the 24 VFATs represent the minimum, the average and the maximum *CFG_THR_ARM* values corresponding to a noise rate of 100 Hz derived from the series of scans.

points (Figure 4.24b).

The issue appeared on 7 out of 153 GEBs when installed on a chamber readout board. They experience a bump in the noise level with a similar amplitude over the same $i\eta$ region, that increases going from the narrow to the wide side of the trapezoid. From the shape of the noise rate curve, it has been hypothesized that the picked up noise has a well defined frequency and amplitude, most probably generated within the frontend electronics components. Since this issue is related to a very subtle increase in the noise level, it can easily be masked by the intrinsic noise and pass unnoticed during the tests.

The *GEB s-bits issue* per se has the only consequence of a mild threshold increase for the affected VFATs. In all of the affected detectors, this increment is at most 10%, with a negligible impact on the chamber performance.

On the contrary, a major effect is recorded with the noise level instability issue. If the applied threshold is positioned at the steep drop of the noise rate curve, a shift in the ENC generates an alternation between 0 Hz and around 20 MHz of noise hits sent to the Level 1 trigger. Naturally, a proper operability cannot be granted in the worst noise condition. This can be clearly seen in Figure 4.25, where the number of hits per strip was recorded in a validation cosmics run for an affected chamber. The extremely large occupancy in VFAT6 and VFAT7 clearly manifests the combination of the aforementioned issues.

Workaround:

Based on the studies presented in Figure 4.23, a workaround has been established in order not to discard the affected GEBs and to ensure the detectors operability even in such conditions. In presence of "GEB s-bits issue" signature, the global VFAT threshold registers of the affected

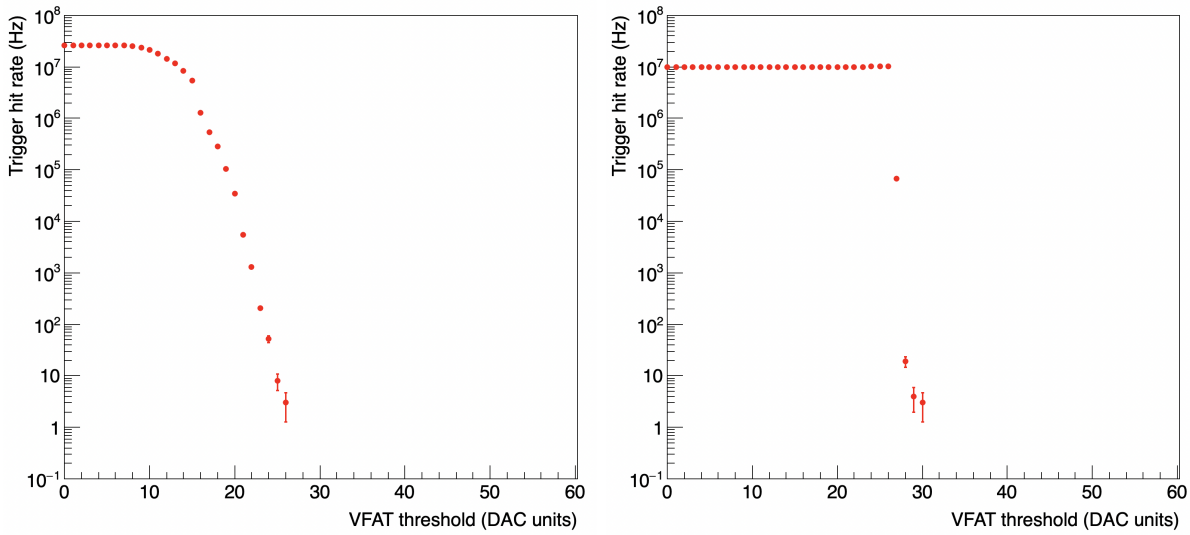

(a) Normal s-bit threshold scan curve (b) S-bit threshold scan showing GEB s-bits issue

Figure 4.24: Examples of a normal shaped s-bits rate against threshold scan curve (left) and a VFAT position affected by the GEB s-bits issue (right). The recognizable symptoms are a much broader initial plateau followed a steeply falling curve with a visually discontinuous set of points.

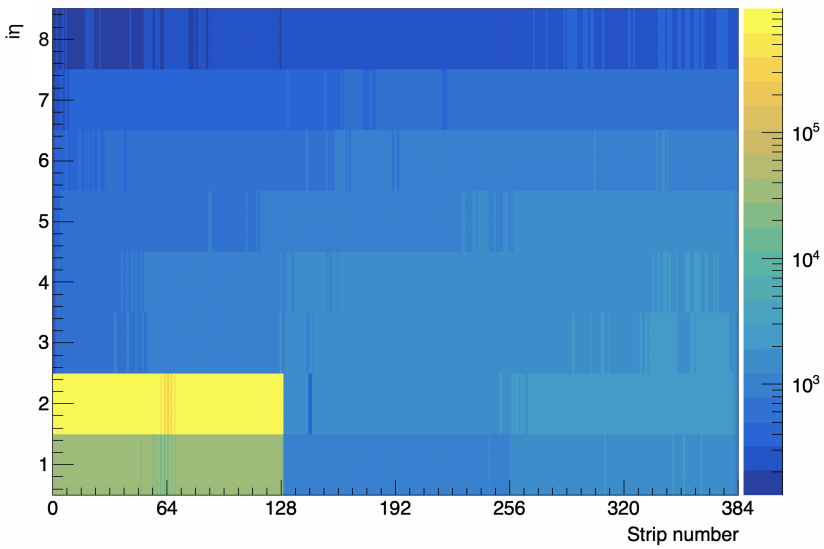

Figure 4.25: Occupancy per strip recorded during a cosmic rays run for the GE1/1-X-L-CERN-0001 chamber. VFAT6 and VFAT7 sport a large number of noise hits recorded, which was generated by the combination of "GEB s-bits issue" and noise level instability issue.

VFATs are incremented by 5 DAC units. This corresponds to an increase in the final threshold of around 0.5 fC, which has a negligible impact on the overall the chamber performance.

4.3.4 Quality control of electronics components

The characterization of the frontend electronics functionality at the stage of the super chamber assembly is performed during a dedicated step of the quality control tests: the QC7. It has

two main targets. First, it defines the optimal values to be assigned to the global VFAT DACs. Second, it identifies the issues related to the on-chamber electronics, including the anomalies in the noise level. The execution procedures foresee:

- An initial verification of the proper communication between backend, OptoHybrid and VFATs, including a check of the CSC trigger links;
- A calibration of the global VFAT DACs to determine the DAC register values corresponding to the recommended analog values;
- An s-curve scan at fixed global VFAT threshold ($CFG_THR_ARM = 100$), monitoring the noise level and verifying to have less than three non-responding channels in each $i\eta$ partition;
- A threshold scan monitoring the s-bit trigger hits (s-bits rate against threshold scan) to ensure the absence of issues in the trigger path;
- A threshold scan with the full granularity data path to verify the proper plugging of the VFATs to the readout board of the chambers.

Once the correct communication between the on-chamber and the backend electronics is assessed, each of the global VFAT DACs is calibrated. The values in their registers are scanned and the applied values are monitored through an ADC. The digital values corresponding to the recommended analog values are then extracted and assigned.
Subsequently, two tests are conducted to assess the proper connection between the on-chamber electronics components. The s-bits rate against threshold scan checks the trigger lines between the Optohybrid and the VFATs. The threshold scan with the full granularity data path probes the connection between the VFATs and the chamber readout board.
The presence of noise hits at a fixed threshold is checked 100 times for each of the global threshold register scanned values. The absence of noise hits in the channels indicates a disconnection from the readout strips. This is due to the presence of a lower intrinsic noise when the capacitance at the channels inputs is reduced. An example of a partially unplugged VFAT is shown in Figure 4.26. The fix consists in a simple re-plug of the VFAT board, which is always possible during this quality control step.

The last main test performed on the on-chamber electronics is the assessment of the noise level. Given that the thresholds applied during the operations are driven by the noise level, two requirements on the intrinsic noise of the readout channels have been defined. The average ENC of the 128 VFAT channels has to be lower than 0.7 fC, while every individual channel ENC has to be below 1.5 fC. If higher, the channel gets masked. Not more than three channels per $i\eta$ partition should be masked, otherwise the VFAT board is exchanged. In the next section, the background necessary to fully appreciate the reasons behind these cuts will be shown and the values chosen will be fully justified.
A visualization of the QC7 requirements in terms of noise level is presented in Figure 4.27.

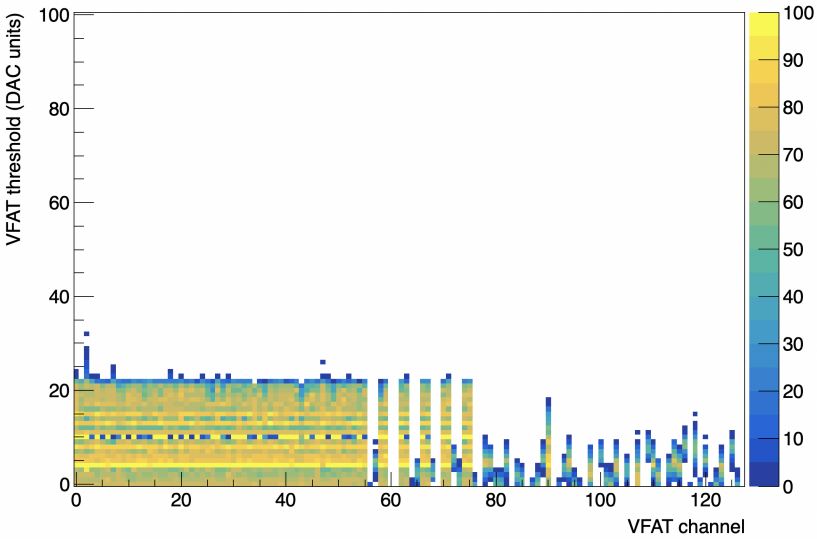

Figure 4.26: Results of the threshold scan with data path for the GE/1-X-L-CERN-0043 chamber during a preliminary QC7 test. The VFAT was partially unplugged on the readout board side, causing a missing connection between the strips and the VFAT channels. This resulted in a very reduced input capacitance to the affected channels, and consequently an unusually low intrinsic noise. In the plot, this can be noticed for the channels in the range $55 - 127$, contrasting with the normal behavior of the ones between 0 and 54.

4.4 Channel response trimming

In the previous section, the electronics noise level has been discussed together with its impact on the definition of the global VFAT threshold. This section will instead be focused on the fine adjustments of the individual readout channel responses.

4.4.1 Definition of frontend channels trimming

From the production of the VFAT board and ASIC chip, each of the components of the 128 channels may come with slight variations that lead to a different signal amplification. Consequently, this leads to a shift in their response with respect to a central design value. Dedicated circuitry is present in the VFATs to compensate for these imperfections by tweaking the individual channels response to the incoming signals. The local DAC values controlling the circuits are stored in 128 $7-$bit sub-registers[7], where 1 bit is dedicated to the polarity, while the other 6 bits are dedicated to the amplitude, allowing to define values from -63 to $+63$. This interval corresponds to a variation of the s-curve mean in the design range of ± 2.1 fC[8]. The adjustment is accomplished through the application of a fine compensation on the voltage level of the global threshold at the

[7]The local DAC register of a single VFAT channel consists of 16 shared bits. Bit 15 controls the enable of the calibration pulse to the channel input, bit 14 stores the channel mask for the trigger and readout output, bits from 13 to 7 are dedicated to the Zero Crossing Comparator timing optimization and the last 7 bits steer the trimming circuit.

[8]The range of variation in the response provided by the trimming circuits varies due to the tolerances in the circuitry components. During the VFAT3 tests, differences have been recorded from a minimum of ± 1.34 fC to a maximum of ± 5.04 fC. Typically the extremes of the corrections are within 2.604 ± 0.525 fC.

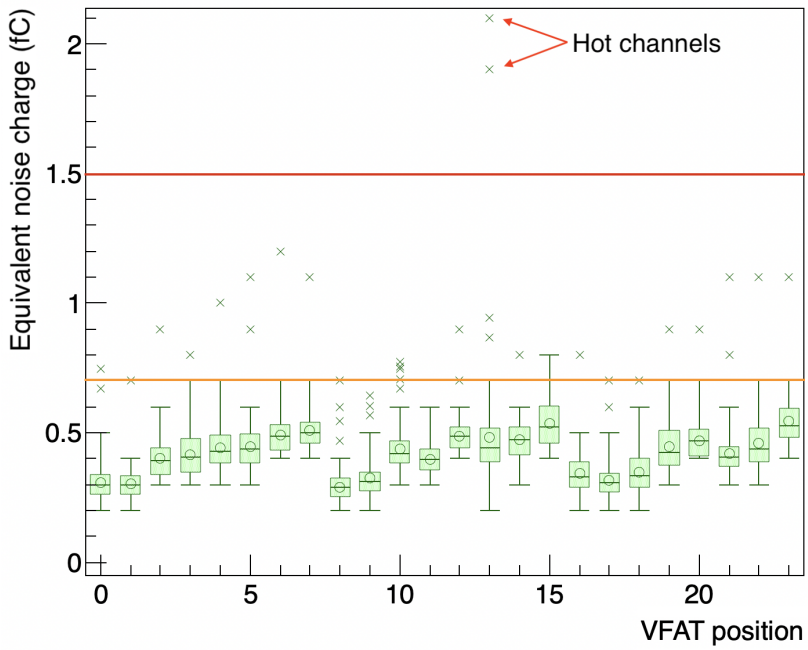

Figure 4.27: Typical box plot of the ENC distributions per VFAT obtained from an s-curve scan. The horizontal orange line represents the requirement on the average to be lower than 0.7 fC. The red line at 1.5 fC refers to the cut to declare a channel as "hot". The hot channels get masked during any data acquisition, thus they do not contribute to the particle detection. The plot correspond to the results of the GE1/1-X-S-PAK-0012 chamber, which has two hot channels in VFAT13.

discriminator stage.
The procedure of alignment of the channel responses is called *trimming*.

The starting point consists on a baseline s-curve scan. The s-curve mean values, i.e. the individual channel thresholds, are evaluated from the sigmoidal fits and the necessary corrections with respect to a reference value are calculated in charge units. From this point onwards two paths with the same outcome can be taken.
The first one is an iterative approach. Even though the trimming circuits do not come individually calibrated, it is possible to compute the local DAC registers values (*trimDACs*) utilizing the compensation they should provide by design. The alignment of the channel responses gets further refined in subsequent iterations of s-curve scans.
An alternative way to perform the trimming is done calibrating the trimming circuits. With the assumption of the full linearity of the trimming circuits over the operational range, three s-curve scans are taken at a fixed global threshold and setting all the trimDAC registers at -63, 0 and $+63$. An '*s-curve mean vs trimDAC*' calibration is then produced for each of the channels by a linear fit. The calibrations can be used to extract the individual trimDAC values corresponding to the required compensation for the channel thresholds.
During the GE1/1 super chamber validation tests, the iterative approach has been adopted. The final software used in the CMS operations will instead follow the trimming circuit calibration

path. Even if this reduces the flexibility of the procedure, it allows for a completely unsupervised derivation of the configurations.
In the following, the majority of the explanations will be presented considering a single VFAT chip. Naturally, the same logic extends to all the 24 VFATs present on a GE1/1 chamber.

4.4.2 Benefits of frontend channels trimming

The trimming procedures stem from the desire to have a uniform response across the entire readout area. This lets to process and measure a certain signal charge consistently in all the VFAT channels.
Together with the homogeneity of the thresholds, the additional expected positive impact is a reduction of the applied global thresholds of the VFATs. To better understand why, let us consider a hybrid with the channels response scattered around a central value, as they come from the production. The global threshold derivation defined by the accepted noise rate is often driven by the single channel with the response curve tail that extends the furthest towards the 0 input charge. Indeed, such channel is the one that has the largest signal amplification or the largest intrinsic noise, thus it results to have the highest chance to fire when a small signal is processed. Therefore, even if the ENC of every channel is reduced to its minimum, the overall VFAT threshold cannot be further diminished due to the presence of channels responding to small input charge.

4.4.3 Trimming procedure and main results

Following the mentioned ideas, the standard trimming procedure historically adopted was to align the individual channel thresholds to a common value. From the initial s-curves scan the mean values were extracted and their average was computed. All the channels were then trimmed to their average 50% response.
The implications of the standard trimming method are that, in presence of non-uniform ENC among the channels, the derivation of the global threshold is driven by the noisier channels. Moreover, if the channels with larger intrinsic noise were initially coincidentally responding later, their alignment to the bulk may even lead to higher global thresholds.
The shortcomings of the standard trimming generated by the noisy channels are overcome by a new procedure developed by the author, which aligns the tails of the responses instead of the threshold values. The parameter considered for the channel response alignment (X) is a combination of the mean s-curve value and the ENC. In formula:

$$X_i = Mean_i - n \times ENC_i \ , \tag{4.4}$$

where i is the channel index and n is a parameter of the new trimming procedure that needs to be tuned by the optimization of the derived global thresholds. The initial studies were performed setting $n = 0, 1, 2, 3$.
For each value of n, three trimming iterations were performed, followed by an s-bit threshold scan to derive the new *CFG_THR_ARM* register configuration corresponding to 100 Hz of noise. A

final s-curve scan provided the conversion into charge units of the new applied threshold.
An example of trimming with $n = 0$ (standard trimming) and $n = 3$ for the same VFAT is shown in Figure 4.28. With the introduction of the new procedure, the noisy channels are set to have a larger individual threshold and all the other thresholds become aligned to a common lower value.

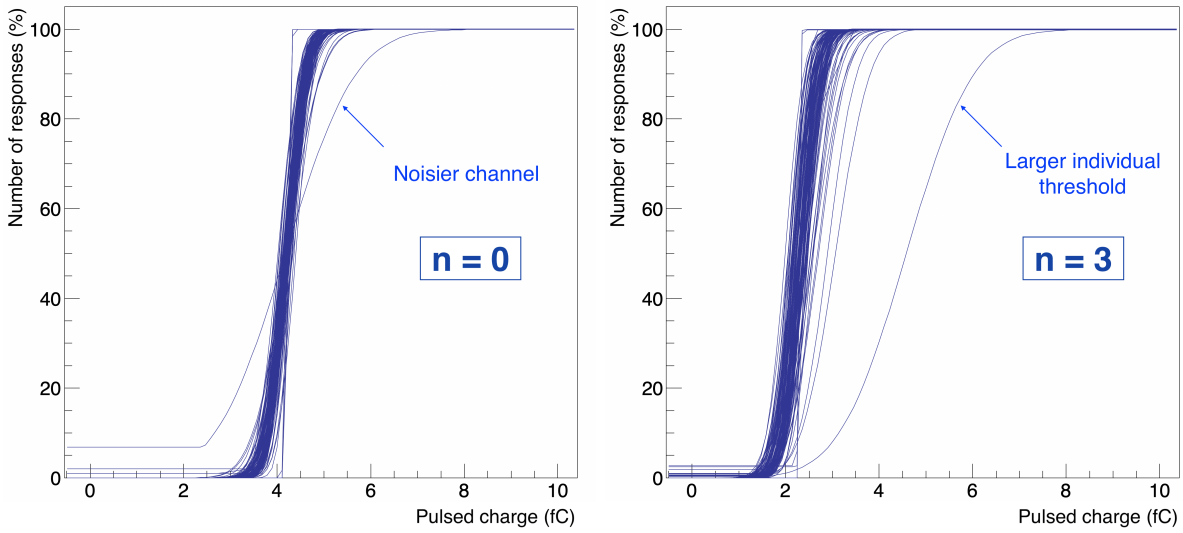

Figure 4.28: Channel responses to test pulses for a VFAT obtained by with the $n = 0$ and $n = 3$ trimming procedures. On the left, the individual channel thresholds are aligned to the common value of 4.2 fC, driven by the noisiest channel. On the right plot, the new procedure is applied, aligning the tails of the channels responses. The majority of the channels have a threshold of around 2.3 fC, while the ones with a larger ENC are pushed towards higher thresholds. Both plots represent the response of the VFAT1 of chamber GE1/1-X-S-INDIA-0017.

Further investigations with $n = 4, 5$ have also been carried out revealing mild improvements. The case with the largest tested value for n demonstrated instabilities in the distribution of the channels individual thresholds. This happens because the errors in the estimation of the ENC get inflated by the n parameter.
Balancing instabilities and capabilities in reducing the final applied thresholds, the chosen value for the trimming adopted during the quality control tests and the operations in the CMS experiment is $n = 4$. The parameter considered for aligning the response is then $X_i = Mean_i - 4 \times ENC_i$.
The comparison between the distributions of the threshold values for the 3072 readout channels of a chamber before and after applying the $n = 4$ trimming can be found in Figure 4.29. The mean value of the two distributions amount to 4.49 ± 0.02 fC and 2.64 ± 0.01 fC, respectively for no trimming and $n = 4$ trimming procedure applied.
After the $n = 4$ trimming, the average thresholds applied to the chambers tested in the cosmic ray stand were between 2.5 fC and 4.0 fC, depending on their intrinsic noise.

Main trimming procedure result:
The application of new trimming procedure reduces the average frontend thresholds by about 40%, while keeping the same noise rate sent to the L1 trigger. This implies that the minimum

amount of signal charge required for a particle to be detected is 40% smaller.
The impact of such a threshold reduction on the detection efficiency for minimum ionizing particles was studied in a cosmic run operating the GE1/1-X-L-GHENT-0022 chamber at an equivalent HV divider current of 680 µA[9]. The efficiency increases from a value of 84.2% before the trimming, to a value of 92.4% after the trimming is applied.

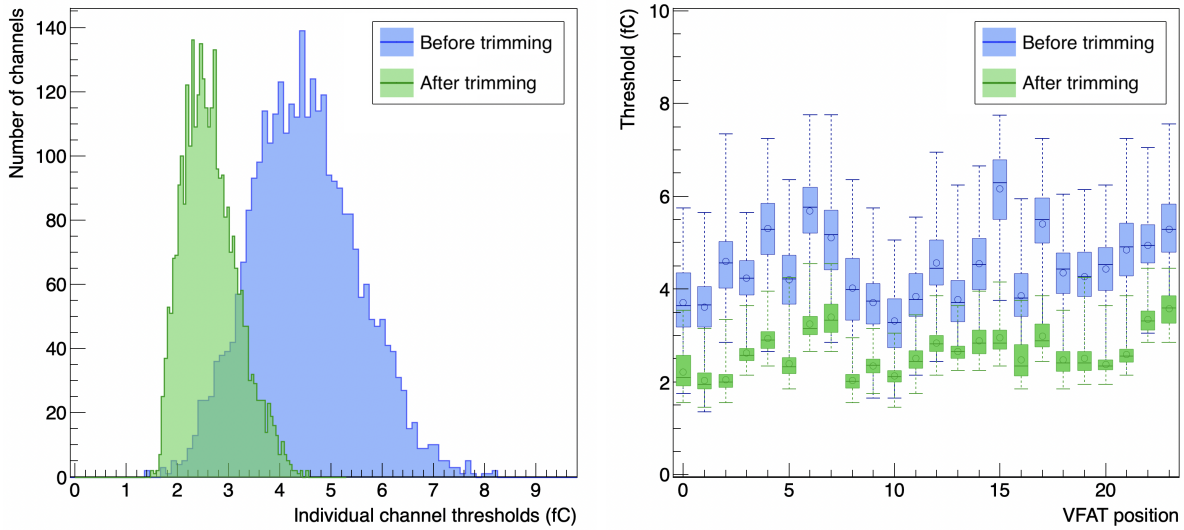

Figure 4.29: On the left, comparison between the threshold distributions of the 3072 readout channels of the GE1/1-X-L-GHENT-0022 chamber with no trimming and after the application of the $n = 4$ trimming procedure. The average applied threshold diminishes from a value of 4.49 ± 0.02 fC before the trimming to a value of 2.64 ± 0.01 fC after the trimming, corresponding to an improvement of 41%. On the right, the same quantities are represented as candle plots per VFAT partition, showing a uniform improvement for the all 24 readout sectors.

4.4.4 Further trimming results and considerations

To understand the relations between the noise level and the applied frontend thresholds, a comparison between the ENC and the single channel thresholds distributions can be made. In Figure 4.30, the two distributions are presented for a chamber that underwent the trimming procedure with $n = 4$. Additionally, the distribution of the ratio between the threshold and the ENC of each of the readout channels is presented.
The threshold improvements introduced by the new trimming paradigm are summarized in the plot in Figure 4.31. The overall average and standard deviation of the applied threshold distributions were derived after applying the trimming at $n = 0, 1, 2, 3$ to a GE1/1 chamber. The average threshold diminishes with larger n values. The threshold standard deviation has its minimum for $n = 0$, since that procedure aligns all the mean values of the response curves. At the same time, though, it remains similar for the other values of the parameter n.
An interesting quantity for the configuration and the operation of the chambers is the ratio between the applied thresholds and the noise value. One the one hand, this parameter confirms

[9]The efficiency plateau normally starts at an equivalent divider current of 690 µA, which is identified as the nominal high voltage working point. The HV working point set in this study is below the one corresponding to efficiency plateau, in order to emphasize the frontend threshold contribution to the detection efficiency.

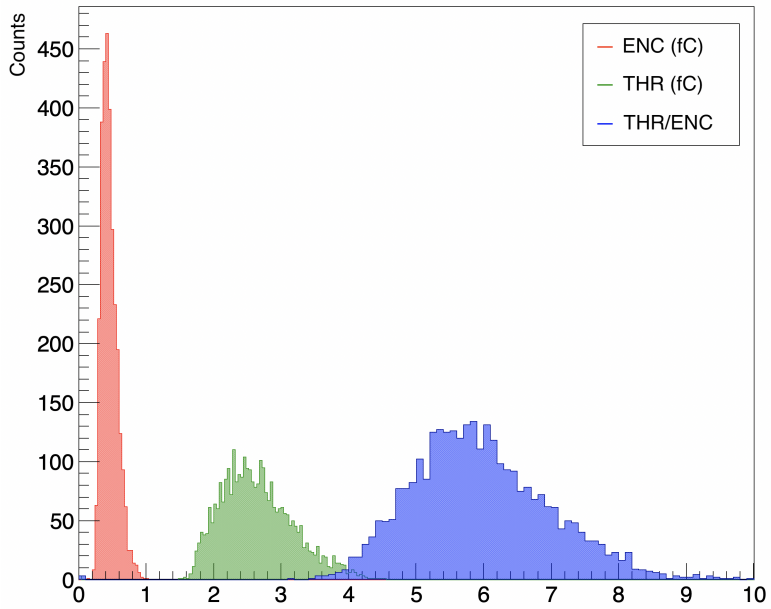

Figure 4.30: Distributions of intrinsic noise (red), derived frontend thresholds (green) and per-channel threshold-ENC ratio (blue) for the 3072 channels of the GE1/1-X-L-GHENT-0022 chamber when the $n = 4$ trimming is performed.

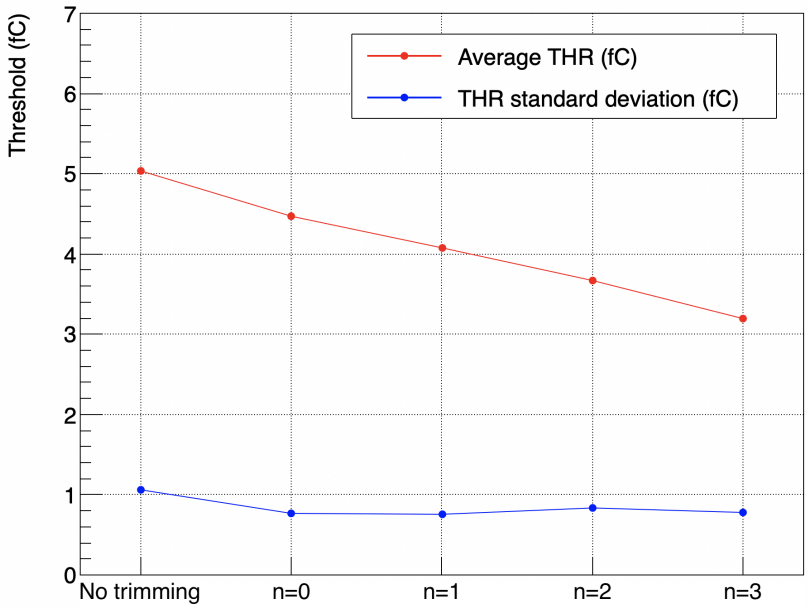

Figure 4.31: Mean and standard deviation values of the threshold distribution of all the readout channels of GE1/1-X-S-INDIA-0017 before and after applying the $n = 0, 1, 2, 3$ trimming procedures (this chamber was not tested for $n = 4, 5$). The average gets lower by increasing the parameter n, while the minimum of the sigma is obtained at $n = 0$, confirming the expectations given by the trimming definition. The error bars are smaller than the symbol size.

the proper threshold assignment and the correctness of the configuration derivation procedures. On the other hand, it allows to make previsions about the thresholds that will eventually be applied by only looking at the ENC values from an initial s-curve scan. The plot in Figure 4.32 has been generated by taking the average value of the threshold-ENC ratio distributions at $n = 0, 1, 2, 3$ for the chamber GE1/1-X-S-INDIA-0017, while $n = 4$ corresponds to the GE1/1-X-L-GHENT-0022 chamber. While the applied thresholds depend on the noise level of each of the detectors, the threshold-ENC ratio is a more general parameter that mostly depends on the n parameter, hence the presence of results of different chambers in a single plot. The average threshold-ENC ratio follows the behavior of the thresholds presented in Figure 4.31, decreasing when n is augmented. The threshold-ENC ratio standard deviation gets lower and lower as well, signifying a better control over the threshold assignment in relation to the actual noise level of each of the channels.

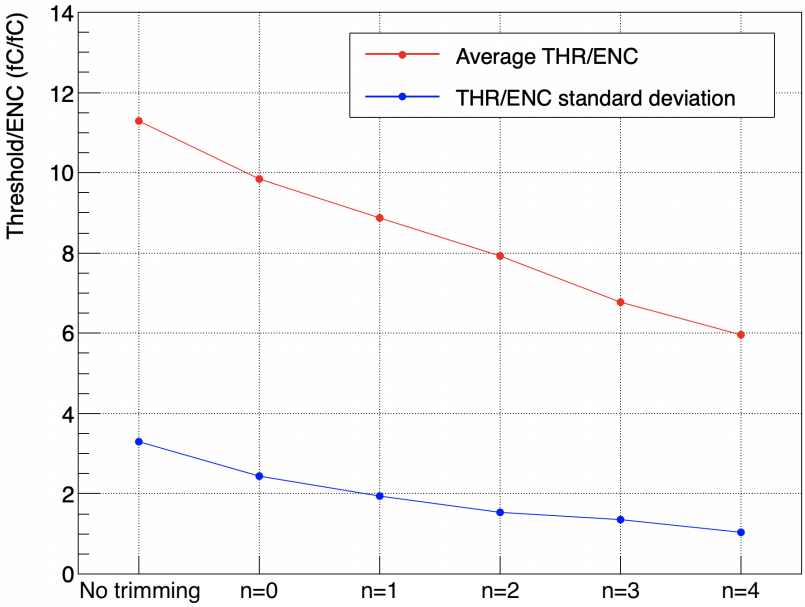

Figure 4.32: Mean and standard deviation values of the per-channel threshold-ENC ratio distribution for the GE1/1-X-S-INDIA-0017 chamber before and after applying $n = 0, 1, 2, 3$ trimming procedures, with the addition of the $n = 4$ results for the chamber GE1/1-X-L-GHENT-0022. Being the ENC almost constant over the different scans, the average follows the behavior of the thresholds, diminishing for increasing values of n.

After having fully explored the reasons and the benefits of the trimming procedure, it becomes natural to justify the cuts applied in the QC7 electronics test introduced in section 4.3.4. Fixing the accepted noise rate per readout sector to 100 Hz, the average VFAT thresholds result to be around 6 times the intrinsic noise value. To get most of the channels thresholds below 5 fC for each of the VFATs installed on a chamber, the derived requirement is to have the average ENC below 0.7 fC. Moreover, since the response of each channel can be adjusted in the range ± 2.1 fC from their original value, a "hot channel" cut at the ENC value of 1.5 fC guarantees a good balance between the possibility of trimming with $n = 4$ and the number of masked channels.

4.5 Conclusions on the chamber performance

This chapter presented the performance of the GE1/1 detector components and constituents. The identification of their strong and weak points guided the development of procedures to guarantee the chamber optimal configuration and functioning.
Initially, the gas gain was examined and the average gas gain as a function of the supplied high voltage was assessed. The gain non-uniformity over the chamber area resulted well within the requirement of $\pm 37\%$ expected for GEM detectors with such a large surface area ($\mathcal{O}(0.5\ \mathrm{m}^2)$).
Subsequently, the high voltage stability was studied establishing a new HV training procedure to ensure reliable long term operations of the GE1/1 detectors. The chamber trip rate was diminished to one every few days when the HV is set to the nominal working point (average gas gain of ≈ 20000).
Finally, the on-chamber electronics was scrutinized analyzing the frontend thresholds and their minimization. A new trimming method allows to uniform the channel response and to reduce the applied VFAT thresholds by around 40%. The procedures developed for the threshold determination circumvent the electronics shortcomings, providing an optimal frontend configuration.

The gas gain characterization, the high voltage stability and the optimized frontend electronics configuration will be essential in the evaluation of the GE1/1 particle detection performance, which is the subject of the next chapter.

Chapter 5

The GE1/1 detection performance

The chamber tests introduced in the previous chapter serve as a foundation for operations in their full final form. All the verified single components can play their role in amplifying and recording the signals generated by the interacting ionizing particles.
This chapter presents the final GE1/1 validation test before the installation in CMS, which determines the detection efficiency, the spatial resolution and the hit cluster size. The main question to be answered is whether the chamber properties satisfy the requirements set for the GE1/1.
The first section exposes the experimental apparatus and the methodology utilized to investigate the principal detection properties. The technical and design choices for the test are explained, together with the analyses performed on the collected data.
In the following section, the efficiency results are presented, highlighting the found issues and the applied mitigations and solutions.
Finally, the properties of the hits are examined. Their spatial resolution and the cluster size represent the main parameters that allow for an effective contribution of the GE1/1 detectors in the CMS endcap trigger and in the reconstruction of the muon trajectories.

5.1 The experimental apparatus: the cosmic ray stand

All the GE1/1 validation measurements are conducted using the *GEM cosmic ray stand* installed at the CERN GEM laboratory, which utilizes the cosmic rays as available MIP particle source.
This section aims to introduce the apparatus, providing a general overview of the system as well as the details that will be essential to interpret the performance results. First, the structure and the conventions are detailed. Then, simulation studies are presented to define the time required for the tests, which is driven by the cosmic muons flux, and to determine the impact of their distribution on the chamber geometrical acceptance.

5.1.1 The structure

The cosmic ray stand has a cubic geometry with dimensions of $200 \times 200 \times 200$ cm^3, which has been designed to maximize the solid angle of acceptance for the cosmic muons. It is constructed using aluminum profiles to create seven layers, as shown in the picture in Figure 5.1.

On the uppermost and lowermost layers, two arrays of plastic scintillators serve as a trigger for the muons traversing the volume of the stand. Five tiles each of the layers are arranged to cover an area of 200×126 cm^2. A logic OR condition is set among the individual layer tiles and a logic AND is applied between the upper and lower layers. The average provided trigger rate is around 95 Hz for the full covered volume.
The GE1/1 detectors are hosted in five rows between the scintillators. Each row is arranged in three columns. Each of the 15 available slots is equipped with adjustable mounting points for both long and short super chambers.
The super chamber installation in the stand takes place from the front. The long detectors are inserted with the readout boards facing upwards, while the short ones are mounted the opposite way. This is due to the positioning of the mounting points required for the installation in the CMS endcaps. The pivot pin on the narrow side of the detectors is hosted on a square panel that slides on a rail. The wide side of the trapezoid gets aligned to the front of the stand, which facilitates the connection of the services to the patch panel.

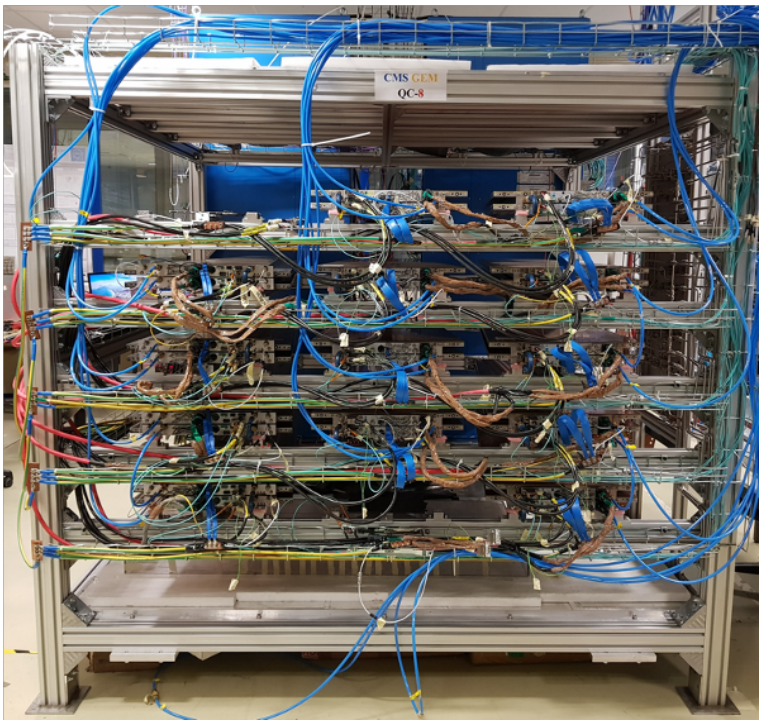

Figure 5.1: Picture of the GEM cosmic ray stand in the CERN GEM laboratory.

5.1.2 The conventions

The naming and numbering conventions of the stand are shown in Figure 5.2. Row 1 is the lowest, and Column 1 corresponds to the leftmost one. Each slot is referred to as '$Row\#/Col\#$'. The addition of '$/\{T, B\}$' (*Top,Bottom*) specifies the single chamber in the super chamber. In CMS the bottom chamber is called 'Layer 1', which faces the interaction point, whereas the top is 'Layer 2'. Whilst all the hardware and the services follow the general mapping, the offline analysis software uses a simpler convention to label the individual chamber positions. The bottom left

position starts with number 0 and the top right is number 29.
All the other numbers appearing on the Figure will be clarified in the following paragraph, when describing the services.

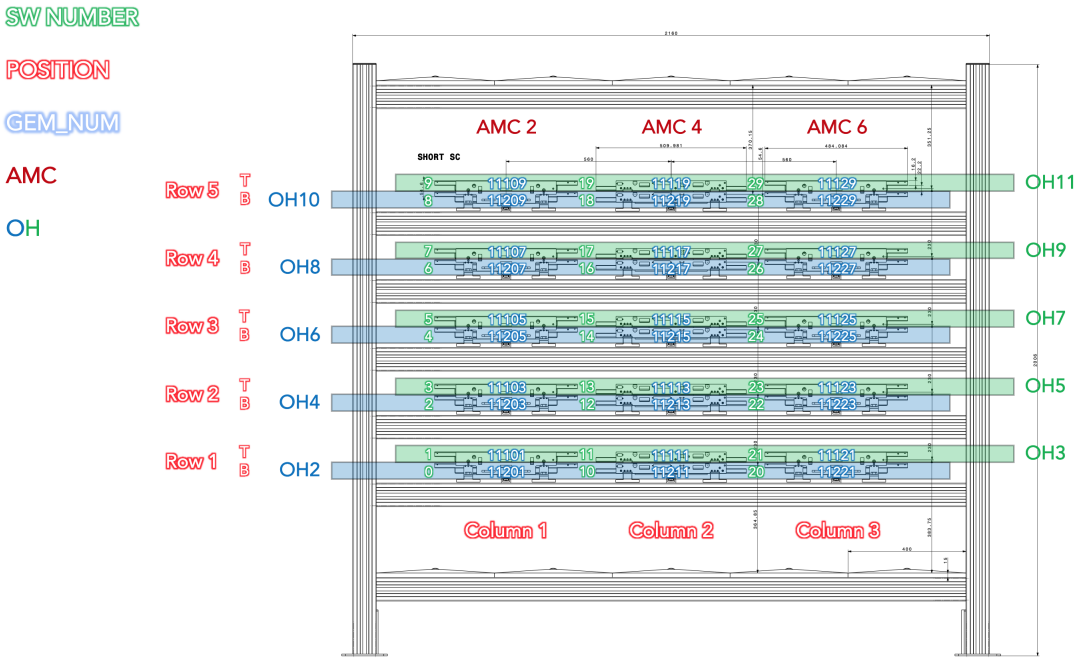

Figure 5.2: Naming and numbering conventions of the GEM cosmic ray stand.

The global coordinate system adopted for the cosmic ray stand is presented in Figure 5.3.
The local coordinate system for each of the chambers has its origin in the center of the trapezoidal area. The chamber surface defines the x-y plane. The x-axis is aligned to the bases of the trapezoid; the y-axis is parallel to η. The local z-axis is normal to the chamber surface.
The definition of the rotation and the translation parameters originates from the global coordinate system. The names attributed to those parameters are shown in Figure 5.3.

5.1.3 The services to the stand

The services required for the GE1/1 operations are provided to each of the stand slots. They are designed as similar as possible to the ones installed in the CMS experiment, with additional flexibility to accommodate the special requirements of a validation test. The hardware of the services is arranged in two racks at the rear of the stand. The HV and LV cables run on the left side from the back to the front of the stand. The gas and cooling pipes and the readout fibers are routed on the right side.
Every system will be briefly presented in the following paragraphs.

The gas system

The gas system of the cosmic ray stand is design to supply the Ar/CO_2 (70/30%) gas mixture to the 15 slots with individual lines. Each line is equipped with a manual flow-controller and a

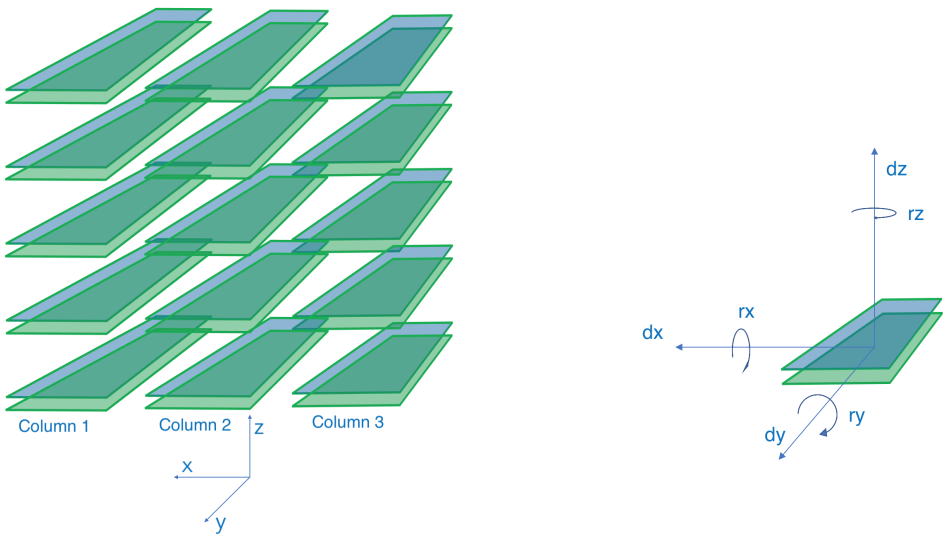

Figure 5.3: Global coordinate system of the GEM cosmic ray stand. On the left the x-y-z axes are represented, while on the right side the naming conventions for translations and rotations are shown.

particle filter (5 µm). The return flow is monitored with a rotameter. In normal operations, the gas flow is set to about 3 l/h for each of the lines in use.
It is worth to mention that there is a substantial difference in the gas system between the cosmic ray stand and CMS. In the lab, each super chamber is fed with a gas line and the two individual chambers are interconnected with a u-shaped plastic pipe. In the final configuration, instead, Layer 1 (or Layer 2) of six consecutive super chambers will be connected in a single chain. The overpressure caused by the load on the line seen by each detector is therefore different in the two setups.
An additional line of pure air has been introduced for the cosmic stand. This is used only in presence of a GEM foil short circuit in order to ease the fix (more about this in section 4.2.4).

The low voltage system

The low voltage system of the stand is similar to the one in CMS. It is composed by a mainframe with a branch controller board (CAEN A1676A), a MAO power supply and five low voltage CAEN A3016 boards (2 'HP' and 3 standard[1]) installed in an EASY3000 crate. Each board powers the three super chambers installed in one row of the stand. The cables and the connectors are in the exact form factor as the final one.
The usual operating voltage is 7 V, which is 1 V lower than the LV provided in CMS. The difference comes from the type of low voltage boards employed in the cosmic stand setup. The standard CAEN A3016 boards cannot provide more than 8 V, which is not sufficient to operate at 8 V while compensating for the voltage drop in the cables. Anyway, no variations in the

[1]The use of standard (non-HP) CAEN A3016 originates from the boards availability in the CERN GEM lab. Indeed, it was preferred to prioritize their installation in the experiment, and employ the spares in the cosmic ray stand.

performance are foreseen due to the 1 V gap: simply, the current absorbed by the FEASTs is expected to increase by around 12%. This has been confirmed by the values registered during the tests.

The high voltage system

The high voltage system of the cosmic stand serve both the GE1/1 chambers by nine CAEN A1515TG stacked-HV boards, and the photomultipliers that readout the scintillators by two CAEN A1526N HV boards.

The distinctive characteristic of the HV system of the stand is the capability to power each GE1/1 chamber independently. On the contrary, in CMS, each super chamber receives a single HV supply, hence the need to match the gas gain performance when coupling the chambers into super chambers.

The additional flexibility introduced during the validation in the lab allows for fine adjustments in the individual working points.

The Detector Control System

The three aforementioned systems are controlled by a unified Detector Control System (DCS), which has been developed by the GEM DCS experts in a similar fashion as the final version for the CMS operations.

The DCS of the cosmic ray stand allows to control and monitor both the LV and the HV hardware that power the chambers and the scintillator PMTs. It is also capable of checking the environmental parameters and the status of the gas mixer. In case of abnormal situations, it is programmed to react preserving the integrity of the detectors and re-establishing the correct conditions for smooth operations, while sending notifications and alarms.

One of its main features is the possibility to set the HV working point of the chambers through an *equivalent divider current*. The DCS then calculates and provides the voltages to the eight electrodes of the chambers as the resistive high voltage divider utilized in the gas gain tests would do.

Additionally, a feature to ease the HV training procedure has been introduced. This feature complements the previous one with the option to rescale the voltage of each of the electrodes by a percentage of the nominal one. It makes possible to set the global working point through an equivalent divider current value, and to keep the induction gap turned off.

The final and most important feature of the DCS is auto-restart of the HV. This feature ensures continuous and reliable data taking during the cosmics runs. When a trip is detected, the DCS automatically turns on the affected chamber again, setting it at the original working point. This usually happens a few times per day when the stand is full and after the chambers have undergone a complete HV training (more details about HV instabilities in section 4.2).

The cooling system

As in CMS, the coolant employed in the cooling system of the cosmic ray stand is water at around 16°C. There is major difference between the two setups, though. In the experiment the water is pumped with an overpressure of around 9 bar; in the lab, instead, the cooling system is

designed to work below the atmospheric pressure. This is meant to reduce the chance of having water insinuating in the chambers in case of any leak during the tests. In addition, the frequent exchange of detectors on the stand can be performed safely and harmlessly.

The trigger system: scintillators and electronics

A total of ten scintillating plastic tiles are arranged in two layers covering the top and the bottom of the stand. Both the scintillators and their photomultipliers come from past experiments and were repurposed for the cosmic ray stand.

Due to their age, the performance of the scintillators in terms of efficiency and time jitter are not optimal, but sufficient to provide a reliable trigger. The theoretical total rate considering an efficiency of 100% would be of about 120 Hz. In fact, only about 95 Hz are recorded, with rates significantly lower than the average in the top-right and in the bottom-left scintillator tiles, as reported in Table 5.1.

Such inefficiencies could not be corrected acting on the present hardware, because it was already operated at the maximum attainable performance. It was also deemed not necessary to replace the old components with new ones, since the GE1/1 validation results are not affected by the trigger system efficiency.

TS1	TS2	TS3	TS4	TS5
25.29 ± 0.11	24.55 ± 0.13	25.10 ± 0.16	25.99 ± 0.09	8.31 ± 0.02

BS1	BS2	BS3	BS4	BS5
7.06 ± 0.06	20.55 ± 0.09	13.05 ± 0.16	19.57 ± 0.11	17.97 ± 0.09

Table 5.1: Average recorded hit rate per scintillator tile in Hz units. TS stands for Top Scintillator, BS for Bottom Scintillator. The tile #1 (#5) is located on the left (right) of the cosmic ray stand.

The data acquisition system

The DAQ system employed in the cosmic ray stand is a scaled down version of the one present in the CMS experiment, except the trigger path, which is not present in the stand.

The backend electronics consists in a µTCA shelf equipped with one MCH, one AMC13 and three CTP7s (AMCs), see section 2.5.4.7. Each CTP7 communicates with a column of detectors, hence the labels *AMC2,4,6* in Figure 5.2 in correspondence to each of the columns. In the cosmic stand, every card serves ten GE1/1 single chambers, utilizing the optical links from 2 to 11, while leaving 0 and 1 empty. This is represented in Figure 5.2 by the *OH* number. The optical links are also referred to as OptoHybrid number due to the univocal correspondence between a chamber and its OH, to which the readout fibers are connected.

When cosmics data are taken, one of the tasks of the AMC13 card is to receive and distribute the trigger coming from the scintillators. After a trigger signal comes, the data are requested and collected from the VFATs through the OptoHybrids and the CTP7s. They are then packed together in the AMC13 and sent to a computer, which eventually writes the data in a local disk.

The very same hardware setup is also in use for taking the scans that check the channels response, perform the trimming, determine the thresholds and derive the final electronics configuration for the quality control tests (chapter 4).

5.1.4 Cosmic muon distributions

Before to start the GE1/1 validation tests, simulations have been performed focusing on the expected muon angular distributions. From the polar plot shown in Figure 5.4, one can see that the ϕ angle around the z-axis of the stand has a uniform distribution, while the θ angle with respect to the same axis follows a $\cos^2(\theta)$ distribution (at the leading order).

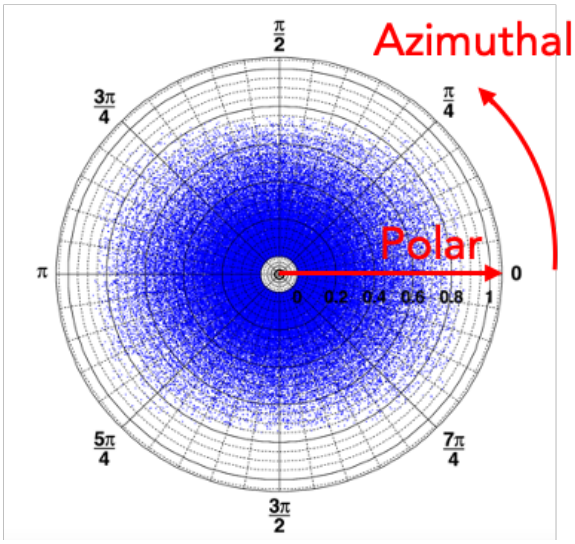

Figure 5.4: Simulated angular distribution of cosmic muons including the trigger acceptance of the cosmic ray stand.

Starting from the general angular distributions, it is possible to include the effects given by the acceptance of the scintillator volume. The results are shown in Figure 5.5 for both ϕ and θ angles. The flatness in ϕ gets deformed by rectangular surface covered by the trigger layers, and the θ is limited to at most $\approx 50°$.
Moving from the ideality of the simulations to the real stand, the inefficiencies of the trigger system have repercussions on the recorded muon track angular distributions. Indeed, since the top right and bottom left scintillators register a lower rate, they give rise to an asymmetry in the $x-z$ plane angle. An example can be seen in Figure 5.6. The angular distribution in the central column is centered at 0 and symmetric, suggesting a proper functioning of the scintillators in that region. Oppositely, in Column 3 the distribution is shifted towards positive angles, in agreement with the non uniformities in the rate recorded by the scintillator tiles.

5.1.5 Technical choices for the operations and analyses

Even with a defined structure of the cosmic ray stand frame, the arrangement of the super chambers in the slots is still to be defined. The main established targets are the maximization

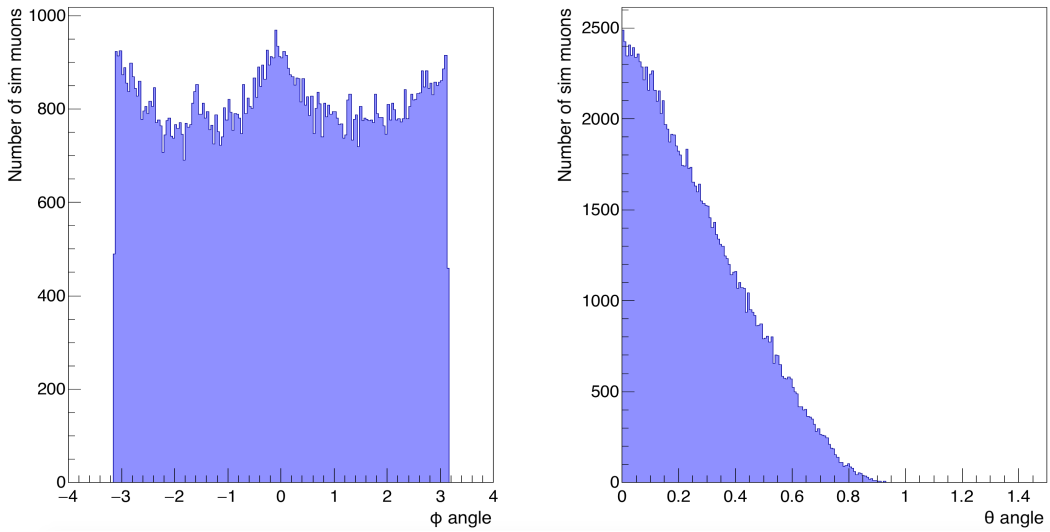

Figure 5.5: Angular distributions of simulated cosmic muons, after the acceptance of the cosmic ray stand trigger system has been included.

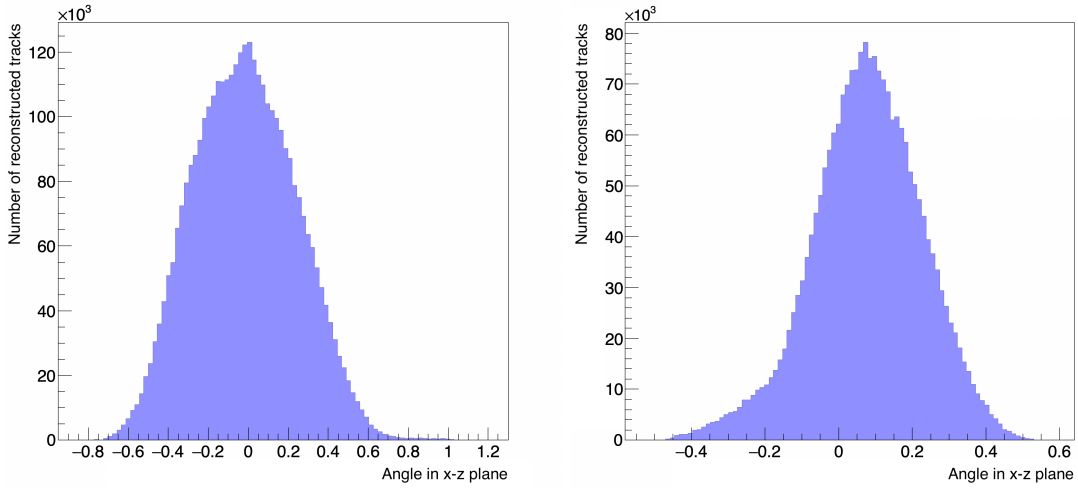

(a) Symmetry in the $x - z$ angle of the column 2 tracks

(b) Asymmetry in the $x - z$ angle of the column 3 tracks

Figure 5.6: Impact of the inefficiencies of the scintillator tiles on the recorded muon track angular distributions in a cosmics run. The distribution in Column 2 is symmetric, while in Column 3 it is shifted towards positive angles.

of the stand versatility, the ease of the detectors installation, the maximization of the collected statistics and the impact on the data analyses.

Inconvenient super chamber dispositions in the columns can be excluded by pure geometrical consideration about the detectors readout board design and the fact that the hits are defined as located at the center of each strip.

For instance, a defined constraint is to have the same type of detectors in each column. It is possible to choose the type of chambers to be inserted in every column, but no mix is allowed. The reason for it can be visualized in the drawing in Figure 5.7. In presence of mixed types, a

reconstructed muon track might be propagated inside the active area of a chamber even if the real particle was passing outside. Such false negative cases would have an impact on the efficiency calculation and have to be avoided. No fiducial area can be established without excluding an entire iη partition, which would not allow to test it.

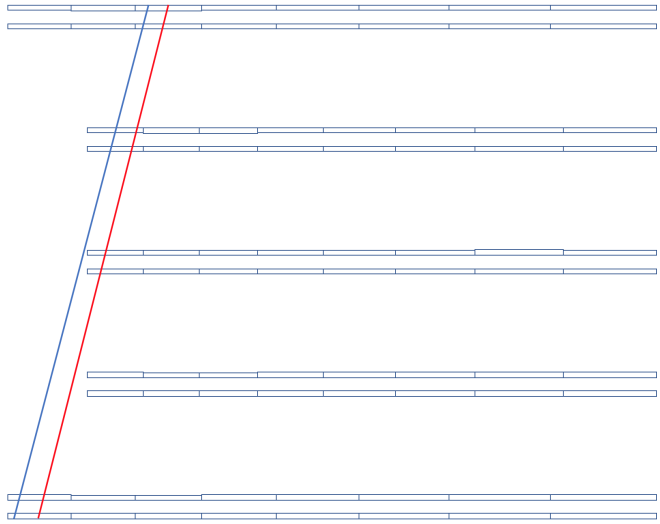

Figure 5.7: Visualization of the reason for an efficiency bias given by different types of detectors in the same column (y-z plane view). Each blue rectangle represents one iη partition. The blue (red) line represents the real (reconstructed) cosmic muon track. Such logic led to the constraint of having the same type of chambers in the same column.

Even with the same type of detectors in a column, a small geometrical effect is present that affects the efficiency calculations in the data analyses. The intrinsically limited resolution along the η-axis might lead once again to false negative cases, if no special requirement on the analyses are applied. A simple correction is represented by the requirement to the tracks to pass through the top and bottom chamber layers.
Still, this technique cannot be always applicable. When testing the top or the bottom chambers, the reconstruction performed with the hits on the other layers still presents a bias on the edges, as in Figure 5.8. Given the cosmic muon angular distributions, the estimated efficiency loss in the sectors i$\eta = 1, 8$ is around 1.5%, with some variations depending on the number of super chambers in the column and their arrangement.
The coarse η-segmentation of the chamber readout has one more consequence on the analyses. As depicted in Figure 5.9, it is necessary to check the presence of hits in a window of three iη partitions around the reconstructed track to cover all the possible real trajectories that could correspond to the reconstructed one.

A last set of simulations has been performed to optimize the configuration of the detector slots. Their target was to find the arrangement that minimizes the time needed to complete the detection performance assessment tests. Some examples are shown in Figure 5.10. Simulations of different geometries were performed keeping the total number of events constant, and counting

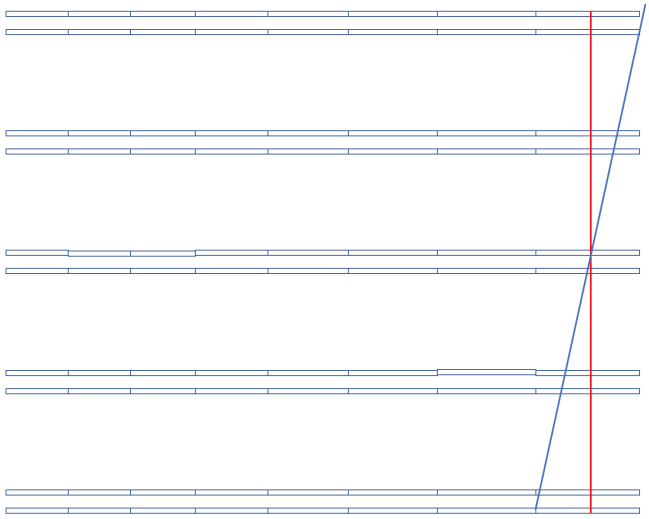

Figure 5.8: Visualization of the reason for an uncorrectable efficiency loss in i$\eta = 1, 8$ of the top and bottom chambers of each columns (y-z plane view). This is due to the wide segmentation of the readout plane along the η direction. The blue (red) line represents the real (reconstructed) cosmic muon track.

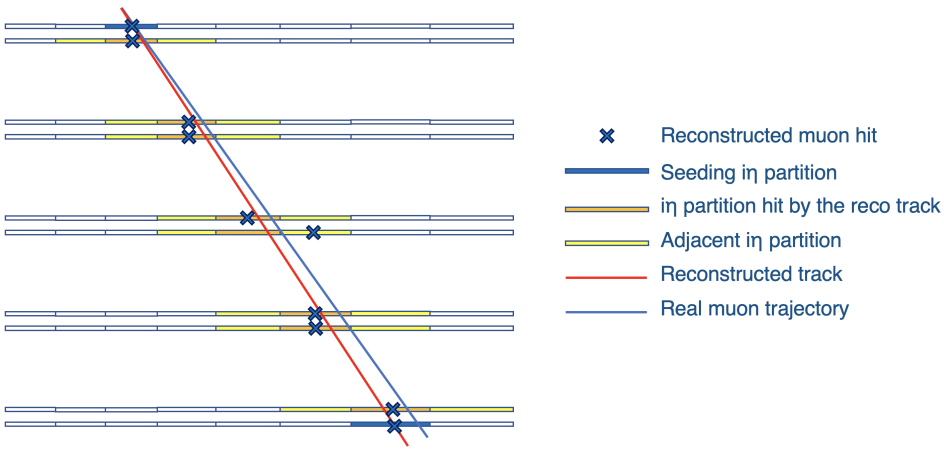

Figure 5.9: Visualization of the need to check the presence of hits in three adjacent iη partitions to properly reconstruct a cosmic muon track and correctly calculate the efficiency. The muon hits (blue crosses) are reconstructed at the center of the iη partition. The blue iη partitions drawn in the top and bottom layers correspond to the starting point of the track reconstruction (seeds) and they are fixed. While the reconstructed track (red line) passes through the orange iη partitions, the corresponding real muon trajectory (blue line) also traversed one yellow iη partition. Hence, the need to check the presence of hits in the iη partitions adjacent to the orange one.

the hits in every chamber readout partition. Even if some peculiar geometries could provide improvements in the statistics of up to 10% with respect to the standard parallel columns, they were far less practical in terms of super chamber installation and connection of the services, therefore they have been deemed not worth to be adopted.

The selected geometry is the three-parallel-column arrangement with 56 cm spacing between their centers. The provided clearance between chambers in different columns allows to easily install the super chambers, while maintaining the required time for validation within the limit of a few days. Details on the calculated time for each of the runs in a high voltage scan with fixed precision on the efficiency are presented in Figure 5.11.

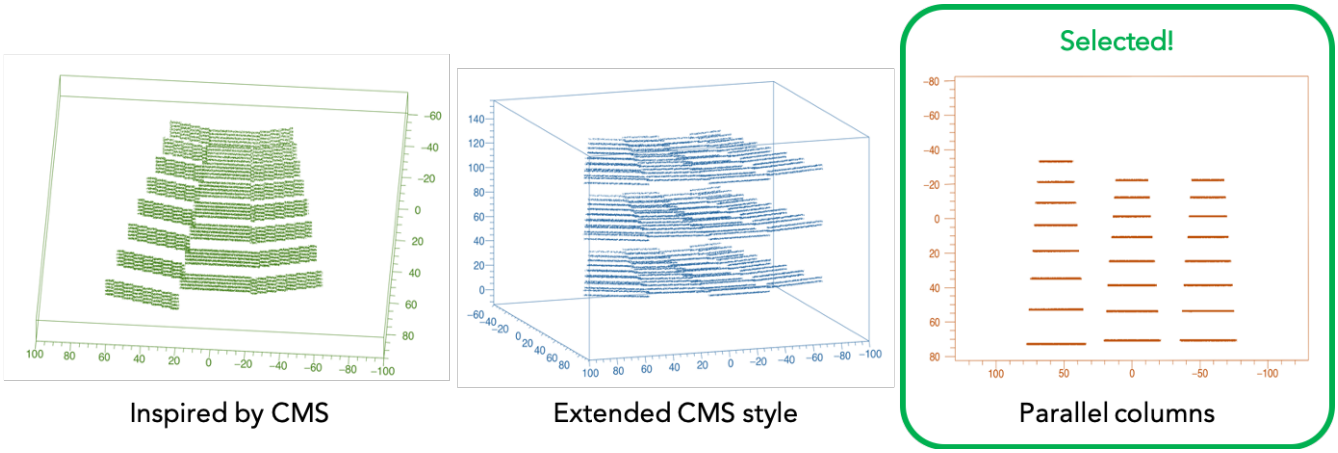

Figure 5.10: 3D representations of the different simulated geometries during the optimization study.

Efficiency	Error Efficiency (%)	# events needed (Million)	Time for each run (h)
80%	1.5%	2,95	9,1
90%	1%	2,94	9,1
95%	1%	1,78	5,5
98%	0.75%	1,73	5,3

Figure 5.11: Estimation of the time required for the GE1/1 validation to allow for a fixed precision on the efficiency of each readout partition. The considered efficiency values are used to calculate the required statistics. The time has been computed using a realistic trigger rate of 90 Hz. The results in this table provided the minimum data acquisition time for each of the cosmic ray stand runs, which consequently usually lasted for 12 hours.

5.2 Data taking at the GEM cosmic ray stand

The first step towards the super chamber validation is to align in time the GE1/1 hits and the trigger signals. This is accomplished by setting the latency of the frontend electronics.
As detailed in section 2.5.5.4, the latency refers to the number of BXs of delay of the processed signals with respect to the incoming trigger. The value stored in the VFAT *CFG_LATENCY* register indicates where to look for interesting data in the VFAT SRAM1 buffers.
The delay only depends on the electronics processing time and the length of the readout fibers, which are the same for all the GE1/1 slots of the stand. Moreover, the MIP time-of-flight between Row 5 and Row 1 amounts to 3 ns, which is negligible compared to the duration of the VFAT

digital signals of 100 ns set for the test. Therefore, only one latency scan test was needed at the beginning of the operations. The test is performed recording the number of hits in the chambers for increasing latency values. A peak in the counts indicates the proper timing. The adopted value is the center of the peak extracted from distributions like the one in Figure 5.12. The provided example refers to one of the chambers under test; the results are compatible among all the stand slots.
The assigned value to all the VFAT *CFG_LATENCY* registers during the validation tests is 62.

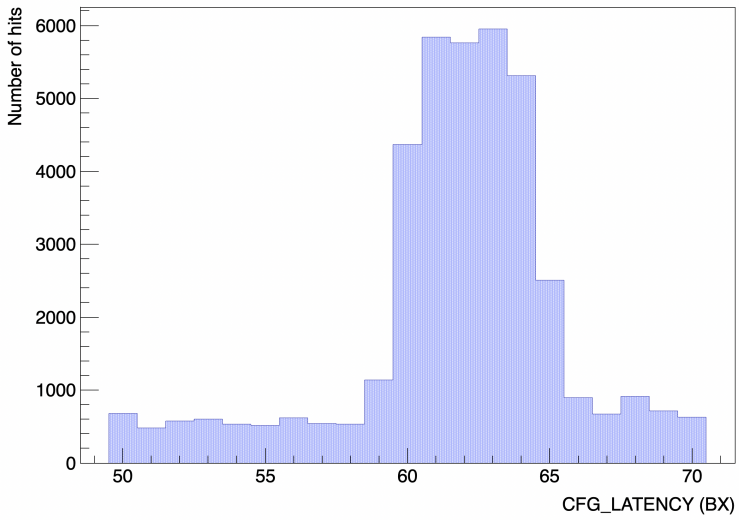

Figure 5.12: Typical output plot of a latency scan performed at the cosmic ray stand. The scanned latency values are plotted on the x-axis, while the number of recorded hits in the 24 VFATs of one chamber under test are on the y-axis. The peak structure indicates the presence of hits correctly timed in with the trigger signal. The central point of the peak defines the optimal latency value (62). The width of the peak is given by the set pulse stretch (4 BXs). The hits outside the peak correspond to noise.

After setting the appropriate latency, the super chamber validation process can start. The procedure foresees a series of runs to characterize the chamber efficiency performance as a function of the applied high voltage. The final target is to determine the shape of the *Efficiency vs HV* curve, the efficiency value at the plateau and the plateau starting point. The HV interval of interest has been extracted from the past experience with GE1/1 prototypes and refined over time.
In the first validation runs, a common value for the average gas gain was set and scanned in the range $[12000 - 21000]$ for every detector under test.
After a few sets of scans, the scanned parameter was changed in favor of a common high voltage working point, set through the equivalent divider current. This parameter is easily applicable to all the detectors in the stand and it gives a better representation of the performance (more in section 5.3.6.3). Moreover, a proper evaluation of the chamber pairing can be done: if the efficiency plateau starts at a similar equivalent divider current (within 10 µA) in the two layers of the super chamber, the match is correct. In the opposite case, a rearrangement can still be performed in the lab, before the installation in CMS.

An *Efficiency vs HV* scan is commonly composed by five runs, in which the equivalent divider current is varied between 660 µA and 700 µA in steps of 10 µA. In most cases, the 700 µA working point does not provide additional information on the detector behavior; it is then skipped or commuted in favor of a lower HV value. This preserves the chamber integrity, keeping them from the unnecessary stress introduced by high values of gas gain.
The final optimized procedure for the GE1/1 validation foresees the following steps:

1. The IDs and the positions of the super chambers present in the stand are stored into the GEM database, utilizing the web interface in Figure 5.13;
2. The configuration of the chamber electronics with optimal values is performed as described in chapter 4;
3. A final set of s-curves with test pulses is taken to derive the thresholds in charge units for each VFAT;
4. The first HV working point is set through the DCS, normally the highest in the scan;
5. All the settings are recorded into the, so-called, *RunInfo* files to be used in the analyses;
6. The frontend is configured without applying any mask for hot strips;
7. The run is taken, ideally for around 12 hours;
8. The following HV working point is set;
9. The last four steps are repeated for all the runs in the scan.

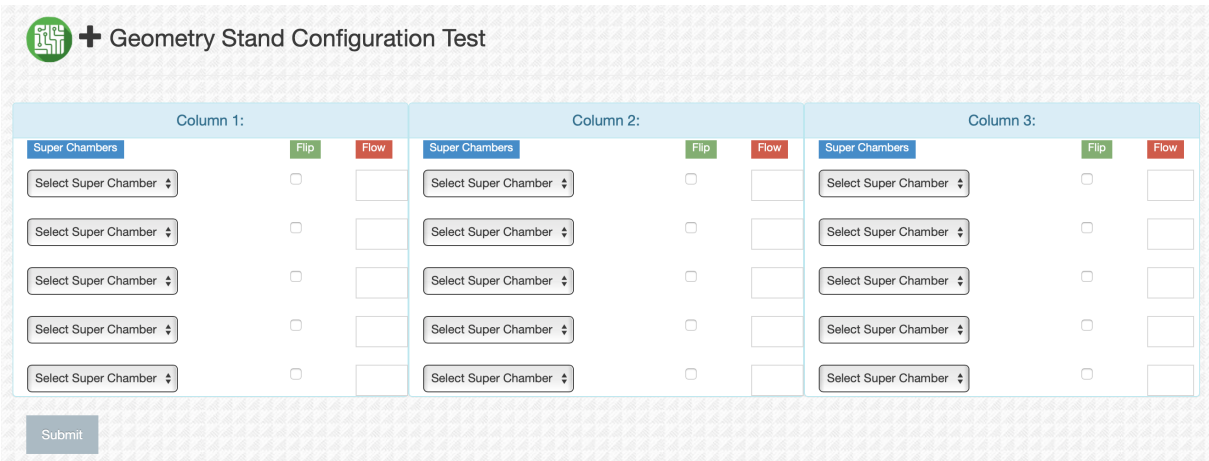

Figure 5.13: Web database interfaced to store the chamber positions and IDs installed in the cosmic ray stand at a given moment in time.

5.3 Detection efficiency

The main parameter under investigation in the GE1/1 chamber validation is the detection efficiency. It is defined as the fraction of detected particles out of the ones that cross the active area. In the GE1/1 chambers, the numerator then depends on various factors, as:

- The number of primary and secondary electrons produced in the ionization;
- The chamber gas gain;
- The time width of the signals induced on the readout strips compared to the electronics integration time;
- The number of strips involved in the avalanche (cluster size);
- The signal amplification and integration in the VFAT;
- The readout channel thresholds.

The assessment of this performance figure defines the eighth - and final - step of the quality control tests (QC8). While the previous QC steps concentrate on specific quantities that depended on the individual components, the QC8 evaluates the GE1/1 detectors as a whole, making it the most complete test.

5.3.1 QC8: the efficiency test with cosmic rays

The targets of the QC8 are:

- Check the functionality of all the chamber components and their integration;
- Monitor the mid-term stability of the chamber foils and of the on-chamber electronics ($\mathcal{O}$(2 weeks));
- Study the tracking capabilities of the chambers;
- Provide efficiency measurements with cosmic ray muons;
- Verify the compliance to the requirements.

The global requirement for a super chamber to pass this quality control is an average efficiency of each of the two layers greater than 95%. In some special cases, however, the criterion was slightly adapted. This applied to the validation tests that took place when the threshold optimization and the final high-voltage training procedures were not yet in place. For around 30 chambers, the minimum target was then set to an average efficiency of 90% when operating at the highest stable HV working point. The efficiency plateau was yet to be reached and there was an ample margin of improvement.
The efficiency of all the chambers will be finally assessed in the GE1/1 commissioning phase in the CMS experiment. The QC8 results will then serve as a reference point, to compare the behavior in the two environments and give the possibility to trace back any potential misbehavior.

5.3.2 The data analyses

The analysis package of the GE1/1 cosmic ray test has been developed within the version 10_6_0 of the CMS software framework (CMSSW). The framework allows an easy interface to the data, and it provides embedded detector descriptions and some specific modules for fitting the tracks. The geometry description files were adapted to match the stand structure, whereas the GEM data unpacker and the GEM hit reconstruction modules were taken from the official CMSSW

distribution. The unpacker reads the raw data stream of each recorded event, extracting the single strip hits (*digis*). The standard hit reconstruction was applied, which checks the presence of contiguous digis, and groups them into clusters (recHits). The recHits have several attributes, which include the position in local and global coordinates and the cluster size. Since the readout is digital, the spatial information assigned to the recHits derives from a uniform distribution over the width of the clusters. In the analyses, the recHits are considered valid if their cluster size is ≤ 10 strips[2].
The rest of specific analysis items, including the track reconstruction, had to be built from ground up.

Every element of the analysis structure will be detailed in the next paragraphs and represented with block diagrams.
The initial steps are dedicated to the identification and the compensation for all the possible sources of efficiency losses intrinsic to the chambers or to undesired events in the operations. In the last steps the efficiency is calculated with two different methods: a fast one, only considering the hits within a super chamber, and one based on the muon track reconstruction.

The first analysis step is the ***Identification of hot and dead strips***. A block diagram in presented in Figure 5.15.
When the frontend is configured for a cosmic run, the noisy strips don't get masked in order to reduce any possible bias. In addition, in the validation tests, the detector configuration information is not passed to the analysis code. Consequently, an identification of both hot and dead strips is performed in the analysis. This allows to mask them during the hit reconstruction and remove the noise hit contributions in the track reconstruction. Moreover, the hit reconstruction algorithm can account for the masks, including them in the clusters if the strips on both sides have fired.
In this analysis phase, only the digis are considered. Initially, an occupancy hit map is generated, together with the distribution of the total number of digis per strip for each single detector under test. A Gaussian curve is fitted to the distribution and the mean (μ) and standard deviation (σ) are extracted.
If a strip records zero digis over the entire run, it is marked as dead. A strip is labeled as noisy (hot) when the number of registered digis is larger than the value of $\mu + 5 \times \sigma$: an example is shown in Figure 5.14. It has been verified that $5 \times \sigma$ allows not to exclude any normally behaving strip, which just happens to be in the tail of the occupancy distribution.
In the CMS operations, the status of the readout channels will be re-evaluated and subsequently monitored both in the frontend configuration and in the analyses. The masked strip information will be stored in dedicated databases, to be consulted both from the DAQ and the reconstruction codes.
The second analysis step is the ***Event certification***. A block diagram in presented in Figure 5.16.

[2]The requirement on the maximum cluster size comes from the muon signal cluster sizes obtained in the simulation studies.

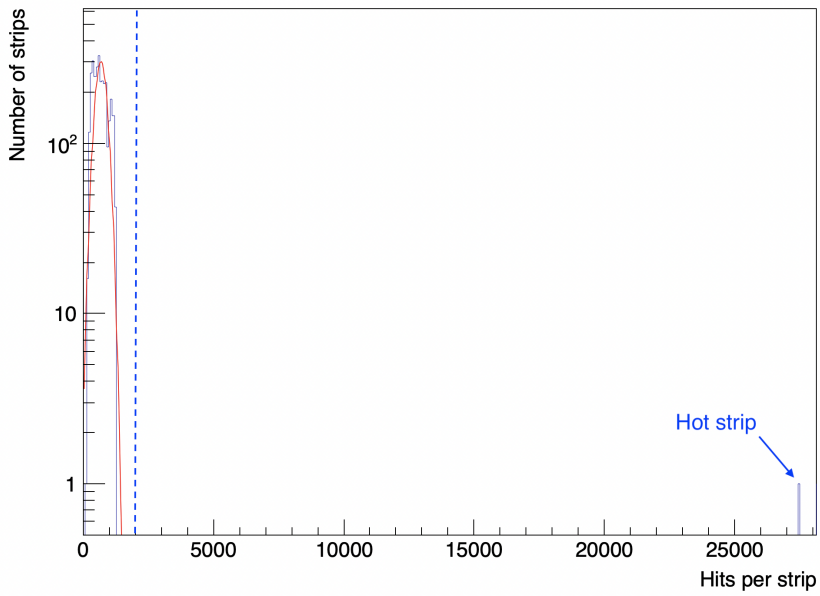

Figure 5.14: Example of hot strip identification plot for the chamber GE1/1-X-S-BARI-0004 in a cosmic ray stand run. The mean value (μ) of the Gaussian fit (in red) is 641 ± 7 hits per strip, the standard deviation (σ) is 270 ± 7 hits per strip. The threshold value to identify a hot strip (dashed blue line) is set to $\mu + 5 \times \sigma = 1991$ hits per strip. One strip has been marked as hot.

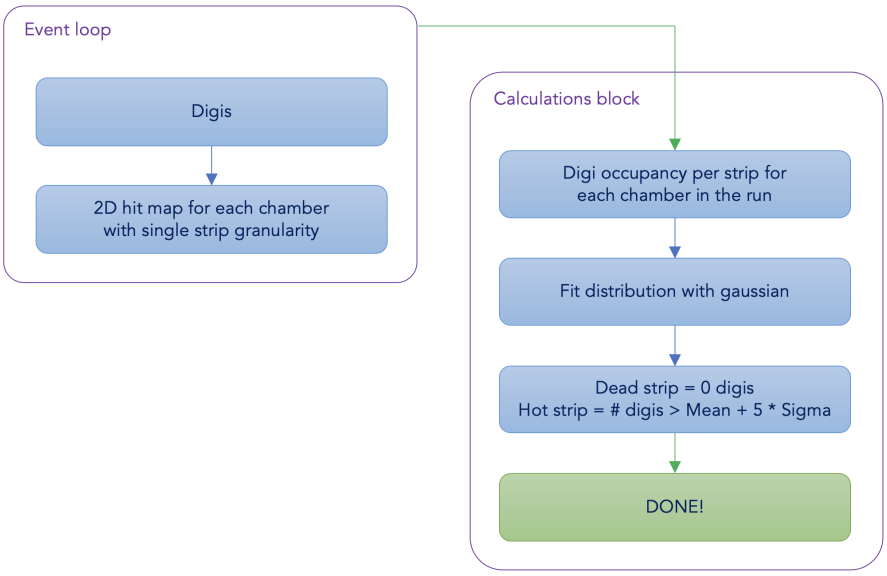

Figure 5.15: Block diagram of the hot and dead strips identification analysis.

During the 12 hours of a typical cosmic run, it might happen that one or two out of the usual 20 chambers under validation experience an high voltage instability. Such behavior is normal, especially in the initial test phases; after a few days of burn-in with HV constantly applied, the rate of instabilities reduces down to an average of less than one per run. If scaled to the CMS chambers number, this would give one trip every couple of hours in the entire GE1/1 subsystem, which is acceptable.

When an instability is detected, the power supply trips turning off the HV. While the detectors are off and being ramped up, they are not able to detect the incident muons. Therefore, those events would lead to a biased calculation of their efficiency. The event certification analysis step is meant to eliminate the aforementioned bias.
The time match between a triggered event and an HV event recorded by the DCS is very intricate. Therefore, a data-only approach has been chosen.
When the high voltage is not at regime, only a very limited amount of hits generated by the intrinsic noise is recorded. The strategy adopted is then to count the number of hits per chamber in blocks of one thousand events, and check if the occupancy ever gets lower than a certain limit. If so, the block is identified as bad for the specific chamber. The bad blocks, the two previous and the two following ones are then discarded in the efficiency computation.
Clearly, the presence of spurious hits would disturb this algorithm, hence the importance of the initial identification of the hot strips.

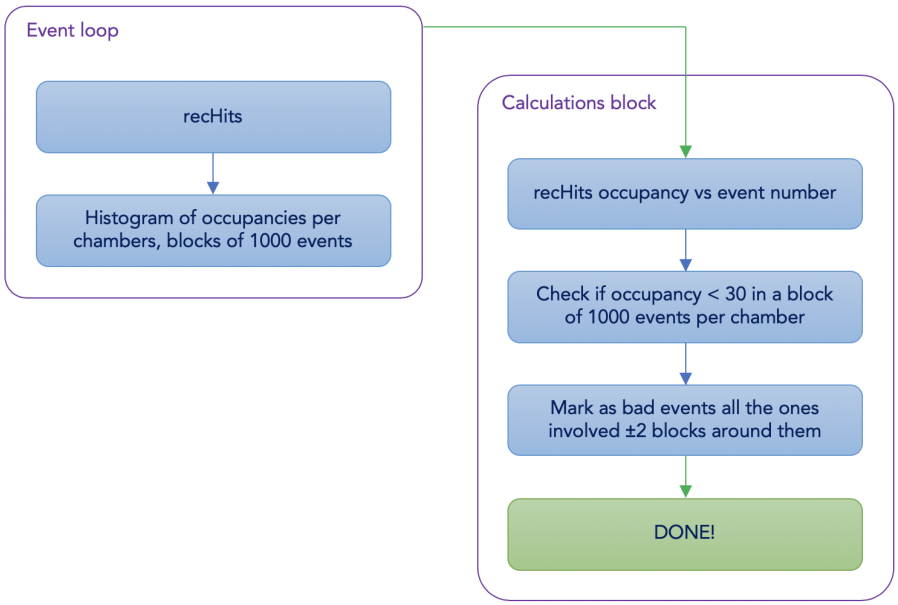

Figure 5.16: Block diagram of the event certification analysis.

The third analysis step is the ***Fast efficiency calculation***. A block diagram is presented in Figure 5.17.
A first rough approach to estimate the GE1/1 chamber efficiency is the so-called fast calculation method. This method does not require much computational power, therefore it results to be a *fast* tool to check the chamber performance even during the data taking. The algorithm analyzes each super chamber separately from the others, considering only the recHits in the two layers. The presence of a hit in one layer translates into an increment of one unit of the efficiency denominator of the other layer. If a corresponding hit is found on the other chamber, its numerator is increased by one unit. The efficiency per chamber is finally calculated by dividing numerator by denominator.

The "reference" hits are selected within a fiducial area that excludes 4.5 cm on the chamber sides, in order to reduce the bias of the geometrical acceptance effects. No cuts can be applied in the η direction without having to exclude a major part of surface of the chambers. This is tolerated in this preliminary computation, since a more precise estimation of the efficiency will come at a later stage of the data analysis.
The intervals around the reference hit to search for a corresponding hit are ± 6 cm along x and ± 1 iη partition. These values were chosen considering the largest possible angles of a triggered muon and the distance between the two layers in the super chambers. The definition of such intervals acts as a noise rejection filter, limiting the introduced positive bias.
The concepts of the 'fast efficiency' have then been refined to increase its granularity, resulting in the *High granularity fast efficiency*. Once again, the two layers act alternatively as reference and test detectors. The active area of each chamber is subdivided in blocks of eight readout strips, corresponding to one sixteenth of a VFAT partition. When a hit is found on the reference layer, its "shadow" is projected on the test chamber. The shadow has a size of ± 6 cm in x and ± 1 iη partition in y. All the blocks that fall inside the shadow receive an increment of one unit in their efficiency denominator. If a hit is found in the test chamber inside the shadow, then all the blocks also have their numerator augmented by one unit. Finally, the efficiency can be computed for each of the blocks or any desired conglomeration of them via the equation 5.1. Often, the efficiency is presented per readout sector.

$$\text{Efficiency} = \frac{\text{Number of test chamber hits within the check window}}{\text{Number of reference layer hits}} \tag{5.1}$$

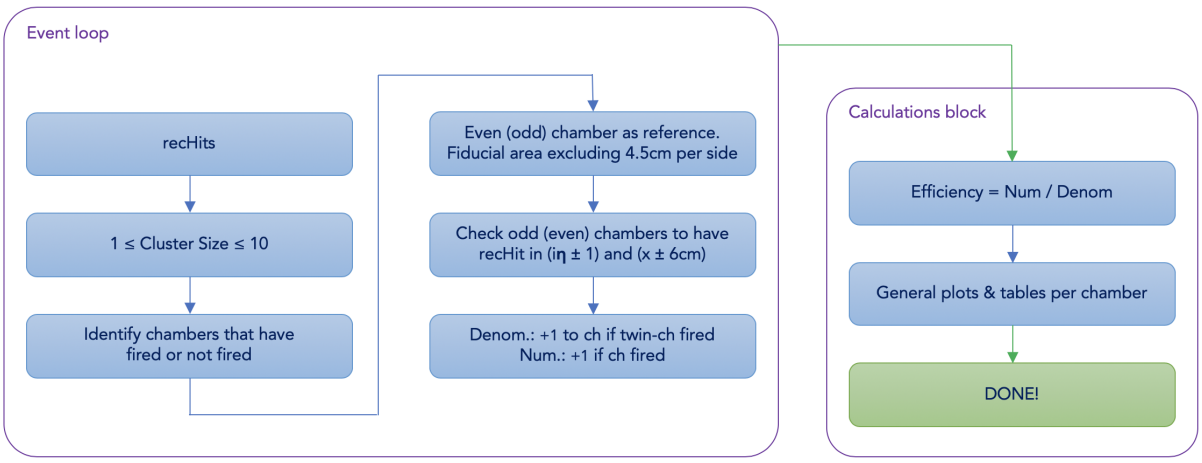

Figure 5.17: Block diagram of the fast efficiency analysis.

The last analysis step is the ***Track-based efficiency calculation***. A block diagram is presented in Figure 5.18.
While a fast calculation of the efficiency is desirable to monitor the status of the detectors along the data taking or when only a single super chamber is under study, a more thorough analysis is needed to precisely evaluate this performance parameter. The method followed in this case is based on the full reconstruction of the muon tracks.

For each recorded event, a loop is performed assigning the role of test layer to a different chamber in each iteration. All the recHits are then collected, excluding the ones recorded in the test chamber in order to avoid any bias. The topmost and bottommost chambers provide the two hits used as a seed for the track reconstruction. An ideal 3D segment is generated for any combination of two seeding hits. Starting from the bottom seed and going upwards, whenever the segment passes through a detector, a window of ± 1.5 cm and ± 1 iη partitions is opened around the segment and any present hit is gathered. The track stub is then computed again, this time with an additional hit. This process continues until it gets to the topmost layer. This technique is commonly known as Kalman filter [93] and it is widely utilized for the track reconstruction in CMS. As a final step, all the gathered hits contribute to the global track fit (smoothing). The smoothed track is required to have at least four associated hits. This allows for an adequate precision of the track and a good rejection of the noise.
Given the possible multiplicity of reconstructed tracks if more than one seed is found, the one with the best reduced χ^2 ($\chi^2/ndof$) is chosen. A cut has been introduced on the reduced χ^2, which has to be lower than 3. The whole process is meant to reduce at the bare minimum the influence of any noise hit.
The selected reconstructed track is eventually propagated to the test chamber and another window is opened around the intersection point. If within ± 5 cm in x and ± 1 iη partitions any hit is found, both numerator and denominator get increased by one unit. Otherwise, only the denominator is incremented. The efficiency is calculated via the equation 5.2

$$\text{Efficiency} = \frac{\text{Number of test chamber hits within the check window}}{\text{Number of propagated track hits}} . \tag{5.2}$$

In track-based analyses, the granularity with which the efficiency is computed can be arbitrarily chosen and it is mostly driven by the precision that is desired. The limiting factor is only the statistics. For the usual twelve-hour runs, three granularities have been chosen. The average efficiency is calculated for the chamber, for each of the 24 VFAT partitions and for thin slices of fixed dimensions (3.33 mm $\times$ 1 iη partition).
It is worth to mention that all the main results of each analysis step are uploaded into the GEM database, to be easily accessible for future reference.

5.3.3 Typical results of the analyses

The description of the algorithms at the basis of the data analysis will be now instrumental to better understand the resulting plots. This section will present the typical outcomes of the different analysis steps.

Initially, the ***Identification of hot and dead strips*** provides the maps for the two types of misbehaving readout channels. Plots like in Figure 5.19a and 5.19b are evaluated and compared to the results obtained during the frontend configuration derivation utilizing the test pulses.
The dead strips are generally randomly distributed. If no major high voltage instability occurred, a chamber is expected to have at most three non-responding channels out of the 384 present in each iη sector. This criterion is imposed by simulations performed during the early R&D phase

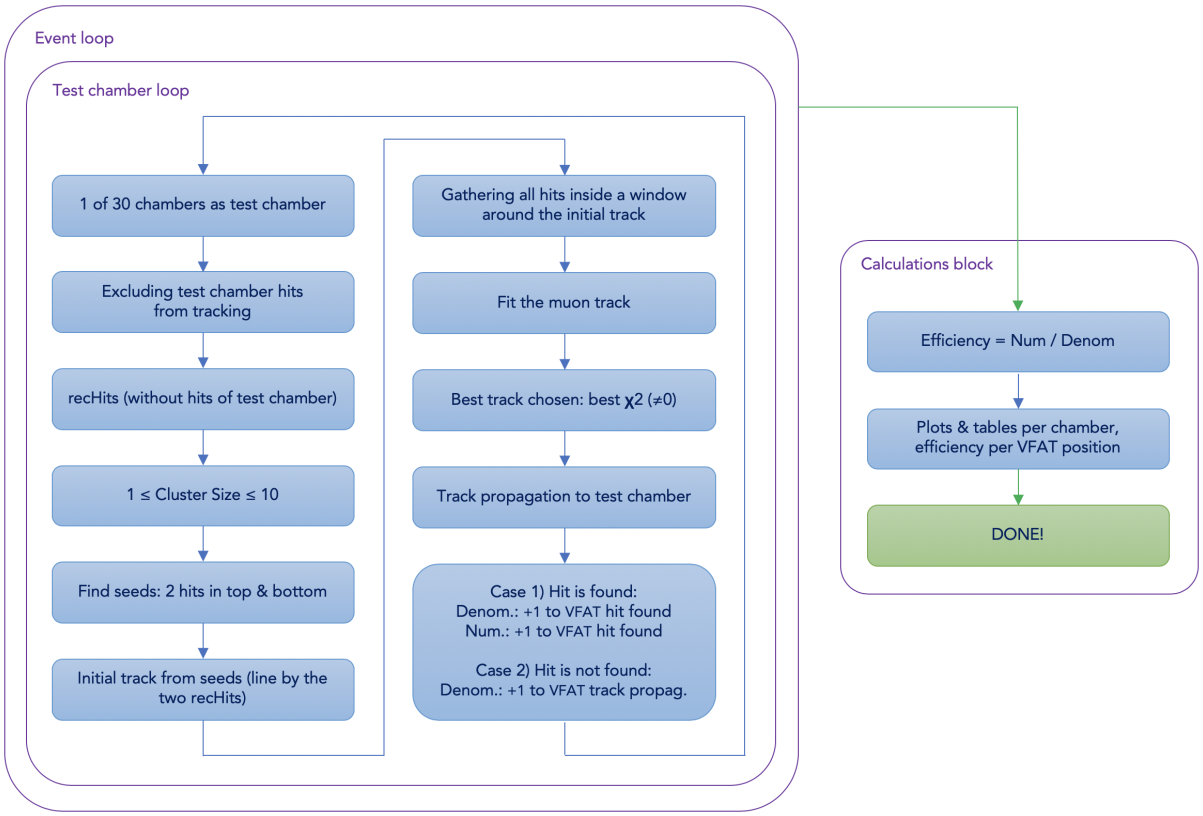

Figure 5.18: Block diagram of the track-based efficiency analysis.

of the GE1/1 project in order to preserve the detection efficiency (no losses), and it was applied during the super chamber assembly when selecting the readout partitions where to install the VFATs with malfunctioning channels from the production.
The noisy strips, instead, are normally close to the edges of the VFAT boards, being proximal to the ground lines and to the exterior parts. They can be then noticed around the strip number 127 and 255 in Figure 5.19b.

A typical plot that summarizes the overall status of the readout electronics is presented in Figure 5.20. All the applied masks are shown as a percentage of the total number of readout channels for each VFAT sector. Usually, the masked channels for one partition are at most 2 out of 128 (1.6%). Any deviation from these numbers reveals a defect that appeared during the validation step. Most of the times, an increased number of dead channels is caused by violent discharges that compromise the VFAT channels. Occasionally, those events require a substitution of the hybrid boards with new ones after the validation. A higher number of noisy channels (up to 100%), instead, might be imputed to the oscillations in the intrinsic noise, requiring a correction of the applied global threshold values.

With the masks correctly determined and applied, the ***Event certification*** analysis can properly identify the blocks of events when the chambers experienced high voltage trips. From plots like the one in Figure 5.21, the threshold for the identification of a bad block has been extracted. If any block of 1000 events contains less than 30 recHits, it is labeled as non valid.

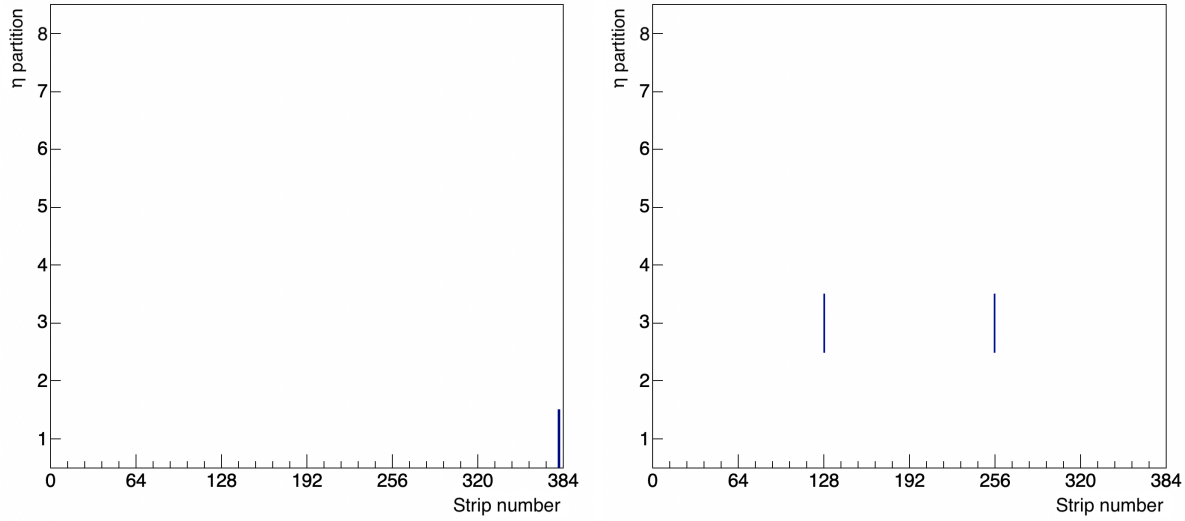

(a) Dead strips map. (b) Hot strips map.

Figure 5.19: Typical dead and hot strip maps for a detector in a cosmic run. The dead and hot strips are marked in blue. The dead strips are normally randomly distributed, while the hot strips tend to be present at the edges of the VFATs. These maps are obtained for the GE1/1-X-S-CERN-0003 chamber operated at an equivalent divider current of 700 µA.

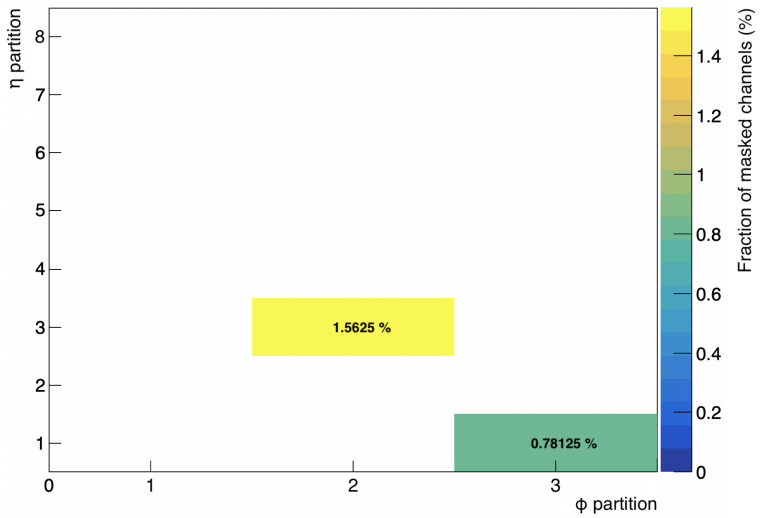

Figure 5.20: Typical map of the fraction of masked channels per VFAT partition in percent units for a detector in a cosmic run. Normally, each of the readout sectors has at most 1.6% of its strips masked. These map is obtained for the GE1/1-X-S-CERN-0003 chamber operated at an equivalent divider current of 700 µA.

For a smooth trip and recovery occurrence, an average of 34000 events get excluded, corresponding to around 6 minutes of data taking. This is fully compatible with the time needed by the DCS to complete all the actions to restore the original high voltage state. In the figure this can be seen around event number 3.4M of run 468 for the chamber GE1/1-X-S-FIT-0002.
Any other variation from a rather flat trend, like a step up or down, is to be imputed to a sudden jump in the noise level or the loss of a proper communication between the frontend and the

backend. Both of the behaviors might be generated by failures of electronics components or to to the loss of synchronization of the electronics after a violent HV discharge[3]. The analysis is not intended to catch those, and they need to be manually checked.

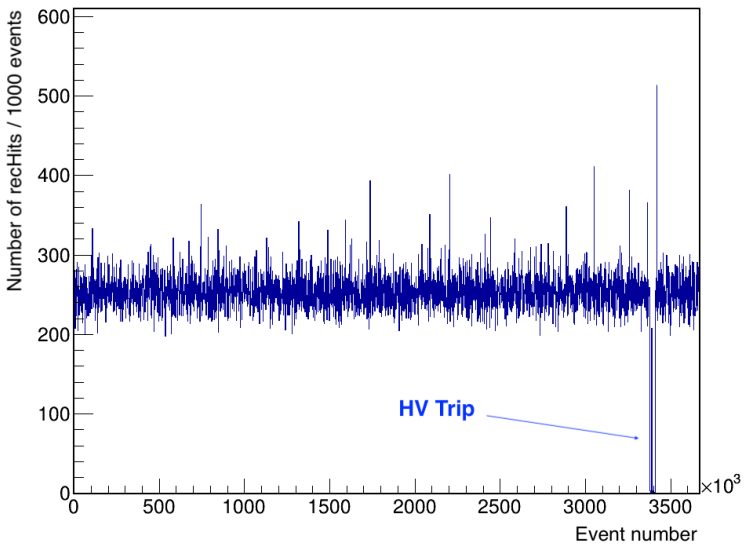

Figure 5.21: Typical event certification output plot. The number of recHits recorded in blocks of 1000 triggered events is presented for the GE1/1-X-S-FIT-0002 chamber operated at an equivalent divider current of 700 µA. Given the chamber area and the acceptance volume of the stand, it is not expected to have a muon passing through a specific chamber in each triggered event. A trip occurrence can be noticed around event number 3.4M, where the hit rate has dropped almost to zero.

A rough estimation of the efficiency of each of the chamber is given by the ***Fast efficiency*** analysis output. Firstly, a quick sanity check of the data processing is done with plots like in Figure 5.22. The difference in x and iη position between the reference and test hits are plotted; ideally, they have to be centered at zero and to follow the cosmic rays angular distribution. Large deviations ($\mathcal{O}$(cm)) of the mean value from zero would point to a mismatch in the mapping between hardware and software. Such non conformities have never been observed. Instead, any bump in the tails would suggest the presence of unmasked hot strips in the super chamber.

Since the fast efficiency analysis has a very reduced set of requirements and cuts on the triggered muon trajectories, the collected statistics is sufficient to subdivide the dataset in blocks of events. With blocks containing six thousand events, the statistical error on the calculated efficiency can be maintained on the order of 1%. It is therefore possible to monitor the performance of the individual chambers for each minute of data taking. From plots as in Figure 5.23, the overall status of the chambers under validation can be monitored at a glance.

Finally, the fast efficiency analysis produces the efficiency maps with the granularities described in the previous section. Examples of these plots can be found in Figure 5.24, where the slight bias introduced by geometrical effects is visible on the edges. Besides these effects, the obtained

[3]Violent HV discharges causing the loss of synchronization of the electronics only happened a handful of times during the entire GE1/1 validation.

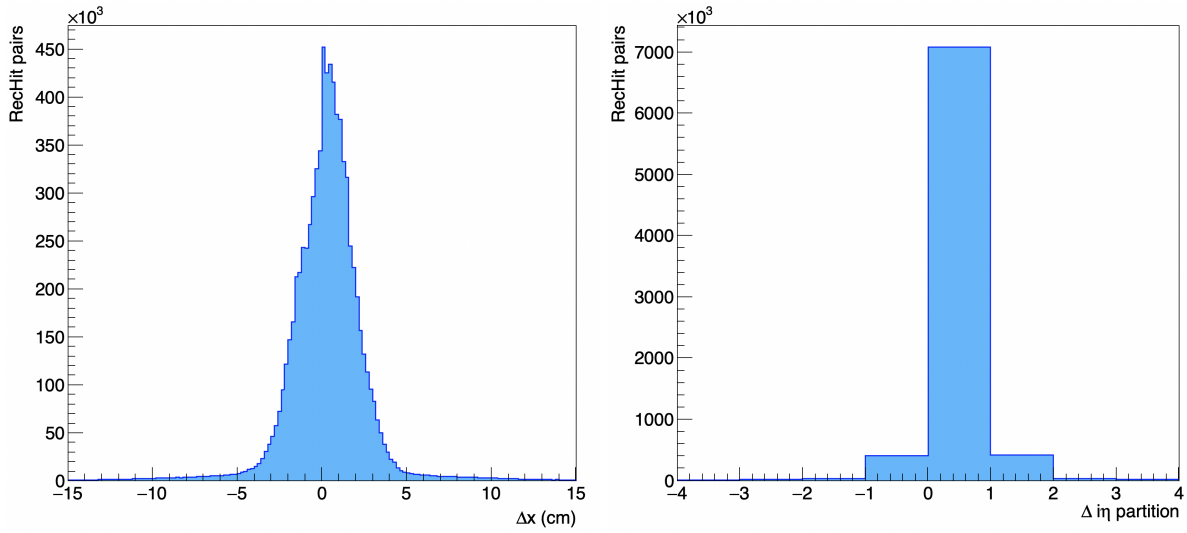

Figure 5.22: Difference in position in global x coordinate (left) and in iη partition (right) between the two hits in the two super chamber layers in a cosmic run. The two distributions match the expectations from the cosmic ray angular distributions, the stand angular acceptance, the scintillator tile inefficiencies and the distance in z between the two layers.

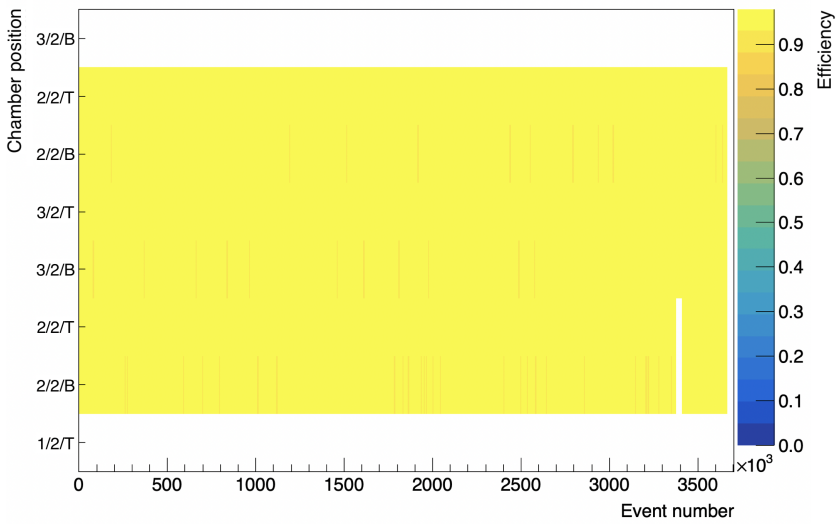

Figure 5.23: Average efficiency per chamber in blocks of 6000 events for detectors operated at an equivalent divider current of 700 µA. The calculations are performed with the fast efficiency method. The discontinuity that can be spotted for chambers in positions 2/2/B and 2/2/T around event number 3.4M are related to the trip that occurred to the GE1/1-X-S-FIT-0002 detector (occupying the position 13 in the software conventions), as presented in Figure 5.21. Those events were excluded not to bias the calculations.

values provide a clear picture of the chamber performance.

The least biased method to attain the GE1/1 efficiency performance is the ***Track-based analysis***. The total number of reconstructed tracks passing through a defined region of the active area are compared to the ones that the readout records. On a first approximation, the amount of muons that cross a region depends on its area. For instance, in long chambers a VFAT par-

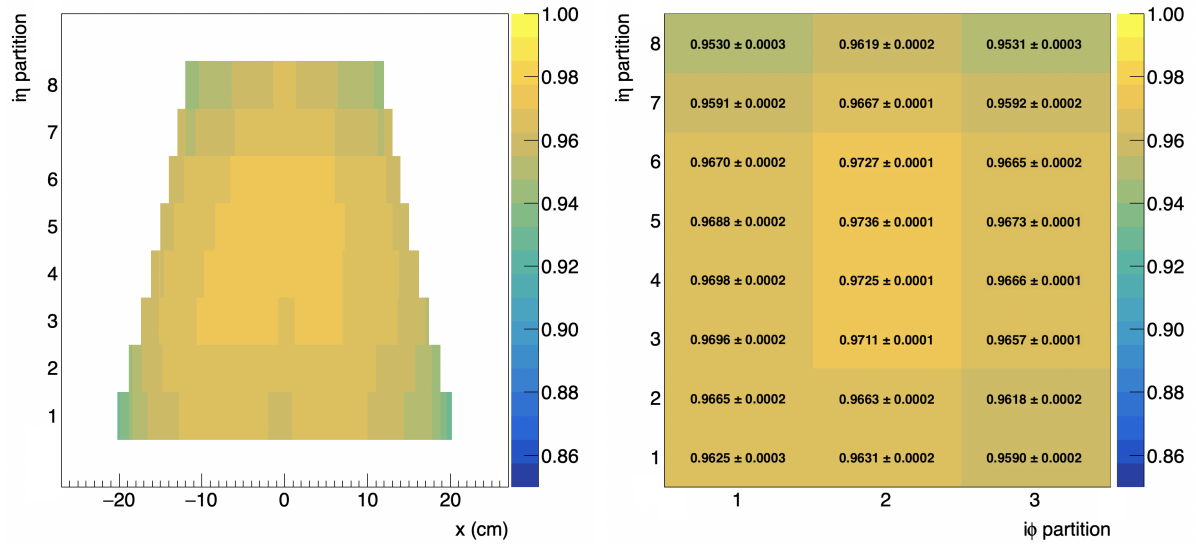

Figure 5.24: Typical efficiency maps for a GE1/1 chamber obtained with the fast efficiency method. On the left, the efficiency results are presented for blocks of 8 strips, while on the right is shown the efficiency per VFAT partition. The errors represent the statistical uncertainties. The plots are relative to the chamber GE1/1-X-S-FRASCATI-0006 operated at an equivalent divider current of 700 µA.

tition in $i\eta = 1$ has around three times the area of one in $i\eta = 8$. Naturally, a distortion in the proportionality of the efficiency denominator to the readout area is expected, when accounting for the many requirements imposed on the reconstructed tracks. This can be seen in Figure 5.25, where numerator and denominator per VFAT partition are plotted for a chamber under test. It clearly appears that the VFAT partitions in the center are probed with more statistics than the ones in the edges, being close to the boundary of the stand acceptance. For instance, this can be noticed in $i\eta = 1$ (e.g. VFAT7) which is the largest, but positioned at the front margin of the stand.

The efficiency for each of the readout partitions is obtained dividing numerator by denominator of plots like in Figure 5.25. From Figure 5.26, it is possible to evaluate the chamber efficiency in the detection of minimum ionizing particles. Firstly, this allows to verify if the requirements are met. Secondly, it is possible to recognize the chamber regions where potential non uniformities are present.
These results can be compared to the previously calculated ones with the fast method, revealing just a few discrepancies (up to 2%) due to the intrinsic limitations of the fast efficiency algorithm.

As a last step, the average efficiency for the entire active chamber area is computed by dividing the sum of the numerators and the denominators of the 24 VFAT sectors. This parameter is employed to determine the compliance of the performance to the established requirements. An example of the GE1/1 average efficiency obtained at different HV settings will be shown in the next section (5.3.4).

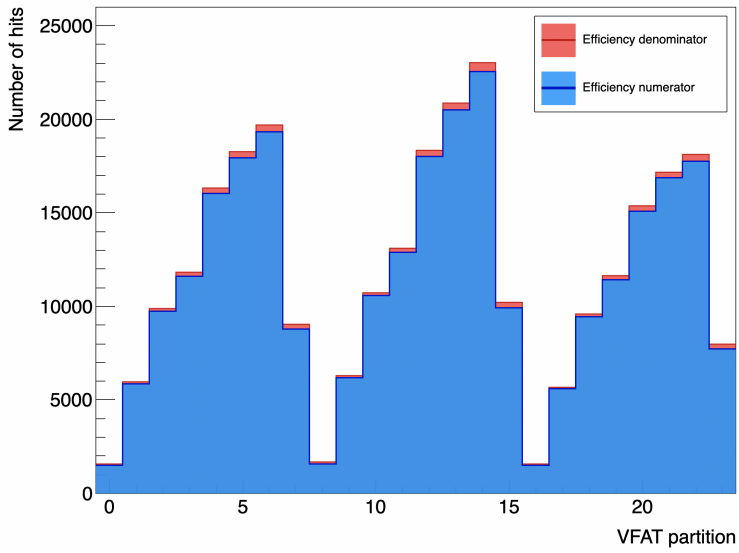

Figure 5.25: Efficiency numerator (blue) and denominator (red) obtained with the track-based analysis for the 24 VFAT partitions of the chamber GE1/1-X-S-FRASCATI-0006 operated at an equivalent divider current of 700 µA. The shape of the distributions is a convolution of several factors, including the surface area of the readout partitions, the position of the chamber with respect to the acceptance volume of the stand and the cuts applied to the reconstructed tracks.

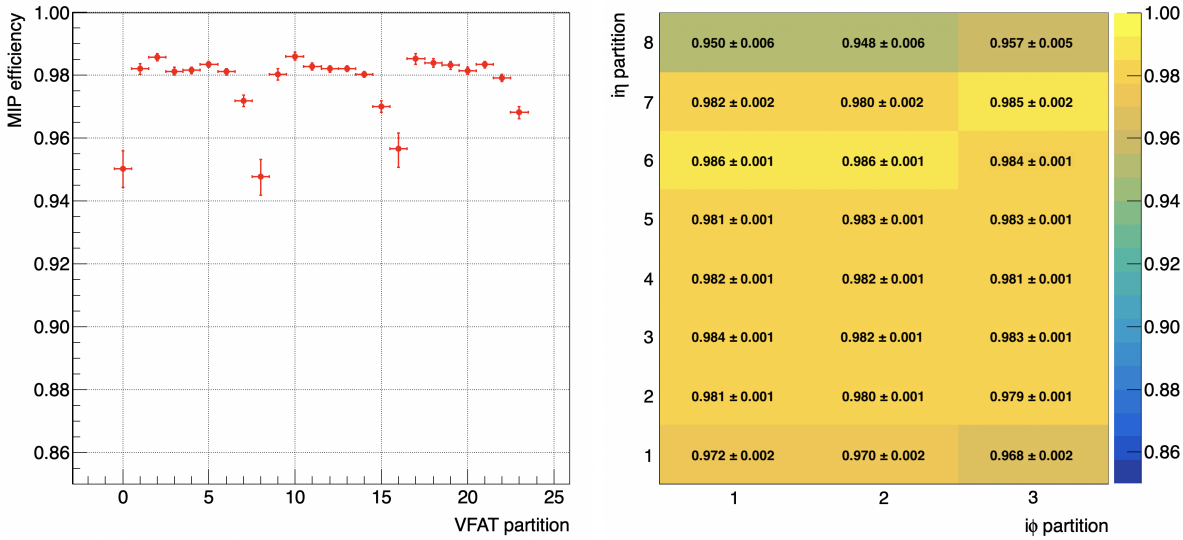

Figure 5.26: Typical efficiency results obtained with the track-based analysis. On the left, the results are presented as a graph with the VFAT partition as the x-axis, while on the right a 2D view is given for a more direct visualization of the efficiency map. The errors represent to the statistical uncertainties. The plots are relative to the GE1/1-X-S-FRASCATI-0006 chamber operated at an equivalent divider current of 700 µA.

5.3.4 Significant efficiency results for the GE1/1 detectors

During the course of the GE1/1 production and validation, a total of 154 single chambers underwent a successful cosmic ray test that assessed their efficiency performance.

For the majority of the detectors, the time available for the tests was very limited and allowed

for an high voltage scan with at most four applied settings. In one occasion, though, the super chambers could remain in the stand for a longer period and the full efficiency curve could be sampled. The equivalent divider current was varied in steps of 10 µA in the range $590 - 700$ µA. The range limits were chosen based on the efficiency results attained run per run, with the aim of sampling the curve from an efficiency of about 10% up to the efficiency plateau. Moreover, since the efficiency plateau was reached at 700 µA for all the chambers under study, the high voltage working point was not pushed further in order to preserve the integrity of the chambers. A smooth efficiency curve was obtained, confirming the expected behavior. For most of the chambers, the plateau of the average efficiency starts around 680 µA and its value stays at about $97 - 98\%$. An example for one of the super chambers that underwent the extended study is presented in Figure 5.27a. The data points do not follow a perfect sigmoid; indeed, the fit curve matches the data only on the upper region. This stems from the GE1/1 effective gas gain characteristic behavior, as shown in Figure 5.27b for one of the two chambers[4]. The gain curve follows two distinct exponential functions at low and high amplification, with a transition region in between. That region corresponds to the HV point where the fit diverges from the data in the efficiency plot. The possible origin has been identified in the trend of the electron extraction efficiency from the third GEM foil as a function of the applied induction voltage [53]. In most of the cases, the transition happens between gain 1000 and 2000.

For the same group of GE1/1 detectors, an additional threshold efficiency scan could be performed. Fixing the high voltage working point at an equivalent divider current of 690 µA, a series of runs were taken starting from the set of thresholds corresponding to 100 Hz of noise hits per VFAT. In the subsequent runs, all the CFG_THR_ARM registers of the VFATs were increased following the pattern: +20 , +35 , +50 , +75 , +100 , +115.

For each of the frontend configurations, s-curve scans with test pulses were taken and the threshold values in charge units were extracted.

Curves like the ones presented in Figure 5.28 were produced by averaging both the efficiency and the threshold values over the chamber active area.

Two main results could be deduced from the study. First, it was confirmed that the trimming parameters for the individual VFAT channels are valid at any global threshold, and their response remains aligned as intended. Second, it was proven that in most cases a threshold increment of about 1 fC with relation to the baseline value doesn't lower the efficiency below the limit of 95%, when the chambers are operated at an equivalent divider current of 690 µA. This justifies the little impact on the efficiency performance of the workarounds to compensate for the noise level instabilities (4.3.3).

5.3.5 Summary plots of the GE1/1 production and validation

Out of the total number of validated GE1/1 detectors, 72 super chambers have been selected for the installation in the two CMS endcaps, while the others were kept as spares.

The histograms of the maximum average efficiency recorded in the cosmic ray test for the 144

[4]The gas gain of the other layer is presented in Figure 5.41b, where the impact of this gain behavior on the hit cluster size is shown.

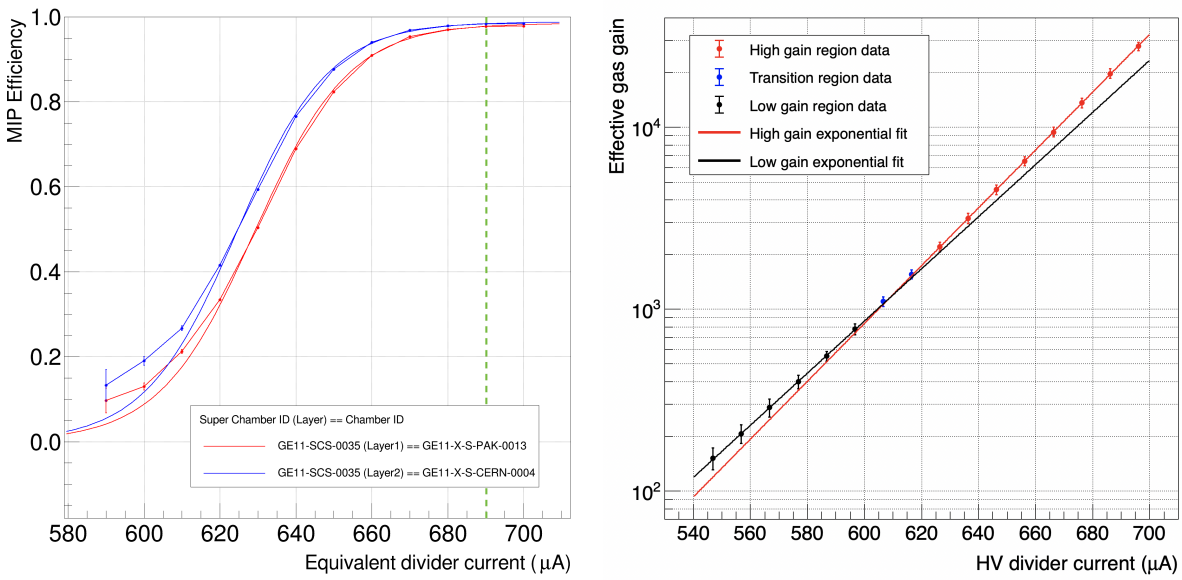

(a) Efficiency vs equivalent HV divider current.

(b) Gas gain vs HV divider current.

Figure 5.27: On the left, detection efficiency as a function of the equivalent HV divider current for the two layers of a super chamber. The efficiency plateau at $97-98\%$ starts at an equivalent divider current of about 680 µA, which is usual for a GE1/1 detector. The green dashed vertical line corresponds to the equivalent divider current nominal value of 690 µA. The plot presents the results obtained for the GE1/1-SCS-0035 super chamber. On the right, gas gain curve of the chamber GE1/1-X-S-CERN-0004 - the Layer 2 of the GE1/1-SCS-0035 super chamber. The HV divider current has been corrected to the environmental parameters present during the high voltage efficiency scan. The effective gain manifests a double curve behavior with an exponential part for low gas gain, a kink between gain 1000 and 2000, and another exponential part for high gas gain. The exponential fit for the low gain region is shown in black, the transition data points are depicted in blue, and the exponential fit for the high gain region is shown in red. To ease the visualization of the double curve behavior, the two exponential fits (black and red lines) are extrapolated to the other region. This trend is reflected in the efficiency curve, which follows two separate sigmoids for low and high equivalent divider currents.

chambers installed in CMS are presented in Figure 5.29. In many cases, the maximum value observed coincides with the detection efficiency plateau, hence the averages around $96-97\%$. It has to be considered that for the negative endcap detector validation the trimming procedures were not yet established, thus the thresholds were not optimal. In addition, the tight schedule for the CMS installation limited the time available for the tests, only allowing for a reduced amount of validation runs. Therefore, the results for some chambers needed to be evaluated extrapolating the efficiency curve to higher working points. This explains the presence of some outliers in the distributions, for which the observed efficiencies of around $92-93\%$ allowed to approve the detectors.

5.3.6 Issues concerning the GE1/1 efficiency

Two main types of issue were discovered during the last step of the GE1/1 quality control. One regarded failures in the individual electronic components, which were immediately corrected in

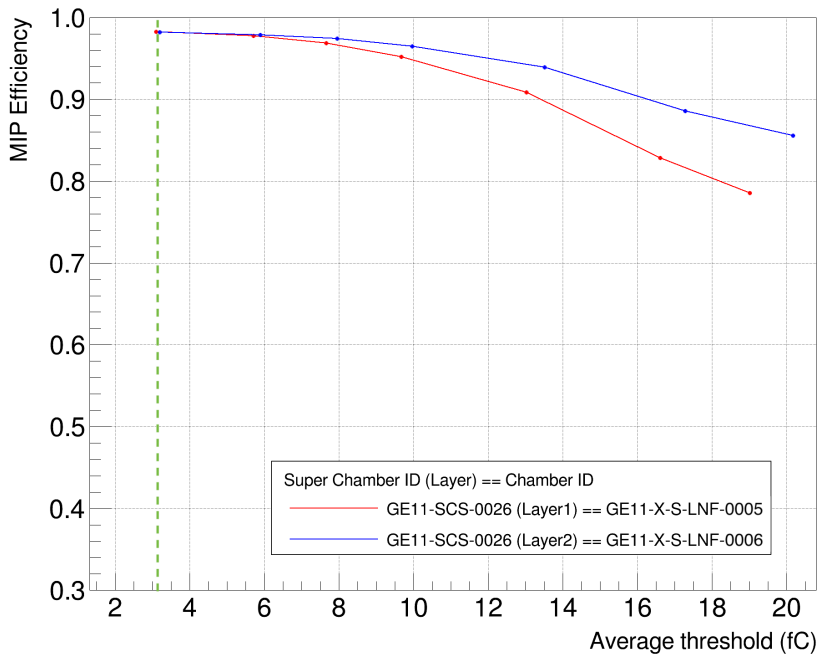

Figure 5.28: Efficiency per chamber for the two layers of the super chamber GE1/1-SCS-0026 in the frontend threshold scan. The high voltage working point was fixed at an equivalent divider current of 690 µA. Both the efficiency and the threshold values are an average over the chamber active area. A threshold increment of about 1 fC with relation to the baseline value corresponding to 100 Hz of noise hits per VFAT (green dashed vertical line) does not lower the efficiency below the limit of 95%.

the GEM assembly lab. The other concerned anomalies in the chamber gas gain that will be detailed in this section.

5.3.6.1 Disconnected high voltage partition

In quality controls precedent to the cosmic ray test, the gas gain can be tested over the entire active area with the granularity of a four readout strips. This is sufficient in the ϕ direction, but occasionally not along η. For instance, it is not possible to evaluate the behavior of the individual high voltage partitions of the GEM foils. Indeed, during the gas gain quality control tests no information can be derived about the HV partitions involved in the amplification process, since each iη region is covered by several of them.

When the efficiency is under study, even though the granularity along η is fixed by design, the sensitivity is enough to spot issues that involve the HV distribution.

An issue that can pass unnoticed until the final QC step is a disconnected HV partition. Indeed, the only clear symptom is a reduction in the rate of particles detected by one iη partition, that then reflects on its efficiency. The cause might be a failure in one protection resistor connected to an HV partition or an interrupted copper trace on one of the three GEM foils. It is still not possible to determine which foil is involved, but only in which readout region lies the affected HV partition.

An example can be seen in Figure 5.30 for the detector GE11-X-S-PAK-0004. In that case,

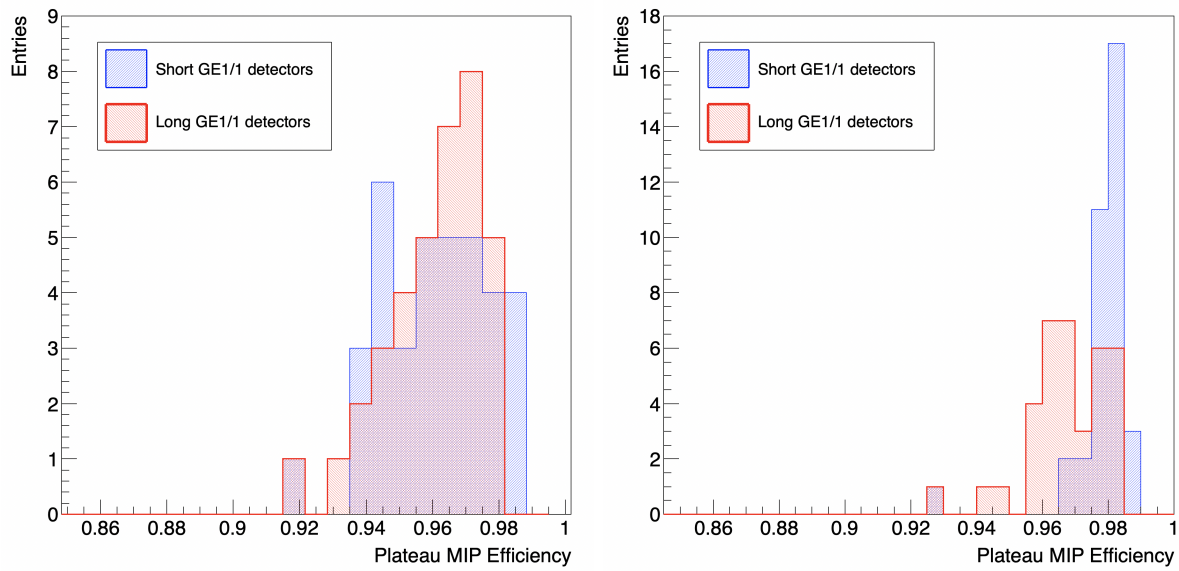

(a) Negative endcap chambers (b) Positive endcap chambers

Figure 5.29: Summary plots of the efficiency per chamber for the GE1/1 detectors installed in the CMS muon endcaps. The efficiency values displayed in the plots are the ones recorded at the maximum high voltage working point set in the cosmic ray tests. The values are not representing the maximum attainable efficiency for each of the chambers, since in some cases the high voltage scans had a very limited set of runs. The performance of those chambers were then evaluated extrapolating the trend of the efficiency against the applied HV to higher working points. The mean value of the average efficiency of both long and short chambers of the negative endcap was $(96.1 \pm 0.3)\,\%$. The positive endcap short chambers had a mean value of the average efficiency of $(97.8 \pm 0.2)\,\%$, the long ones $(96.8 \pm 0.2)\,\%$. The errors reported on the mean values of the average efficiency corresponds to the error of the mean of the histograms.

around 20% of the area covered by the i$\eta = 4$ region does not provided a proper amplification to the electrons.

Spotting this kind of issues is easier on the narrow side of the detector, where only a handful of HV partitions cover each iη. Oppositely, on the wide side, the strips are longer and the HV partitions are narrower.

In the GE1/1 validation, disconnected HV partitions have been recorded in 4 chambers out of 156. Unfortunately, no non-destructive fix is available, and the chambers have to be either rejected or approved on the basis of their average efficiency. For instance, the GE1/1-X-S-PAK-0004 chamber shown in Figure 5.30 was considered validated, since it could detect more than 95% of the muons traversing it.

Consequently to these findings, a specific test has been foreseen for the future iterations of CMS GEM detectors in order to properly identify such malfunctions at an early stage.

5.3.6.2 Basin effect

Another issue that has been discovered thanks to the efficiency measurements is the so-called *basin effect*. It consists in an efficiency non-uniformity, characterized by a depression in the central $\phi-$partition around the i$\eta = 2$ region (VFAT14). An example can be seen in Figure 5.31

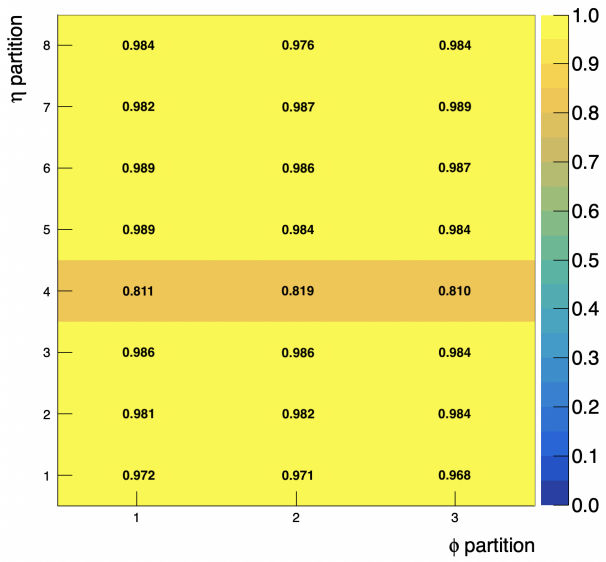

Figure 5.30: Example of an HV partition issue present in the chamber GE1/1-X-S-PAK-0004. While all the rest of the chamber is fully efficient, the i$\eta = 4$ partition has a common drop of around 20%. This is the typical signature of a detached protection resistor in the high voltage distribution of one of the foils.

for the detector GE1/1-X-L-CERN-0005. A limited subset of long detectors exhibited a clear signature: 12 out of the 78 that underwent the cosmic ray test.

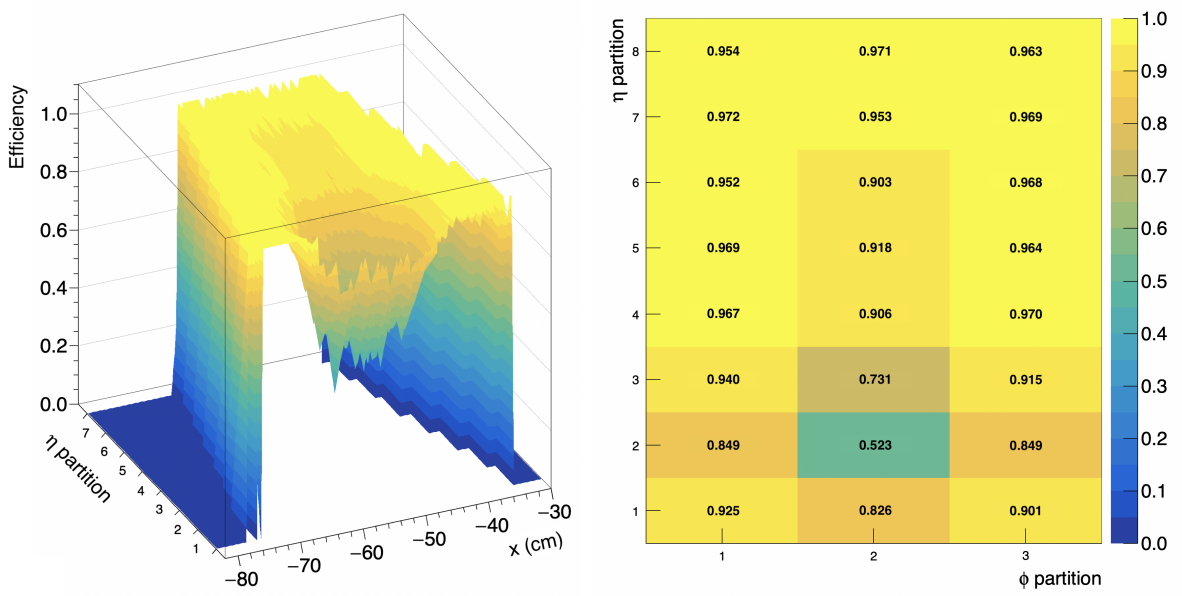

(a) 3D efficiency map.

(b) Efficiency map per readout partition.

Figure 5.31: Typical signature of the efficiency "basin effect". The presented results refer to the GE1/1-X-L-CERN-0005 chamber operated at 690 µA.

The investigations on the causes of the efficiency "basin effect" did not find any match with possibly defective batches of GE1/1 components. Instead, a deformation in the planarity of the

readout and drift PCBs could be visually noticed on the affected chambers. The flatness of the PCBs ensures the correct spacing between foils and boards, generating the appropriate electric fields uniformly across the chamber active area. An outward bending as in Figure 5.32 causes a longer drift path for the electrons and a reduced intensity of the drift and the induction fields. This has two consequences. The first is a reduction in the collection efficiency from the third GEM foil. The second is an increase of the time width of the signals induced on the strips.

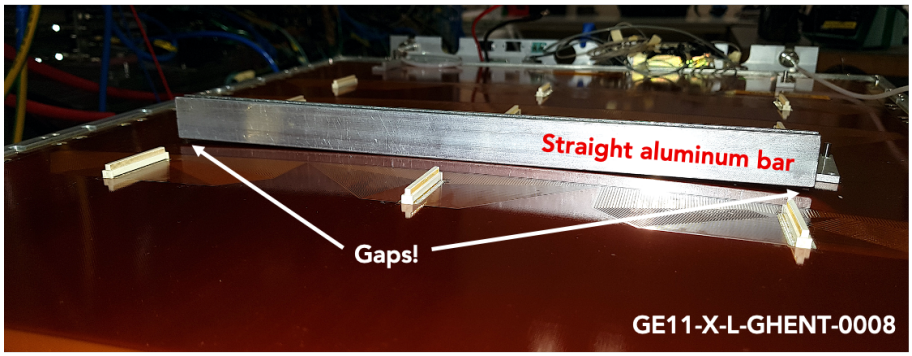

Figure 5.32: Picture illustrating the bending of the readout board in the i$\eta = 2$ region of the GE1/1-X-L-GHENT-0008 detector. This chamber manifested a clear basin effect signature in the efficiency results.

While during the gas gain uniformity measurements this issue could be noticed, the different readout electronics did not reflect the same losses. Indeed, the measured gain in the VFAT14 partition of the affected chambers is typically only half of the one in i$\eta = 7, 8$. This reduction alone would not lead to inefficiencies when operating at an average gain of about 20000. The reason can be identified in the limited signal integration time of the VFATs.
In section 2.4.2 it was shown that, in presence of a doubled induction gap, the signals are stretched in time. Thus, the maximum setting for the VFAT preamplifier peaking time (45 ns) allowed to integrate only the 70% of the total charge induced on the strips.
Convoluting the two effects, the "perceived gain" becomes around one third of the ideal one.

In order to mitigate the issue, it is possible to implement one or a combination of these strategies:

- Reduce the threshold applied to the affected VFATs;
- Augment the induction field;
- Increase the overall HV working point.

All the three points show benefits (Figure 5.33). However, they come at a price.
When the thresholds are lowered by a fraction of a femtocoulomb, the noise rates become orders of magnitude larger. Instead of the standard 100 Hz, it is possible to accept up to 10^4 Hz without having a major impact on the trigger, if compared to the expected background rate. Normally, this allows to shave off between 0.5 and 1.0 fC.
Increasing the high voltage might generate instabilities and discharges that damage the foils or the readout electronics.

Subsequently, a thorough high voltage training and an intrinsic noise reduction are of the utmost importance. A compromise between pros and cons, and a combination of the mitigation actions, can finally lead to a stable and more uniformly efficient chamber.

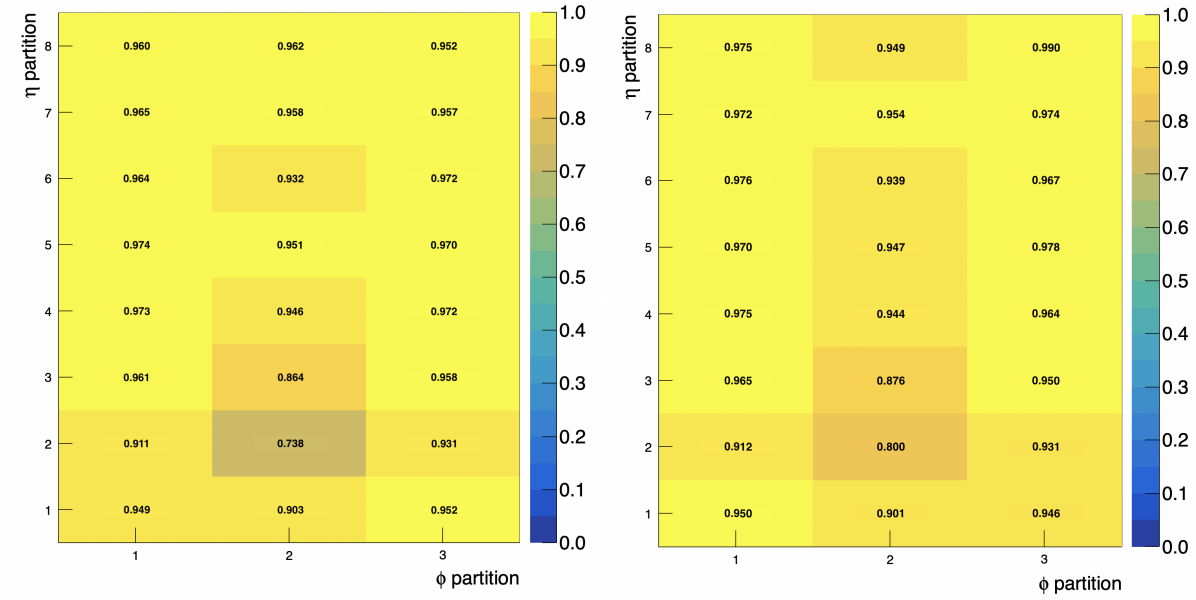

(a) VFAT14 threshold at 4.02 fC

(b) VFAT14 threshold at 3.16 fC

Figure 5.33: GE1/1-X-L-CERN-0005 operated at 700 µA, which corresponds to an average gain around 30000. The "basin effect" is clearly mitigated by an increased HV working point, if compared to Figure 5.31, and by lower frontend thresholds applied to the VFAT14.

Considering the plot in Figure 4.9, a comparison can be made between gas gain uniformity and efficiency uniformity. A marked basin effect appears when the gain uniformity parameter σ/μ is greater than 25% or more. Depending on the frontend thresholds applied and the high voltage settings, a small efficiency drop ($\leq$ 10%) in the central readout partitions is also visible with a gain uniformity between 20% and 25%.

5.3.6.3 HV working point and environmental conditions

The first period of super chamber validation with cosmic rays was performed operating the detectors at fixed average gain values. The HV working points were calculated utilizing the gas gain curves from the tests described in section 4.1.3, and applying a correction for the environmental conditions of the CERN GEM lab. Nevertheless, unexpected inefficiencies were obtained for some of the chambers. They revealed an incongruity between the expected and the actual effective gas gain, which pointed to an inaccurate correction for the environmental conditions. In the following, the derivation of the standard correction will be shown, together with the results obtained by applying it. Subsequently, a more refined correction will be presented.

Simple model:

Starting from the gas amplification theory developed by Townsend (equation 2.33), the gas gain G can be expressed as

$$G = \frac{n}{n_0} = \exp\left(\int \alpha\left(s\right) \mathrm{d}s\right) = \exp\left(\int \alpha\left(E, gas\right) \frac{\mathrm{d}s}{\mathrm{d}E} \mathrm{d}E\right) , \tag{5.3}$$

Where the first Townsend coefficient $\alpha\left(E, gas\right)$ depends on both the applied electric field and the gas conditions, i.e. the environmental conditions.
In the case of a GEM detector, the chamber can be thought as a stack of parallel plate capacitors. Consequently, $\mathrm{d}E/\mathrm{d}s$ is constant within each amplification stage, while the electric field becomes proportional to the voltage applied across the foils. As a first approximation, it is possible to assume that α depends on gas density as $\alpha\left(gas\right) = \alpha_0 \cdot \rho_0/\rho$. Plugging the leading order factors into the equation 5.3 and performing the integration, one obtains

$$G = \exp\left(g \cdot \alpha_0 \cdot \frac{\rho_0}{\rho} \cdot \sum_{n=1}^{3} \Delta V_i\right) , \tag{5.4}$$

Where $\Delta V_{i=1,2,3}$ are the voltages applied across the three GEM foils.
Finally, since $\rho = mass/volume$, the density is proportional to the pressure and inversely proportional to the temperature of the gas. Considering that the ΔV_i are normally proportional to the (equivalent) divider current ($I_{divider}$), the final equation for the GE1/1 gas gain becomes

$$G = A \cdot \exp\left(B \cdot I_{divider}\left(\frac{p_0}{p}\right)\left(\frac{T}{T_0}\right)\right) , \tag{5.5}$$

$$I_{divider,0} = I_{divider}\left(\frac{p_0}{p}\right)\left(\frac{T}{T_0}\right) . \tag{5.6}$$

In the cosmic ray stand tests, p_0 and T_0 represent the atmospheric pressure and temperature of the CERN lab.

The results obtained in the cosmic ray tests have proven this correction for pressure and temperature conditions to be inaccurate. The example reported in Figure 5.34 shows the efficiency maps of the chambers GE1/1-X-L-CERN-0024 and GE1/1-X-L-GHENT-0022 for an HV working point corresponding to a *presumed* average gain of 21000. It is worth to report that the frontend thresholds were similar for the two chambers, with an average close to 3 fC.
Clearly, while the GE1/1-X-L-CERN-0024 detector was at its efficiency plateau, the GE1/1-X-L-GHENT-0022 detector was underperforming. Checking the equivalent divider currents applied, it was noticed that the GHENT chamber was operated at 675.9 µA, whereas the CERN chamber was set at 696.5 µA.
The performance of the GE1/1-X-L-GHENT-0022 chamber was also tested applying an equivalent divider current of 700 µA. The results can be seen in Figure 5.35: with a working point similar to the GE1/1-X-L-CERN-0024 chamber, the efficiency plateau was reached.
Similar behaviors were noticed for other chambers tested for QC5 in Ghent. Conversely, the ones that underwent the QC5 in Pakistan systematically required HV equivalent divider currents larger than 710 µA for gains above 10000.
The reason was found to reside in the extremely different pressures and temperatures between those testing sites and the CERN GEM lab or the CMS cavern. In such cases, the provided cor-

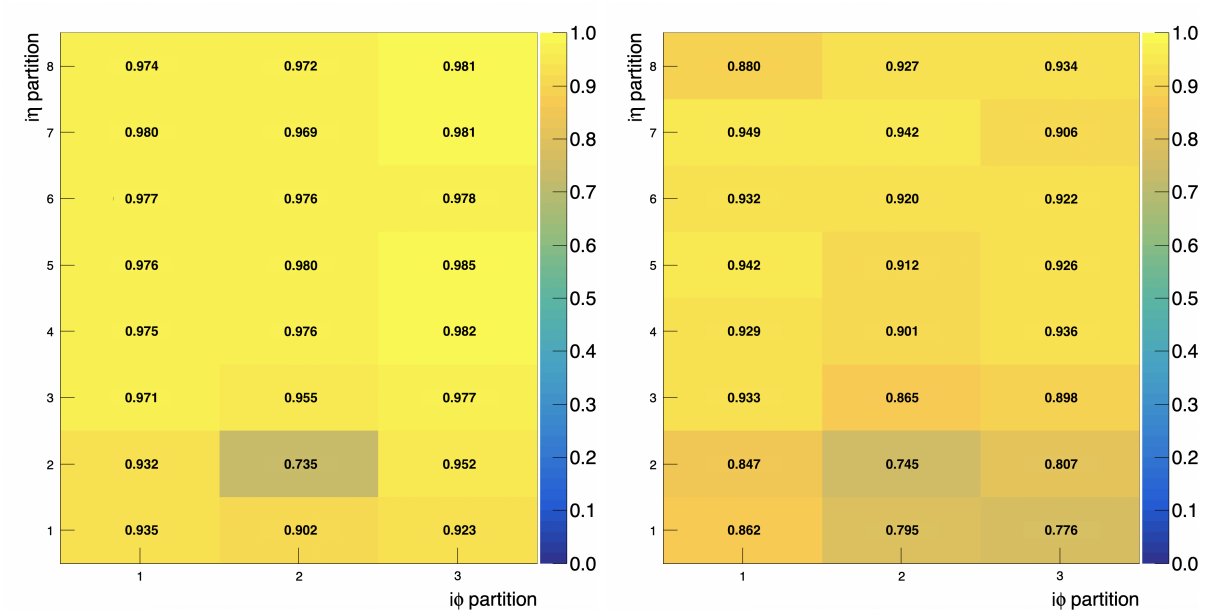

(a) Efficiency map of GE1/1-X-L-CERN-0024. (b) Efficiency map of GE1/1-X-L-GHENT-0022.

Figure 5.34: Efficiency maps of the chambers GE1/1-X-L-CERN-0024 and GE1/1-X-L-GHENT-0022 for a *presumed* average gain of 21000. Their high voltage working points were derived from the gas gain test curves with standard pressure and temperature corrections applied.

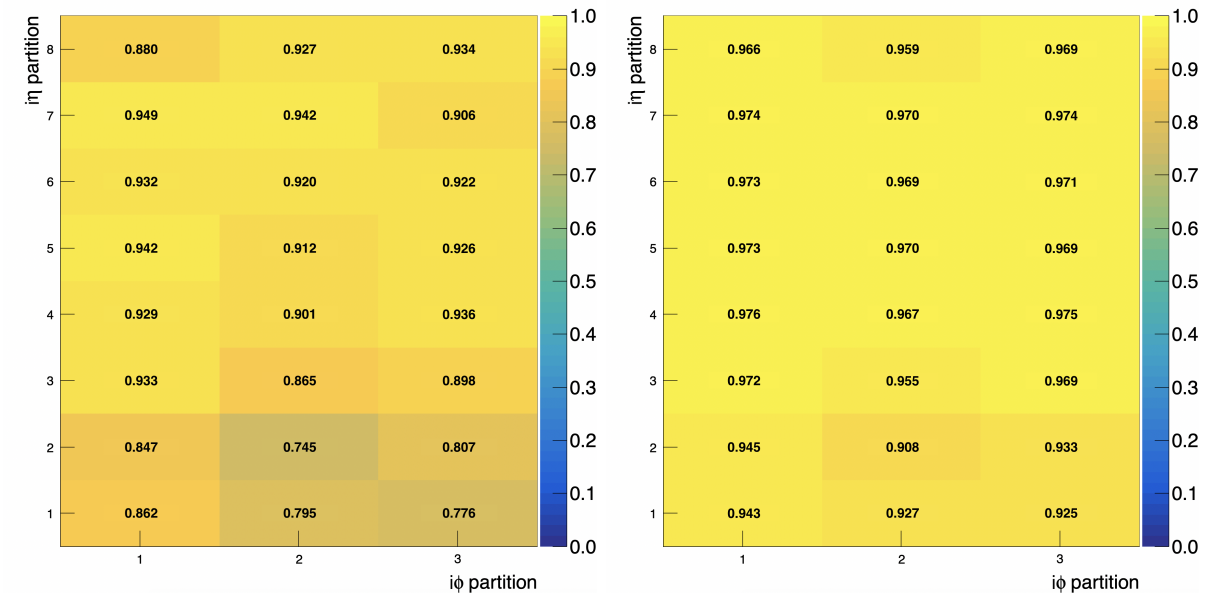

(a) GE1/1-X-L-GHENT-0022, at 675.9 µA. (b) GE1/1-X-L-GHENT-0022, at 700 µA.

Figure 5.35: Efficiency results for the GE1/1-X-L-GHENT-0022 detector applying an equivalent divider current of 675.9 µA (left) and 700 µA (right). The frontend thresholds were kept the same between the two runs.

rections overcompensated the $I_{divider}$ values. That is why in the previous results the corrections had a much greater impact on the GHENT chamber than on the CERN chamber.

Figure 5.36 shows a comparison between the QC5 gain results for these two detectors without

any correction and applying the standard one. After the corrections, the two curves are changed so much that they even change their relative position.

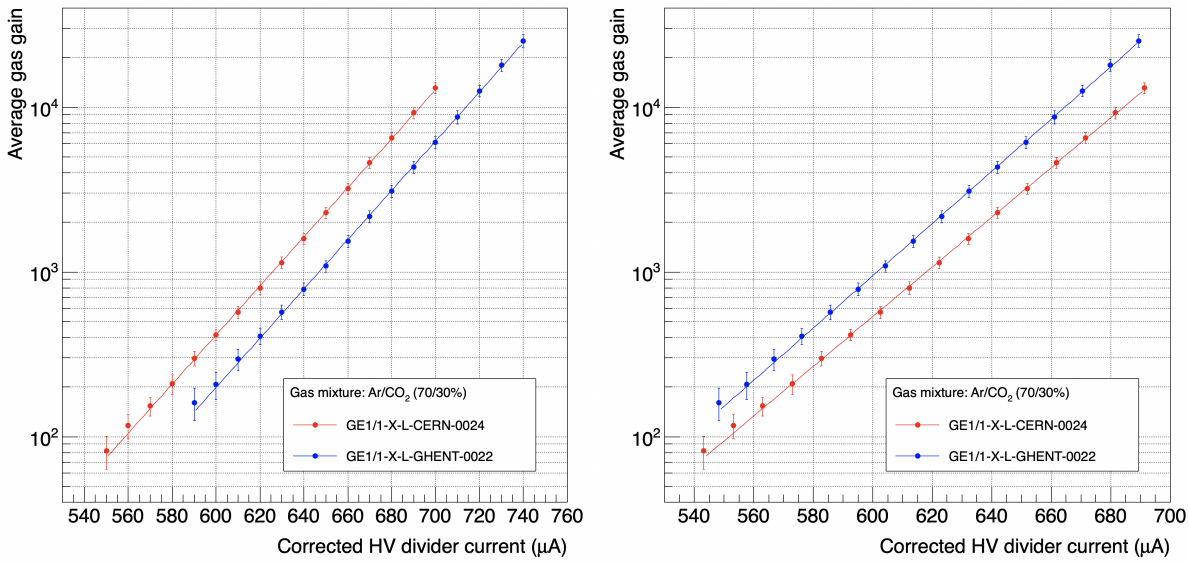

(a) Average gain without correction.

(b) Average gain with standard correction.

Figure 5.36: Comparison of the gas gain curves of the chambers GE1/1-X-L-CERN-0024 and GE1/1-X-L-GHENT-0022, before (left) and after (right) having applied the standard pressure and temperature corrections to the equivalent divider current. Here, p_0 and T_0 are assigned the average CMS cavern condition values. The gain curve of the CERN chamber got a little correction, since the environmental conditions in the CERN lab and in the CMS cavern are similar. On the contrary, the pressure and temperature in Ghent are very different from the CERN ones, that determine a large correction factor.

For reference, the environmental conditions present in the GE1/1 production and test sites are presented in Table 5.2.

Production site	Temperature $\mu \pm \sigma$ (K)	Pressure $\mu \pm \sigma$ (mbar)	$T/T_0 \cdot p_0/p$ $\mu \pm \sigma$
CERN	295.8 ± 1.0	970.9 ± 7.8	0.989 ± 0.007
BARI	296.1 ± 1.4	1000.1 ± 18.8	0.961 ± 0.0018
FRASCATI	297.3 ± 2.2	993.3 ± 19.8	0.972 ± 0.018
GHENT	296.3 ± 3.4	999.0 ± 20.2	0.963 ± 0.024
FIT (Florida Tech)	298.3 ± 1.3	1014.0 ± 11.8	0.955 ± 0.009
INDIA	295.8 ± 0.8	974.3 ± 7.0	0.985 ± 0.007
PAKISTAN	294.7 ± 1.4	948.3 ± 12.7	1.009 ± 0.012

Table 5.2: Average and standard deviation values of pressure, temperature and correction factor recorded during the gas gain tests at the GE1/1 production and test sites. $p_0 = 964.4$ mbar and $T_0 = 297.1$ K are assigned as the average CMS cavern condition values. For PAKISTAN only short chambers have been considered, since some of the long ones have been testes at CERN by the Pakistan group.

These results motivated the derivation of an improved model to describe the gain variations with the atmospheric pressure and temperature.

Improved model:
From a theoretical perspective, the first Townsend coefficient can be thought to be proportional to the inverse of the average distance between two ionizing collisions. In formula, $\alpha\,(gas) = \lambda_{ioniz}^{-1}$. λ_{ioniz} defines a spatial unit in the direction of motion of the electrons, approximately the direction of the electric field, therefore one axis in the 3D space. Thus, $\alpha\,(gas) = \alpha_0 \cdot (V_0/V)^{1/3}$, with V being the unitary gas volume, and α_0 absorbing all the other gas constants. Following the same steps as above, one gets the correction factors defined by the cubic roots of pressure and temperature.

The description is still not fully accurate, since in fact α has a much more complex formulation. Therefore, it has been deemed necessary to let the gain formula to be as general as possible and then derive the parameters through a dedicated study.

Empirical model:
For the empirical model, the gain and the divider current were chosen to be described by

$$G = A \cdot \exp\left(B \cdot I_{divider}\left(\frac{p_0}{p}\right)^a \left(\frac{T}{T_0}\right)^b\right) , \tag{5.7}$$

$$I_{divider,0} = I_{divider}\left(\frac{p_0}{p}\right)^a \left(\frac{T}{T_0}\right)^b . \tag{5.8}$$

The experiment to determine the a and b exponents was carried out in the GEM QC lab in Aachen employing the GE1/1-X-S-CERN-0002 chamber. Over the course of three days, a series of 46 effective gas gain tests was performed on the readout sector $(i\phi, i\eta) = (2, 4)$. One hour of delay interleaved two subsequent measurements. The atmospheric conditions were recorded for each of the gain measurements, with variations in the ranges $p = [978.81, 988.58]$ mbar and $T = [21.78, 23.41]$°C.
In Figure 5.37, the superimposition of all the 46 effective gas gain curves is presented without and with the standard corrections applied to the divider current. While on the left plot the raw measurements manifest the influence of the atmospheric conditions, the plot on the right clearly shows that the standard corrections ($a = 1$, $b = 1$) provide an overcompensation. The data points are not aligned to the exponential fit curve, but rather they are distributed in bunches with less inclination than the fit. This is due to an over-stretch of the x-axis, thus the overcompensation.
The pressure and temperature exponents were scanned in the intervals $[-1.0, 3.0]$. For each pair of values, an exponential fit was performed on the entire dataset. The reduced χ^2 as a function of the correction exponents was then extracted (Figure 5.38a). The minimum was found for $a = 0.433$ and $b = 0.547$, which are both below $a = b = 1$, as predicted by the improved model. Clearly, the complexity of a real GEM chamber is still not well represented in the model. At any rate, it provides a good initial reference point to check the plausibility of the experimentally

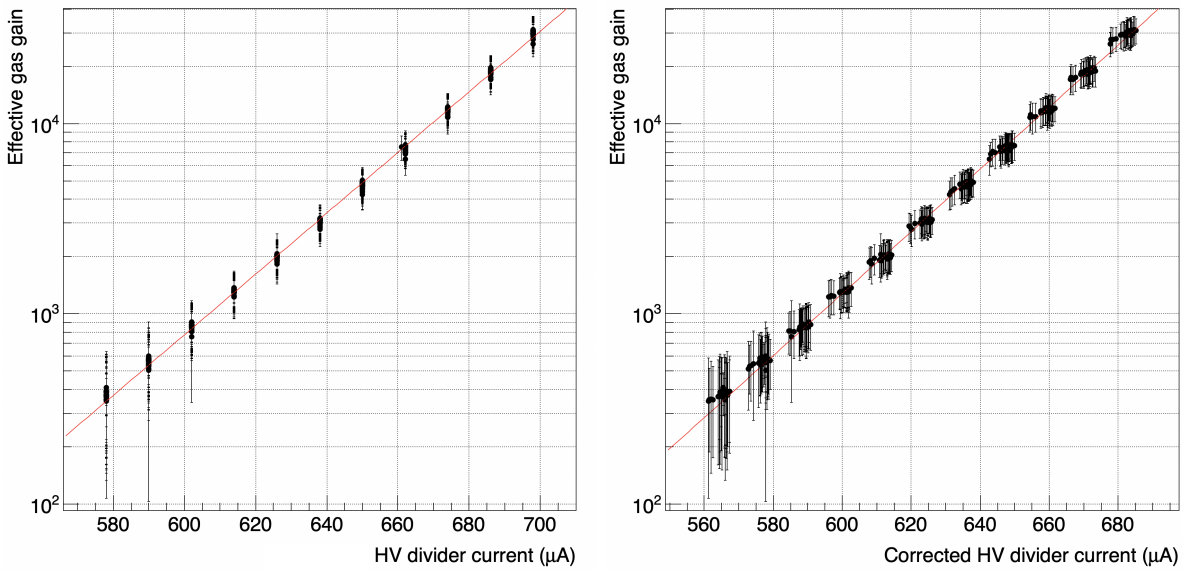

(a) Effective gain without correction.

(b) Effective gain with standard correction.

Figure 5.37: Results of the 46 subsequent effective gas gain test on the chamber GE1/1-X-S-CERN-0002. The points represent the measured gain values in each of the tests and the vertical bars represent the measurement errors. The gain curves are presented before (left) and after (right) having applied the standard pressure and temperature corrections ($a = 1$, $b = 1$) to the divider current.

derived exponents.

A summary of the gain correction exponents for environmental pressure and temperature variations derived in the three described models is presented in Table 5.3.

Simple model	$a = b = 1$
Improved model	$a = b = 0.33$
Empirical model	$a = 0.433$, $b = 0.547$

Table 5.3: Summary of the gain correction exponents for environmental pressure and temperature variations derived in the three described models.

Figure 5.38b shows the data points and the relative fit for the optimized empirical exponents. All the points are well aligned, demonstrating the validity of the model and the experimental procedures.

The average gas gain curves for the GE1/1-X-L-CERN-0024 and GE1/1-X-L-GHENT-0022 detectors with the improved corrections applied can be seen in Figure 5.39. A good agreement between the gas gain and the efficiency behaviors is finally present.

The chamber pairing was already done prior to the presented study. Fortunately, all the chambers with overcompensated corrections (in both the directions) were identified as matching. Therefore, the detectors tested in Ghent were often combined; and similarly it happened for the Pakistan ones. Moreover, the efficiency performance evaluated in the cosmic ray stand test confirmed a good pairing.

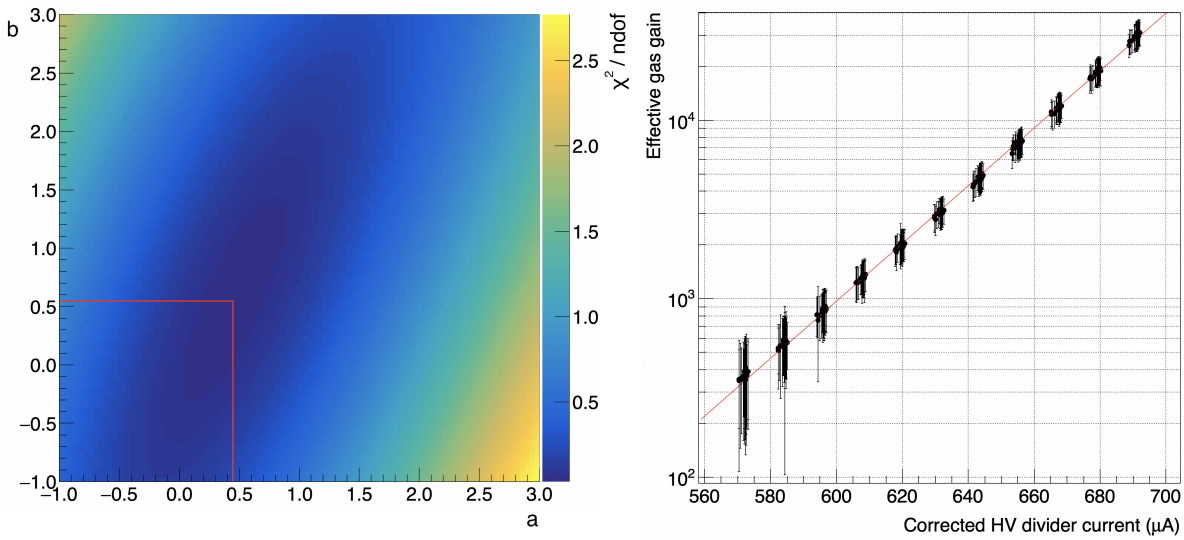

(a) $\chi^2/ndof$ of fit, varying a,b.

(b) Average gain with optimized correction.

Figure 5.38: On the left, reduced χ^2 of the exponential fit to the data of the 46 subsequent effective gas gain test as a function of the exponents a and b for the environmental condition correction. The a and b values corresponding to the minimum of the reduced χ^2 have been applied to the correction of the divider current to obtain the plot on the right.

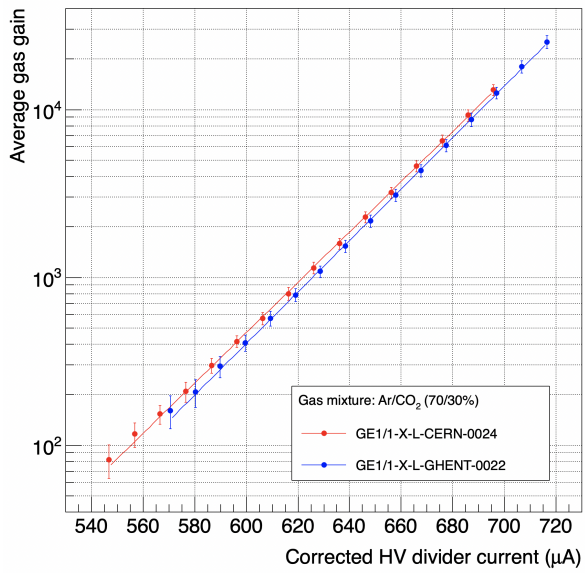

Figure 5.39: Effective gas gain curves of the chambers GE1/1-X-L-CERN-0024 and GE1/1-X-L-GHENT-0022 after having applied to the equivalent divider current the empirical corrections for the environmental pressure and temperature. The exponents utilized were $a = 0.433$ and $b = 0.547$.

5.3.7 Conclusions on efficiency

The efficiency studies presented in this chapter allowed to globally characterize the detectors as a whole, combining the structure, the electronics and the services. Indirectly, this performance parameter has also shed some light on subtle issues that were impossible to spot on previous

quality control steps. Finally, it gave the chance to acquire a better understanding of fine details of the GEM physics and the utilized electronics.
The most important conclusion is that the GE1/1 efficiency performance satisfies the requirements. Each of the layers of a fully functional GE1/1 detector tested at its optimal high voltage working point exhibits the following performance:

- An average efficiency above 95% for MIPs;
- An efficiency larger than 90% for all the 24 readout partitions.

The relaxed condition on the single readout sector derives from the uncorrectable geometrical biases of the GEM cosmic stand presented in section 5.1.5. Each of the special cases has been individually examined and reviewed before to declare the detector validation. If the cause of the inefficiencies was discovered to reside in the chambers, dedicated follow up studies were performed, as presented in section 5.3.6. In the cases of marked non uniformities within the chambers, ad-hoc threshold settings and high voltage fine tunings were put in place to comply with the specifications. This has helped the GEM community as a whole to gain experience in the operations of these large size GEM detectors, that will be employed in the CMS experiment.

Implications for the future CMS GEM detectors:
Thanks to what has been presented in this section, improvements in the design of the GE2/1 and ME0 detectors have been introduced to ensure the flatness of the readout and drift PCBs. Moreover, additional tests will be performed during the future quality control to catch imperfections at an early stage. Lastly, a more precise gas gain dependence on the environmental conditions will allow an effective match of the several modules present in the other stations of CMS GEM detectors.

5.4 Cluster size

One of the main characteristics of an electron avalanche is its size. More specifically, what has an impact on the performance of a gaseous detector is the spread around its central axis of symmetry. Since the avalanche is a statistical process that involves a large sequence of scatterings, its profile can be approximated by a Gaussian curve, with a standard deviation described by the formula

$$\sigma(t) = \sqrt{2Dt}, \tag{5.9}$$

where D the diffusion coefficient, and t the elapsed time. The theoretical formulation of D has been reported in section 2.3.2.
Empirically, it is possible to study the size of the avalanches by scrutinizing the number of strips involved in each of the recorded hits, i.e. the cluster size. Multiplying the cluster size by the strip width in the region of the hit, one can attribute a transverse size to the avalanche in the direction across the strips (ϕ).
A typical cluster size plot for a chamber in a cosmic ray test can be seen in Figure 5.40. In

this specific case, the mean value of strips involved by an avalanche is 2.63 ± 0.008. Considering that the recorded hits do not retain any information about the signal amplitude after the VFAT processing, it is only possible to attribute to them a flat distribution over the involved strips. With an average strip width of about 838 ± 17[5] µm in the i$\eta = 4$ partition (calculated with data in Table 2.3), the mean value of the avalanche spread can be estimated as $\langle\sigma\rangle = \langle cluster\ size\rangle \cdot \langle strip\ width\rangle/\sqrt{12} \approx 650$ µm. This value only serves as a rough approximation of the avalanche characteristic width, and it will be compared to the result of a more refined analysis later in the text.

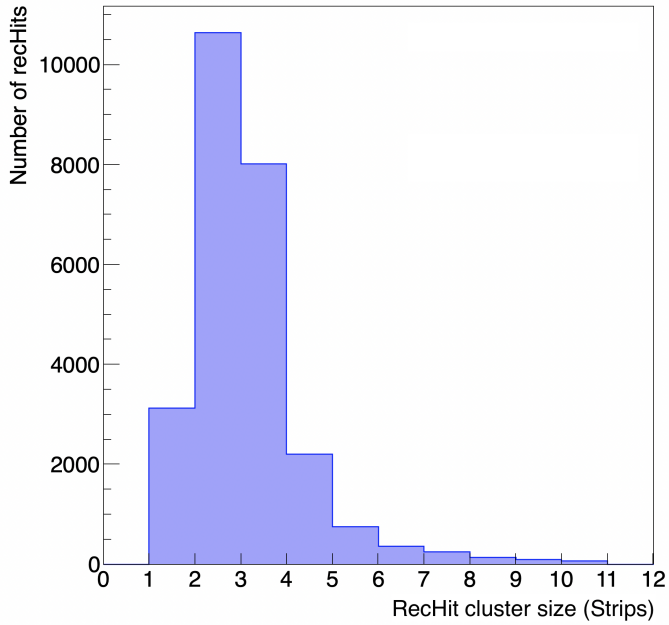

Figure 5.40: Cluster size plot for the hits recorded in the i$\eta = 4$ partition of the chamber GE1/1-X-S-PAK-0013 in a cosmic ray test. The mean value amounts to 2.63 strips, while the sigma is 1.28. The detector was operated at an equivalent divider current of 690 µA, which corresponded to a gas gain of about 20000.

5.4.1 Impact of cluster size on operations

The spread of the electrons over the active area of the detector has multiple consequences, both on the signal formation and the signal processing.

First, the spread of the electrons in the avalanche determines the charge density. This has repercussions on the amplification due to the shielding effect of large electron and ion clouds that, drifting in opposite directions, modify the local effective electric field. Hence, wider avalanches provide larger gas gain.

Second, a broad avalanche distributes the charge over many finely segmented readout strips. As a consequence, the signals that come to the individual VFAT channel discriminators are a fraction of the total one. If the fraction is too small, the signal might be lost.

[5]The error on the strip width accounts for the variations in the transversal dimension due to the shape of the radial strips.

Finally, the last implication regards the frontend electronics. In the VFAT shaping circuits an undershoot normally comes after the main peak (section 2.5.5.4). To restore the baseline level, around 500 ns are required[6]. In normal operations, the main peak is much larger than the undershoot. Therefore there is no efficiency loss, even if two consecutive particle hits are closer in time than 20 BXs. Conversely, if the second avalanche is much smaller than the first one, for example a MIP coming after a heavily ionizing particle[7] (HIP), the chance to miss the MIP is non negligible. Thus, the less strips are involved in an event, the less readout area with dead time there will be present.

5.4.2 Results of cluster size studies

In most of the comic rays tests, the chamber cluster size is only checked to be within the expectations, in order to spot potential issues. Instead, for the extended high voltage and threshold scans described in section 5.3.4, it is possible to perform a focused analysis to get a deeper understanding of the cluster size behavior.

First, the average cluster size per chamber can be studied as a function of the high voltage working point. An example is given in Figure 5.41a for the detector GE1/1-X-S-PAK-0013. Contrarily to the expectation of a monotonically increasing cluster size with the HV working point, the data could be well fitted by a quadratic function. The minimum of the parabola is located at an equivalent divider current of 617.5 µA. Interestingly, it corresponds to the crossing point of the two exponential fits of the effective gas gain curve (Figure 5.41b), which is situated at a divider current of around 619 µA.

Second, the cluster size can be studied as a function of the applied frontend thresholds. An example for the GE1/1-X-S-CERN-0012 chamber is presented in Figure 5.42a. Each data point refers to one readout partition in one of the scan runs. The displayed values of both cluster size and VFAT channel threshold result from an average over the readout sector area. The trend suggests a reduction of the recorded hit cluster size for increasing frontend thresholds. A further elaboration of those data allows to extract information about the avalanche shape and size.

First, the results for the VFAT partitions are considered one at a time. Then, the axes are swapped, the cluster size is halved and the data is mirrored. The results for the sector $(i\phi, i\eta) = (2, 5)$ are reported in Figure 5.42b. This representation can be thought as sequence of sections of the average avalanche with horizontal planes at the height of the applied thresholds. Each data point corresponds to the width of every section.

Only the data points that corresponded to an efficiency above 80% were utilized. This cut has been performed in order not to introduce biases in the cluster size measurement. Indeed, when applying large thresholds, only the largest avalanches are recorded, thus giving an overestimation of the average cluster size. This is the main limit of studying the avalanche shape with digital electronics.

By fitting the graph with a Gaussian function, it is possible to infer the charge distribution width

[6]The 20 BXs intrinsic dead time that allows for a complete baseline restoration of the VFAT channels is fully compliant with the required specifications. The maximum rate per channel is indeed 2 MHz by design.

[7]The expected maximum background hit rate given is presented in Figure 4.16, and it is around 1.5 kHz/cm^2. Only a small fraction (in the order of a percent) of it heavily ionizes the gas.

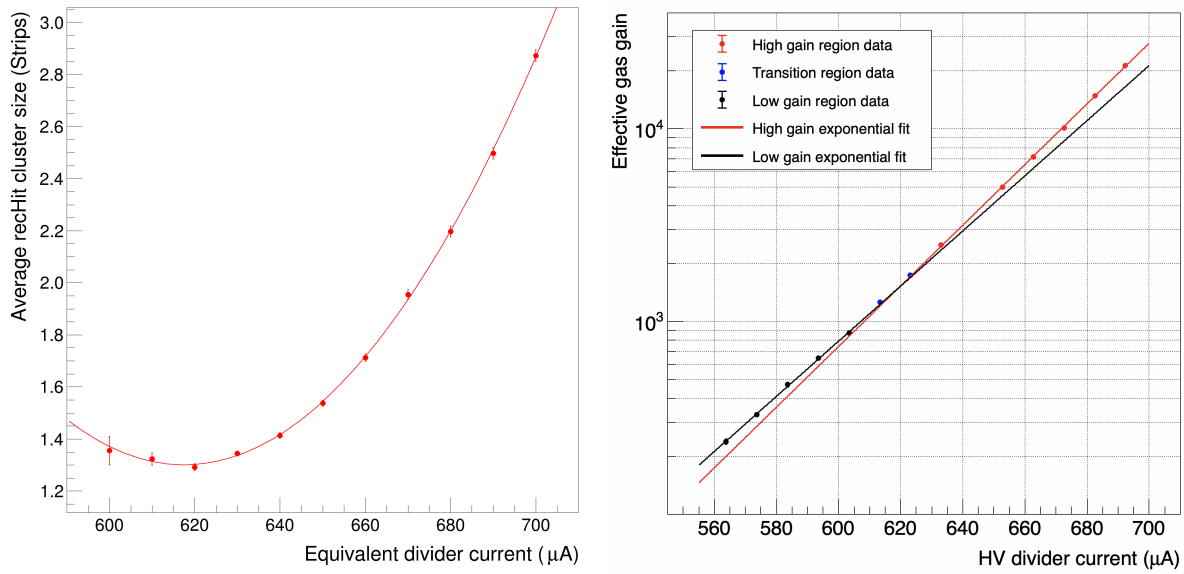

(a) Cluster size as a function of the equivalent HV divider current.

(b) Gas gain curve as a function of the HV divider current.

Figure 5.41: On the left, hit cluster size as a function of the applied equivalent divider current for the chamber GE1/1-X-S-PAKISTAN-0013 in the cosmic rays high voltage scan, fitted with a quadratic function. The increasing cluster size going to low equivalent divider current values may be explained by the relatively low electric fields applied in the gaps, which do not manage to direct the electrons perpendicularly to the chamber surface when exiting the holes, hence their increased spread. On the right, effective gas gain as a function of the applied equivalent divider current of the same chamber. The HV divider current has been corrected to the environmental parameters present during the high voltage efficiency scan. The effective gain manifests a double curve behavior, with a kink between gain 1000 and 2000. The exponential fit for the low gain region is shown in black, the transition data points are depicted in blue, and the exponential fit for the high gain region is shown in red. To ease the visualization of the double curve behavior, the two exponential fits (black and red lines) are extrapolated to the other region. This trend is reflected in the cluster size curve, which exhibits a minimum around the same HV working point.

(standard deviation, σ).

From Figure 5.42b it is possible to extract the width of the average avalanche, which is equal to $\langle\sigma\rangle = 508 \pm 2$ µm. In the other tested chambers, $\langle\sigma\rangle$ varies between 500 and 650 µm. This gives a more precise estimation than the assumption of a flat distribution of the charge over the cluster strips, which provided a slightly overestimated width of about 650 µm.

5.4.3 Conclusions on cluster size

From the studies performed on the cluster size, it was possible to characterize the size and the magnitude of the avalanches in the GE1/1 detectors under normal operations.

The avalanche size has been determined to scale as a parabola with the high voltage working point, with a width of $\langle\sigma\rangle \approx 500 - 650$ µm at an equivalent divider current of 690 µA.

The number of strips involved in one ionization event by a cosmic muon (MIP) in a normally operated chamber with no magnetic fields is around 3, which amounts to one per mille of the

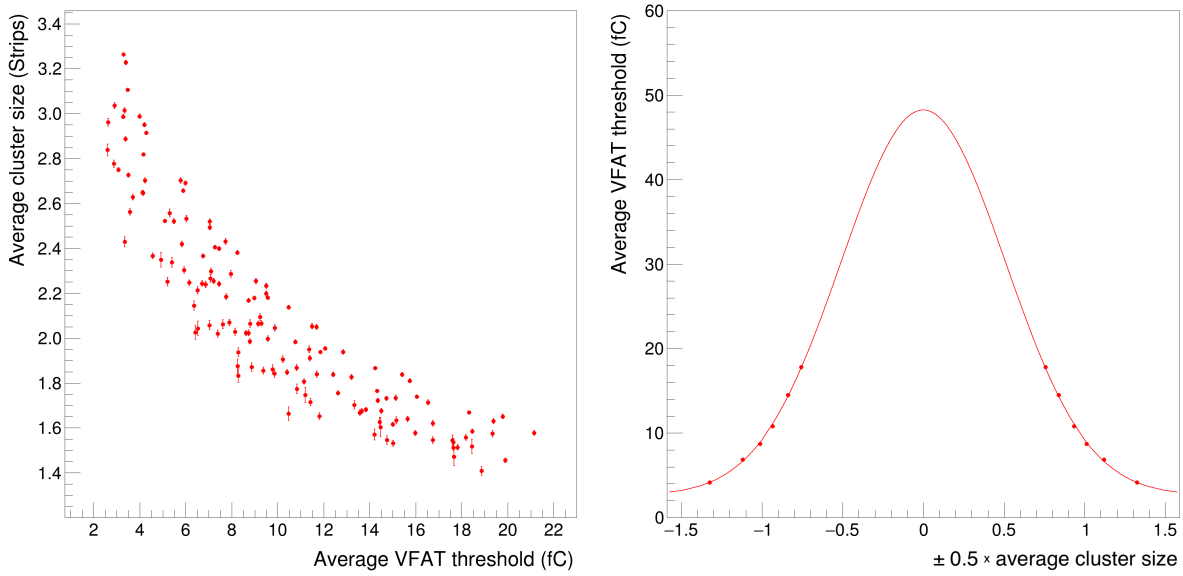

(a) Cluster size as a function of frontend thresholds.

(b) Frontend threshold vs cluster size.

Figure 5.42: On the left, average cluster size of the hits in the GE1/1-X-S-CERN-0012 chamber as a function of the average of the applied frontend thresholds. The chamber was operated at a fixed equivalent HV divider current of 690 µA. On the right, the same two observables shown in the left plot are presented with swapped axes for the readout sector $(i\phi, i\eta) = (2, 5)$; the cluster size values have been halved and mirrored across the vertical axis. A Gaussian fit has been performed on the data points, assuming that the avalanche profile in the $x - z$ plane has a Gaussian distribution.

total chamber active area. From the simulations presented in [34], one can see that the avalanche transverse size in the CMS magnetic field is expected to be around 20% lower, thus giving a smaller average cluster size.

No issues are then foreseen for the frontend electronics in terms of capability to sustain the rate of particles produced by LHC that will interact with GE1/1.

5.5 Spatial resolution

The last performance parameter that has been analyzed is the spatial resolution of the GE1/1 chambers.

To adequately carry out the task of triggering and tracking detectors in the CMS muon endcaps, the GE1/1 chambers will have to provide a precise location of the particle hits. The requirement set by the trigger needs is a combined spatial resolution between GE1/1 and ME1/1 better than 300 µrad. As a clarification, these units do not refer to an actual bending angle of the muon track. Rather, it is the total uncertainty in the measurement of the hit ϕ coordinates in the two subsystems, where ϕ is expressed as an angle.

Being $\Delta\phi = \phi_{GE1/1} - \phi_{ME1/1}$ the interesting quantity for the trigger, the requirement can be expressed as $\sigma(\Delta\phi) < 300$ µm.

In the past years, the ME1/1 intrinsic resolution was around 50 µm [22], equivalent to 21−37 µrad, depending on the radius with respect to the beam pipe. The remainder in the total uncertainty

is shared between the intrinsic spatial resolution of the GE1/1 detectors and the uncertainties on the relative alignment between the chambers of the two subsystems. The multiple scattering is not considered here, since the material budget in between GE1/1 and ME1/1 is very small: only 20 (40) cm of air are present between the second layer of a long (short) GE1/1 super chamber and the first layer of ME1/1.
Therefore, the requirement $\sigma(\Delta\phi) < 300$ µrad provides only an upper limit: the spatial resolution of the GE1/1 chambers needs to be only a fraction of that.
In the following, the algorithm for the evaluation of the GE1/1 spatial resolution with cosmic ray data will be detailed. Finally, the results will be presented and discussed.

5.5.1 Software alignment of chambers for the cosmic ray stand

When the GE1/1 detectors are installed in the cosmic ray stand, they are mechanically aligned by means of screws and aluminum stoppers. The mechanical constraints only grant a precision in the chamber positioning along the x-axis[8] on the order of ±1 mm. Therefore, two super chambers in the same column can have a relative shift of up to 2 mm. Such misalignment has almost no impact on the efficiency calculations, with a loss of at most 0.2% in some of the chamber readout partitions. On the contrary, when assessing the spatial resolution in the ϕ coordinate, any unaccounted displacement in x can spoil the evaluation. Here is where the software alignment comes into play.
Contrarily to the mechanical alignment, which physically moves the super chambers in the stand, the software alignment aims at matching the positions of the detectors in the code with the real ones. This way, the reconstructed hits (recHits) can be correctly placed in the global coordinate system of the stand. As it happens in the stand, the super chambers are considered as single identities in the code. Indeed, the two layers of a super chamber are tightly bound together with no major misalignments between them.
The derivation of the alignment parameter follows a track based alignment method. Due to the GE1/1 coarse segmentation of the strips along the η direction, the standard procedures were not viable and an ad-hoc alignment code was developed. The software is based on the calculation of the residuals of the recHits against the reconstructed muon track propagation position, as detailed in the diagram in Figure 5.43. For each pair of iη partitions of a super chamber, the mean of the residual distribution is extracted fitting a Gaussian curve.
The mean of the residual distributions relative to the eight iη partitions are then plotted against the central point of the iη partitions along the y-axis of the stand. An example of this *residual correlation plot* is presented in Figure 5.44. A linear fit provides the two alignment parameters impacting on the spatial resolution calculation: the translation along the x-axis and the rotation around the z-axis.
A single step of software alignment does not provide an adequately accurate set of parameters. Thus, multiple iterations are performed to refine the rotation and translation values. As presented in Figure 5.45 for all the detectors in the extended high voltage scan, a minimum of four steps

[8] Here only the x coordinate is considered, since it has an impact on the calculation of the spatial resolution in the ϕ direction.

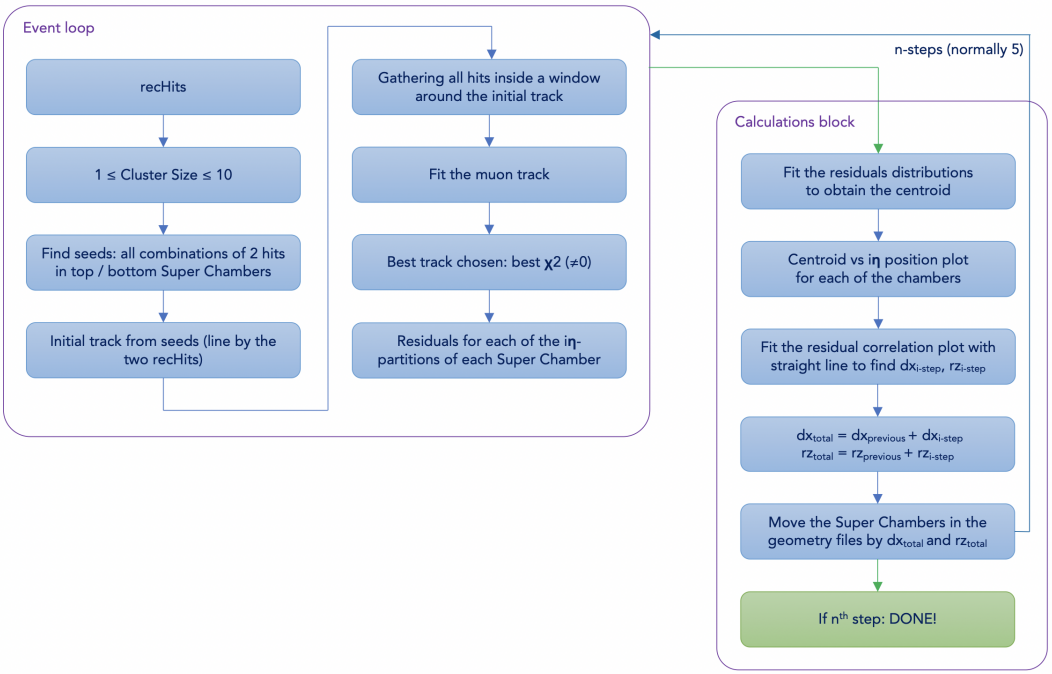

Figure 5.43: Block diagram of the software alignment.

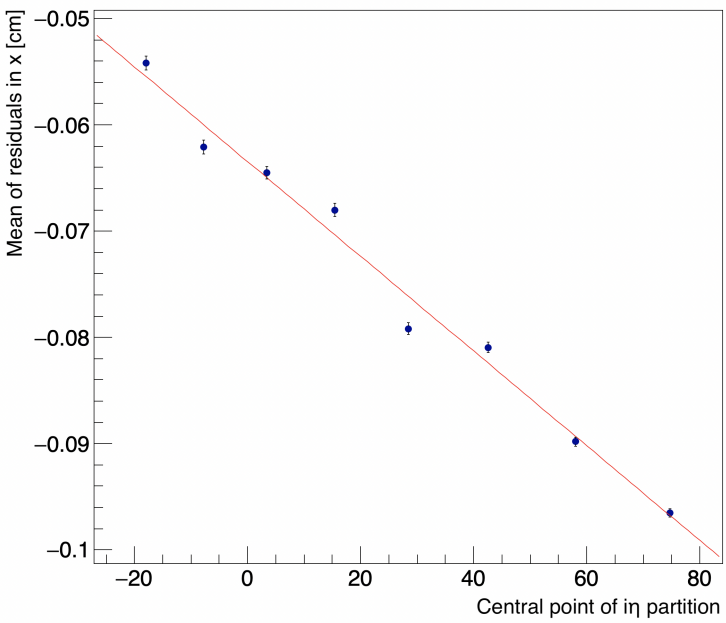

Figure 5.44: Residual correlation plot for the super chamber GE1/1-SCS-0036 in the first step of the alignment procedure in a cosmic rays run. The centroid of the Gaussian fit to the residuals along x for each of the iη partitions are plotted against the mid point of the partitions along the x-axis. The inclination and the intercept of the linear fit refer to the rotation and the translation of the super chamber in the stand.

are required for a full convergence. In order to improve the reliability of the procedure, it has been chosen to fix the number of alignment steps to five.

The last step in Figure 5.45 reported a maximum incremental correction for the translations of $dx_i = 17 \pm 3$ µm, and for the rotations of $rz_i = 26 \pm 7$ µrad.

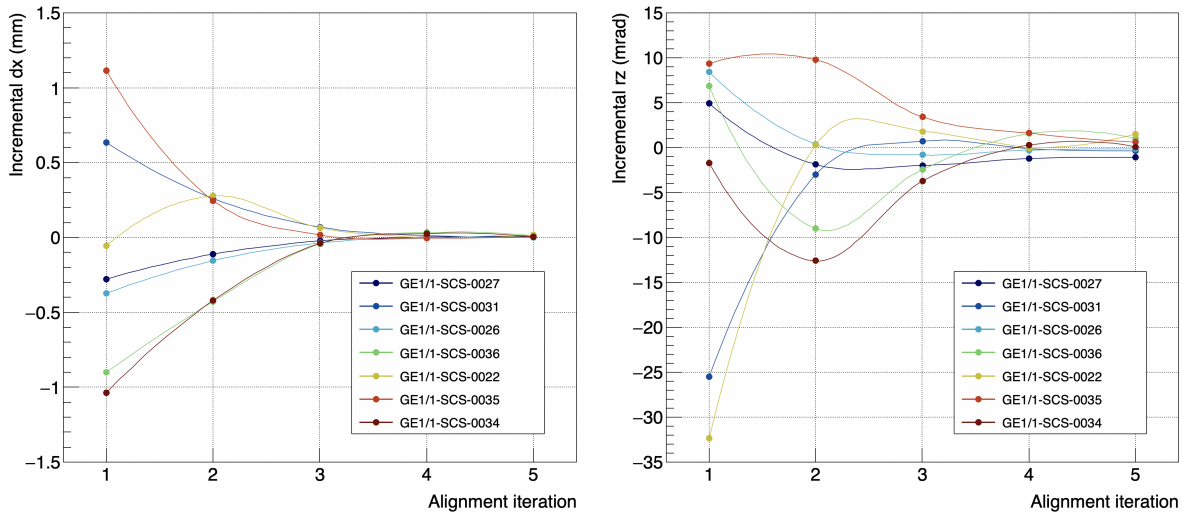

(a) Translation along the x-axis.

(b) Rotation around the z-axis.

Figure 5.45: Incremental corrections applied to the super chambers in the extended high voltage scan for each of the five steps of software alignment. Their convergence confirms a smooth and proper execution of the procedure.

Finally, Figure 5.46 presents the decrease of the reduced χ^2 of the reconstructed tracks over the alignment procedure iterations for the detectors in the extended high voltage scan. The selection applied to the reconstructed tracks in both the distributions is the verticality in the y-z plane, which practically corresponds to muons passing through the same iη partition in all the chambers.
In this case, applying the parameters derived in the iterative software alignment, the mean value of the reduced χ^2 diminishes from 1.12, before the alignment, to 0.59, in the last alignment step.

5.5.2 Spatial resolution results

The minimization of the misalignment influence is an essential component to conduct a proper study on the GE1/1 spatial resolution; still, it is not the only factor that can bias the results.
The cosmic ray stand has no external reference detector that can provide reconstructed tracks. Therefore, the intrinsic limits imposed by the GE1/1 chamber design reflect on the precision of the reconstructed tracks. While for the characterization in terms of efficiency (for which the stand has been conceived) these limits have a minimal impact, the same cannot be said for the spatial resolution. As a consequence, cuts on the reconstructed tracks need to be applied in order to reduce any undesired contribution.
The first cut is a constraint on the angle in the y-z plane. Given the strip geometry and the chamber arrangement in the cosmic stand, the most stringent selection is to require the tracks to cross the same iη partition in all the chambers.
The second cut acts on the x-z plane angle of the track. In this case, the fine division of the readout strips allows to set a precise constraint on the verticality of the track. It has been chosen

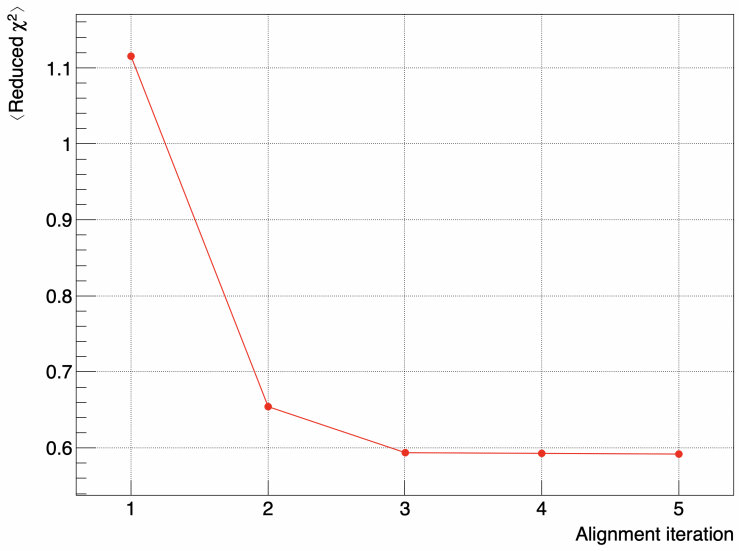

Figure 5.46: Mean value of the reduced χ^2 of the reconstructed tracks over the alignment procedure iterations for the detectors in the extended high voltage scan. The tracks that pass through the same iη partition in all the chambers are selected, as in the spatial resolution studies. The mean value of the reduced χ^2 diminishes from 1.12, before the alignment, to 0.59, in the last alignment step. The errors of the mean values are smaller than the marker size.

to accept angles lower than 5°, which corresponds to the average azimuthal bending angle of muons with $p_T = 10$ GeV in the CMS magnetic field when crossing the GE1/1 chambers [34]. Both the selections can be visualized in the distributions in Figure 5.47.

The first step in the calculation of the spatial resolution is the muon track reconstruction excluding the hits in the layer under study. The tracks are then selected as presented in Figure 5.47, and finally propagated to the test chamber. The intersection between the detector readout plane and the propagated trajectory defines the, so-called, *trajectory hit*. The closest recHit found in a window of ±5 cm in x around the trajectory hit and within the same iη partition is considered the *confirming hit*. A very similar procedure is also adopted for the efficiency calculation. In this case, though, the accent is not put on the presence of the confirming hit, but rather on the distance between the confirming hit and the trajectory hit.

In terms of detection performance, the parameter of interest is the width of the distribution of $\Delta x = x_{confirming\,hit} - x_{trajectory\,hit}$. Indeed, this is the convolution of the GE1/1 chamber intrinsic resolution and the component along the x-axis of the track propagation error (tpe_x). The spatial resolution in metric units can then be calculated with the formula

$$Resolution\,(x) = \sqrt{(\sigma\,(\Delta x))^2 - \langle tpe_x \rangle^2}\,. \tag{5.10}$$

Typical distributions of Δx and tpe_x for a chamber iη partition are presented in Figure 5.48. For the iη region in the plot, $\sigma\,(\Delta x)$ is equal to 370±10 µm, and the mean value of the tpe_x amounts to 273±2 µm. The intrinsic spatial resolution is 250±15 µm, which is compatible with the expected value given by the strip width and the digital readout electronics: $Resolution\,(x)^{Theoretical} = strip\,width/\sqrt{12} = 242$ µm.

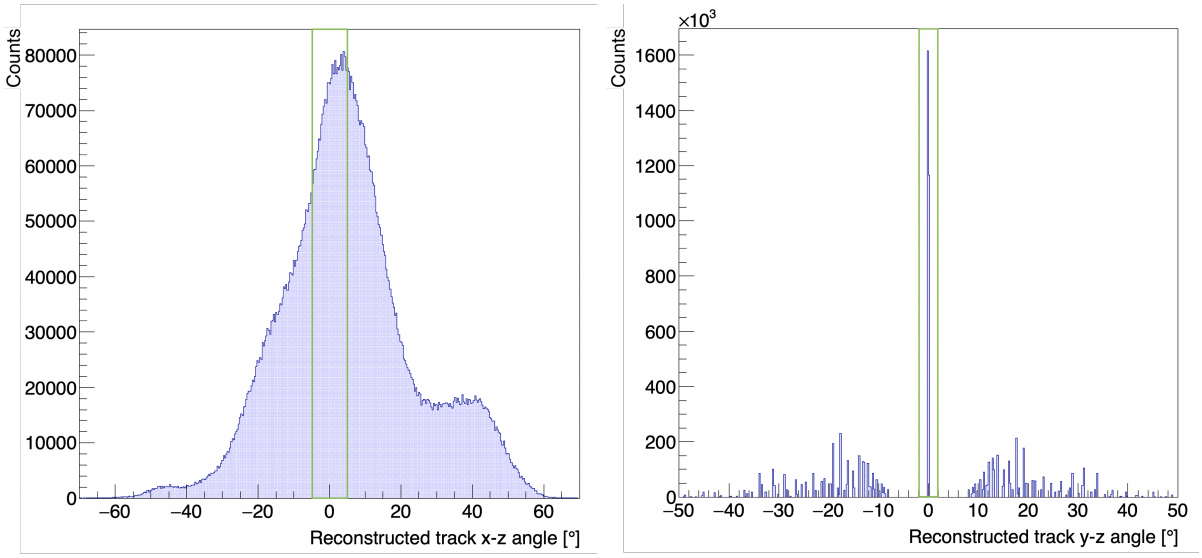

(a) Cut on $x - z$ plane angle.

(b) Cut on $y - z$ plane angle.

Figure 5.47: Cuts applied to the reconstructed track angles in the spatial resolution analysis. For the angle in the $x - z$ plane, the cut has been set to 5°. In the $y - z$ plane, the tracks are required to pass through the same iη partition in all the chambers in the column by selecting the central peak (around zero); the structures outside the central peak are due to reconstructed tracks crossing different combinations of iη partitions in the chambers in the column. The angular distributions are relative to one of the runs at the cosmic ray stand.

The residuals and the track propagation errors for each of the iη partitions of the chamber are then converted into angular units and merged into a single distribution. The GE1/1-X-S-PAK-0013 chamber operated at an equivalent divider current of 700 µA has $\sigma(\Delta\phi) = 205 \pm 2$ µrad and $\langle tpe_\phi \rangle = 132.1 \pm 0.3$ µrad. Its intrinsic resolution results then 157.1 ± 2.8 µrad.
All the tested long and short detectors exhibited a spatial resolution in the interval $150 - 200$ µrad, as presented in Figure 5.49. Comparing these values to the expected one from the strip width, 133.2 µrad, they appear overestimated. This can be due to a residual misalignment of the chambers after the software procedure, to the intrinsic uncertainties given by the radial strip length, and to the multiple scattering of the cosmic muons on the up to 10 layers of chambers in the stand columns. On the other hand though, the most important result of the study is the proof that the GE1/1 intrinsic spatial resolution is well within the requirements.

5.5.3 Further results of the resolution studies

To understand the spatial resolution dependence on the chamber working point and the applied frontend thresholds, the data from the same scans described in section 5.3.4 have been analyzed. On the left of Figure 5.50 is presented a typical plot of the spatial resolution against the applied equivalent divider current. The trend is almost flat for all the tested chambers, especially for equivalent divider currents greater than 650 µA. At low HV working points, variations are recorded due to the lower efficiency and, therefore, the reduced statistics.
On the right side of the figure, the dependence of the resolution on the frontend thresholds is presented. As for the HV working point, the recorded trend is rather flat for all the probed

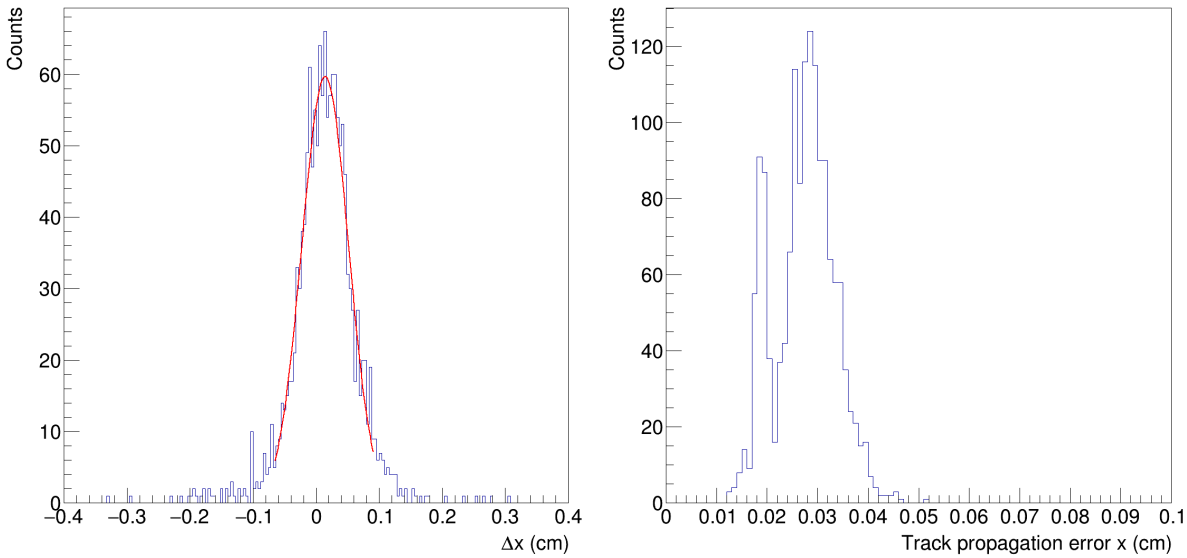

(a) Distribution of the residuals along x.

(b) Distribution of the component along x of the track propagation error.

Figure 5.48: Residuals (left) and track propagation errors (right) along the x-axis for i$\eta = 4$ of the chamber GE1/1-X-S-PAK-0013 operated at an equivalent divider current of 700 µA. The multiple structures present in the right plot stem from the combinations of the cluster size of the hits contributing to the track reconstruction. The standard deviation of the residual distribution amounts to 370 ± 10 µm. The mean value of the track propagation errors equals to 273 ± 2 µm. The obtained intrinsic spatial resolution along the ϕ direction is 250 ± 15 µm.

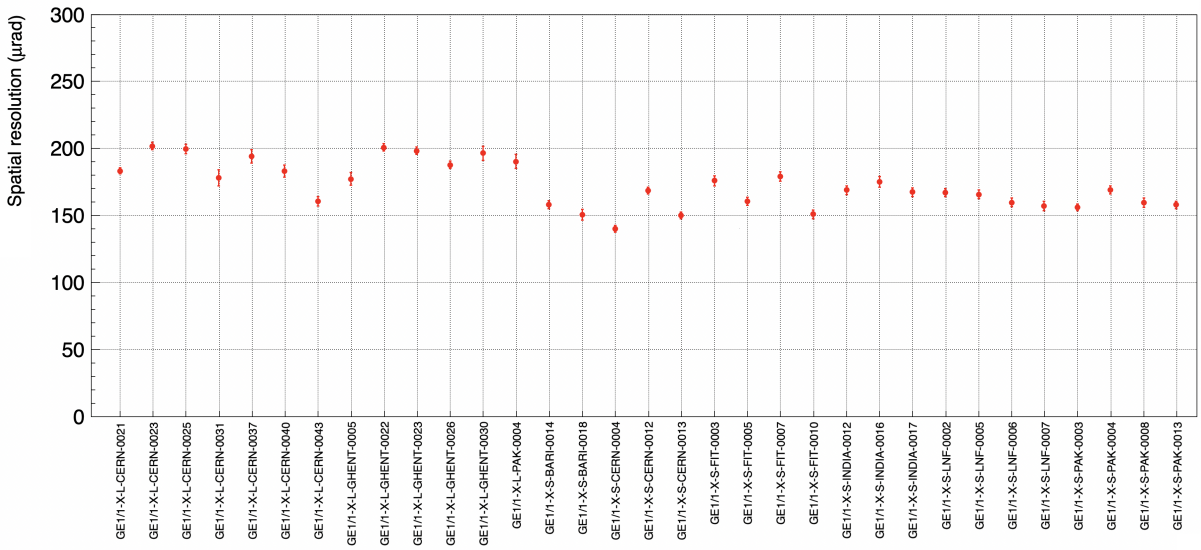

Figure 5.49: Spatial resolution in ϕ for a significative subset of GE1/1 chambers operated at an efficiency plateau HV working point. All the chambers exhibit a spatial resolution in the interval $150 - 200$ µrad, well below the imposed limit of 300 µrad.

chambers.

Everything considered, for a chamber operated in standard conditions, the spatial resolution

does not significantly depend on the working point, nor on the thresholds. For the entire range of applied settings, the requirements were greatly satisfied.

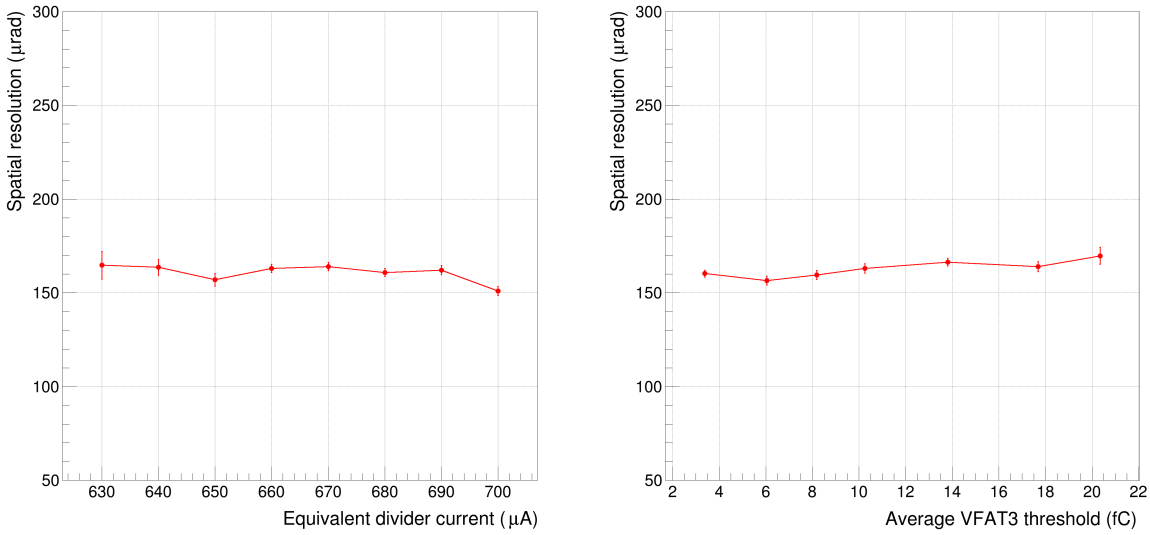

(a) Average spatial resolution against HV.

(b) Average spatial resolution against average frontend thresholds.

Figure 5.50: Spatial resolution of the chamber GE1/1-X-S-CERN-0013 as a function of the applied equivalent divider current (left) and the average frontend thresholds (right). An almost flat trend has been recorded for both, especially around the usual working point.

5.5.4 Basin effect impact on spatial resolution

In a cosmic rays run with a suboptimal HV working point, the chamber GE1/1-X-L-CERN-0025 has shown an evident efficiency basin effect, with efficiency values of around 50% in the VFAT14 partition. The chance has been taken to check the influence of the enlarged induction and drift gaps on the spatial resolution. The spatial resolution in ϕ is presented for the 24 VFATs of the chamber in the left plot in Figure 5.51. It can be noticed that the spatial resolution degrades around the sector $(i\phi, i\eta) = (2, 2)$. A good correspondence can be found when comparing the spatial resolution and the efficiency maps in Figure 5.51.

Even though in the readout sector $(i\phi, i\eta) = (2, 2)$ the spatial resolution along ϕ is 350 µrad, the average value over the entire active area is within the acceptance criteria.

The same correlation has been observed in the other chambers affected by the basin effect. The most severe case (GE1/1-X-L-PAK-0005) exhibited a spatial resolution of 400 µrad in sector $(2, 2)$, where the efficiency was 48.1% at an HV working point of 710 µA. That chamber was rejected in the validation step.

It was also discovered that, conversely to the efficiency, the spatial resolution in the affected regions does not improve for higher gas gain settings. This confirms the results presented in Figure 5.50, suggesting that the spatial resolution is influenced only by large variations of the gap thickness and the applied electric fields, like the ones caused by the bending of the drift and readout PCBs.

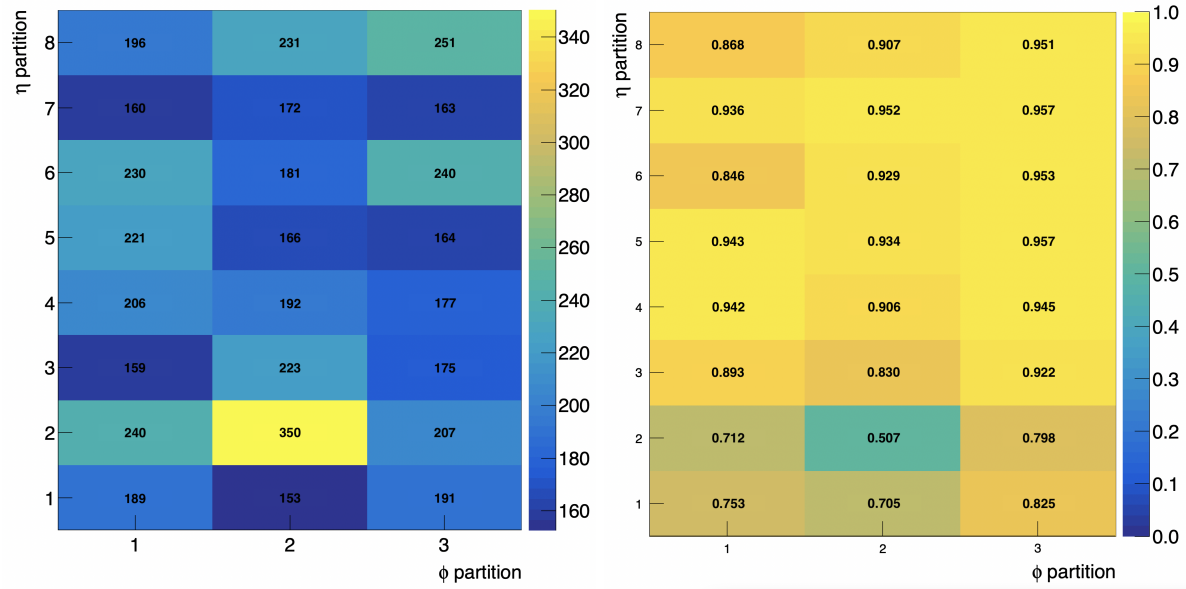

(a) Map of spatial resolution per VFAT partition.

(b) Map of efficiency per VFAT partition.

Figure 5.51: Maps of spatial resolution in ϕ in µrad units (left) and efficiency (right) for the chamber GE1/1-X-L-CERN-0025 in a cosmic rays run with a suboptimal HV working point. It results clear that a pronounced basin effect gives rise not only to a lower efficiency around the sector $(i\phi, i\eta) = (2, 2)$, but also to a degraded spatial resolution.

5.5.5 Conclusion on spatial resolution

The studies performed on the GE1/1 spatial resolution have proven excellent performance, well within the value required for the first GEM station to improve the CMS muon endcap Level 1 trigger.

The high voltage working point and the frontend thresholds have little influence on the spatial resolution. Conversely, the basin effect locally worsens the spatial resolution. Overall, though, the average spatial resolution over the entire area of the affected chambers satisfies the requirements.

Chapter 6

Conclusions on the GE1/1 performance

The previous chapters provided a thorough description of the GE1/1 detector performance. Initially, the components were presented emphasizing the main characteristics and properties. This guided the predictions on their interactions once assembled into the final detectors. Subsequently, the strong points and the issues of the assembled super chambers were delineated. In-depth analyses defined workarounds and solutions to overcome the imperfections, which were explained along with their implications. Finally, the main performance results were shown.
The reported tests determined the GE1/1 detector capabilities, and expanded the knowledge about the fundamentals of the GEM technology. The experience gained in the chambers tests is essential for the CMS operations.

6.1 Principal results and compliance with the requirements

The comparison between the examined GE1/1 performance figures and the requirements listed in chapter 3 shows that overall the imposed requisites are satisfied.

6.1.1 Gas gain

The average effective gas gain tests confirmed an exponential increase with the applied HV working point, reaching a gain of 20000 when applying an equivalent HV divider current of 690 µA. A new correction for the pressure and temperature influence on the gas gain was developed, allowing to precisely account for variations in environmental parameters.
The short chambers exhibited a gain non-uniformity over their active area of (12.6 ± 0.4) % on average and a maximum of 24.1%; the long chambers had an average of (19.6 ± 0.7) % and a maximum of 33.9%. Thus, the obtained gas gain uniformity results are well within the imposed 37% requirement.
The observed non-uniformities are expected given the chamber large area - for the first time GEM detectors cover a surface of around 0.5 m^2. The better uniformity attained in short chambers can be explained by their 20% reduced length with respect to the long chambers. Consequently, this influences the uniformity of the other performance parameters.

6.1.2 Detection efficiency

The mean value of the recorded GE1/1 average detection efficiency was $(97.3 \pm 0.2)\,\%$ for short chambers and $(96.6 \pm 0.2)\,\%$ for long chambers.
To reliably and continuously attain such an efficiency, a new high voltage training procedure was introduced. Additionally, an ameliorated threshold derivation was established employing a new concept of channels response trimming. This reduced the applied frontend thresholds by 40%.
The non-uniformities of the gas gain are reflected in the efficiency measurements. 13 out of 78 long detectors exhibited an efficiency degradation around the $(i\phi, i\eta) = (2, 2)$ readout partition (basin effect). This stems from the outwards bending of the readout and drift PCBs, that causes larger drift and induction gaps with diminished electric fields, hence a reduced effective gas gain. Therefore, the basin effect can be compensated by an increase of the HV working point and a simultaneous reduction of the local frontend thresholds. Larger noise rates have to be accepted: 1000 Hz per readout partition, instead of the usual 100 Hz. These values are well below the expected total background rate of 10^6 Hz per readout partition. Such measures allow to increase the $(2, 2)$ readout partition efficiency by up to 30%.
Everything considered, the GE1/1 detectors satisfy the imposed requirement of an average efficiency over the chamber area above 95% for MIPs.

6.1.3 Spatial resolution

The GE1/1 spatial resolution in the ϕ coordinate was tested for a significant subset of long and short chambers, including detectors affected by the basin effect.
All the studied chambers have an average spatial resolution in the interval $150 - 200$ µrad, therefore well within the required 300 µrad.
The long chambers manifesting the basin effect exhibited a local spatial resolution increase in the $(2, 2)$ readout sector up to 350 µrad. The very restricted area affected by this mild excess did not compromise the overall average chamber resolution, which in all cases was below 200 µrad.

6.2 Final thoughts

The most important result of this thesis is the compliance of the GE1/1 performance with the requirements, validating the chambers for installation in CMS.
The steps coming after the assembly and the quality controls are described in the next chapter. Initially, the journey from the CERN GEM laboratory to the CMS endcaps is shown, followed by the initial results obtained in the experiment.

Chapter 7

An outlook on the GE1/1 integration in CMS

The positive results that have been presented in the previous chapters allowed to validate the GE1/1 super chambers for the installation in the CMS experiment.

7.1 The GE1/1 installation in CMS

In July 2019, the first two detectors were installed in the negative endcap. This allowed to test the insertion procedures and to define and establish a series of tests to verify the chambers integrity in all the stages. Indeed, the transportation between the GEM laboratory in the CERN Prevessin site (FR) and the CMS site in Cessy (FR) takes place on around 12 km of public roads by means of a dedicated trolley loaded on a truck. After that, when at the CMS site, the transportation trolley has to be lowered down to the experimental cavern by a crane. In all these manipulations, any abrupt acceleration might cause damages to the structure or to the electronics.
A quick check with the MEGGER was performed on the GEM electrodes to spot disconnections or short circuits and ensure the foils integrity. Moreover, a fast check of the electronics (*trolley test*) was introduced before the departure and after the arrival at the experimental cavern in order to spot electronics issues.
The aforementioned process is described in pictures in Figure 7.1.
The initial installation has been followed by the completion of the negative endcap with the remaining 34 GE1/1 super chambers between September and October 2019. Finally, the positive endcap detectors installation has been carried out between July and September 2020.
The installation process of a GE1/1 detector is performed with the aid of a dedicated jig. It can be seen in the form of a yellow metallic frame in the pictures in Figure 7.2, where some phases of the installation are depicted. The pivot pin slides in a rail that guides the narrow basis of the super chamber to its final position. Once fully inserted, the L-brackets on the wide basis are fixed by means of screws to dedicated supports installed on the CMS endcap disk.
Once the detectors are in place, the services can be plugged. This includes the connection of gas and cooling pipes, high and low voltage cables, RADMON sensor cables, optical fibers and

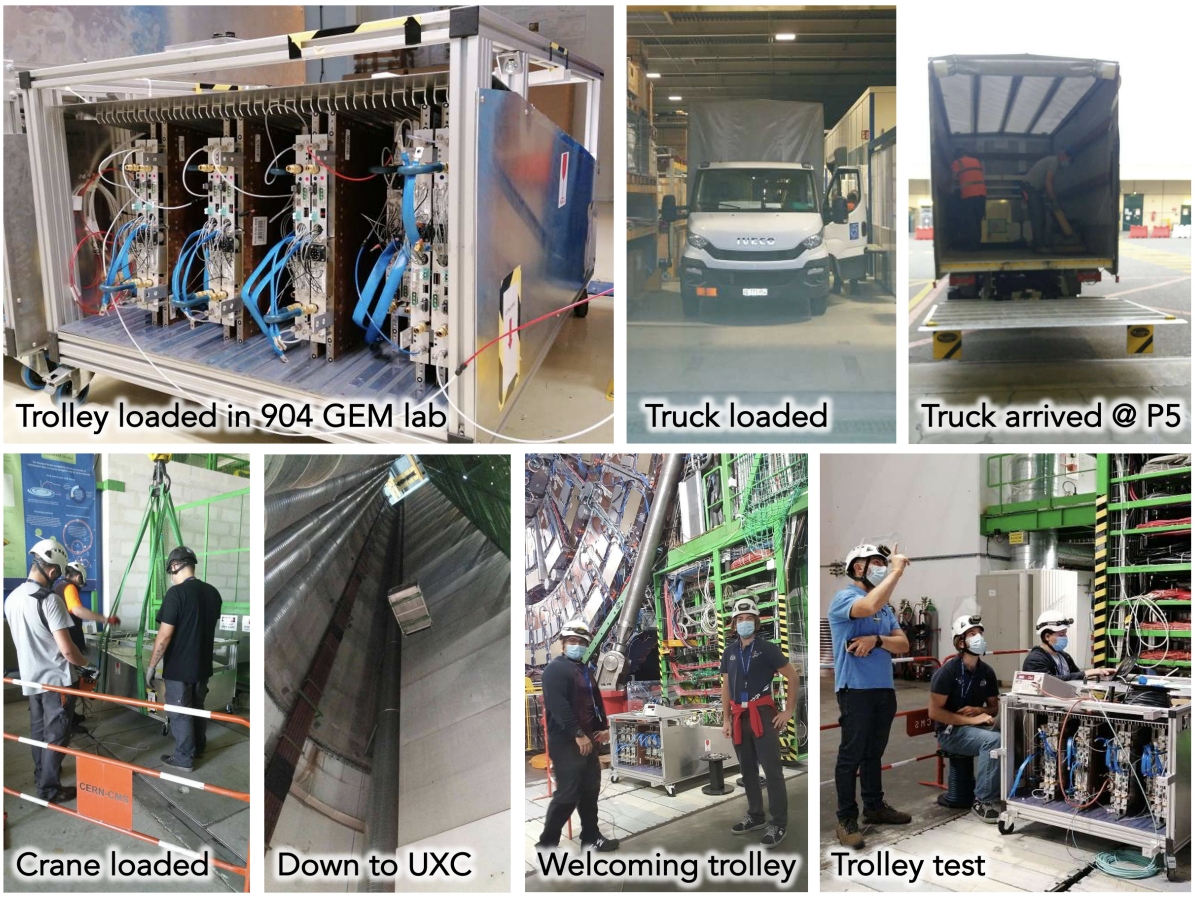

Figure 7.1: Collage of pictures taken by the GEM group during the the GE1/1 transportation and tests.

safety ground cables. All the services were tested prior to the GE1/1 chambers installation and their proper functioning was verified. Subsequently, dedicated checks were performed to ensure no leaks and the correct fastening of the connectors.
Pictures of the installed GE1/1 detectors can be seen in Figure 7.3.

7.2 The GE1/1 commissioning in CMS

The phase that follows the installation of the detectors in the experiment is called *commissioning*. It corresponds to an intense period of tests that aims to establish the optimal functioning of the whole system. The process can be ideally divided into two main parts, *local* and *global* commissioning, which will be delineated in the following sections, including brief descriptions of the individual tests and the preliminary results obtained.
Even though the two commissioning parts will be presented separately, in reality they take place at the same time with interleaved activities, depending on the needs and the system availability. Indeed, the operations in the CMS environment are bound to the general schedule, resulting as a compromise among the plans of all the CMS subsystems.

Figure 7.2: Collage of pictures taken by the GEM group during the GE1/1 installation.

7.2.1 Local commissioning

In the *local commissioning*, the GE1/1 subsystem is tested in standalone. Initially, all the GE1/1 components are individually scrutinized. This involves both the backend and the frontend, and the links between the two.

First come the checks of the functionality and the mapping of the DCS and DAQ chains. While turning on the chamber voltages one by one, the electronics is pinged via the DAQ and a cross check is done. Subsequently, the integrity of chambers and electronics components can be examined. The conducted tests are an adaptation of the ones performed in the CERN GEM lab, following the sequence QC6-QC7-QC8. The process starts with an HV training in pure CO_2, as in QC6, followed by one in Ar/CO_2, as in QC8. Concomitantly, a QC7-like test is carried out on the electronics. A connectivity check provides the information on the responding links and VFATs. Test pulses are then employed to verify the good status of the readout channels, which also supplies information on the noise level. Finally, a threshold scan is performed monitoring the trigger hits. This investigates the status of the s-bit trigger lines routed between the VFATs and the OptoHybrid board.

The possible non-conformities involving the electronics might be the non-responsiveness of single trigger lines and readout channels or non-communicating VFATs. A group of non-responding VFATs might indicate failures of FEASTs or optical links. For what concerns the chambers, instead, the detectable issues might arise from the HV filters, or from short circuits that develop in the GEM foils.

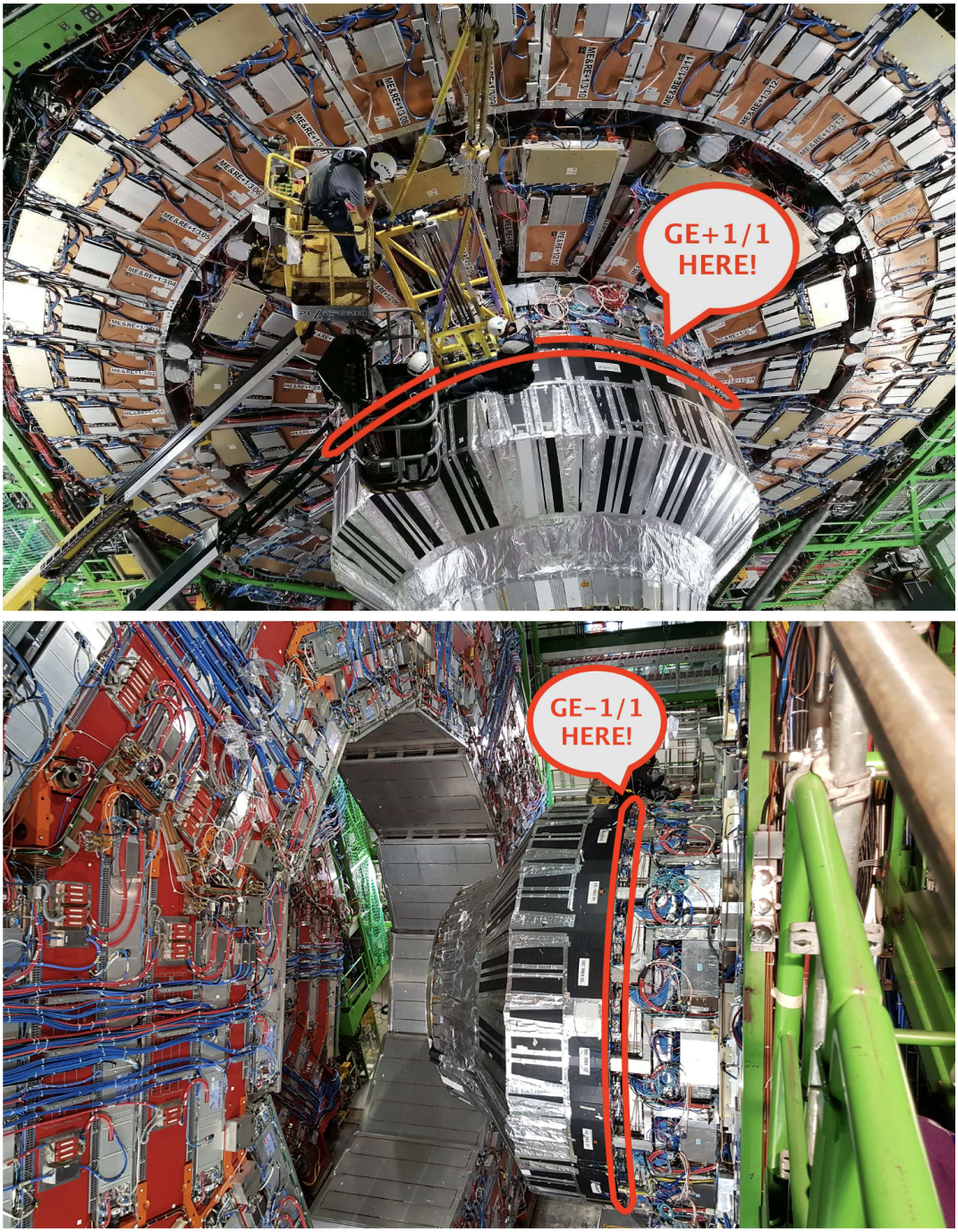

Figure 7.3: Pictures of the installed GE1/1 detectors.

While a short circuit can often be cured in situ and individual non-responding channels and trigger lines are tolerated, the other issues require the super chamber to be extracted and fixed in the laboratory. During the first round of local commissioning of the installed detectors, both in the negative and in the positive endcap some issues were detected, which required the replacement of the affected super chambers with spare ones. The issues involved a short circuit in the HV filter, a faulty FEAST, a grounding issue, non responding VFATs and permanent losses or

instabilities of optical links. In the negative endcap, the substitution of four GE1/1 detectors took place in November 2020, while in the positive endcap, four super chambers were replaced in March 2021.
The second major part of the local commissioning is the frontend configuration. As in the cosmic rays stand, an optimization of the noise level and of the global and local thresholds applied to the channels is required. Those processes, even though with more complications due to the CMS environment, are conceptually identical to the ones performed in the lab.

7.2.2 Global commissioning

The *global commissioning* consists in the activities that aim at the GE1/1 integration with the other CMS subsystems.
First and foremost, the GEM DCS and DSS had to be included in the central systems, in order to grant safe operations when running together with the rest of the CMS detector. As a consequence, all the actions and the alarms can be managed coordinately for every different part.
In parallel, the integration of the readout and trigger chains took place. Such process require a series of activities that are going to take place throughout the whole year 2021, including

- the integration of the GEM data stream into the CMS global data taking;
- the realization and the verification of the GEM-CSC trigger link;
- the inclusion of the GEM trigger into the Endcap Muon Track Finder (EMTF);
- the consolidation of the algorithms to fully exploit the addition of the GE1/1 trigger hits;
- the optimization of the configuration of the frontend and the chambers to attain the desired efficiency;
- the monitoring of the performance of frontend and backend during intensive data taking.

The ultimate target of all these tasks is to provide a complete and reliable configuration of the GE1/1 system, to ensure an optimal data taking with CMS during the LHC Run 3 starting in spring 2022.
Most of these efforts are conducted in cooperation with experts of different CMS subsystems, and involving different GEM areas such as the Run Coordination (RC), the DAQ team, the Technical Coordination (TC), and the Detector Performance Group (DPG). The latter is dedicated to the development of the analyses that evaluate the status and the performance of the GE1/1 detectors, both during the data taking (online) and once the runs are concluded (offline). These include

- the OnlineDQM (Online Data Quality Monitoring) to be integrated with the central DQM;
- the OfflineDQM (Offline Data Quality Monitoring) on the express data stream, with the aim of a fast calculation of the detection efficiency and the hit residuals utilizing the CSC track segments;
- the Offline Prompt Feedback Analysis (PFA), which elaborates the common CMS muon system data to quickly check occupancies, rates and efficiencies utilizing fully reconstructed tracks;

- the Data Certification (DC), that has the task to validate the data collected by GEM in the global data taking;
- the software alignment of the GE1/1 chambers, which is essential to properly handle the trigger hits and to perform the track reconstruction.

7.2.3 Preliminary results from the commissioning

Although at the time of writing (April 2021) the commissioning is still in progress, already many milestones have been reached. These act as a foundation for the steps to come, providing at the same time an encouragement for the future developments.
Since the very beginning of the operations in CMS in 2020, the GEM DCS developers provided a robust DCS version that could control and monitor the power to the chambers, as well as to check the status of the gas and the DSS. Even though it could only be utilized in *local mode* by a GEM operator, it gave the chance to perform many tests both for the local and the global commissioning. At the beginning of 2021, further developments allowed its inclusion in the central DCS system. A picture of the main GEM DCS panel is presented in Figure 7.4.
The first achievement obtained in the global commissioning was the inclusion of a small set of GE1/1 detectors in the global data taking at the beginning of 2020. At that time, the HV training was being performed in pure CO_2, which made possible only to record noise hits.
In the following global data takings, which took place during the so-called Middle Week Global Runs (MWGR), the number of detectors could be gradually increased, compatibly with the ongoing activities in the CMS endcaps. A switch of the gas in favor of the Ar/CO_2 mixture, and the introduction of many fixes and features by the DAQ team contributed to create the conditions for the detection of cosmic muons. Preliminary signs of detected particles were recorded in a frontend latency scan performed in October 2020. In plots like in Figure 7.5a, a clear peak around a latency of 150 BX manifested the presence of in-time muons, contrasting with the scattered random noise hits at the other latency values. This allowed to narrow down the interval to be considered, and in the last MWGR of 2020 came the confirmation of a muon hit peak around the same latency (Figure 7.5b).
After having fixed the latency at 155 BX, GEM participated in a long cosmics run with GE1/1 detectors of both endcaps. Only a reduced number of chambers could actually detect the cosmic ray muons, due to the gas mixture in use and the ongoing activities on the ME1/1 chambers. Nevertheless, numerous muon tracks reconstructed by the CSC could be matched to the GE1/1 hits: the GEM subsystem could therefore declare to have detected its first muons in CMS. An event display of GE1/1 hits matching with a muon track is presented in Figure 7.6.
The path towards the completion of the commissioning still foresees many tasks to be accomplished. The milestones set so far give a good perspective on the future of the GE1/1 subsystem, in preparation of the first proton-proton collisions of the LHC Run 3, scheduled for 2022.

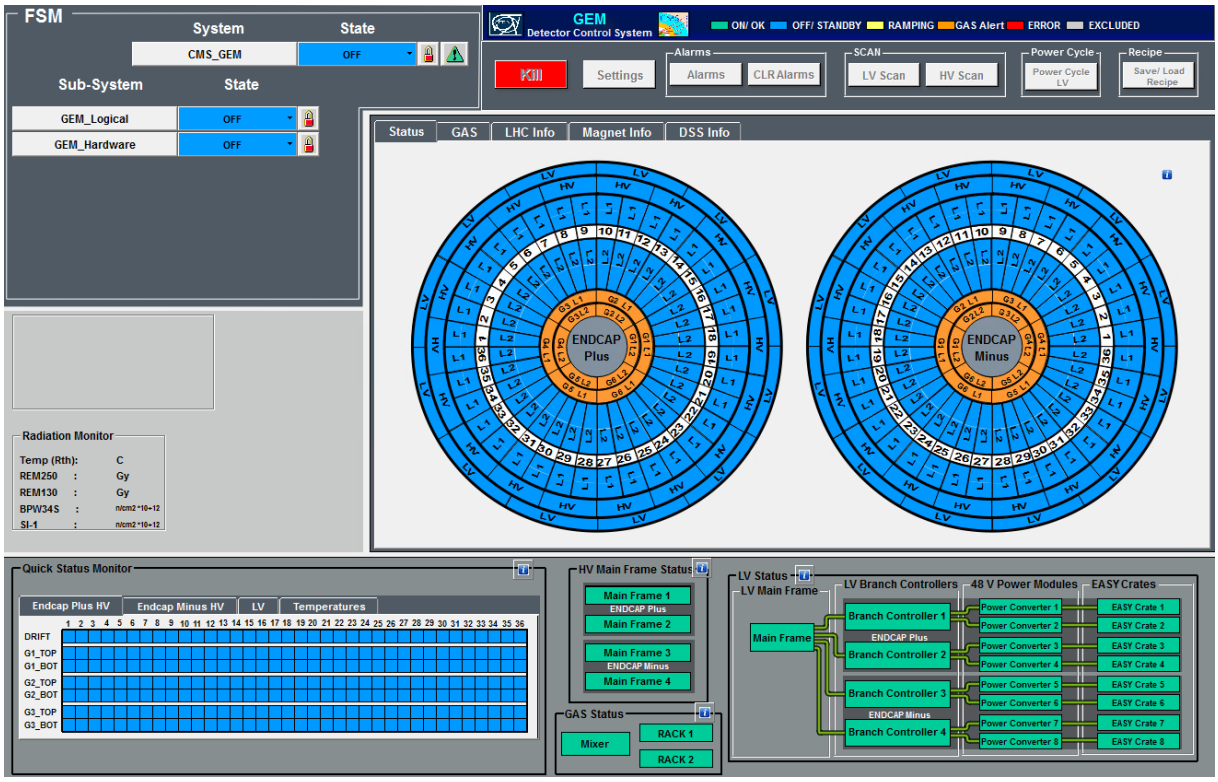

Figure 7.4: GEM main DCS panel. On the top left is shown the status of the main GEM FSM nodes; below that there is the RADMON display. On the top right, a series of buttons allow to quickly act on large parts of the GEM system. For instance, it is possible to kill all the LV and HV power delivery at once, in case of major issues, and to manage the alarms when an issue is detected. In the center is summarized the status of the 144 chambers, arranged in two disks that mimic the positive and negative endcaps. LV, HV and gas can be monitored at a glance, allowing also to modify the individual working points. On the bottom left, the individual channel status is displayed, while on the right is shown the power supply hardware status. Credits to the GEM DCS team.

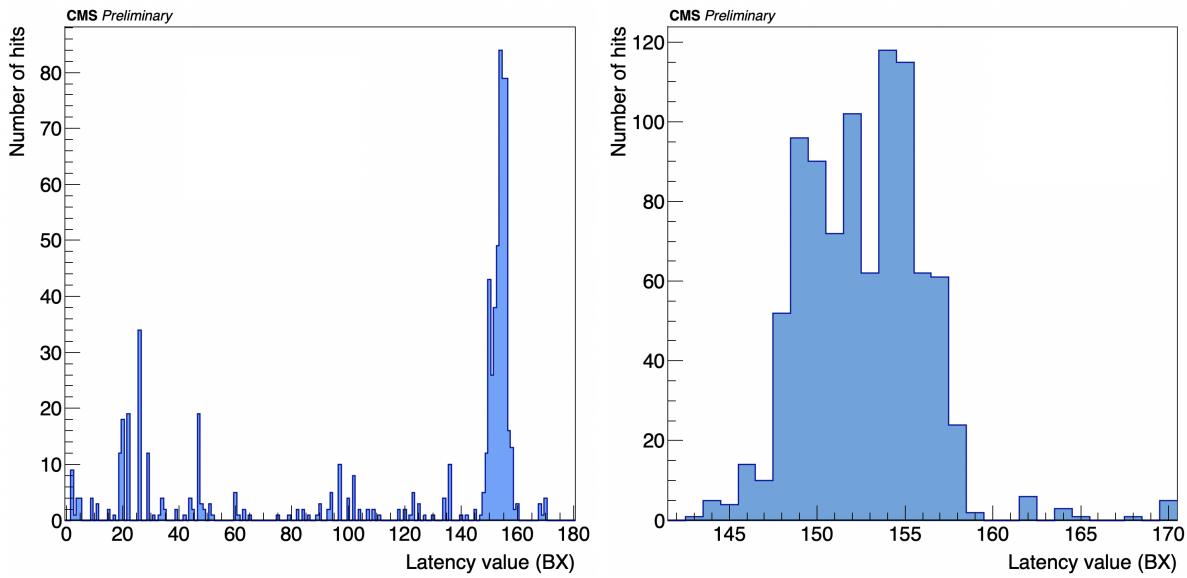

(a) GE11-M-12L2 broad-range latency scan.

(b) GE11-M-12L2 narrow-range latency scan.

Figure 7.5: Frontend latency scan results for the GE1/1 chamber in the slot GE11-M-12L2. A broader interval of values was chosen for the run 337973 (left); subsequently, it was narrowed for the run 338702 (right). In both cases a very distinct peak is found around a latency of 150 BX. In both the runs, the pulse stretch was set to 7 (8 total BXs), which causes the broad width of the peak. Such a large value was chosen to ease the peak identification in the first CMS tests; it will be reduced and optimized in the following operations. Credits to the GEM DAQ team.

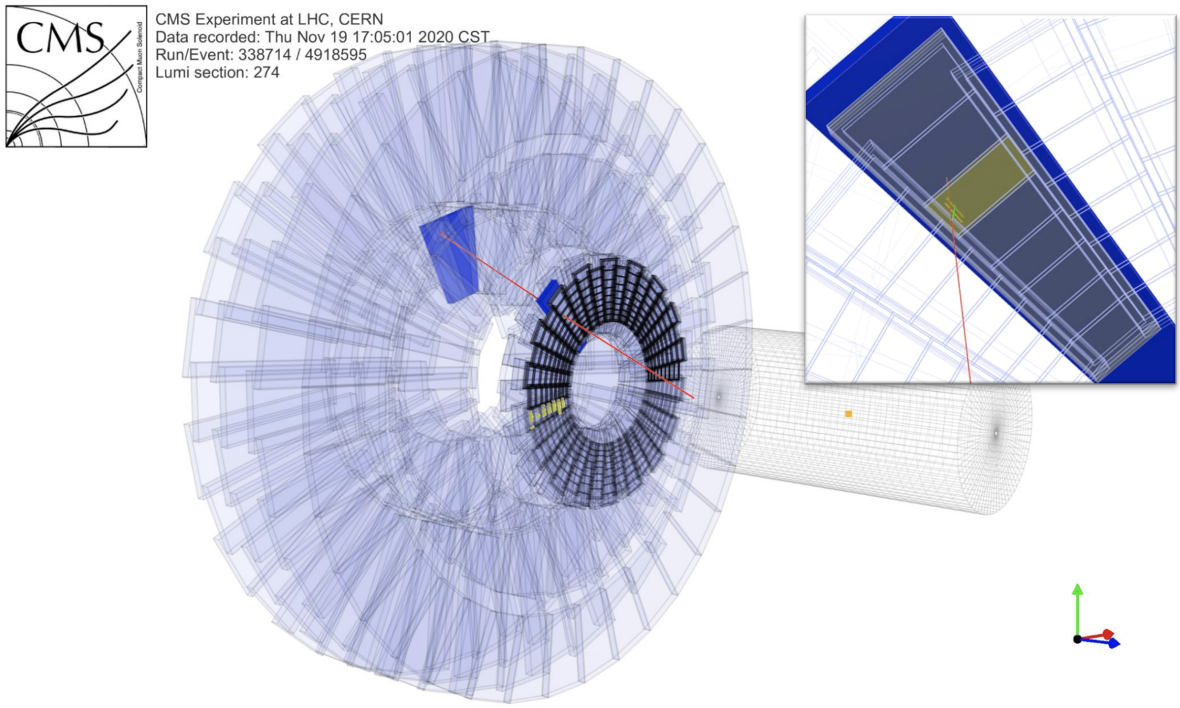

Figure 7.6: Event display of one of the first cosmic ray muons detected by the GEM GE1/1 subsystem in CMS. The GEM chambers are shown in black, with one green track segment reconstructed from the two yellow hits in the two layers of the super chamber traversed by the muon. The non-involved CSCs have blue edges, while the CSC chambers that contributed to the muon track (in red) are depicted in solid blue. Credits to the GEM DPG team.

Acknowledgements

All the work done to complete this thesis would have never been possible without the moral, technical, and also financial support of family, friends, colleagues and working group.
First of all, I want to thank the entire RWTH Aachen CMS group, and especially Professor Hebbeker, Kerstin Hoepfner and Markus Merschmeyer who gave me the chance to embark on this fantastic adventure. They not only created a welcoming working environment in Aachen, but also supported and encouraged the travels around the world. I'm grateful for your supervision and guidance, for your patience in explaining every detail and technicality of the bureaucracy, and for every offered occasion to become a better physicist (Lab course included!).
A big thanks goes also to the Aachen postdocs Carsten, Dima and Shawn that made the life at the physics department (and outside) a great joy. The work done together, the shared knowledge, the enriching discussions, the bike tours and the countless lunches and dinners judging the food will always be part of me. Worth of honorable mention are the two amazing PhD students that shared part of their journey with me: Henning (already a doctor!) and Francesco. All the lively discussions, the little discoveries, the shares successes and the failures, the entire days spent wondering how these darn things work, and why they usually don't, kept my scientific spirit alive. Thanks also for all the trips and tours done together, the beers and the days spent chatting about everything... even physics!
Many thanks also to the CMS IIIA workshops, to Mr. Zantis, Mr. Philipps, Christian and Tim who patiently supported all the technical activities performed in the Aachen labs.
And now, it's time to thank each and every great person who shared the CERN adventures.
Special thanks to Archana, Michele, Gilles, Mohsin, Daniel, Marcello for all the encouragements, the lessons taught, the GEM parties, the coffees, the trips, the wine and cheese on Saturdays. All the moral, technical and physical supports will be never forgotten!
Impossible not to mention all the incredibly knowledgeable amazing GEM friends: (take a breath) Ciccio, Brendan, Federica, Johny, Jeremie, Felipe, Milena, Caterina, Antonello, Agostino, Simone, Davide, Camilla, Laurent, Ilaria, Martina, Marek, Bala, Nimantha, Yasser, Byeonghak, Stephen, Francesco... et al. I'll be always grateful to you for having made life at CERN shine... like a GEM![1] Thank you guys for all the fun, the shared loads, the mountain trips, the barbecues, the dinners[2]: the best team building ever!
And huge thanks to all the other friends in the various parts of the world: Alberto, Erica, Nicola, Daniele, Marta, Jonas, Adam, Gaia. Thanks to you all the downs could be turned into ups.

[1] Poor physicists' jokes... sorry that you had to read that!
[2] Never try to work after GEM dinners: it's not harmful, but quite pointless..!

I want also to express my gratitude to my former supervisor Anna Meneguzzo and to Fabrizio Gasparini, who always followed my steps during the PhD, providing copious valuable advices and continuous support.
Finally, I have to thank my whole family who kept me safe and sound, and full of good Italian food, throughout the PhD years.

Appendix A

List of acronyms

AC: Alternating Current, referred to electronics
ADC: Analog to Digital Converter
ALICE: A Large Ion Collider Experiment
AMC: Advanced Mezzanine Card employed in the µTCA crates
AMC13: CMS-specific µTCA data concentration and clock distribution card
APV25: Analog Pipeline Voltage, frontend chip developed for the CMS tracker
ARM: Arming comparator (VFAT)
ASIC: Application Specific Integrated Circuits
ATLAS: A Toroidal LHC Apparatus experiment
BMTF: Barrel Muon Track Finder
BX: Bunch Crossing, also 25 ns time interval
CBM: Calibration, Bias and Monitoring unit (VFAT)
CERN: European Organization for Nuclear Research
CFD: Constant Fraction Discriminator
CMOS: Complementary Metal-Oxide Semiconductor
CMS: Compact Muon Solenoid experiment
CMSSW: CMS Software
CSC: Cathode Strip Chamber
CTP7: Calorimeter Trigger Processor card, AMC employed in the CMS GEM µTCA crates
DAC: Digital to Analog Converter
DAQ: Data acquisition
DC: Direct Current, referred to electronics
DC: Data Certification, in DPG context
DCS: Detector Control System
DPG: Detector Performance Group
DQM: Data Quality Monitoring
DSS: Detector Safety System
DT: Drift Tube
ECAL: Electromagnetic Calorimeter
EMTF: Endcap Muon Track Finder

ENC: Equivalent Noise Charge, frontend channels' noise in charge units
EYETS: Extended Year End Technical Stop
FBG: Fiber Bragg Grating employed in the GE1/1 temperature sensors
FEAST: Radiation tolerant DC-DC converter
FIFO: First In First Out, referred to buffers
FPGA: Field Programmable Gate Array
FSM: Finite State Machine
GBTX: GigaBit Transceiver ASIC
GE#/#: GEM in the CMS Endcap region installed in disk # / ring #
GEB: GEM Electronics Board
GEM: Gas Electron Multipliers
HB: Hadron Calorimeter in the CMS Barrel region
HCAL: Hadron Calorimeter
HE: Hadron Calorimeter in the CMS Endcap region
HEP: High Energy Physics
HF: Forward Hadron Calorimeter
HGCAL: High Granularity Hadron Calorimeter
HIP: Highly Ionizing Particle
HL-LHC: High Luminosity LHC
HLT: High Level Trigger
HPD: Hybrid Photodiodes
HV: High Voltage
iRPC: improved Resistive Plate Chamber
L1 trigger: Level 1 trigger
L1A: Level 1 Accept
LEP: Large Electron Positron accelerator
LHC: Large Hadron Collider
LHCb: LHC beauty experiment
LS#: Long Shutdown #
LUT: Lookup table
LV: Low Voltage
MAO: CAEN A3486, LV crates' power supply
MB#: Muon Barrel chamber (DT) installed in station #
MCH: MicroTCA Carrier Hub, service card for the µTCA crates
ME#/#: Muon Endcap chamber (CSC) installed in disk # / ring #
ME0: GEM in the CMS Endcap region 0
µGMT: Global Muon Trigger based on µTCA standard
µGT: Global Trigger based on µTCA standards
Micromegas: Micro-Mesh Gaseous Structures
MIP: Minimum Ionizing Particle
MPGD: Micro-Pattern Gaseous Detectors
MSGC: Micro-Strip Gas Counters

µTCA: micro Telecommunications Computing Architecture
MWGR: Middle Week Global Runs
MWPC: Multi-wire Proportional Chambers
NIM: Nuclear Instrumentation Module
NTP: Normal Pressure and Temperature ($p = 1$ atm and $T = 20°$)
OH: OptoHybrid board, CMS GEM frontend communication and trigger board
OMTF: Overlap Muon Track Finder
P5: LHC Point 5, location of the CMS experiment
PCB: Printed Circuit Board
PMT: PhotoMultiplier Tube
PROM: Programmable Read-Only Memory
QC: Quality Control
R&D: Research and Development
RADMON: Radiation Monitor installed in the GE1/1 detectors
RB#: RPC in the CMS Barrel region installed in station #
RC: Run Coordination
RE#/#: RPC in the CMS Endcap region installed in disk # / ring #
RF: Radio frequency
RPC: Resistive Plate Chamber
SCA: Slow Control Adapter ASIC
SLVS: Scalable Low Voltage Signaling
SRAM: Static Random Access Memory
SRS: Scalable Readout System
SX5: Surface Experimental area at LHC Point 5
TC: Technical Coordination
TCDS: Trigger Distribution and Control System
TDR: Technical Design Report
TMB: CMS CSC Trigger Mother Board
TOTEM: TOTal Elastic and diffractive cross section Measurement, LHC experiment
TTC: Timing and Trigger Control (CMS)
USC55: Underground Service Cavern at LHC Point 5
UXC55: Underground eXperimental Cavern at LHC Point 5
VFAT: Very Forward Atlas and Totem, CMS GEM frontend ASIC (it may also indicate the frontend board)
YETS: Year End Technical Stop
ZCC: Zero Crossing Comparator (VFAT)

Bibliography

[1] Lyndon Evans and Philip Bryant, *LHC Machine*, JINST 3 S08001, 2008.

[2] HL-LHC project, *LHC Machine*, https://project-hl-lhc-industry.web.cern.ch/content/project-schedule, April 2020.

[3] The ATLAS Collaboration, *The ATLAS Experiment at the CERN Large Hadron Collider*, JINST 3 S08003, 2008.

[4] The CMS Collaboration, *The CMS experiment at the CERN LHC*, JINST 3 S08004, 2008.

[5] The LHCb Collaboration, *The LHCb Detector at the LHC*, JINST 3 S08005, 2008.

[6] The ALICE Collaboration, *The ALICE experiment at the CERN LHC*, JINST 3 S08002, 2008.

[7] E. Mobs, *The CERN accelerator complex - 2019*, CERN-GRAPHICS-2019-002, 2019.

[8] C. Fluder, E. Blanco-Vinuela, J. Casas-Cubillos, P. Dubert, P. Gomes, M. Pezzetti, A. Tovar-Gonzalez, L. Zwalinski *The Development of the Control System for the Cryogenics in the LHC Tunnel*, 12th Large Scale Systems Symposium, 2010.

[9] B. J. Holzer, *Lattice Design in High-energy Particle Accelerators*, CAS - CERN Accelerator School: Advanced Accelerator Physics, pp.61-100, 2013.

[10] J. Wenninger, *Operation and Configuration of the LHC in Run 2*, CERN-ACC-NOTE-2019-0007, 2013/01/29.

[11] B. Schmidt, *The High-Luminosity upgrade of the LHC: Physics and Technology Challenges for the Accelerator and the Experiments*, J. Phys.: Conf. Ser. 706 022002, 2016.

[12] S. Lusin, *The CMS Detector Power System*, Proceedings of the Topical Workshop on Electronics for Particle Physics, pp.490-493, 2008.

[13] The CMS Collaboration, *The CMS Detector Power System*, https://cms.cern/news/cms-detector-design.

[14] International Organization for Standardization, *ISO 80000-2:2019*, Quantities and units - Part 2: Mathematics, 2019.

[15] CMS Collaboration, *Performance of the CMS Drift Tube Chambers with Cosmic Rays*, JINST 5 T03015, 2010.

[16] The Tracker Group of the CMS Collaboration, *The CMS Phase-1 Pixel Detector Upgrade*, arXiv:2012.14304, 2020.

[17] V. Veszpremi, *Operation and performance of the CMS tracker*, JINST 9 C03005, 2014.

[18] CMS Collaboration, *The Electromagnetic Calorimeter Technical Design Report*, CERN/LHCC 97–33, 1997.

[19] P. Adzic et al., *Energy resolution of the barrel of the CMS electromagnetic calorimeter*, JINST 2 P04004, 2007.

[20] CMS Collaboration, *CMS Technical Design Report for the Phase 1 Upgrade of the Hadron Calorimeter*, CERN-LHCC-2012-015, 2012.

[21] The CMS Collaboration, *Precise Mapping of the Magnetic Field in the CMS Barrel Yoke using Cosmic Rays*, JINST 5 T03021, 2010.

[22] CMS Collaboration, *Performance of the CMS muon detector and muon reconstruction with proton-proton collisions at* $\sqrt{s} = 13\ TeV$, CERN-EP-2018-058, 2018.

[23] CMS Collaboration, *Performance of the CMS drift-tube chamber local trigger with cosmic rays*, JINST 5 T03003, 2010.

[24] D. Acosta et al., *Large CMS cathode strip chambers: design and performance*, Nuclear Instruments and Methods in Physics Research A 453, 2000.

[25] The CMS Collaboration, *The performance of the CMS muon detector in proton-proton collisions at* $\sqrt{s} = 7\ TeV$ *at the LHC*, JINST 8 P11002, 2013.

[26] N.P. Ghanathe, A. Madorsky, H. Lam, D.E. Acosta, A.D. George, M.R. Carver, Y. Xia, A. Jyothishwara, M. Hansen, *Software and firmware co-development using high-level synthesis*, Journal of Instrumentation. 12. C01083-C01083, 2017.

[27] CMS Collaboration, *The Phase-2 Upgrade of the CMS Muon Detectors*, CERN-LHCC-2017-012, 2017.

[28] P. Paolucci et al., *CMS Resistive Plate Chamber overview, from the present system to the upgrade phase I*, JINST 8 P04005, 2013.

[29] K. Bunkowski, *Optimization, Synchronization, Calibration and Diagnostic of the RPC PAC Muon Trigger System for the CMS detector*, CERN-THESIS-2009-160, 2009.

[30] V. Khachatryan et al., *The CMS trigger system*, JINST 12 P01020, 2017.

[31] CMS Collaboration, *Commissioning of the CMS High-Level Trigger with cosmic rays*, JINST 5 T03005, 2010.

[32] A.M. Sirunyan et al., *Performance of the CMS Level-1 trigger in proton-proton collisions at* $\sqrt{s} = 13$ *TeV*, JINST 15 P10017, 2020.

[33] CMS Collaboration, *The Phase-2 Upgrade of the CMS endcap calorimeter*, CERN-LHCC-2017-023, 2018.

[34] A. Colaleo et al., *CMS Technical Design Report for the Muon Endcap GEM Upgrade*, CERN-LHCC-2015-012 ; CMS-TDR-013, 2015.

[35] P.A. Zyla et al. (Particle Data Group), *Review of Particle Physics*, Prog. Theor. Exp. Phys. 2020, 083C01, 2020.

[36] C. W. Fabjan, H. Schopper, *Elementary Particles, Subvolume B: Detectors for Particles and Radiation*, Springer Verlag, Landolt-Börnstein New Series, 2011.

[37] G.F. Knoll, *Radiation Detection and Measurement*, Fourth edition, Wiley, 2010.

[38] W. R. Leo, *Techniques for Nuclear and Particle Physics Experiments*, Second Revised Edition, Springer-Verlag, 1994.

[39] F. Sauli, *Principles of operation of multiwire proportional and drift chambers*, CERN-77-09, 1977.

[40] V. L. Highland, *Some practical remarks on multiple scattering*, Nuclear Instruments and Methods, Volume 129, 1975.

[41] G.Charpak et al., *The use of multiwire proportional counters to select and localize charged particles*, Nuclear Instruments and Methods, Volume 62, 1968.

[42] F. Sauli, *Fundamental understanding of aging processes: review of the workshop results*, Nuclear Instruments and Methods in Physics Research Section A: Accelerators, Spectrometers, Detectors and Associated Equipment, Volume 515, Issues 1–2, 2003.

[43] A. Oed, *Properties of micro-strip gas chambers (MSGC) and recent developments*, Nuclear Instruments and Methods in Physics Research Section A: Accelerators, Spectrometers, Detectors and Associated Equipment, Volume 367, 1995.

[44] Y. Giomataris, Ph. Rebourgeard, J.P. Robert, G.Charpak, *MICROMEGAS: a high-granularity position-sensitive gaseous detector for high particle-flux environments*, Nuclear Instruments and Methods in Physics Research Section A: Accelerators, Spectrometers, Detectors and Associated Equipment, Volume 376, 1996.

[45] J. Manjarres et al., *Performances of Anode-resistive Micromegas for HL-LHC*, Journal of Instrumentation, 2012.

[46] F. Sauli, *The gas electron multiplier (GEM): Operating principles and applications*, Nuclear Instruments and Methods in Physics Research A 805, Pages 2–24, 2016.

[47] J.M. Madson, H.J. Oskam, *Mobility of Argon ions in argon*, Physics Letters A Volume 25, Issue 5, 1967.

[48] J. A. Merlin, *Study of long-term sustained operation of gaseous detectors for the high rate environment in CMS*, CERN-THESIS-2016-041, 2016.

[49] Ö Şahin et al., *Penning transfer in argon-based gas mixtures*, JINST 5 P05002, 2010.

[50] F. Eggenberger, G. Pólya, *Über die Statistik Verketteter Vorgänge*, Z. Angew. Math. Mech. 3, 1923.

[51] S. Bachmann, A. Bressan, M. Capeáns, M. Deutel, S. Kappler, B. Ketzer, A. Polouektov, L. Ropelewski, F. Sauli, E. Schulte, L. Shekhtman, A. Sokolov, *Discharge studies and prevention in the gas electron multiplier (GEM)*, Nuclear Instruments and Methods in Physics Research Section A: Accelerators, Spectrometers, Detectors and Associated Equipment, Volume 479, Issues 2–3, 2002.

[52] M. Seidel, *Microscopic Simulation of GEM Signals*, Bachelorarbeit in Physik, 2018.

[53] H. Keller, *Novel GEM detectors for CMS and exotic physics searches at the HL-LHC*, CERN-THESIS-2018-349, 2018.

[54] Hyun Jae Cho, Seung Kook Ko, Sang Kyun Nha, *Double K-Shell Vacancy Production in the Electron Capture Decay of* ^{109}*Cd*, Journal of the Korean Physical Society, Vol. 31, No. 2, 1997.

[55] Texas Instruments, *THS3202, 2GHz Current Feedback Amplifier*, Datasheet, 2010.

[56] L. Benussi, S. Bianco, M.A. Caponero, S. Colafranceschi, M. Ferrini, F. Felli, L. Passamonti, D. Pierluigi, A. Polimadei, A. Russo, G. Saviano, C. Vendittozzi, *A Novel Temperature Monitoring Sensor for Gas-Based Detectors in Large HEP Experiments*, Physics Procedia, Volume 37, 2012.

[57] CAEN, *A1676A EASY Branch Controller*, Manual, 2020.

[58] CAEN, *A3486 3-phase 220/400 Vac . 48 Vdc (2 ch x 2 kW/1 ch x 4 kW) Converter*, Manual, 2007.

[59] CAEN, *A3016 6 Channel 8 V / 16 A / 90 W Power Supply Board*, Manual, 2012.

[60] CAEN, *SY4527 Universal Multichannel Power Supply System*, Manual, 2020.

[61] CAEN, *A1515TG 14 Channels 1 kV (1 mA) Individual Floating Channel Dual Range Boards for Triple GEM detectors*, Manual, 2020.

[62] E.R. Starling, *Status of the Readout Electronics for the Triple-GEM Detectors of the CMS GE1/1 System and Performance of the Slice Test in the 2017-18 LHC Run*, PoS(TWEPP2018)132, 2018.

[63] PICMG, *MicroTCA Overview*, https://www.picmg.org/openstandards/microtca.

[64] A. Svetek et al., *The Calorimeter Trigger Processor Card: the next generation of high speed algorithmic data processing at CMS*, JINST 11 02 C02011, 2016.

[65] P. Aspell et al., *VFAT3: A Trigger and Tracking Front-end ASIC for the Binary Readout of Gaseous and Silicon Sensors*, IEEE Nuclear Science Symposium and Medical Imaging Conference Proceedings (NSS/MIC), 2018.

[66] J. Hauser et al., *Experience with Trigger Electronics for the CSC System of CMS*, 10th Workshop on Electronics for LHC and Future Experiments, pp.292-297, 2004.

[67] CERN, *FEASTMP Radiation and magnetic field tolerant 10W DC/DC converter module*, Datasheet, 2016.

[68] P. Moreira et al., *The GBT, a Proposed Architecture for Multi-Gb/s Data Transmission in High Energy Physics*, Proceedings of the Topical Workshop on Electronics for Particle Physics, pp.332-336, 2007.

[69] P. Leitao et al., *Test bench development for the radiation Hard GBTX ASIC*, JINST 10 C01038, 2015.

[70] A. Caratelli et al., *The GBT-SCA, a radiation tolerant ASIC for detector control and monitoring applications in HEP experiments*, JINST 10 C03034, 2015.

[71] P. Aspell et al., *VFAT2: A front-end "system on chip" providing fast trigger information and digitized data storage for the charge sensitive readout of multi-channel silicon and gas particle detectors*, IEEE Nuclear Science Symposium Conference Record, 2008.

[72] Sharma R.K. et al., *Test Beam Study of Gas Electron Multiplier (GEM) Detectors for the Upgrade of CMS Endcap Muon System*, Springer Proceedings in Physics 203, 2018.

[73] G. Mocellin, *Commissioning and prospects of the first GEM station at the CMS experiment*, PoS(ICHEP2020)755, 2020.

[74] F. Fallavollita, *Triple-Gas Electron Multiplier technology for future upgrades of the CMS experiment: construction and certification of the CMS GE1/1 detector and longevity studies*, CERN-THESIS-2018-349, 2018.

[75] Amptek, *Mini–X X-Ray Tube*, Manual, 2018.

[76] M. Deutsch et al., *X-Ray Spectrometry of Copper: New Results on an Old Subject*, Journal of research of the National Institute of Standards and Technology 109, 75-98, 2004.

[77] M.J. Berger, J.S. Coursey, M.A. Zucker, J. Chang, *Stopping-Power & Range Tables for Electrons, Protons, and Helium Ions*, NIST Standard Reference Database 124, 2017.

[78] M. Bianco, B. Dorney, J.A. Merlin, *GE1/1 Quality Control : instructions*, CMS GEM INTERNAL NOTE, 2016.

[79] Keithley, *Keithley Model 6487 Picoammeter/Voltage Source*, 6487-901-01 Rev. D, 2020.

[80] M. Ressegotti, *A new design using GEM-based technology for the CMS experiment*, JINST 12 C07003, 2017.

[81] CMS GEM Detector Performance Group, *GEM DPG Public Page*, https://twiki.cern.ch/twiki/bin/view/CMSPublic/GEMDPGPublic.

[82] M.J. French, L.L. Jones, Q. Morrissey, A. Neviani, R. Turchetta, J. Fulcher, G. Hall, E. Noah, M. Raymond, G. Cervelli, P. Moreira, G. Marseguerra, *Design and results from the APV25, a deep sub-micron CMOS front-end chip for the CMS tracker*, Nuclear Instruments and Methods in Physics Research Section A: Accelerators, Spectrometers, Detectors and Associated Equipment Volume 466, Issue 2, 2001.

[83] S. Martoiu et al., *Development of the scalable readout system for micro-pattern gas detectors and other applications*, JINST 8 C03015, 2013.

[84] M. Abbas et al., *Detector Control System for the GE1/1 slice test*, JINST 15 P05023, 2020.

[85] I. Vai, *Commissioning and performance of the GE1/1 slice test detectors*, Nuclear Instruments and Methods in Physics Research Section A: Accelerators, Spectrometers, Detectors and Associated Equipment Volume 936, 2019.

[86] E.R. Starling, *Detection and Mitigation of Propagating Electrical Discharges Within the Gas Electron Multiplier Detectors of the CMS Muon System for the CERN HL-LHC*, CERN-THESIS-2020-229, 2020.

[87] N. Pozzobon, *The CMS Muon System performance during the LHC Run-2*, JINST 14 C11031, 2019.

[88] F. Ivone, *Discharge mitigation strategies for the CMS GE1/1 Triple-GEM detectors*, JINST 15 C05009, 2020.

[89] Megger, *MIT485 insulation and continuity tester*, User Guide.

[90] L. Felipe Ramirez and J. Jaramillo, *GE1/1 QC6 quality control instructions*, CMS GEM INTERNAL NOTE, 2019.

[91] A. Irshad et al., *Production, Quality Control and Performance of VFAT3 Front-end Hybrids for the CMS GE1/1 Upgrade*, PoS TWEPP2019 080, 2020.

[92] *Box plot*, https://en.wikipedia.org/wiki/Box_plot.

[93] R. Frühwirth, *Application of Kalman filtering to track and vertex fitting*, Nuclear Instruments and Methods in Physics Research A262 444-450, 1987.

Eidesstattliche Erklärung

Declaration of Authorship

I, Giovanni Mocellin

declare that this thesis and the work presented in it are my own and has been generated by me as the result of my own original research.

Hiermit erkläre ich an Eides statt / I do solemnely swear that:

1. This work was done wholly or mainly while in candidature for the doctoral degree at this faculty and university;

2. Where any part of this thesis has previously been submitted for a degree or any other qualification at this university or any other institution, this has been clearly stated;

3. Where I have consulted the published work of others or myself, this is always clearly attributed;

4. Where I have quoted from the work of others or myself, the source is always given. This thesis is entirely my own work, with the exception of such quotations;

5. I have acknowledged all major sources of assistance;

6. Where the thesis is based on work done by myself jointly with others, I have made clear exactly what was done by others and what I have contributed myself;

7. None of this work has been published before submission.

date

signature